

5/28/86

Proposal for Upgrading
the
Collider Detector at Fermilab

CDF Collaboration*

With the successful test run of CDF during September-October, 1985 and the beginning of physics running later this year, now is the appropriate time to begin a specific program of detector upgrades so that the full physics potential of CDF at the Tevatron Collider can be exploited in an optimum way. We seek PAC guidance and approval of our plans to go beyond the original scope of CDF.

The basic design and physics goals of CDF have not changed substantially from our 1981 Design Report. Experience at the CERN S \bar{p} pS collider confirms that CDF will be a very powerful instrument for exploring new physics. Essentially all of the hardware will be completed for the first physics run in late 1986; final quantities of some front-end electronics and partial sampling in the forward hadron calorimeters had to be delayed until FY1987 because of actual funding schedules. Thus, by the beginning of 1987, we will have completed the base detector and will begin to explore the new physics regime made possible by the Tevatron.

Numerous suggestions have been made for enhancing the physics potential of CDF by building additional detector components. The collaboration has examined these in workshops and informal discussions and is prepared to move forward with certain upgrades as soon as support can be secured. Because of our commitment to an aggressive and intensive physics program with the base detector, we have limited current upgrade plans to projects with very high priority. These high priority improvements are:

- 1) Completion of the Level-3 trigger system. This is a fully programmable trigger system based on a farm of ACP microprocessors that can run detailed analysis codes for event selection to reduce the rate of events logged for off-line analysis. Level-3 will also be used to aid in monitoring the experiment and to isolate rare events for rapid analysis.
- 2) Construction of muon spectrometers (super-toroids) to provide muon identification, momentum measurements, and triggers in the intermediate angle range between the forward muon toroids and the central muon detectors where there is no muon coverage in the base plan.

*See Appendix A

- 3) Construction of a transition radiation detector system to cover the forward/backward region for improving electron identification in this region where magnetic analysis is ineffective.
- 4) Development of a micro-vertex detector system to aid in identifying particles with intermediate lifetimes such as tau leptons and hadrons containing bottom quarks.

Each of these high priority upgrades differs in its stage of development and overall effort required. Therefore, we are treating them separately and we seek different kinds of advice and approval from the PAC. Nevertheless, all of these upgrades are very important to CDF and all must be completed in a timely fashion to best exploit the physics opportunities of Tevatron I.

It has long been recognized that a "FORTRAN-Programmable", Level-3 trigger system is very important when the collider luminosity exceeds roughly $10^{29} \text{ cm}^{-2}\text{s}^{-1}$. Since this is likely to happen by the end of 1987, CDF decided to begin constructing a Level-3 system even though full funding has not been secured. After an extensive internal review, CDF decided to base its Level-3 system on the Fermilab ACP system. The system is described and its current status is summarized in Appendix B.

Funds to build the necessary data acquisition system interfaces and first pieces of the ACP farm were taken from contingency and were provided through the US/Japan Accord. However, new sources of support are required to complete Level-3 and bring it up to full performance. As indicated in Appendix B, approximately \$367K is needed for this. We are requesting PAC concurrence with our plans for Level-3 and its support for our efforts to secure funding to complete Level-3.

With the experience gained in assembling CDF and moving large detector pieces in and out of the B0 collision hall, it is now possible to design a single muon toroid system that covers the polar angle range 16° to 55° . This system, the Muon Supertoroids, can thus join our existing forward/backward muon toroids and the central muon system giving continuous muon detection, triggering, and momentum determination over nearly 8 units of rapidity. The proposed muon upgrade is described in Appendix C. Final engineering of this system can be completed during FY87 and construction could be finished in FY89. We are requesting PAC support of this upgrade so that final engineering and construction can begin as soon as possible.

In the forward/backward regions, electron identification can be improved significantly by adding a TRD system as described in Appendix D. Because the momentum analysis from the solenoid is essentially nonexistent at these small angles, we view the TRD system as necessary to bring our forward electron capabilities up to a level comparable with the central and end plug regions. This uniformity of response over the full acceptance is a very

important part of the CDF design. The success of the Leingrad-Fermilab TRD system in recent hyperon fixed target studies gives us confidence that such TRD systems can be engineered reliably. In the case of CDF, this is a natural addition because of the relatively long available free space between the end plug and the forward EM shower counters. Our program for the TRD system is to begin detailed engineering, design and prototyping studies early in FY87 so that construction of the chamber and radiator assemblies could begin by the end of that year, pending the successful outcome of the design effort. The entire system would be installed in CDF by the end of FY88. Therefore, we are seeking PAC support for the TRD upgrade to begin as soon as possible so that it can be completed before the end of FY 1988.

The power of micro vertex detectors has been demonstrated in a number of experiments. Indeed, this may be the only technique possible for identifying b-quark mesons and the tau leptons with sufficient reliability and efficiency to allow physics studies with these particles. CDF is engaged in a development project with the goal of installing a micro vertex detector based on Si strip technology after the first or second full running period (during FY88, most likely). The detector and the current R&D activity is described in Appendix E. We have reviewed the development project carefully within CDF and recognize that several milestones must be met before a full system can be built and installed. These include: 1) the successful operation of the special front-end electronics in conjunction with the silicon strips, 2) a complete mechanical design that maintains alignment of the Si strips without causing unacceptable backgrounds in other parts of CDF, and 3) physics studies based on actual CDF events which demonstrate that such secondary vertices can be found with reasonable efficiency.

We recognize that there are risks in installing a Si vertex detector along with the strong physics benefits. We feel that an aggressive R&D program is indicated in this case because the potential physics return is so high. As soon as the above milestones are reached, we shall move forthwith to installation of the Si vertex detector so that physics studies using it can begin during FY88. We are seeking the endorsement by the PAC of this plan to develop a Si vertex detector.

A summary of the estimated costs for these upgrades is given in Appendix F. An optimum funding profile is also given there. Note that the line for facility improvements has been discussed with Fermilab and the DOE at our last DOE Review. This represents the minimal equipment support needed for routine development and upgrading of CDF.

The first three upgrades discussed above can be viewed as extending the capabilities of CDF within the general scope of the base detector design. For example, the muon supertoroids and TRD fill out the lepton coverage over the full CDF acceptance. On the other hand, the Si VTX detector will add a significant new capability to CDF.

Another upgrade that has been studied is to increase the amount of absorber and tracking outside the central calorimeters for improving muon identification in the central region of CDF. Such a system appears feasible, but we have decided not to propose this upgrade until after we have actual running experience with CDF.

Fermilab is considering an improvement program to increase significantly the luminosity of the Tevatron Collider. We are now studying the impact of this upgrade on CDF. Some modifications to our electronics and trigger systems will be required and these needs will be presented to the PAC when a firm luminosity upgrade plan is established.

CDF COLLABORATION

R. Diebold, W. Li, L. Nodulman, J. Proudfoot, R. Rezmer,
P. Schoessow, D. Underwood, R. Wagner, A. Wicklund

Argonne National Laboratory

J. Bensinger, C. Blocker, M. Contreras, L. DeMortier,
P. Kesten, L. Kirsch, H. Piekarz, S. Tarem

Brandeis University

D. Amidei, M. Campbell, H. Frisch, C. Grosso-Pilcher,
J. Hauser, T. Liss, G. Redlinger, H. Sanders, M. Shochet,
R. Snider, J. Ting, Y. Tsay

University of Chicago

M. Atac, E. Barsotti, P. Berge, M. Binkley, J. Bofill, J.T. Carroll,
J. Cooper, C. Day, F. Dittus, T. Droege, J. Elias, G.W. Foster,
J. Freeman, I. Gaines, J. Grimson, J. Huth, H. Jensen, R. Kadel,
R. Kephart, A. Mukherjee, C. Nelson, C. Newman-Holmes, J. O'Meara,
A. Para, J. Patrick, D. Quarrie, S. Segler, D. Theriot,
A. Tollestrup,* K. Turner, C. van Ingen, R. Vidal, R. Wagner,
Y. Yamanouchi, G.P. Yeh, J. Yoh

Fermi National Accelerator Laboratory

S. Bertolucci, M. Cordelli, M. Curatolo, B. Esposito,
P. Giromini, S. Miozzi, S. Miscetti, A. Sansoni

INFN - - Frascati, Italy

G. Brandenburg, D. Brown, R. Carey, M. Eaton, A. Feldman, E. Kearns,
J. Oliver, E. Sadowski, R. Schwitters,* M. Shapiro, R. St. Denis

Harvard University

*Spokesmen

G. Ascoli, S. Bhadra, R. Downing, S. Errede, L. Holloway,
I. Karlinger, H. Keutelian, U. Kruse, R. Sard,
V. Simaitis, D. Smith, T. Westhusing

University of Illinois

Y. Arai, Y. Fukui, S. Mikamo, M. Mishina

KEK, Japan

W. Carithers, W. Chinowsky, R. Ely, M. Franklin, C. Haber,
R. Harris, B. Hubbard, J. Siegrist

Lawrence Berkeley Laboratory

D. Connor, L. Gladney, S. Hahn, N. Lockyer, M. Miller,
T. Rohlay, R. VanBerg, J. Walsh, H. Williams

University of Pennsylvania

G. Apollinari, F. Bedeschi, G. Bellettini, N. Bonavita,
L. Bosisio, F. Cervelli, R. Del Fabbro, M. Dell'Orso, E. Focardi,
P. Giannetti, M. Giorgi, A. Menzione, R. Paoletti,
G. Punzi, L. Ristori, A. Scribano, P. Sestini,
A. Stefanini G. Tonelli, F. Zetti

INFN -- University of Pisa, Italy

V. Barnes, A. Byon, K. Chadwick, A. Di Virgilio, A. Garfinkel,
S. Kuhlmann, A. Laasanen, M. Schub, J. Simmons

Purdue University

S. Belforte, T. Chapin, G. Chiarelli, N. Giokaris,
K. Goulios, R. Plunkett, S. White

Rockefeller University

A. Beretvas, T. Devlin, U. Joshi, K. Kazlauskis,
N. Pearson, T. Watts

Rutgers University

J. Buchholz, S. Cihangir, D. DiBitonto, F. Marchetto,
P. McIntyre, T. Meyer, R. Webb

Texas A&M University

F. Abe, Y. Hayashide, M. Ito, T. Kamon, S. Kanda, Y. Kikuchi, S. Kim,
K. Kondo, M. Masuzawa, T. Mimashi, S. Miyashita, H. Miyata, S. Mori,
Y. Morita, T. Ozaki, M. Sekiguchi, M. Shibata, Y. Takaiwa,
K. Takikawa, A. Yamashita, K. Yasuoka

University of Tsukuba, Japan

J. Bellinger, D. Carlsmith, D. Cline, R. Handler, J. Jaske, G. Ott,
L. Pondrom, J. Rhoades, M. Sheaff, J. Skarha, T. Winch

University of Wisconsin

Appendix B

To: CDF
From: Terry Carroll, Tom Devlin
Subject: Level 3 Status

INTRODUCTION

The Level 3 trigger for CDF is a "processor farm", a system of parallel single board computers, each capable of applying selection criteria to events passed onto it by the hardware triggers at Levels 1 and 2. Level 3 is essential for CDF operation at luminosities of $10^{30}/\text{cm}^2/\text{sec}$. At this luminosity, roughly 50,000 interactions/sec are expected. The Level 1 Trigger uses direct analog outputs from the detector electronics to apply thresholds on such quantities as transverse energy, E_{\perp} in $3.5\mu\text{sec}$ between crossings. Thus, it is essentially free of deadtime. It will pass 10% of the events - 5,000 events/sec. Level 2, still working with analog information, applies more sophisticated criteria in event selection, e.g. clustering algorithms in the calorimetry. It is expected to reduce the trigger rate by another factor of fifty to about 100 events/sec. Level 2 requires several tens of μsec and introduces a deadtime of 10-20%. Thresholds at both levels are tunable to allow a reasonable balance of selection criteria and deadtime.

The 100 events/sec which pass Level 2 will be digitized (in about 1 msec) and sent to Level 3 for application of further trigger requirements in software. It is the goal of the Level 3 software to reduce the trigger rate to roughly 1 event/sec for archiving and 0.1 event/sec for "express line" processing. The hardware must have the input/output bandwidths and the processing speed to handle 100 events/sec in and up to 5 event/sec out.

The system chosen for Level 3 is ACP, the Advanced Computer Program, which was developed at Fermilab for offline data analysis, and is now being developed for commercial production, marketing and support. The initial implementation of ACP single-board computers uses the Motorola 68020, a 32-bit, 16.8-MHz microprocessor (μP) with an associated floating-point coprocessor. Early benchmarks on this board with the Absoft Fortran-77 Compiler indicate a performance of about 0.6 Vax-780. Boards using other μP chips can added to the system as advances in technology occur.

The immediate goal of the Level 3 project is the develop hardware and software necessary for online operation of a prototype system with ~ 10 Vax equivalents of processing power for the December, 1986, run. A fully-implemented system with roughly 50 Vax equivalents of processing power is needed for the run in late 1987.

SPECIFICATIONS

A number of requirements have been placed on the Level 3 hardware and software system. Some are dictated by the data rates expected, and others by our goal of making it easy to transport offline analysis algorithms to the online code in Level 3.

1. Level 3 must be fully integrated into the data acquisition system (DAQ). It must be capable of exchanging messages with the Buffer Manager, a μ Vax which controls the flow of data in the DAQ.
2. The system must be capable of processing Level 2 triggers at 100 Hz and support Level 3 output rates up to 5 Hz. This requires a data transfer rate from Fastbus to the ACP processor memory of about 20 MBytes/sec (100 events/sec, 100 KBytes/event, 50% duty factor).
3. Easy transport of trigger algorithms from offline programs to the online environment is essential. Level 3 will provide online filtering with algorithms written in Fortran-77. Various general-purpose software facilities used offline will be available in the online environment. Examples of this are: the YBOS memory management system, histogram entry routines, and parts of CERNLIB.
4. The trigger data base for Level 3, whereby trigger requirements are specified for a given data run by GDF operations crews, will be compatible with those for Levels 1 and 2 triggers.

HARDWARE STATUS

A Level 3 test system is currently installed on the 9th floor of Wilson Hall immediately adjacent to the ACP development area. The host computer for the system is a Vax-780 (BSNDBG) equipped with a UPI interface to Fastbus. Figure 1 shows the hardware components currently installed and in use for hardware and software development.

The ACP hardware resides in two VME crates (standard, commercially-available crates with high-bandwidth backplanes). High-speed data transfer between the ACP system and other devices occurs over the Branch Bus (BB), a 32-bit bus with appropriate control lines. The modules, on loan from the ACP group, are:

- two CPU's, 68020 single-board processors with 2 MBytes memory,
- a VRM (VME resource module) crate controller,
- a BVI, Branch Bus to VME interface,
- a BBC, DEC Q-bus to Branch Bus interface,
- a QVI, Q-bus to VME interface,

- a VME memory board, MEM, and
- two Branch Bus terminators, BBT's.

The development of software for the nodes is concentrated in the lower right-hand area of Fig. 1. It consists of a μ Vax which can communicate to the Branch Bus through a Q-bus interface (DRV11-WA). The full package of routines used by the ACP group for creating 68020 programs exists in the μ Vax (and other computers DECnetted to it). These include the Absoft Fortran-77 compiler, linkers and debuggers.

The CDF hardware development (upper left-hand area of Fig. 1) is focused on the FBBC, an interface between Fastbus and the Branch Bus. This is the channel for passing events from CDF to the ACP system, and is a critical-path item for the December, 1986, run.

Tests of the FBBC are controlled from the Vax-780 by an interactive program which allows the user to select any of a number of operating modes. Single-word and block transfers can be executed from the Vax memory through a data path which includes the UPI interface to Fastbus, the FBBC to Branch Bus, BVI to the VME backplane and into the CPU memory.

Transfer through the UPI is rather slow, and cannot test the full bandwidth of the FBBC-BVI combination. In order to test the system at high rates, the same interactive test routine includes the option of setting in motion an identical set of data transfer tests driven by a Fastbus-resident processor, the SSP. Test summaries and error logs are reported back to the Vax in the same form as its own tests. In addition to its advantage of higher speed, the SSP can run for extended periods without degrading the performance of the host Vax.

The SSP can currently block transfer to memory in 68020 nodes at a rate of 13 MBytes/sec with error rates of about 1 per million 32-bit words on average. Power, cabling and grounding are being cleaned up as a first step in eliminating the low-level error rates. The SSP has also executed pipelined writes to node memory at a rate of 18 MBytes/sec, - close to the design goal of 20 MBytes/sec.

CDF currently has two wirewrap FBBC modules. The design is quite stable, and during recent weeks, the BVI has been the subject of most hardware modifications to support high data transfer rates. This the first opportunity for the ACP development group to test the BVI at these rates, and they will produce an upgraded version of the BVI when these tests are complete. ACP is also interested in producing a printed-circuit or multi-wire version of the FBBC.

SOFTWARE DEVELOPMENT: CONTROL OF FASTBUS

For the current tests, subroutines have been written in Fortran to control various control and data transfer operations involving the FBBC. They have been coded in the standard CDF structure for compound Fastbus operations.

They generate commands for the Fastbus interface (UPI) which can be executed immediately, or incorporated into longer lists of UPI operations for more efficient execution. These should be useful without change in the main CDF online programs.

The interactive test program for the FBBC described in the previous section should continue to be useful for in situ tests of the FBBC and processor farm after it is moved to BO. Standard CDF software packages were used for user menus and memory management. The database defining the farm and the status and addresses of each node in the farm is the same as that which will be used by the online programs. The test program contains facilities for adding and deleting processors from the farm inventory, and testing the full system or any part of it.

SOFTWARE DEVELOPMENT: GENERAL FACILITIES

A number of software packages have been transferred directly or rewritten to run in the ACP node environment. The library of routines for the YBOS memory management systems is now operating in ACP. A number of routines from CERNLIB and UTILIB have been transferred to ACP. Some were originally in Vax-Macro, and had to be re-written in Fortran or in 68020 assembly language.

SOFTWARE DEVELOPMENT: TRIGGER ALGORITHMS

A prototype jet algorithm has been written for the nodes¹ and tested with data generated by a Monte Carlo simulation of CDF calorimeter data in standard YBOS format. The algorithm decodes the raw data banks, searches for transverse energy clusters in y - ϕ space (rapidity and azimuthal angle) and calculates jet parameters.

The algorithm has been run in both the real ACP nodes and in a node simulator which actually executes on a Vax. The latter was useful for implementing the Host/Node structure, but was immune to certain Vax/68020 differences.

Although errors in the Absoft Fortran-77 compiler have required some kluges, the trigger algorithm is fully operational in the nodes. A comparison with the Vax simulation shows identical results for the central calorimetry data. Benchmark comparisons between 68020 and Vax operation are being performed at this writing.

A new release of the Absoft compiler is now available. The trigger algorithm and associated libraries will be recompiled to eliminate the known bugs and kluges.

FUTURE HARDWARE DEVELOPMENT REQUIRED

In parallel with Level 3 another group is developing a Fastbus device call the Event Builder to assemble in one place the data from the many devices

which collect information from the various CDF detector subsystems. It is essential to high-speed data collection and transfer to the Level 3 processor farm.

The hardware Event Builder is unlikely to be ready before early 1987. Therefore, until it is ready, its function in the data acquisition system will be performed in the host Vax by software. Under these conditions, Level 3 will be served by a "consumer process" in the Vax which copies events from the data stream and transfers them back through Fastbus to the FBBC and the processor farm. This mode restricts Level 3 to a role as a monitor of accepted events, rather than an active data filter. It does constitute an extremely valuable opportunity to integrate Level 3 into the data acquisition network, to simulate the Level 1/Level 2 operation and check consistency between the trigger hardware and corresponding software model.

Level 3 should be prepared for the possibility that the Event Builder becomes operational early in 1987, prior to completion of that run.

A fully-integrated hardware Event Builder and Level 3 system is scheduled for the run later in 1987, and should be prepared for full luminosity. At this stage, two complete Event Builders are required, each served by a separate FBBC interface to the ACP processor farm.

Another important piece of hardware for high-speed operation is the Bus Switch to be built by the ACP group. This device will permit the Level 3 processor farm to be served by several parallel Branch Buses in order to increase bandwidth. It will allow simultaneous data transfer from each FBBC to the farm, and output of data from the farm to the data-logging system.

PERSONNEL

The following personnel are now working on the Level 3 project:

Andy Beretvas	Rutges	30%
Terry Carroll	Fermilab	
Tom Devlin	Rutgers	50%
Brenna Flaughner	Rutgers	
Ping Hu	Rutgers	(Summer)
Umesh Joshi	Rutgers	
Mark Larwill	Fermilab	
Youhei Morita	Tsukuba	50%
Zhizhong Zhang	Rutgers	(Summer)

Terry Watts is beginning a sabbatical leave from Rutgers and will spend about 50% of his time working on Level 3 compatibility with Level 1 and Level 2 triggers.

Irwan Sidharta, a Rutgers E.E. graduate, will spend the summer at Fermilab working with the group developing the Event Builder.

Ping Hu will complete his course work at Rutgers during the Fall semester and rejoin this project full time in December, 1986.

Bob Hollebeek from Penn has expressed interest in working on Level 3. Mark Larwill is supported in the development of the FBBC by other members of the technical staff of the data systems group. We have received a great deal of help from many members of the ACP group: Glenn Case, Rick Hance, Hari Areti and Art Cook in hardware development; Irwin Gaines, Joe Beal, Mark Fischler in software development. The overall interest, support and encouragement provided by Tom Nash has been very important.

SCHEDULE AND MILESTONES

1-Jun-86	Prototype trigger algorithm studies complete
20-Jun-86	FBBC development complete
1-Jul-86	Start installation of 2-crate processor farm with FBBC at CDF
31-Jul-86	Conversion of μ Vax management of processor farm to online environment, interface to Fastbus and exchange of messages with data acquisition controller
11-Aug-86	Move μ Vax to CDF
15-Sep-86	Complete development of "consumer process" to copy events from data stream to Level 3 processor farm
Dec-86	Beam. First operation of Level 3 with real events.
Early 87	Hardware Event Builder operational. Possible tests of Level 3 at high speed with real events before end of current run, processing power \sim 10 Vax-780 equivalents. Bus Switch complete
Fall 87	Full implementation of Level 3, $>$ 50 Vax-780 equivalents.

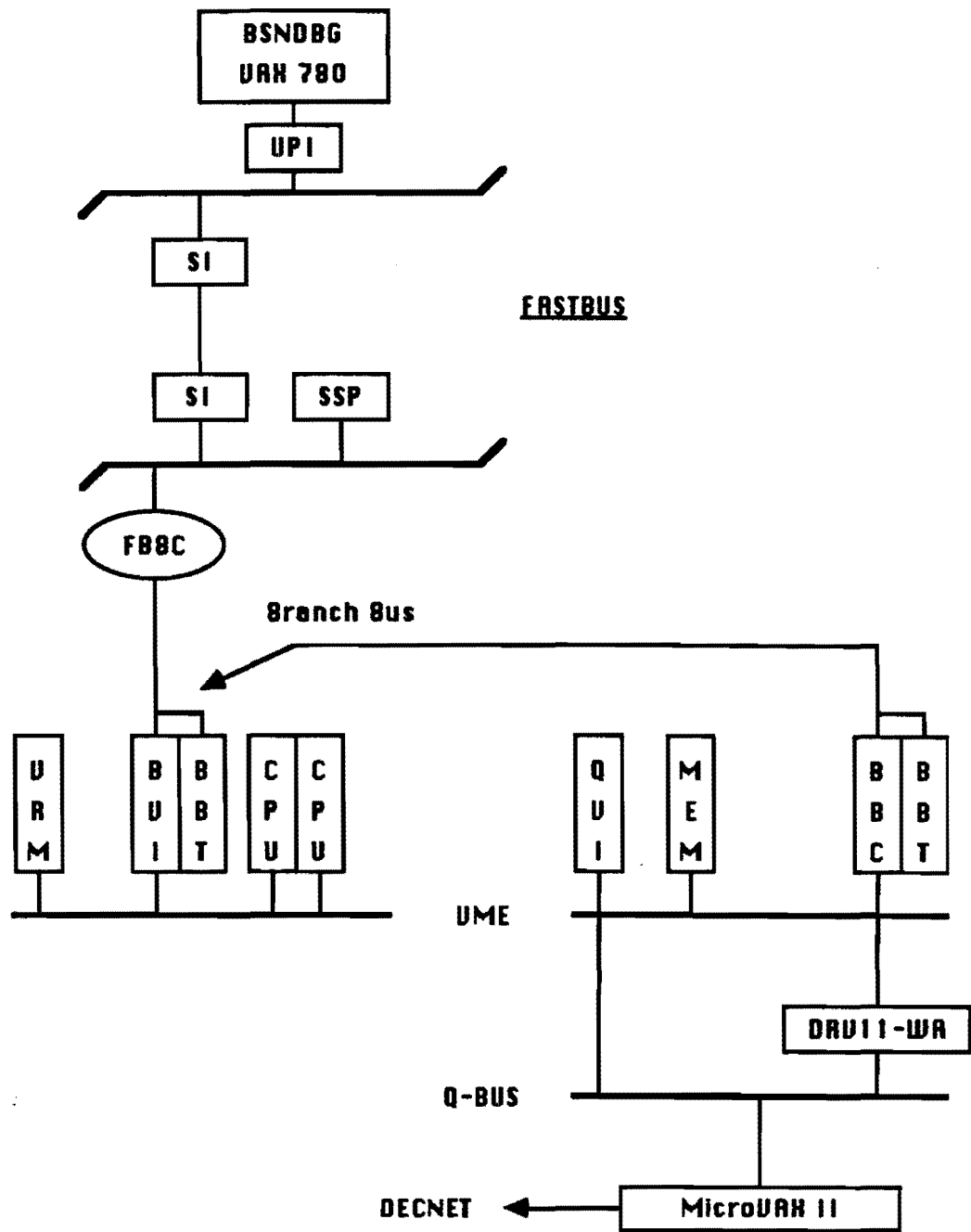


Fig. 1: LEVEL 3 TEST SYSTEM

May 22, 1986

T0: Dennis Theriot
 From: Terry Carroll
 Subject: Level 3 Cost Estimate

ITEM	UNIT COST	FY86		FY87	
		#	Cost	#	Cost
VME crate + power +cooling	\$2,000	4	\$8.	5	\$10.
(1) BBC	1,375	2	2.8	2	2.8
(1) BT	225	4	.9	4	.9
(1) BVI	1,525	4	6.1	8	12.2
(1) QVI	960	2	1.9	1	1.
(1) VRM	450	4	1.8	6	2.7
(1) 68020 CPU with 2 Mbytes DRAM	2,797	23	64.	60	168.
2 Mbyte memory expansion	800			80	64.
Branch Bus Switch	5,000			1	5.
(2) Misc. VME modules			7.		5.
FBBC	3,000	2		2	6.
QPI	8,000	1		1	8.
Limits & Alarms	1,500	1	1.5	2	3.
Rack	1,500	1		2	3.
MicroVAX II			24.3	1	22.
Misc. parts & documents			10.		3.
Contingency			15.		50.
(3) TOTAL			\$143K		\$367K

- (1) Prices are quotes from OMNIBYTE in West Chicago for operational modules with a 2 year warranty.
- (2) VME display modules, extender cards, memory modules, etc.
- (3) Estimate for FY86 includes funds from Tsukuba University and \$36K from Rutgers.

20 May 1985

SUPERTOROIDS FOR CDF:COMPLETING THE MUON COVERAGE

D. Carlsmith, D. Cline, R. Handler, A. Jaske, G. Ott,
L. Pondrom, J. Rhoades, M. Sheaff, J. Skarha, T. Winch
University of Wisconsin, Madison, WI

D. Theriot
Fermilab, Batavia, IL

ABSTRACT

It is proposed to complete the CDF muon coverage with a single toroidally magnetized spectrometer in the shape of a sunflower at each end of the central detector. The system would provide a high Pt muon trigger and momentum analysis over the range 16 to 55 degrees in polar angle.

INTRODUCTION

The proposed supertoroid system would complete the muon detection capability of the CDF detector from a polar angle of 3 degrees to 177 degrees relative to the circulating protons, corresponding to ± 3.6 units of pseudo-rapidity. In its present form the CDF detector has a gap in muon coverage between 17 and 55 degrees, or 1.25 units of pseudo-rapidity on each side of the collision point. This gap represents 35% of the total 7.2 units of rapidity in the central region of phase space accessible to CDF.

The physics capability of the CDF detector is substantially increased by this improvement in muon coverage. The identification and momentum measurement of single muons are important for missing ET measurements, for the study of W decays, and for tagging heavy flavors. Single muon detection increases linearly with phase space coverage. The efficiency of the detector for multi-lepton events increases faster than linearly because of the correlations among the sources of several prompt muons. Hence the completed muon coverage between 3 and 177 degrees has a very high priority as a detector upgrade.

The scope of this proposal is similar to previous proposals to provide 1) a toroidal spectrometer for the range 16-32 degrees and 2) additional unmagnetized iron and drift chambers patched on the central detector for the range 32-55 degrees, but is an integrated system with momentum analysis for the entire angular region 16 to 55 degrees. The system provides additional absorber for muon identification and an independent momentum measurement which may be compared with the measurement in the central tracking chamber for purposes of background rejection.

MAGNET DESIGN

Figure 1 shows a preliminary design of the magnet. At intermediate angles, the sunflower shape is natural: particle trajectories are normal to the bend direction and to the drift chambers, and detector area is minimized. Below 30 degrees, the magnet is 40 inches thick and has the shape of a standard toroid with a projective inner surface. The central 16 degree hole for the forward calorimeter could accommodate a previously proposed transition radiation detector. A conical shape for polar angle greater than 30 degrees is approximated by flat 'petals', 32 inches thick, with machined mating surfaces. Each petal covers 30 degrees in azimuth and weighs about 48 tons.

The geometry of the CDF detector and collision hall and the need to extract the endplug imply that any system in this angular range must be carefully sculpted. A number of interferences must be specially dealt with :

1) The largest interference is with the floor. We propose that steel be embedded in the floor to provide a smooth path for the magnetic flux in the petals of the sunflower. Whether this region (approximately 20% of the solid angle of the supertoroids) would be instrumented is under study.

2) The top 20 ton of the magnet does not fit in the door. We propose to assemble as much as fits in the assembly area and piece on the top in the collision hall under the assumption that the sunflower would not often be removed to the assembly area.

3) The I-beam supports for the beam-beam counters would be cut off and the counters supported from the sunflower inner surface.

4) The arms which support the plug would be cut off and an independent support system ('ATLAS') would be brought in for plug extraction. A reduced thickness of steel in the petals is nevertheless required to clear the plug supports at 0 degrees in azimuth.

5) The magnet would split in the center and each half would be pulled out and around the central detector for plug extraction.

6) The dewar would be moved.

The magnet would be saturated by four water-cooled coils with 40 Kamp-turns per coil of design similar to those used for the forward toroids. The design field varies from 16.5 Kg at the inner radius to 19.5 Kg at the outer radius.

CHAMBERS

We propose a double plane of electrodeless chambers (Figure 2), similar to the forward muon chambers, on the front and rear surfaces of the sunflower magnet. Chambers are arranged in the form of a pinwheel with each sense wire tracing out a 30 degree chord of a circle. The track position in azimuth is measured by 5 degree pads. As in the forward system, the cells are graded (proportional to polar angle), and project to the nominal interaction point, to provide for a Level 1 Pt threshold on the basis of a coincidence of hits in the front and rear chambers. The rear plane of chambers is set 10 inches off the magnet face to maximize analyzing power.

Given an accurately known vertex position, the momentum of the muon is determinable from the entrance and exit points with a multiple Coulomb scattering limited resolution of $\approx 20\%$. The central tracking chamber should measure the momentum with better resolution over most of the solid angle. Two planes are sufficient to provide a Level 1 muon trigger and a momentum measurement which may be compared with the central

tracking measurement.

TRIGGER

A trigger similar to the 300 % trigger of the forward system would consist of the OR of the set of coincidences of cell I in the front chamber with cells I-1, I, and I+1 in the rear chamber. To provide a Pt threshold at Level 1 similar to the forward muon system requires 118 trigger cells at about .011 units of pseudo-rapidity per cell, roughly twice the number of trigger cells in the forward system. The minimum and maximum drift times are 330 ns and 1116 ns respectively. In so far as the field of the solenoid is cylindrically symmetric, angular momentum conservation requires that a particle exit the flux return path pointing at the origin, rotated somewhat in azimuth, so unless central tracking information is used in the trigger, the solenoid field has no visible effect.

This trigger scheme is potentially compromised by the expected vertex distribution: the projective cells can not simultaneously image a distributed source efficiently and provide a high Pt threshold. Consider an infinite momentum track which passes through a fixed cell in the front plane of chambers. As the production point shifts away from $z=0$, the projection through the front chamber to the rear chamber shifts out of the projective cell. The displacement in units of cells at the rear chamber is approximately 1.4 cells per foot of displacement in z . To good approximation, the displacement in units of cells for graded cells is independent of polar angle.

This suggests a modified trigger which incorporates vertex information from the beam-beam counters. The rear chamber trigger bits are latched in a long shift register and shifted by an amount depending on the vertex position prior to forming the $1 * 3$ coincidences. The vertex position is provided at Level 1 by a simple meantimer circuit.

An idealized Monte Carlo simulation was made to study this trigger scheme. The sunflower and calorimeters were approximated as pieces of spherical shells with an average of 70 radiation lengths assumed for the calorimeters. The vertex resolution of the BBC meantimer was assumed to be 6 inches and was digitized in bins of 6 inches. In Figure 3, we show the trigger efficiency (including edge losses) as a function of Pt for a gaussian vertex distribution with the nominal r.m.s. of 1 foot, with and without the vertex correction. The improvement in the threshold function is limited by the crude resolution assumed for the Level 1 beam-beam counter information. The relatively high asymptotic efficiency after the vertex correction was found to be maintained for a vertex distribution with a sigma of 1 meter which implies that the trigger would be sensitive to interactions virtually anywhere on the axis of the central detector.

BACKGROUNDS

Three types of backgrounds may be anticipated: cosmic rays, pion and kaon decay in flight in the central tracking volume, and leakage from showers in the calorimeters (including decays of particles generated in the hadronic cascade). We present below rate estimates for each of these backgrounds.

An estimate of the cosmic ray background is found using the flux

$$\frac{dN}{d\Omega} = I_0 \sin^2(\theta) \sin^2(\phi)$$

and the trigger solid angle

$$\Delta\Omega \simeq 3 \times \text{cell area}/t^2$$

where $I_0 = 5 \times 10^{-3} (cm^2 - str - s)^{-1} (p > 2 GeV/c)$, t is the chamber separation and the cell area depends on polar angle. Integrating the flux times the solid angle over the top half of a sunflower and assuming that a trigger in the bottom half would have triggered the top half of the other sunflower, we find for 3 bunch operation at a luminosity of $10^{30} (cm^{-2} - s^{-1})$:

Rate = 558 Hz * 2 ends * (.171 live time) * (.5 probability of a BBC hit per Xing) = 95 Hz.

This rate could be reduced by a factor 6 if the azimuthal bite of a trigger cell were restricted to 5 degrees by incorporating the pad information into the trigger. Most of the cosmic rays which satisfy the trigger are at large polar angle where some rejection is expected from the requirement that a matching track be found by the central track processor.

We estimate the punchthrough and decay in flight using the single charged hadron inclusive production cross section from UA1:

$$\frac{d\sigma}{dP_t dY} = \frac{2 \pi A P_t}{(1 + \frac{P_t}{1.3 GeV/c})^n}$$

where $A=0.47 \text{ barn}/(GeV/c)^2$ and $n=8.07$ is the power extrapolated to 2 TeV using both ISR and collider data. (see PL 118B,169 (1982).)

To estimate the trigger rate from decay in flight, we numerically integrate the production cross section times a luminosity of $10^{30} (cm^{-2} - s^{-1})$ times the trigger efficiency as a function of P_t described above, times the decay probability assuming 20 % kaon content with .63 branching fraction to muons and a conservative angle independent decay length of 2 meters. The resulting rate estimate is 4.4 Hz per sunflower. This rate should be regarded as an order of magnitude estimate as it is extremely sensitive to the trigger rejection at low P_t and to the shape of the production distribution.

The momentum measurement by the sunflower should aid in the rejection of the problematic 'seagull' decays of low energy pions and kaons which fake high P_t tracks in the central tracking chamber.

For under 3 meters of iron equivalent, shower leakage is dominated by hadronic punchthrough rather than by real muons from decays of shower particles (see F.S. Merrit et al., NIM A245,27 (1986)). To estimate the trigger rate from shower leakage, we use the Snowmass '84 parameterization of the probability of greater than zero particles exiting an absorber length x of Fe equivalent:

$$P(x, p) = 0.13 p^{1.62} e^{-x/23cm}$$

Integrating the single charged hadron production rate times the leakage probability for a fixed absorption length of 2 meters Fe equivalent over the angular range of the sunflower, we obtain a rate of 5.5 Hz of leakage events at the rear of the each sunflower. The leakage rate into the front chambers is a factor of roughly 75 higher. All leakage events may not satisfy the trigger. However, the presence of a leakage particle in a rear chamber is likely to be associated with hits in more than one cell in the front chamber so the effect of the P_t threshold trigger is difficult to estimate without a detailed simulation of hadronic cascades.

A multiplicity cut in the front chamber could be used to eliminate such events. For the remaining events, a 2 GeV/c Pt threshold reduces the trigger rate due to leakage by a factor of 10.

COSTS

An estimate of the cost is obtained by scaling the costs of the present toroids. The surface area of a sunflower is about 2300 ft^2 , approximately 1.9 times the chamber area of three forward muon chamber planes. Each magnet is 812 tons, approximately equal to the volume of a toroid magnet pair. We require 8 coils with about 1600 feet of conductor per coil. For 118 trigger cells in polar angle, assuming half as many cells to resolve the ambiguity, with each cell covering 30 degrees in azimuth, each sunflower requires 4248 TDC channels. For 5 degree azimuth pads, dividing the polar angle into 10 regions, there are 1440 pads per sunflower. We then find the following estimates (both ends together):

Cost estimates(kilodollars)

Magnet Design		\$100k
Magnet		1590
Coils		300
Base		200
Power Supply		100
Chambers		558
ADC's	2880 ch * \$100/ch	288
TDC's	8496 ch * \$100/ch	850
Total		\$3986k

The total does not include the floor modification or the endplug support ATLAS.

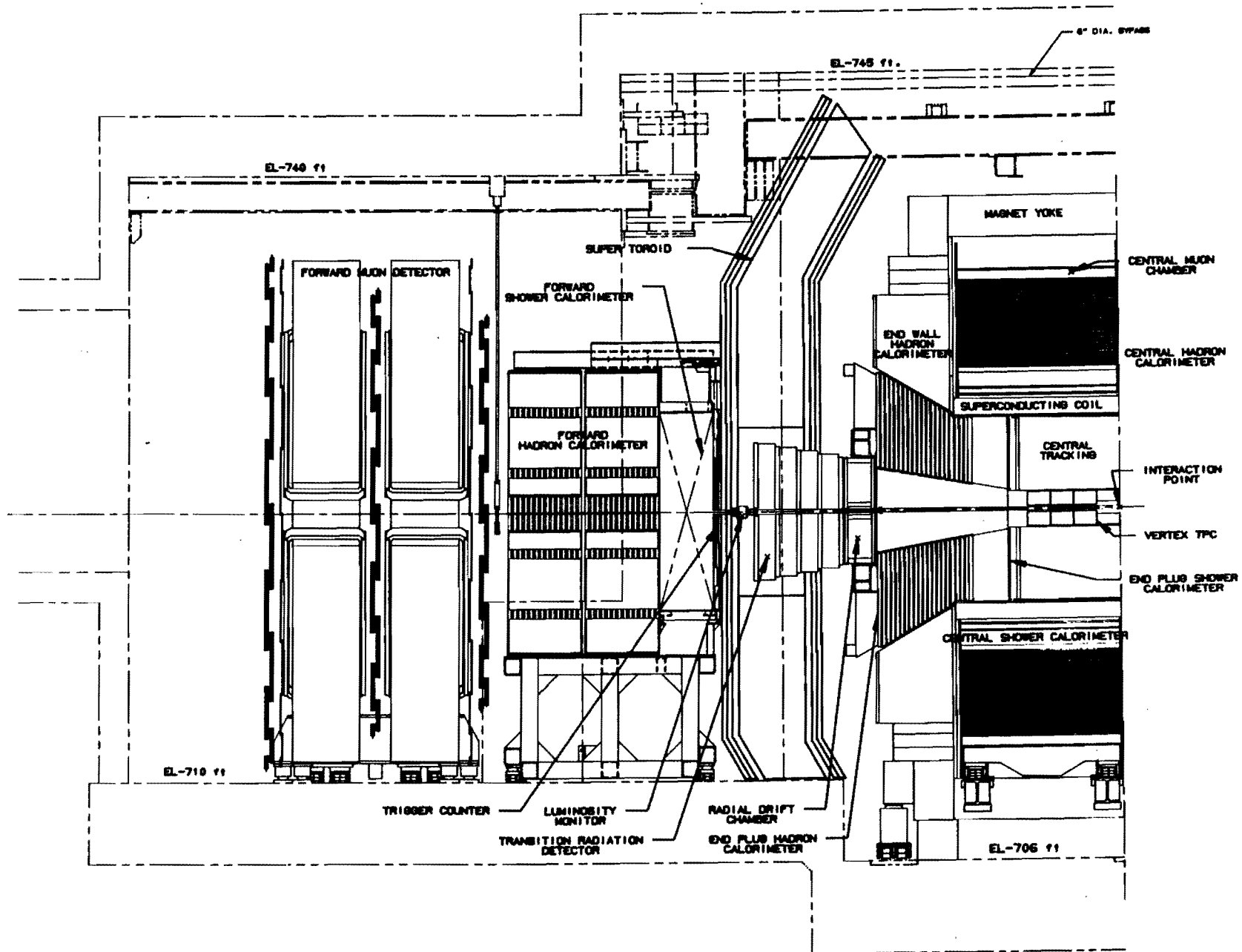


Figure 1

FIGURE 2

Supertoroid DMST Chambers (front face)

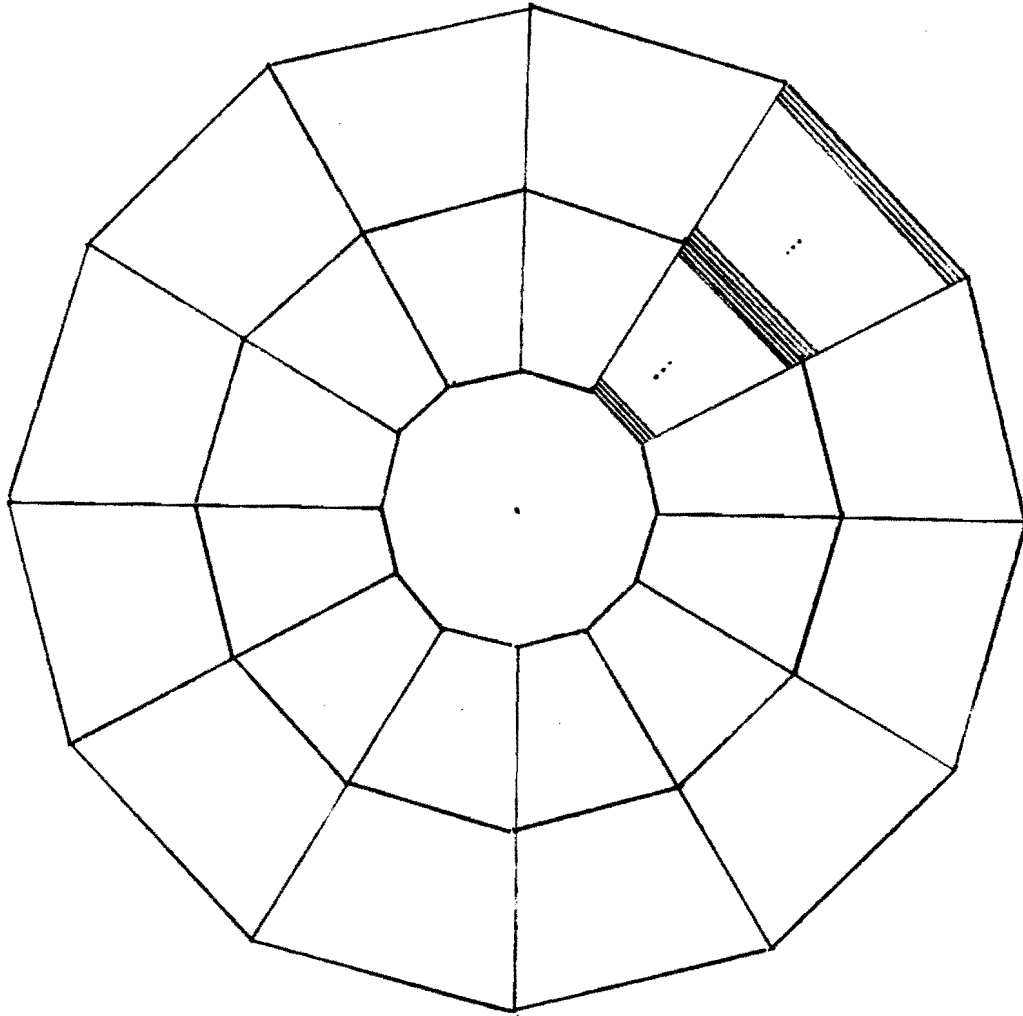


Figure 2

4'

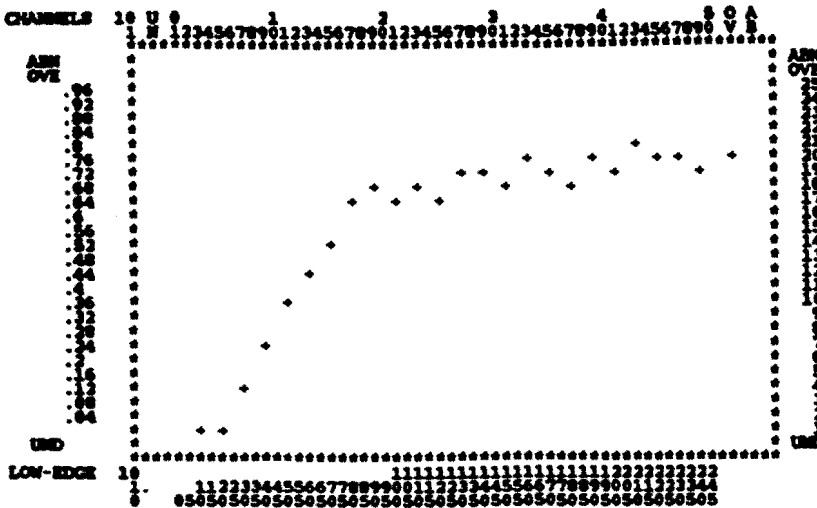
```

INITIALIZATION
SUPERS
FIELD 1.000000  BEAD DELI 43.45920  MESHCH 1.000000
SIZE 30.480000  FT THRESHOLD 0.000000  PTCHELL 0.000000
DELTA 0.1000000  INHIS 0 A 0.5004920  B 3.0000000
IRIG 0.000000  I INROAD 3 RAD 70.000000
NUMBER OF 300% CELLS 110 MIN FULL CELSZ 1.655000  MAX CELSZ 648.4800
S 100473
RADI OR PLANES 487.5200  $10.0000  $10.0000  648.4800
TRIGGER RATE 1.652231  FOR FT=0 TO 25

```

EFFICIENCY VS FT

BOOK ID = 1 DATE 7/ 5/86 NO = 1



300% 118 cells
no BBC correction

```

* SERIES = 25          PLOT -----|-----|-----
* SATURATION AT= INFINITY          STATISTICS -----|-----|-----
* SCALE = 1, 2, 3, 4, A, B
* STEP = 1, 2, 3, 4, MINIMUM=0

```

RESOLUTION

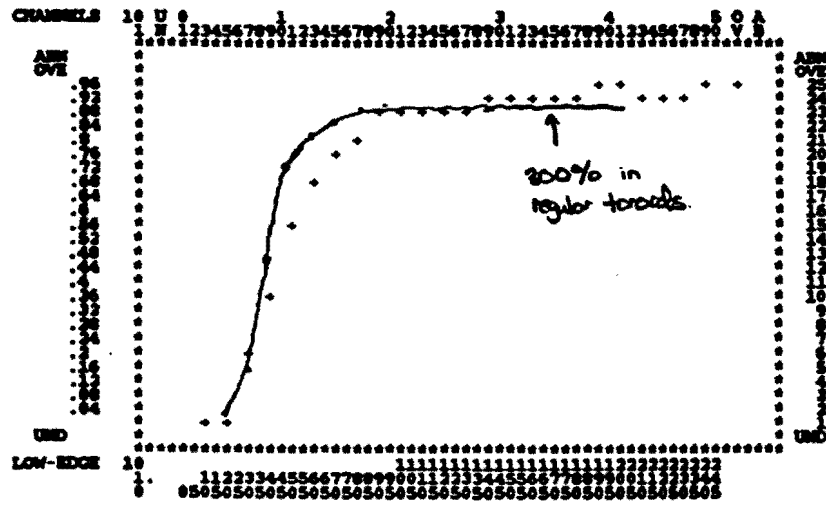
```

INITIALIZATION
SUPERS
FIELD 1.000000  BEAD DELI 43.45920  MESHCH 1.000000
SIZE 30.480000  FT THRESHOLD 0.000000  PTCHELL 0.000000
DELTA 0.1000000  INHIS 0 A 0.5004920  B 3.0000000
IRIG 0.000000  I INROAD 3 RAD 70.000000
NUMBER OF 300% CELLS 110 MIN FULL CELSZ 1.655000  MAX CELSZ 648.4800
S 100473
RADI OR PLANES 487.5200  $10.0000  $10.0000  648.4800
TRIGGER RATE 3.513911  FOR FT=0 TO 25

```

EFFICIENCY VS FT

BOOK ID = 1 DATE 7/ 5/86 NO = 1



300% corrected for
118 cells vertex with 6" resolution

```

* SERIES = 25          PLOT -----|-----|-----
* SATURATION AT= INFINITY          STATISTICS -----|-----|-----
* SCALE = 1, 2, 3, 4, A, B
* STEP = 1, 2, 3, 4, MINIMUM=0
* TRIGGER RATE REAR3 REAR3

```

Figure 3

Appendix D

A Proposal to Build a Transition Radiation Detector System for the Forward Angle Region of CDF

G. Brandenburg, M. Atac, J. Bensinger, E. Sadowski

1. Introduction

We propose to add a Transition Radiation Detection system in the forward/backward angle region of the Collider Detector at Fermilab (CDF) to improve electron identification. In this region such devices are ideally suited to the physics needs of CDF and to the geometrical space available. This region has no magnetic field to aid in particle identification, yet there is sufficient space along the beam line for a low mass TRD system. Such a system would not interfere with any existing CDF components.

The current version of the CDF detector has tracking chambers, calorimetry, and muon detectors covering most of the available solid angle. At 2 TeV, the 176 degrees of polar angle which are covered are totally within the "central region". Specifically, the total rapidity range of 2 TeV interactions is approximately ± 7.5 units, while the CDF detector covers ± 4 units. Thus the forward/backward region (2° - 10° at either end), which covers the pseudorapidity range of 2.4-4.0, is an integral part of the central region. The forward/backward region already has good muon detection efficiency; a TRD system in this region would provide electron identification with similar precision.

Good lepton identification is essential for much of the interesting physics available to CDF. In particular the production of heavy quark flavors, of W 's and Z 's, and "new physics" such as Higgs bosons will all have distinctive lepton signatures. The importance of good coverage of the small angle region is seen in Fig. 1, which shows the rapidity distribution of the decay leptons from W 's produced at 2 TeV. It is clear that the identification and measurement of both electrons and muons is required to the smallest lab angles possible. In a more general sense the decay products of any object with $\sqrt{s} \approx 80$ GeV will extend to rapidities of ± 4 . It is also possible that the production of heavy quark pairs may be enhanced by a diffraction-like mechanism at small angles and that their decay products would populate the forward region.

For the first CDF run the various detectors will be deployed as shown in Fig. 2. The smallest angles are covered by the forward tracking chambers (FTC), the Forward Electromagnetic and Hadron Calorimeters (FEMC and FHC), and the Muon Toroids. The existing calorimetry in the forward (and backward) region has a granularity of $\Delta\eta=0.1$ and $\Delta\phi=5^\circ$. The tower structure of these calorimeters is diagrammed in Fig. 3. The combination of FEMC, FHC, and FTC is able to adequately measure the position and energy of isolated electrons, provided they can be identified. However, because there is no appreciable magnetic field in this region, this identification must rely on the relative amounts of energy deposited in the three depth segments of the calorimetry, correlation of tracking information and shower centroids, and the width of the showers.

The lack of effective momentum measurement in the forward direction prevents using a comparison of the measured track momentum to calorimeter energy for electron identification. This comparison when used in the rest of the detector is an effective way of identifying the low pt pion plus photon background. We estimated that a TRD will give us an improvement of a factor of 10 to 50 over what we can do with the CDF fringe field alone. An improvement of this order is essential for such things as identifying semileptonic decays of heavy quarks.

A pion can masquerade as an electron in one of several ways: (a) a low momentum charged pion overlaps with with a π^0 , (b) a π^0 Dalitz pair is not properly correlated, (c) a charged pion produces an early electromagnetic shower in the calorimetry. Eliminating (a) and (b) currently depends on the the ability to match tracking information and shower positions. The problem of charged pion shower development , (c), is addressed in Figure 4, which shows the total energy deposited by 60 GeV π 's and e's in the Forward Electromagnetic Calorimeter. Figure 5 shows a correlation plot of the energy deposited in the two depth segments of the EM calorimeter for the same particles. Cuts were made on the ratio of EM energy to total energy, the ratio of the front half of the EM calorimeter to the total EM energy, and the shower width. For the test beam case shown here there was no hadron calorimeter data, so the measured beam momentum was used for the total energy. The table below shows that after all three cuts the π survival probability is less than 1% for reasonable e efficiencies. In a colliding beam environment, the total π survival probability will be about 1%. This is clearly not good enough if we need to uniquely separate electrons from the much more prolific pion background. A transition radiation detection system would improve the electron identification capabilities for both cases (a) and (c).

<u>Cut (cumulative)</u>	<u>e Efficiency(%)</u>	<u>π Survival Probability(%)</u>
EM/Total Energy	95	1.5
Depth Segmentation	94	0.5
Shower Width	90	0.4

The Forward Tracking Chambers are drift chambers with radial wires. This design gives an excellent measurement of the azimuthal coordinate, but a poor measurement of the polar angle. This will be mitigated somewhat by implementing current division on the wires. It has been proposed to build a second set of tracking chambers with azimuthal wires ("theta chambers") to provide an accurate orthogonal coordinate. Measuring both coordinates well will be important in cases (a) and (b) above for matching trajectories with showers in the FEM. We propose to build the TRD system with chambers that are similar in design to the theta chambers, and which will serve the dual function of measuring particle trajectories and detecting transition radiation.

The proposed TRD system is located approximately 5 m. from the interaction point. At this distance particles are separated sufficiently to be separately identified. In particular the typical separation of particles inside a jet will be ≈ 4 cm. at the inside edge of the detector.

2. Transition Radiation Detectors

The radiation of low energy photons as extremely relativistic particles pass through the successive layers with different indices of refraction is strongly dependent on the Lorentz factor $\gamma = 1/\sqrt{1-\beta^2}$. It saturates at $g \approx 10^4$. It is possible to enhance this effect by building a radiator which consists of many successive thin sheets of very lightweight material. Figure 6 shows the average number of TR photons produced when electrons and pions pass through a block consisting of ≈ 200 sheets of $17\mu\text{m}$. thick polypropylene. For electrons with energies above 5 GeV the number of expected photons is constant at approximately two. The number of TR photons for pions in the same energy range is seen to be much less than one.

A transition radiation detector system which consists of several modules of radiator and photon counting chambers will maximize the number of observed TR photons by decreasing the amount of material that a photon must traverse before detection. A Russian group has built a detector which consists of twelve such modules, each consisting of a 210 sheet radiator block and a photon-counting proportional chamber. Figure 7 shows the number of TR photons detected for π 's and e's in the 10-80 GeV region. On the basis of this distribution they obtain a π rejection factor of 1500 with an electron inefficiency of 0.5%.

In CDF we have a space in front of the forward calorimeters which is approximately 1.5m. in length. This is sufficient room for a four module TRD system. Based on the TR photon output for a single module shown in Fig. 6, we can estimate the pion survival rate as a function of electron inefficiency for such a four module system. This is shown in Fig. 8. It is predicted that less than 2% of pions will be misidentified as electrons with an electron inefficiency of less than 2%. This factor of 50 is independent of the factor of 100 obtained from the calorimeter depth segmentation, resulting in an overall π rejection factor of ≈ 5000 .

3. Construction Details

The transition radiation detection system we are proposing consists of four radiator blocks and five drift chambers as illustrated in Fig. 9. The system will immediately follow the FTC package. The proposed Muon Supertoroids are omitted in the drawing: if they are present the system will fit inside their aperture and no additional support strut will be necessary. The TRD system will be moved to the side together with the beam pipe if the end plug is to be removed.

The radiator blocks have an octagonal cross section to the beam and extend from the beam pipe to just beyond the ten degree cone. They consist of 250 sheets of 13 μm . mylar separated by 1 mm. and stretched between G10 frames. The sheets are randomly dimpled so that they maintain their separation from each other. This makes it possible to eliminate all framework from the "active area" of 2° - 10° . A method of dimpling the sheets with a warm rounded iron has been successfully tested. It is preferable to build each radiator block as a single unit not only to eliminate framework, but also because it is much easier to stretch the mylar sheets from a symmetrical frame. The mylar sheets are glued to the the frame with contact cement making it possible to add several sheets to the structure each day. It is also necessary to glue two strips of mylar together to form a wide sheet: commercially-available rolls will not cover the entire frame.

The drift chambers are proposed to have wires strung in the "theta chamber" geometry — see Fig. 10. There will be approximately 30 sense wires extending from 2° to 10° . These wires will be read out independently for each octant resulting in 240 signals per chamber. The frames of the chambers will be built from lightweight materials such as hexcell wherever possible. It will be necessary, however, to have an outer aluminum support structure. The chambers will be divided into halves for easy insertion and removal without necessitating the removal of the beam pipe.

Each chamber has a cell width along the beam of 2 cm. The actual drift chamber cell is separated by a fine mesh grid from a photon conversion gap which is 2.5 cm. in width. A section of a chamber is shown in Fig. 11. The entire chamber volume is filled with a Xenon-Argon gas mixture to enhance the radiation length. The ionization clusters produced from TR photons in the conversion gap are slowly drifted through a uniform field region to the mesh grid. From there they are accelerated to one of the sense wires. The signals from the TR photon conversions are delayed in time by at least 100 nsec. from the primary charged particle signals, allowing them to be counted separately. The chamber closest to the interaction point will be used for charged particle tracking purposes only, but will be built using the same design as the others.

The construction of both the radiator blocks and the conversion gap drift chambers would take place at the Harvard High Energy Physics Lab. The facility which was used to construct the FEM system will be retooled for this task. This area consists of a large clean room and six large jig plate tables. A possible layout for the radiator block production is shown in Fig. 12. This facility will be available for this work starting Sept. 1986. It should be possible to complete the entire system in time for the second major CDF run in 1987.

Some tests are planned for early 1987 using up to five prototype transition radiator blocks and test chambers to determine the necessary parameters for the readout electronics. Figure 13 shows a cross section view of one of the test chambers. A small number of 100 MHz flash ADC channels will be used for counting ionization clusters arriving from TR X-ray conversions in the conversion gap. The amplifier pulse shaping will be tuned in order to enhance the cluster counting efficiency. This study will be done by varying electron drift times in the conversion gap. The electric field in this gap can be varied independently on the test chamber.

4. Readout Electronics

The readout electronics for this system must serve two purposes. First it must perform a normal drift chamber TDC function for tracking purposes. Secondly it must scale the number of hits in an extended time window in order to count TR photon conversions. The initial tracking function takes place in the first ≈ 100 nsec. after the beam crossing. The second scaling function extends over the next ≈ 2 μ sec. It may be possible to implement a dynamic switching between these two functions, however, a simpler procedure is to split the signal and to perform the two operations in parallel.

The number of electronics channels per chamber is approximately 240. When both ends are included this means of total of 2400 channels for the entire system.

5. Cost Estimate

<u>Item</u>	<u>Cost</u>
Radiator Block Materials	\$ 35K
Drift Chamber Materials	\$ 45K
Assembly Labor (2MY)*	\$ 85K
Hardware and Supplies	\$ 30K
Tooling	\$ 20K
Shipping	\$ 5K
Electronics (2400 channels)	\$230K
Total Cost	\$450K

*This is additional labor — Harvard would supply approximately 4MY of technical labor to the project.

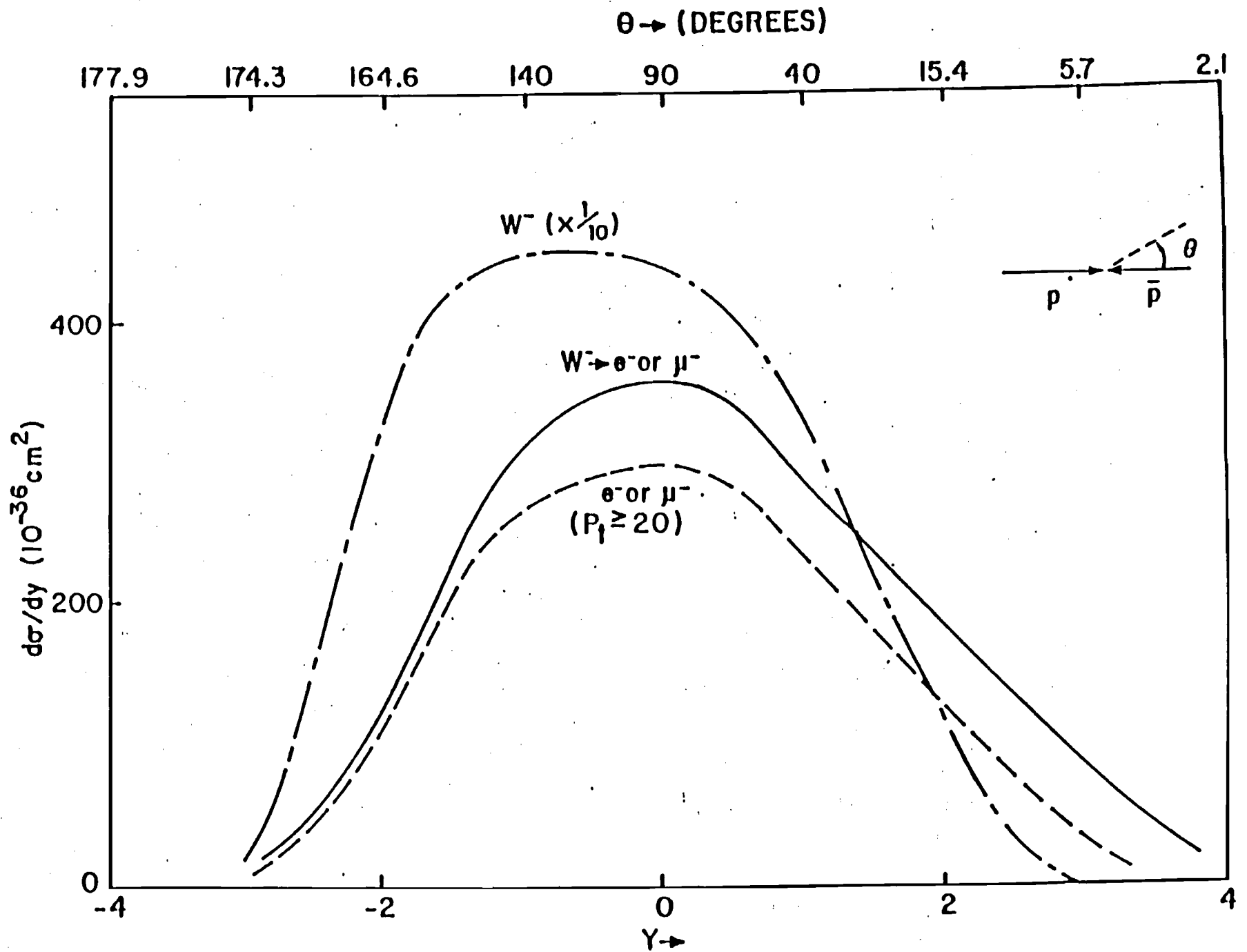


Figure 1

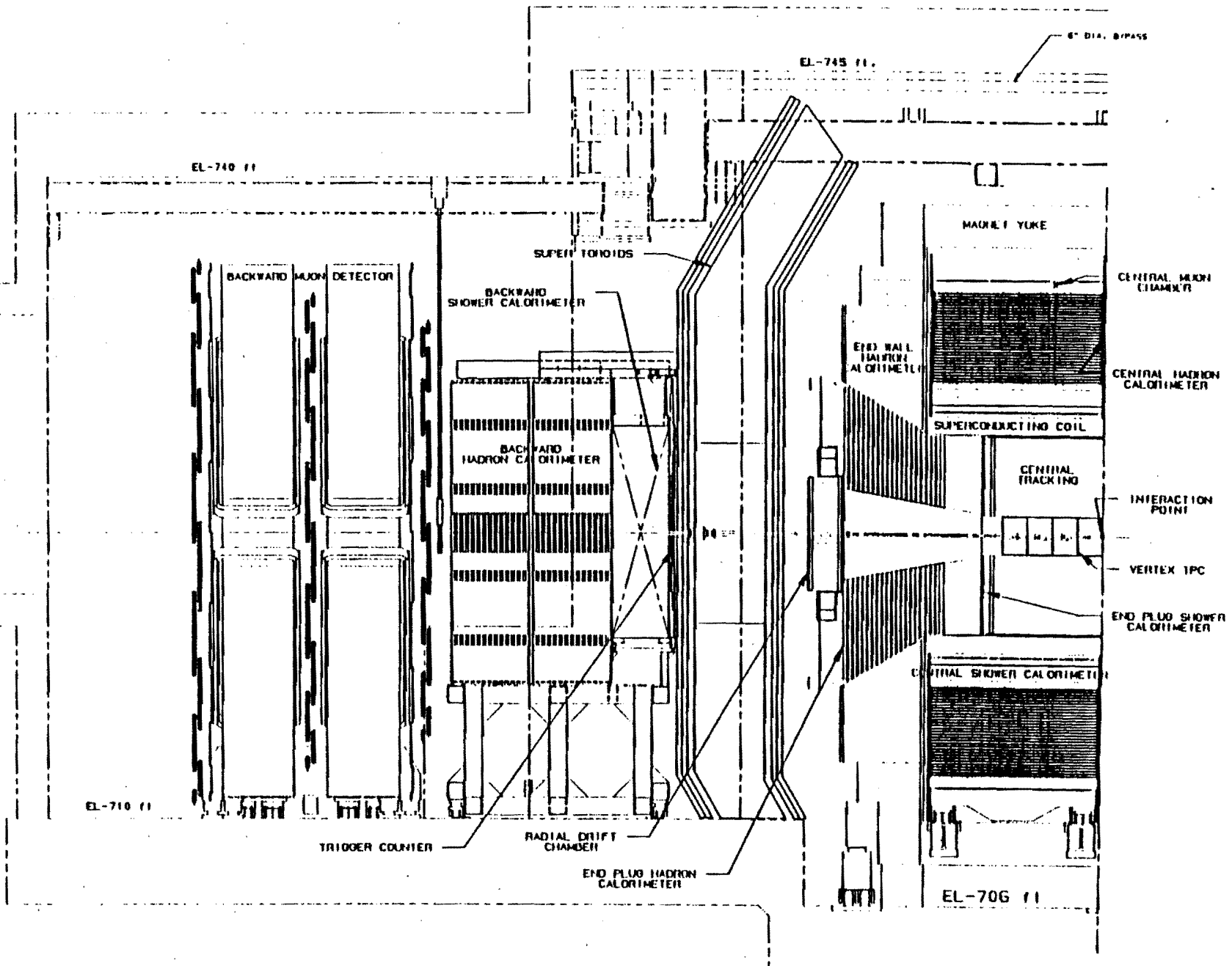


Figure 2

FORWARD EM CALORIMETER, PLANE 1

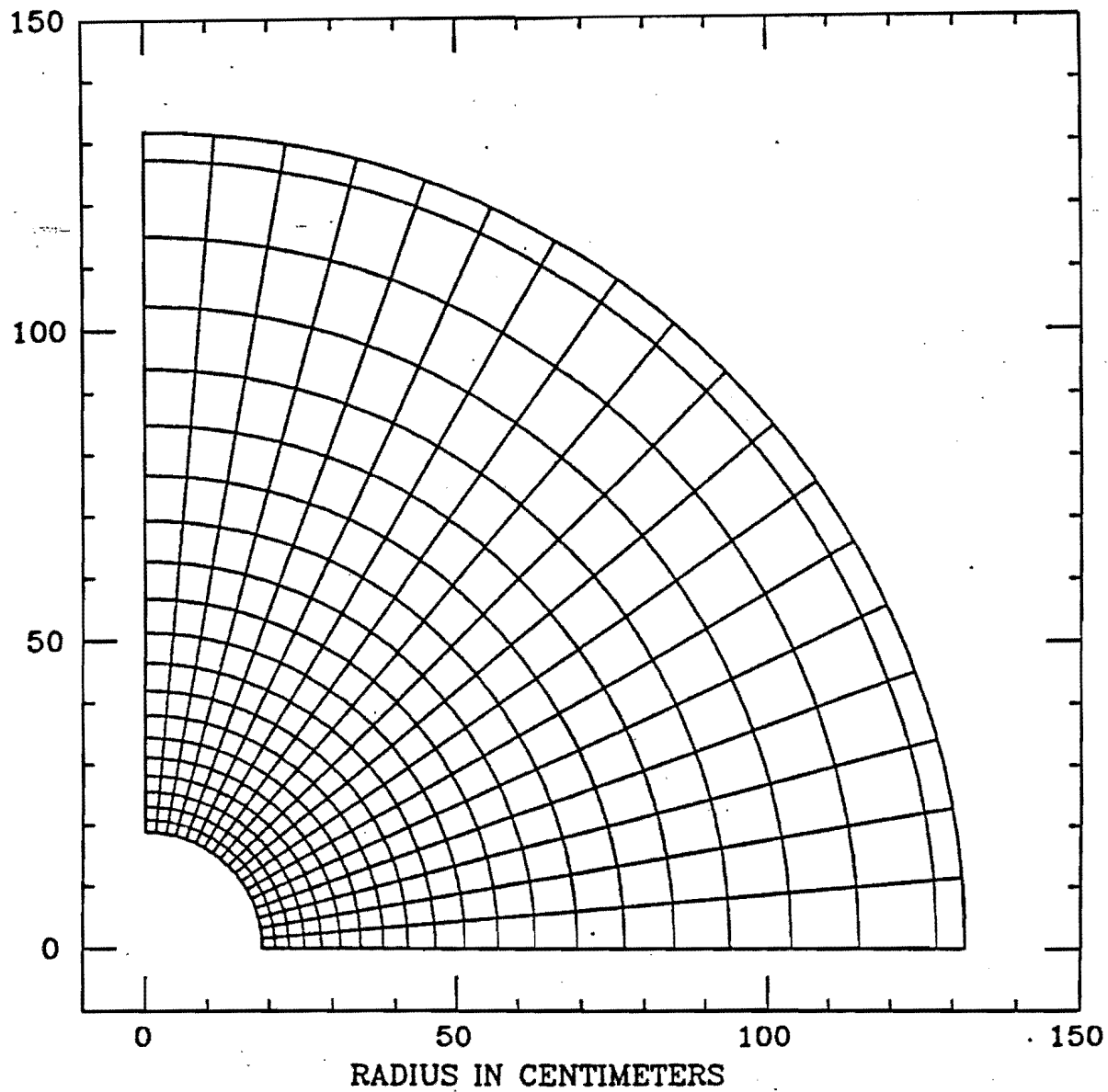


Figure 3

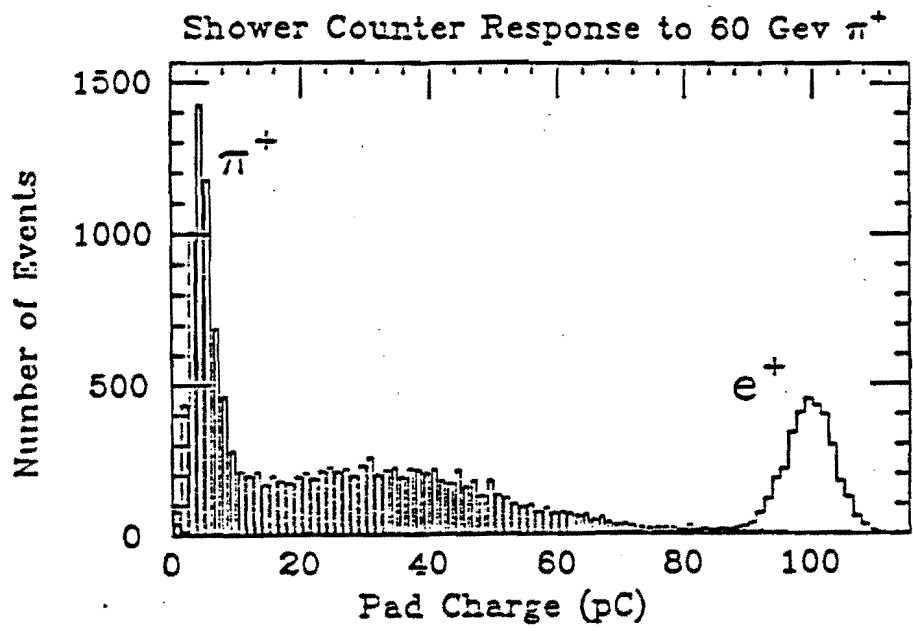


Figure 4

Correlations in Shower Counter Depth Segments at 60 Gev

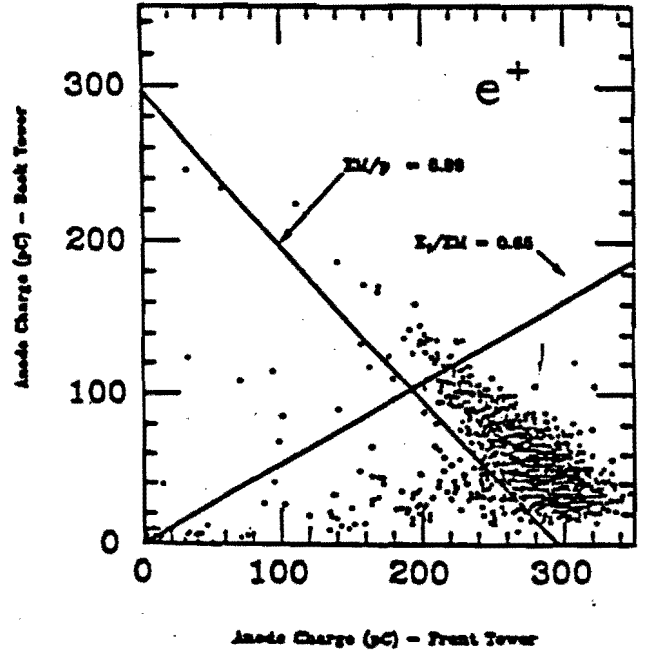
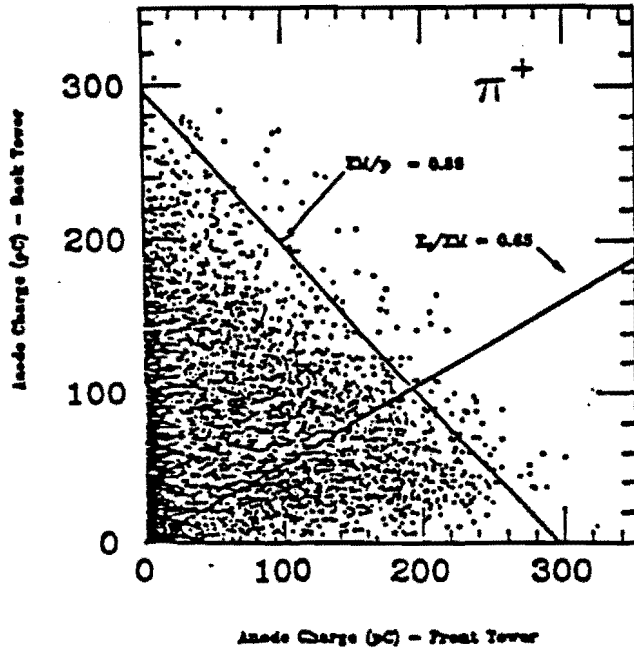


Figure 5

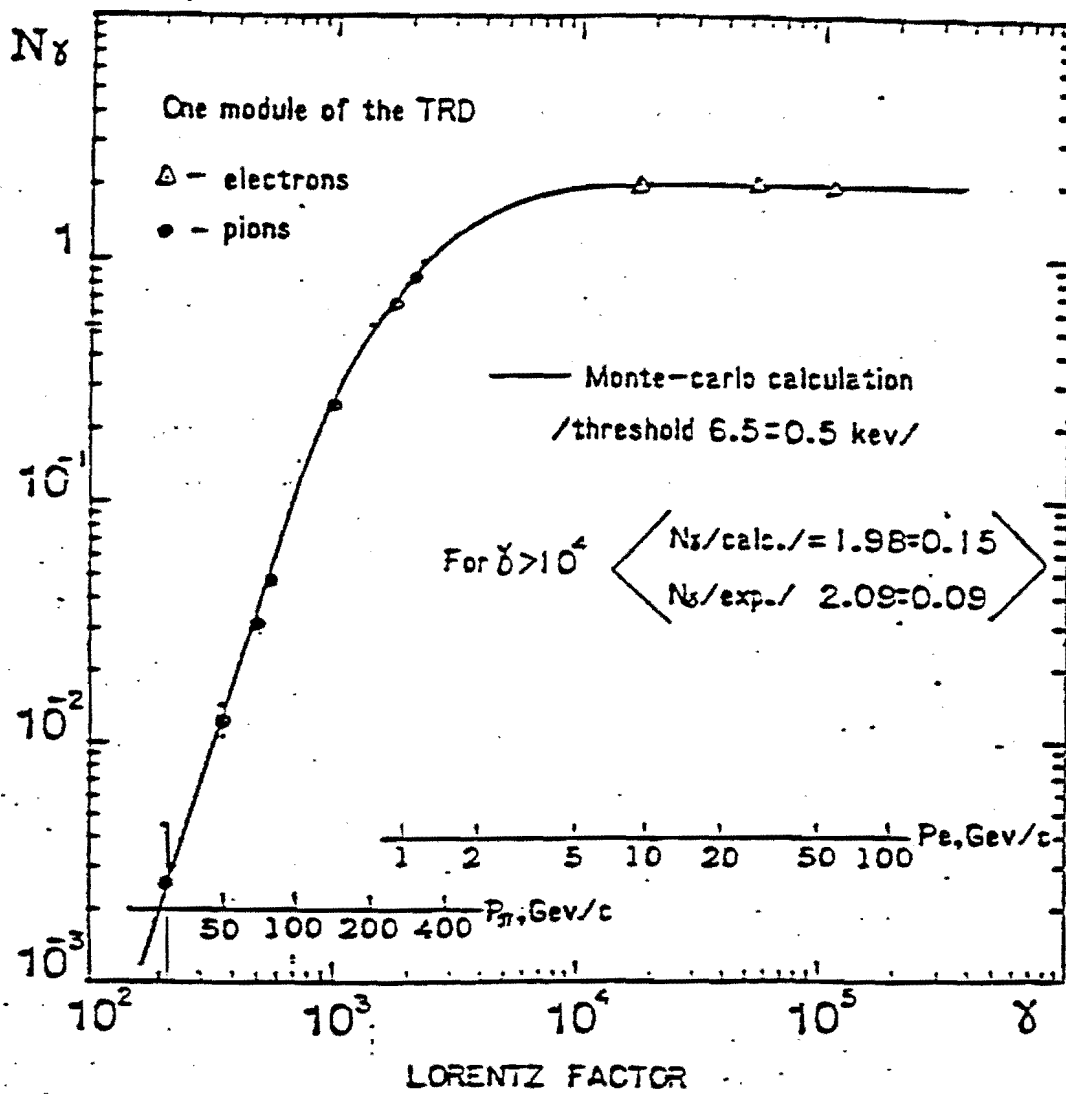


Figure 6

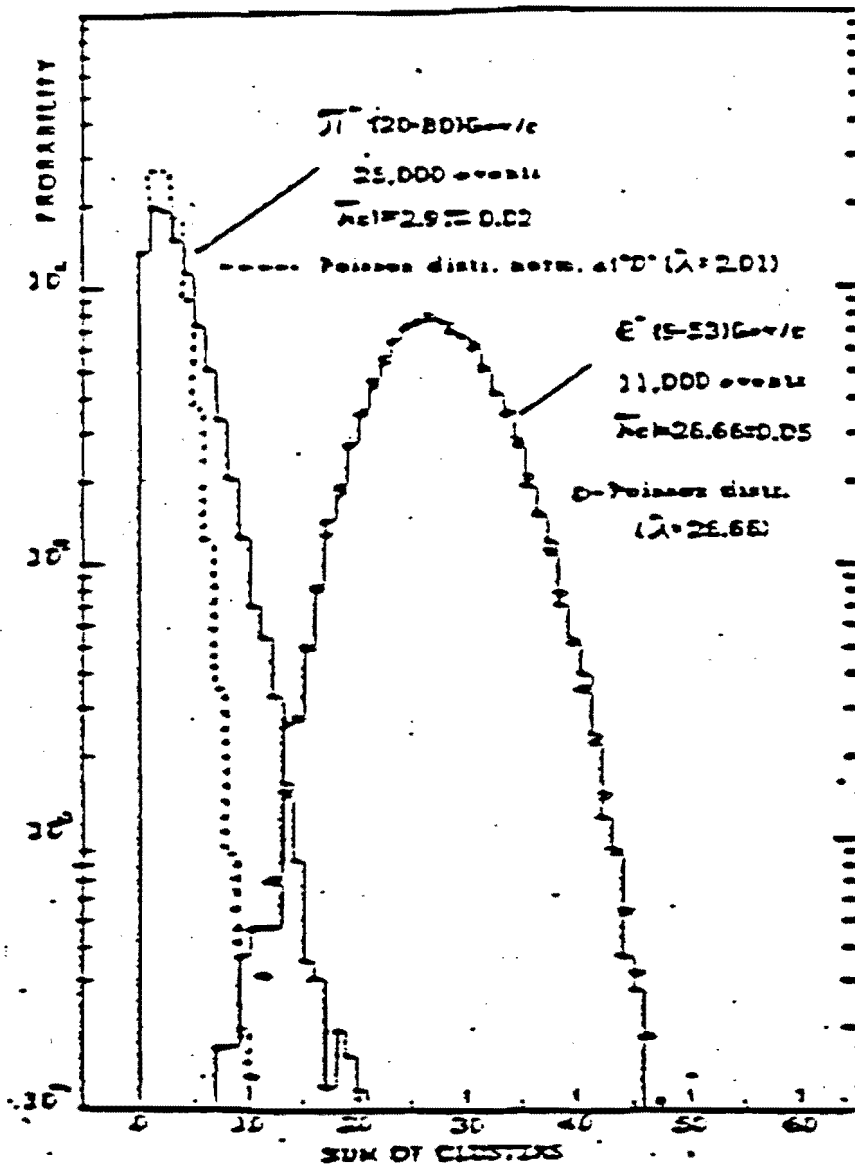


Figure 7

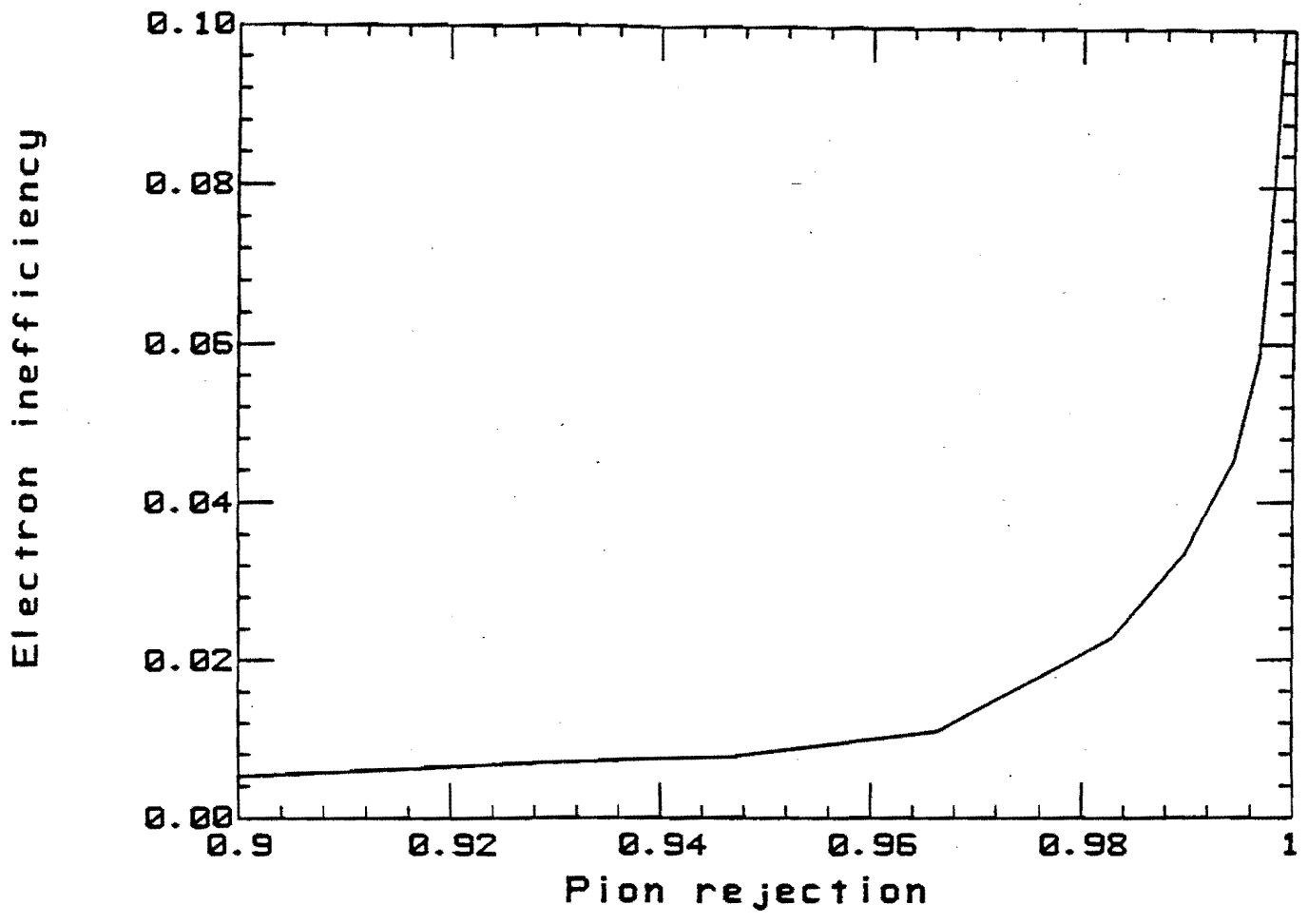


Figure 8

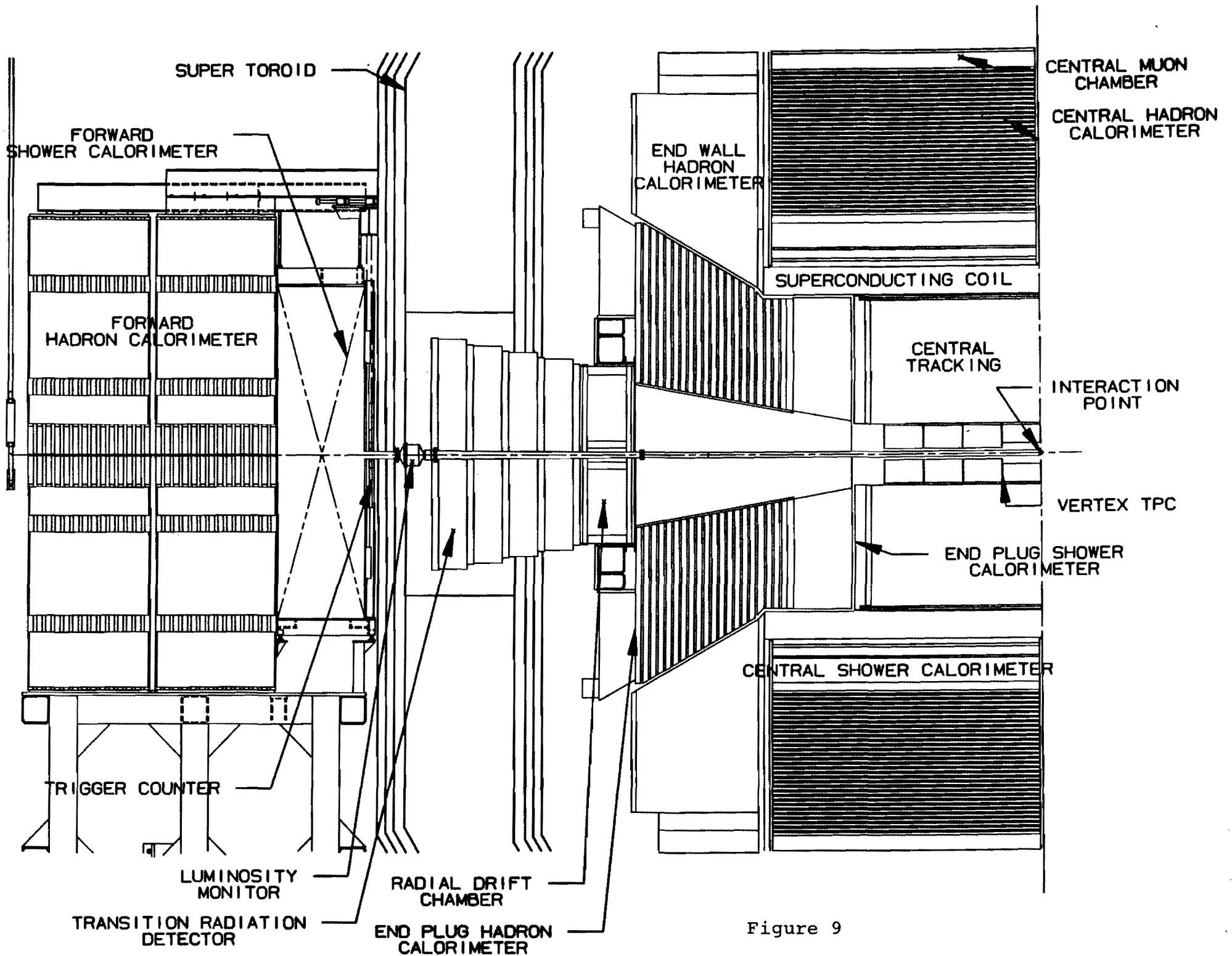


Figure 9

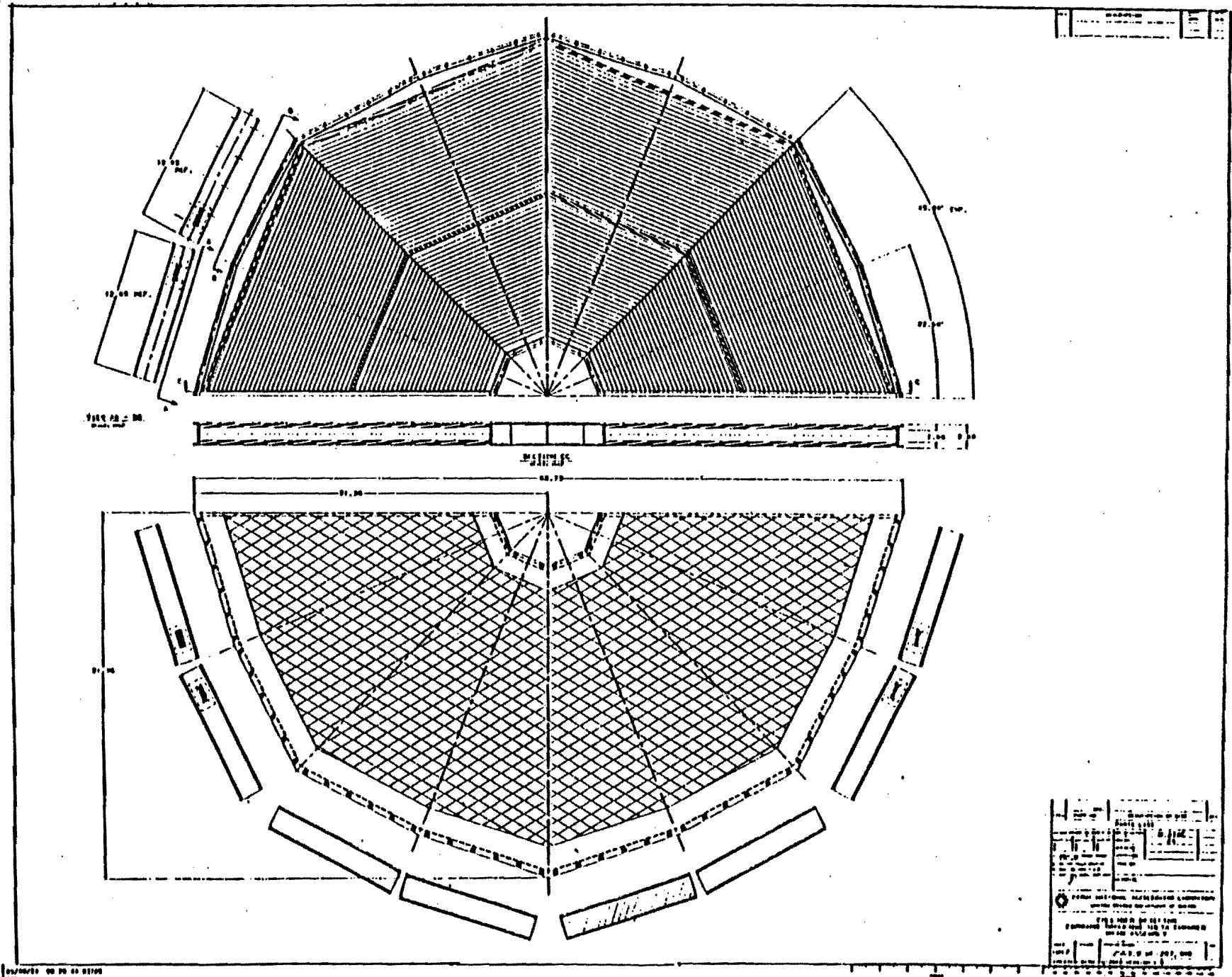


Figure 10

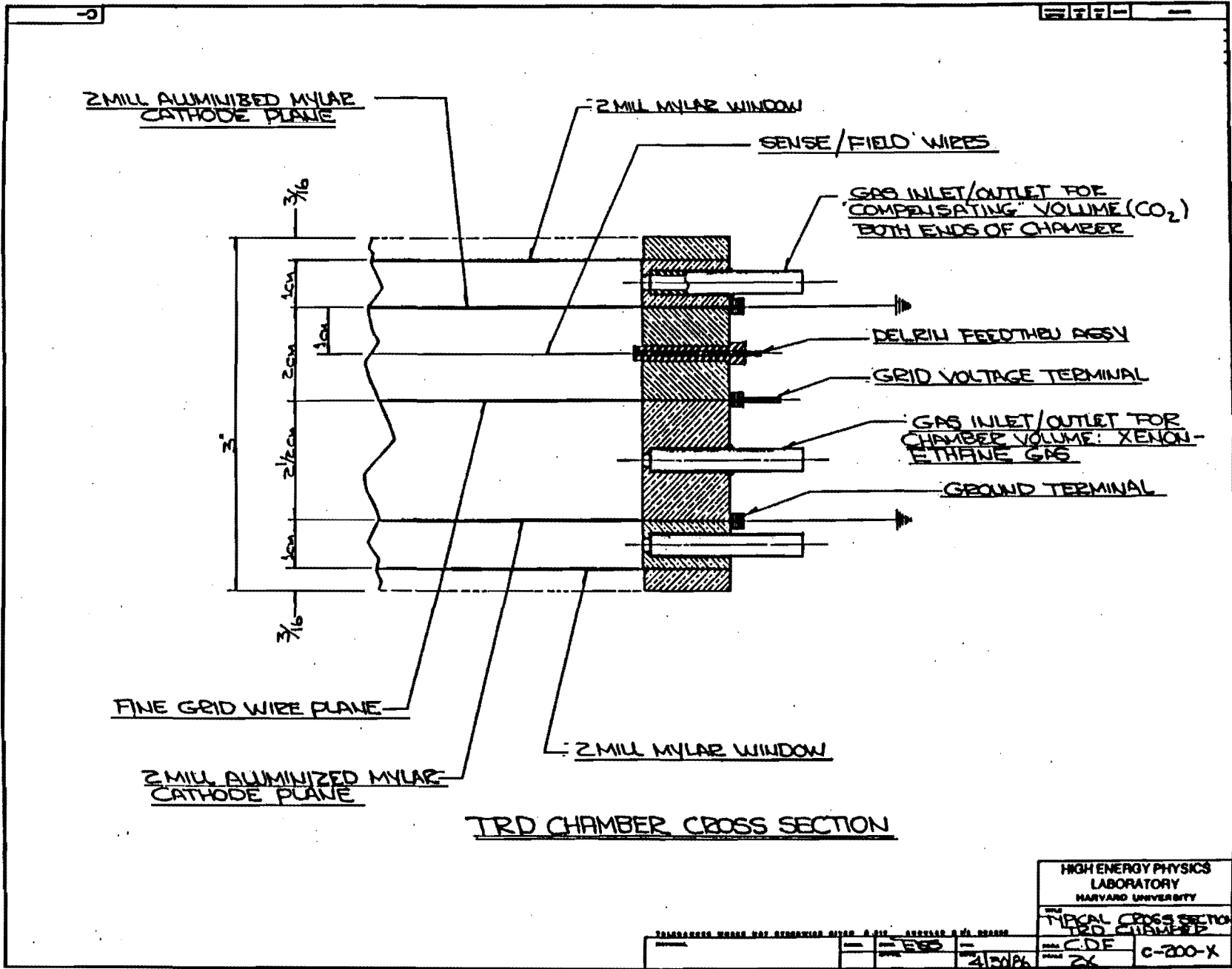


Figure 11

ASSEMBLY ROOM

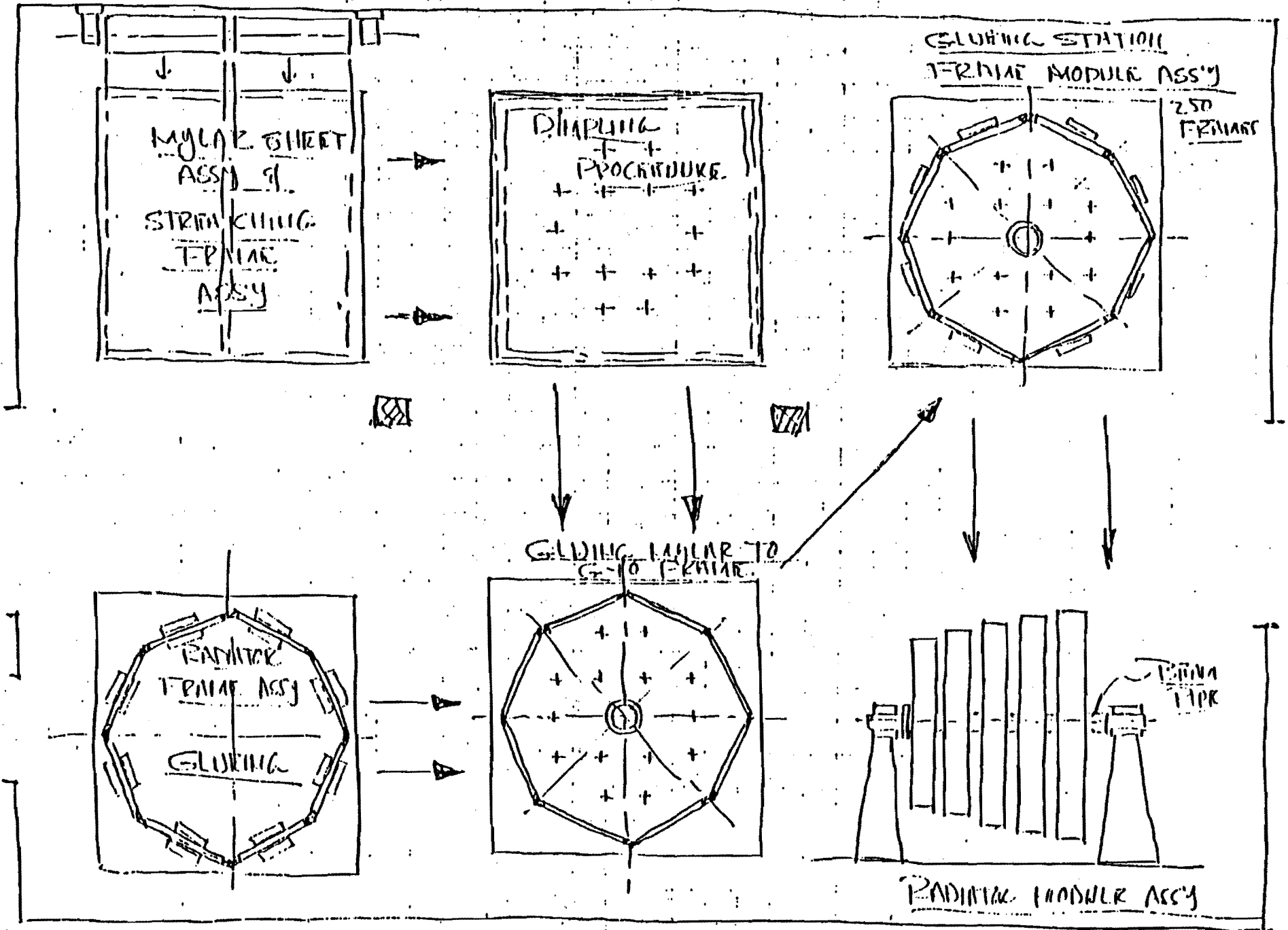


Figure 12

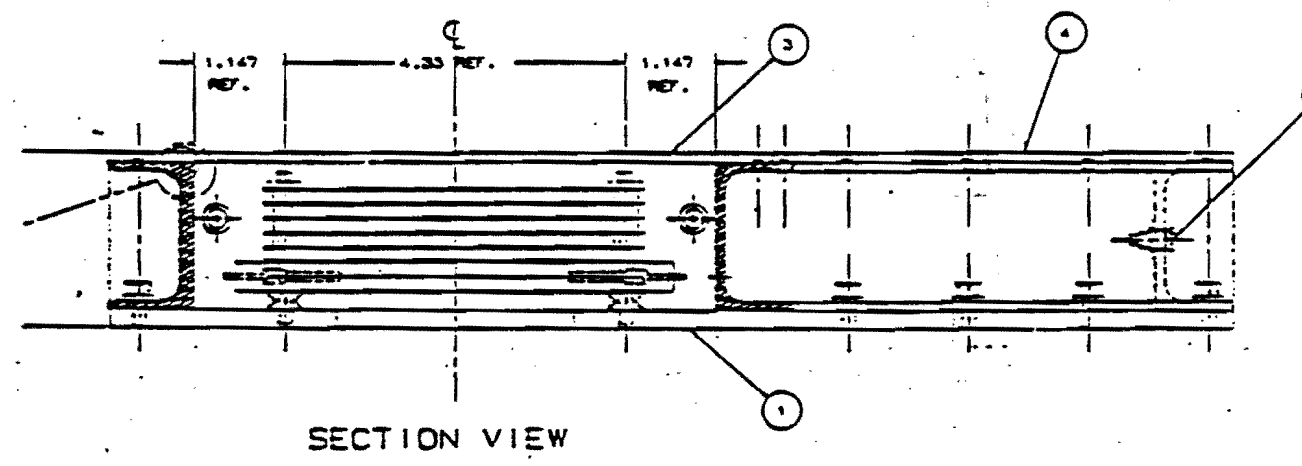
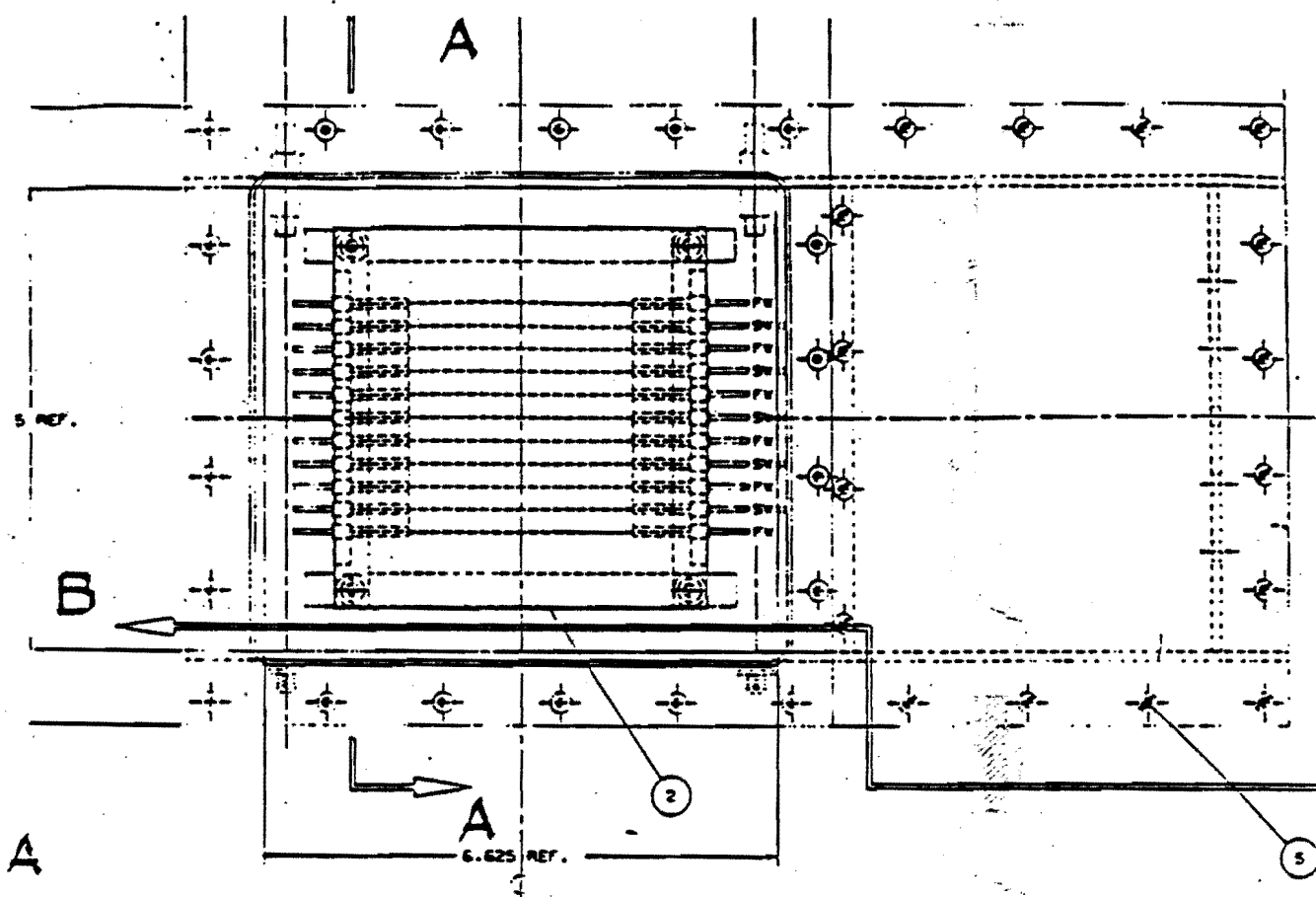


Figure 13

Appendix E

The Silicon Vertex (SVX) of CDF

R. Kephart, A. Tollestrup
Fermi National Accelerator Laboratory

W. Carithers, R. Ely, C. Haber
S. Kleinfelder, H. Spieler
Lawrence Berkeley Laboratory

F. Bedeschi, G. Bellettini, E. Focardi
A. Menzione, L. Ristori, G. Tonelli
INFN, Pisa, Italy

I. Introduction

The main task of SVX is to provide a precise R-phi tracking of charged prongs as close as possible to the interaction point of CDF. This will allow the tagging of secondary vertices from decay of beauty and heavier flavours.

The layout consists of four layers of silicon crystals around the beam pipe as sketched in Fig. 1. The electrodes are thin longitudinal strips, parallel to the beam. The relevant parameters are listed in Table 1. The detector provides four points with a resolution of $15 \mu\text{m}$ for each charged secondary between $-2 < y < 2$, thus improving greatly the resolution in momentum and in impact parameter of CDF (see Table 2 for a comparison of CD resolutions with and without SVX).

In this crowded region of limited volume it is crucial to use a high granularity detector. In our proposed design, a total of 40,000 channels are separately amplified and multiplexed. This requires special electronics as will be discussed later.

Monte Carlo studies indicate that the system is capable of tagging secondary vertices with lifetimes between 10^{-13} - 10^{-12} sec with an efficiency of the order of 30 percent. A primary goal is to tag the decay chain of heavy flavoured quarks. This will allow the detection of rare decay channels of new heavy particles involving t, b, c quark with reduced QCD background. The simulation studies show that the SVX can sort out signal from the background in cases of physical interest, and Table 3 quotes efficiencies for a few examples.

The SVX places some undesirable material in the path of secondary particles in a delicate region upstream from the other detectors. Our design goal is a total weight of SVX of less than 1.5 Kg. The maximum thickness traversed by particles at any angle is $< 2\% X_0$ which reduces the number of secondary interactions to a tolerable level.

The readout system for the silicon strip detector poses many difficult problems. The pitch of the strip is 50μ , and this must be matched to read out electronics and the channels multiplexed if one wishes to avoid 40,000 wires coming from the detector. This problem has been attacked in an elegant manner at Stanford by S. Parker and Terry Walker who have developed a multiplex chip which has all the electronics on it for reading out 128 channels in a serial manner. It can be "daisy chained" if desired and in addition has calibration circuits incorporated. However, there are several potential problems with this chip which are discussed below. As a result an alternate path is being pursued at LBL where a new chip is under development. At present it is not known which solution will be used. We describe here the two alternatives and indicate the approximate costs associated with each.

IIa. Microplex Readout Chip

The present SVX design is based on the availability of a custom VLSI preamp matched to our strip geometry. The only presently existing chip which satisfies this constraint is the Microplex developed to read out the Mark II silicon vertex detector. The Microplex contains 128 channels on a $50 \mu\text{m}$ pitch. Each channel has a charge sensitive preamp and two sample-and-hold capacitors for sampling the charge before and after beam crossing. With an on-chip shift register, the sampled charge can be serially multiplexed to a differential amplifier for external digitization. An early version of the Microplex gave a signal to noise ratio of 14 to 1 for minimum ionizing particles in a single crystal detector.

Although we are still considering this chip for our application, it still has some serious drawbacks. The first issue is power dissipation. The Microplex is implemented with nMOS technology and consequently generates about 20 mW per channel. Since the time between crossings at the Tevatron will be comparable to the settling time of the chip, the power cannot be turned off between crossings, and the device must be run DC. The heat of over 650 watts must be carried away by some cooling scheme that inevitably introduces unwanted material near the beam pipe.

A second issue involves the effect of strip capacitance on the signal to noise ratio. Given the long interaction region at the Tevatron the vertex detector for CDF must have long strips and the source capacitance become correspondingly large. This increases the noise which depends linearly on the source capacitance.

The third issue is readout speed. Again because of the short interbunch time, it is impossible at the Tevatron to read every channel on the Microplex between bunches. On the other hand this would be necessary if a secondary vertex trigger is to be developed.

These problems are all being studied. A test stand for the Microplex chip has been set up at LBL and reproduced at Fermilab and measurements on the electrical properties of the circuit are being made.

The problem of heat removal is under study at Pisa. Water cooling is very efficient but, of course, the additional material added to the system should be kept to a minimum. The present design of the end flanges of the detector is based upon 300 μm thick Al pressed into a suitable shape as sketched in Fig. 2. This provides the required mechanical strength, and heat exchange is provided by a 2,000 μm o.d., 1600 μm i.d. Al pipe in which water is circulated. The overall weight of an end plate is 120 gr.

Measurements on a prototype show that a water flow of 10 l/hour at a pressure of 1.5 Atm can remove most of the heat with an increase of water temperature of 2 ~ 3 C^o. The prototype was also tested at a much higher pressure (6 Atm), and no difficulties were encountered, and the resulting flow was still linear.

At present, the most efficient dielectric material to be used as a substrate for the electronics is being studied. Alumina was used for the prototype tests. Boron nitride, Beryllium oxide, and other heat conductive ceramics are being considered. The construction schedule for the mechanical support calls for a first prototype in 1986.

II.b. LBL CMOS Extension of the Microplex

LBL is designing a CMOS enhancement of the Microplex to address the issues noted above for application at hadron colliders. The CMOS technology should reduce the power dissi-

pation by about an order of magnitude. The signal-to-noise should also be significantly improved. A CMOS preamp should have a much higher single stage open loop gain which in turn results in a larger effective input capacitance for the preamp.

There are substantial architecture differences between the LBL design and the Microplex. The Microplex front end uses a conventional double sampling scheme to remove certain sources of noise. This scheme does not remove contributions of detector leakage current which can vary from channel to channel. The LBL design uses a novel switched capacitor circuit that is functionally equivalent to a triple sampling scheme that removes the leakage current contribution. In addition, a sparse data scan readout is being designed where every channel has a discriminator and latch. The readout speed should improve by the inverse of the occupancy - typically a factor of 10 to 100.

A prototype design exists, and a preproduction prototype has been ordered for evaluation by July 1986. If this is successful, a production prototype could be ready by October 1986.

III. Costs

The estimated costs of the vertex detector are shown below.

SILICON VERTEX DETECTOR COSTS

	<u>Italy</u>		<u>U.S.</u>	
	<u>Equip</u>	<u>Eng</u> (MY)	<u>Equip</u>	<u>Eng</u> (MY)
1. Silicon crystals	283			
2. Preamp/Microplex 500 chips			130	1
3. Cables, electronics	103	1	33	1
4. Mechanical support,	<u>40</u>	<u>1/2</u>	<u>75</u>	<u>1-1/2</u>
Total	426	1-1/2	238	3-1/2

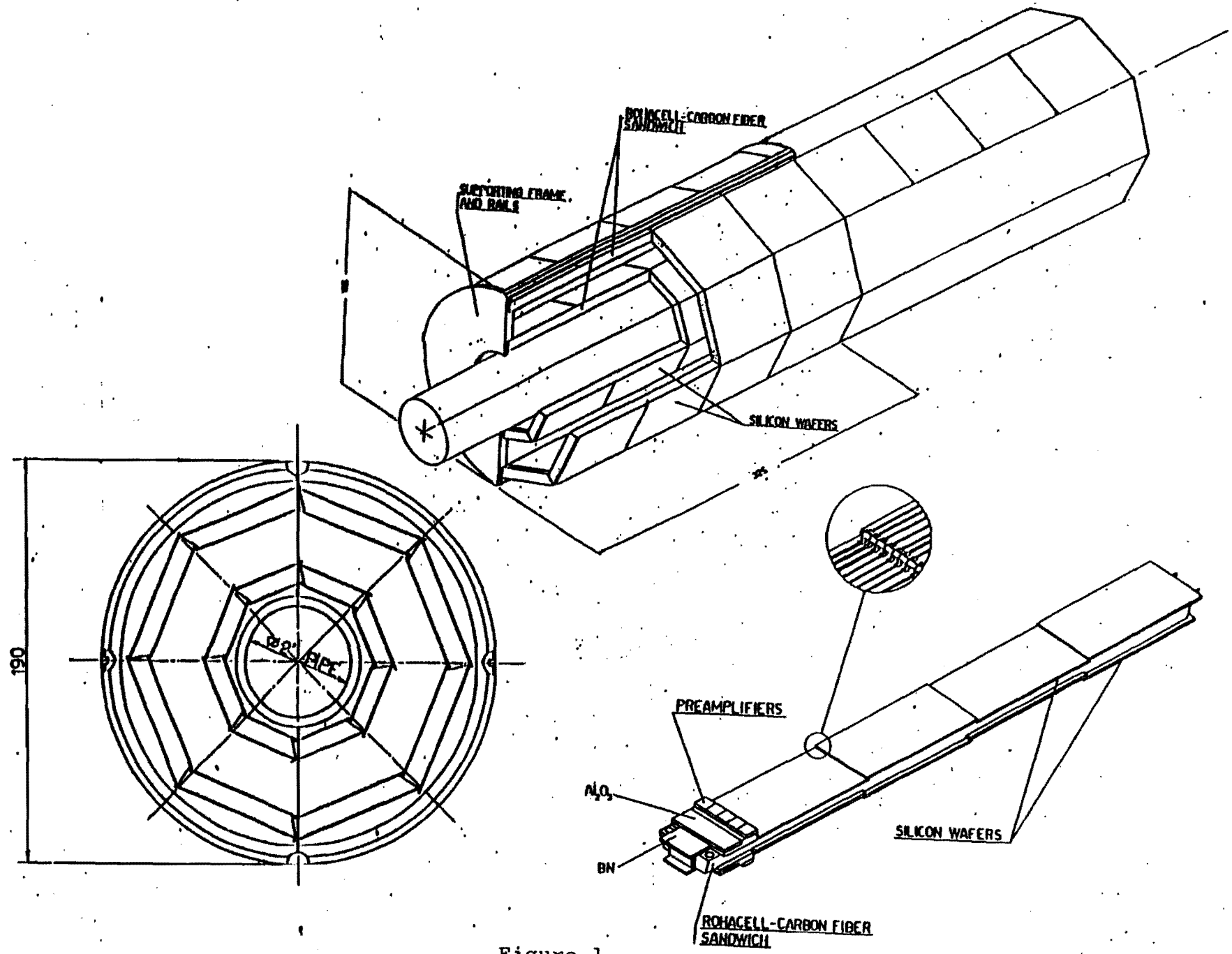


Figure 1

Table 1

Layer	Thickness (μm)	Shape	Internal Diameter (mm)	Length (mm)	Size of crystals (mm^2)	Pitch (μm)	Channels
1	200	Octogonal	30	600	26x75	50	8.032
2	200	"	43	600	33x75	50	11.200
3	200	"	70	600	48x75	100	7.680
4	200	"	80	600	55x75	100	8.800

Table 2

	Momentum Resolution (10^{-3} GeV^{-1})	Polar Resolution (mrad)	Impact param. Resolution (μm)
without SVX	1.0	.9	200
with SVX	.5	.3	25

Table 3

Process	ϵ_3 (%)	ϵ_4 (%)
$W \rightarrow t\bar{b}$	36.5	17.0
$W \rightarrow c\bar{s}$	2.0	0.8
$QCD \rightarrow b\bar{b}$	35.3	22.4
$QCD \rightarrow c\bar{c}$	1.8	0.4
$QCD \rightarrow u, d, s, g. \text{ pairs}$	0.8	0.4

SVX efficiency for tagging a number of physics channels.

ϵ_3 = efficiency for finding a vertex containing three tracks.

ϵ_4 = efficiency for finding a vertex containing four tracks.

APPENDIX F

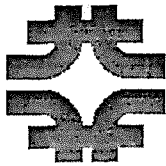
COST OF CDF UPGRADE PROGRAM (FY86\$)

SUPERTOROIDS	\$3986K
TRD	450K
SILICON VERTEX	240K
LEVEL 3 TRIGGER	<u>367K</u>
	\$5043K
CONTINGENCY (25%)	1261K
SWF (15%)	<u>946K</u>
	\$7250K

CDF UPGRADE PROGRAM (FY 86\$)

	<u>FY87*</u>	<u>FY88</u>	<u>FY89</u>	<u>TOTAL</u>
SUPERTOROIDS	\$333K	\$1610K	\$2043K	\$3986K
TRD	250K	200K	0	450K
SILICON VERTEX	50K	190K	0	240K
LEVEL 3 TRIGGER	367K	0	0	367K
FACILITY IMPROVEMENTS (CONTINGENCY, SWF, MISC.)	500K	1000K	957K	2457K
	_____	_____	_____	_____
TOTALS	\$1500K	\$3000K	\$3000K	\$7500K

*note: FY87 is the final year of construction for CDF. Following the March, 1986 DOE/CDF review and additional FY86 funds, the current CDF budget plan calls for \$3.4M in FY87 equipment funds to complete the base detector.



Fermilab

May 11, 1988

TO: Taiji Yamanouchi
FROM: A. Tollestrup/R. Schwitters
SUBJECT: CDF Vertex Detector Proposal

ADJ

We are submitting the revised copy of the proposal for the CDF Silicon Strip Vertex Detector. The design has now matured, and the prototype work has reached a point where we feel comfortable proceeding with construction. Hence, we are asking for approval of the proposal.

AVT:RFS/cip

PROPOSAL P-775

To upgrade CDF with a Silicon Vertex Detector in order to tag long-lived heavy flavors

1. Introduction and Summary

This document is a proposal to upgrade CDF with a silicon strip micro-vertex detector (the CDF SVX). The addition of this device to CDF would permit the tagging of the decays of long-lived heavy particles produced in $\bar{p}p$ collisions on an event-by-event basis. This will give CDF a very important, perhaps crucial, capability to untangle possible new physics revealed at the very high center of mass energy of Tevatron-I. In addition, it will give CDF new access to the study of QCD-induced heavy flavor production in $\bar{p}p$ collisions. The implementation of the CDF SVX is made possible by recent advances in the application of micro-electronic technology to high energy physics. These techniques will likely be used increasingly in modern detector systems.

Over the past few years we have carried out a development program (described below) leading toward the construction of this device. We are ready now to proceed in the construction of the CDF SVX. It is our intention to install this detector into CDF for the 1990 physics run. By then we will already have collected $\sim 1pb^{-1}$ of data, which permits exploration of new mass scales. Following that major run, we believe, will be the appropriate time to extend the sensitivity of CDF for new physics by improving the capability of the detector.

The total estimated cost for this upgrade is \$2.05M; close to half of this (\$840K) will be provided by the Italian contingent (INFN-Pisa) within CDF. The remainder, is requested from Fermilab equipment (\$1098K) and R&D (\$119K) funds. We are asking the PAC for approval of this upgrade to CDF.

The body of this document details the physics motivation, design, and expected performance of the CDF SVX. Here we summarize the basics technical points discussed below.

- **Configuration:** The device we have designed [1] consists of 4 radial layers of silicon strips surrounding the beam pipe. The SVX will track only in the $R\phi$ plane. Thus it will function well with the existing CTC (Central Tracking Chamber). The intention is to link tracks in the CTC with segments in the SVX. Tests have shown the position resolution of the SVX to be $8\mu m$ at each layer. For $1 GeV/c p_t$ tracks this will result in a $\sim 30\mu m$ resolution on impact parameters. For tracks above $10 GeV/c p_t$ we reach an asymptotic impact parameter resolution of $\sim 10\mu m$. We note that the B meson natural lifetime ($c\tau_B$) is $300\mu m$.
- **Material Near the Beam:** To minimize the impact on the rest of CDF from interactions in the SVX, lightweight materials have been used extensively in the design. Particles traversing active regions of the detector will pass an average of 3% of a radiation length. Thin regions on the ends and in the center, which form a support structure are not active. Particles crossing vertically through those will pass an average of 3.5% of a radiation length.

- **Front End Electronics:** The resolution of the SVX comes at the expense of a high channel count. For our configuration, there will be ~ 40000 individual readout channels. To deal with this, we have developed a custom VLSI (Very Large Scale Integrated) circuit [2], which amplifies, samples, sparsifies, and multiplexes data from the SVX. This dramatically reduces the data size and cabling burden.
- **Signal-to-Noise Ratio:** The signal to noise ratio (S/N) has been shown from the analysis of test beam data [6] to be 12 with a preliminary version of the front end electronics, an 8 *pf* detector capacitance, and 280 μm thick silicon detectors. An accurate evaluation of the latest version of our front end electronics indicates that the S/N will be even better in the final detector configuration. This is in spite of the large input capacitance of the full detector (see Section 3.2).
- **Detector Efficiency:** The efficiency of the silicon microstrip detectors was measured in a beam test to be 99.8% and the shape of the pedestal distributions remarkably Gaussian.
- **Data Acquisition Electronics:** Integration of the SVX into the existing CDF data acquisition system will be straightforward. The necessary modules are well specified at present and have been prototyped in during a beam test. Because the front end electronics performs a local sparsification, the additional data generated by the SVX will be a small addition to the present record size. Work is underway to design a full system for CDF.
- **Expected Performance:** Simulations have shown that the calculated efficiency for reconstructing secondary vertices with the strong signature of three charged tracks is 20%–40% [3],[4],[5]. Furthermore, we find the chance of detecting a fake secondary vertex is $10^{-3} - 10^{-4}$ in a high p_t jet event if no B 's are produced.

The remainder of the document is organized as follows. In Section 2 we discuss the general physics motivation for identifying heavy flavor decays. In Section 3 we describe the detector mechanical design and fabrication, the front end electronics, and the necessary additions to the CDF data acquisition system. In Section 4 we describe the expected performance of the SVX based on simulations and studies we have undertaken. In Section 5 we describe results of a beam test made on a prototype of the CDF SVX. In Section 6 we discuss a construction timescale and cost estimate. Finally, in Section 7, we present our conclusions.

2. Physics Motivation

The primary motivation for upgrading CDF with a vertex detector is that it will provide us access to a range of new and perhaps fundamental physics. Examples of processes where secondary vertices occur include decay modes of the W, Z and top quark and possibly other unknown particles (W', Z' , etc.), leading to b quarks in the final state. If we can learn to tag the b content of these final states, then a new handle to isolate cleaner samples of these important events becomes available to us. For these events the complexity of various QCD induced final states will provide a sizable background. The secondary vertex tag (or conversely its absence) can be a decisive factor in selecting the event. With reduced efficiency, also, final states including τ leptons can be exploited.

For any particular reaction leading to the production of a heavy particle, with b quarks in the final state, the SVX will enhance the signal and increase the level of rejection against QCD backgrounds. However, the expected cross sections are small and with present Tevatron-I luminosity the rate of any particular reaction is low, and therefore will be near the limit of CDF's detectability. In these cases, the SVX may provide the extra level of discrimination needed to identify the events. We therefore believe the real usefulness of the SVX in the near future will be in its cumulative application to the entire class of complex events indicated above, rather than to any single channel. In addition it is important to note that there will be an important area of inclusive B physics which we can study with this device with good statistics. This includes heavy quark production rates and b jet fragmentation, which are basic QCD tests. Finally, the experience we gain operating the SVX in the $p\bar{p}$ environment will be crucial for future applications at higher luminosity, where the above-mentioned rate problems are not expected to be a limitation.

The types of events for which the SVX will have an impact are listed below and some illustrative examples are discussed.

- $W \rightarrow t\bar{b}$ followed by the semileptonic decay $t \rightarrow l\nu b$: The process is indicated in Figure 1a. This process has been studied extensively as a means to detect the top quark. Traditionally, the approach has been to look at the kinematics and topology of events with an isolated lepton and two jets. Unfortunately, backgrounds to this type of analysis can be severe. The difficulties experienced by UA1 in setting mass limits for the top quark are a good example of this situation [7]. In their muon analysis UA1 derived an upper limit $m_t > 41 \text{ GeV}/c^2$ by studying events with a large p_t muon and two jets. The conclusion was that about 40% of these events were consistent with being due to pion and kaon decay background, and 60% to $\bar{b}b$ and $\bar{c}c$ QCD production. Such an analysis is based upon an indirect and inclusive signal. It should be pursued further, but in order to provide a clear cut proof of top production by this channel it may be necessary to strengthen the event signature. To this aim, a natural way to proceed is to study the production vertex in more detail. With accurate vertex tagging, (assuming the t lifetime to be small compare to b) the isolated μ would be seen to originate from the main event vertex. This is opposite to what is expected for $\bar{b}b$ and $\bar{c}c$ QCD background. Furthermore, the event would show, for the dominant hadronic channel $t \rightarrow b$, two secondary vertices. Studies have been carried out within CDF on the possibility of selecting a sample of semileptonic top decays at Tevatron energies, based on the p_t , isolation and topological cuts referred to above [8]. The results of these indicate a signal to noise ratio between 1.8 and .4 for a $40 \text{ GeV}/c^2$ top mass depending on the QCD generator used. If we require the hard lepton to be prompt we find that the background is reduced by a factor of 2. Furthermore, the vertex detector should allow us to study a set of background event configurations with the possibility of extrapolating the remaining background under our signal.
- $W \rightarrow t\bar{b}$ followed by the hadronic decay $t \rightarrow q_1q_2b$: This process, indicated in Figure 1b, is the archetype for studying the hadronic decays of massive states. The pattern of secondary vertices that is generated here can be complex. We have attempted to get a rough estimate of the efficiency for sorting out hadronic top decays in $W \rightarrow t\bar{b}$

(and charge conjugate) events by means of a combination of conventional calorimeter analysis and B meson tagging [5]. Several cuts need to be imposed in order to suppress the huge QCD background. These include: requiring at least 4 jets with $p_t > 5$ GeV/c ; requiring the pseudorapidity difference between any two jets to be less than 1.5; requiring both B mesons in the event to be tagged; after associating each B meson with a specific jet, requiring that the energy of the harder B -jet be > 15 GeV ; and finally, requiring the angle between the two B mesons to be in the range of 120 to 180 degrees. Having applied these cuts, we may plot the invariant mass spectrum of the 4 highest energy jets and look for a peak in the W mass region. The results, with no correction for double tag efficiency, are shown in Figure 2. The application of the cuts reduces to a negligible level the indicated QCD background except for the $\bar{b}b$ continuum component. The remaining signal to noise is ~ 1 . The resulting cross sections, after accounting for double tag efficiency, is a few tens of picobarns. We note that an additional handle, not considered here, would come from requiring a 3 jet system to reconstruct the top mass.

- **Inclusive B production:** At the Tevatron a large production rate of B jets is expected. The QCD background of light quark jets is however 2 to 3 orders of magnitude larger. Tagging of b 's with a micro-vertex detector is probably the only way to sort out a clean sample of bottom jets for inclusive studies. In Figure 3 we show the number of bottom jets that can be tagged, in comparison with inclusive production, given our efficiency. Even though most of the production is at low p_t , several thousand events per pb^{-1} can be selected with the very stringent double tag request and a realistic CDF jet trigger threshold. This is particularly interesting because heavy quark-antiquark production via gluon fusion, gluon decay, and $q\bar{q}$ annihilation are well calculated in perturbative QCD [9]. By studying events in which we tag one, two, or more secondary vertices we may hope to measure our efficiency. Thus, an absolute production rate can be determined.
- **B jet fragmentation studies:** By tagging jets which originate from b quarks we can compare fractional momentum ("z") distributions with those of light quark and gluon jets.
- **$gg \rightarrow t\bar{t}$ followed by semileptonic or hadronic t decays into b :** At the Tevatron, top production by this mechanism has a larger cross section than via W decay. Unfortunately (for low mass t) this process lacks the W mass constraint. Again, there are many possible configurations possible each with its associated background. For the case of one t decaying semileptonically we again have the background from $gg \rightarrow g\bar{b}b$ where one b decays semileptonically. Here the lepton comes from a secondary vertex. We can reduce this background by requiring a prompt lepton tag.
- **$W \rightarrow \tau\nu$ and $Z \rightarrow \tau^+\tau^-$:** Tagging τ 's in an event could be crucial to accounting for backgrounds to other new physics.
- **$t \rightarrow Wb$ (if $m_t > m_W$):** If the top mass is $m_t > m_W$, the dominant decay will be $t \rightarrow b + \text{real } W$. There are many possible final state topologies here depending upon the

various W decay modes. In some cases these events might be very dramatic, however there are situations where a vertex tag could be very useful in discriminating against QCD backgrounds. Some of these may look like single W +jet events. Secondary vertex tagging by indicating the presence of bottom decays in the event would provide a strong additional signature.

- $Z \rightarrow \bar{b}b$: In 1 pb^{-1} we can expect to tag both b decay vertices in a few dozen of these events. This should be an important calibration for the $W \rightarrow t\bar{b}$ analysis discussed above.
- Decays into heavy flavors of a new massive particle: Both the semileptonic and hadronic decays can be studied with the vertex tag as above for the W and Z .
- Higgs detection: The Higgs should preferentially decay into heavy fermions. However, calculations place the Higgs production cross section far below the background from $t\bar{t}$ production. While detecting the Higgs with or without the SVX does not seem realistic in the near future at CDF, we believe that the experience gained studying events with the SVX may be crucial for future Higgs (or Higgs like) physics at higher luminosity.

Beyond pointing out the specific physics processes which can be studied better with a micro-vertex detector it is worthwhile to recall the general argument in support of such an addition to CDF. The physics of $\bar{p}p$ has been approached so far with a certain set of analysis handles: leptons, jets, large E_T , and large missing E_T for example. Secondary vertex tagging is a new handle that promises great potential in a different direction. It is a handle with which we have no real experience, but we need to learn how to exploit it. The decays of heavy objects, as well as gluons, are for the most part flavor independent, and may even select out heavier quarks and leptons. If we can learn how to use the secondary vertex tag then a new set of interesting processes become accessible to us. Like leptons and missing E_T , secondary vertices should be a signal of other interesting physics.

3. Hardware Design

In this section we will discuss the mechanical design, construction, and alignment procedure for the SVX, the integrated front end electronics, and the necessary additions to the CDF data acquisition system.

3.1 Detector Mechanical Design and Assembly

The CDF SVX is designed to measure track positions with $\sim 10\mu\text{m}$ accuracy at the silicon detectors. This specification imposes serious requirements on the mechanical design and stability of the device as a whole [1,10]. It is our intention to align the SVX to the required accuracy during fabrication. The final alignment can be verified inside CDF with tracks but this is not envisioned as the primary method of alignment. In this section we will describe the overall mechanical layout and construction of the CDF SVX and indicate how we will maintain the necessary mechanical tolerances.

Some remarks on the general design requirements are in order first.

1. The interaction region at B0 is extended longitudinally with a σ of roughly 35 cm. The detector must be long enough to cover a substantial portion of the interaction region.
2. In principle, the best resolution is obtained by placing a high precision measurement as close to the interaction point as possible and linking that with a track segment in an outer tracking chamber (the CTC in our case). However, the realities of the $\bar{p}p$ environment, coupled with considerations of noise and reliability, require a certain amount of redundancy in the track position measurement. As described below we therefore choose a multilayer device with the innermost layer at small radius.
3. All material must be kept to a minimum for two reasons. First, multiple scattering is a limiting factor in the position measurement resolution for low p_t tracks. Second, the SVX will become the source of background for the rest of CDF due to interactions and conversions which occur in it.
4. The scale of the mechanical tolerances required is comparable to the resolution of the detectors involved [10]. The internal consistency of the location of the silicon microstrips in the SVX should be the same as the intrinsic detector resolution, while the SVX needs to be positioned with respect to the CTC only to an accuracy of the order of the CTC resolution.
5. Different types of misalignments affect the measurement of the track position in different ways. While some misalignments can in principle be corrected for after they have been measured, in other cases (rotations around an axis perpendicular to the detector face, or relative misalignments of microstrips which are read out by the same electronic channel, for example) such construction errors can be corrected only partially or not at all. In these cases particular care must be taken.

The SVX overall layout is shown in Figures 4, 5, and 6. It is located with its center on the nominal B0 interaction point and consists of two cylindrical modules placed end to end with their axes coincident with the beam axis. It is meant to track primarily in the $R - \phi$ plane. The SVX consists of 4 radial layers of silicon strip detectors. These detectors are arranged as a twelve sided barrel at each radial position. The strip detectors are 280 μm thick. The inner three have strips on a 60 μm pitch while the outer layer is on a 110 μm pitch. The detectors are electrically bonded to each other along the beam direction in groups of three. These bonds are made with 25 μm wire which is ultrasonically fused to pads on the detector surface. This bonding technique is a standard procedure in the micro-electronics industry. At each radius and on each of twelve faces there are thus a total of six detectors, in two groups of three. These are read out electronically at the two ends. This is shown in Figure 4. Each detector is 8.5 cm long so that an individual readout channel sees a 25.5 cm long strip. The total longitudinal coverage is thus 51 cm. The source capacitance of each strip is about 30 pf.

The choice of four layers is based upon the following considerations. Clearly, most of the impact parameter resolution is coming from the innermost layer. However one must be able to link the points recorded in the SVX with an incoming track from the CTC. We have studied this problem with a Monte Carlo program, in which estimates are made for false hits from soft particles, interactions, and electronic noise. Recent experience with

real $\bar{p}p$ data indicate that we are probably underestimating the soft backgrounds. Given that caveat, we find that with four layers, the probability of failing to link a well measured CTC track to the SVX is $\sim 1\%$. With four layers we have a more powerful correlation for the hits and we are also protected against the possibility of an electrical failure on any one layer. In the event of such a failure, the estimated track matching inefficiency rises to $\sim 5\%$. In addition, with four layers we may be able to search for tracks in the SVX alone. We note that the silicon vertex detectors being built for electron-positron colliders all have effectively three measurement layers and they are expected to operate in a much cleaner environment.

A group of three connected detectors is called a *Ladder*, the basic subdivision of the device (Figure 4). The *Ladders* will be fabricated of Rohacell, a light weight foam, and reinforced with carbon fiber strips. All the detectors within a *Ladder* must be well aligned to each other since the readout cannot distinguish between the three detectors. Each *Ladder* will be individually assembled and mounted. Thus, in the event of a failure, one particular *Ladder* can be replaced. The total number of *Ladders* is 12 faces \times 4 layers \times 2 ends = 96, or 24 of each size. In its position on the face of the barrels, each *Ladder* will be rotated by 3 degrees about its major axis to allow some overlap between adjacent faces (see Figure 7). At the outside end of each *Ladder* will sit a small circuit board called an *Ear*. The *Ear* contains the readout chips (see Section 3.2) for that *Ladder* as well as auxiliary components and buswork needed for the operation of the chips. This is shown conceptually in Figure 8 while the actual layout is in Figure 9. A second "dummy" *Ear*, sits at the opposite end of the *Ladder* for mechanical alignment. The *Ear* will be fabricated using a multilayer thick film process on 15 mil Alumina (Al_2O_3). The *Ear* will also receive cables going to other *Ears* carrying various bussed signals. Three silicon detectors (a *Ladder*), and the two *Ears* form a single rigid unit. The *Ear* will be precision laser cut and contain a precision mounting hole to allow for the alignment of *Ladders* with respect to a pair of bulkheads. These pieces will support the full lattice of *Ladders* in a barrel. A group of four *Ladders* at fixed azimuth projects back to the interaction point. This unit is called a *Wedge*. An external conductive cylindrical *skin* will surround each barrel to isolate them from E.M. noise and to add rigidity to the system. This element will be fabricated as a sandwich of two layers of $50\mu m$ Aluminium separated by 1.5 mm of Rohacell foam. Details of the detector geometry are given in [1] and in Table 1a,b,c, and d.

The assembly of the *Ladder* is very demanding in terms of the mechanical tolerances required; indeed since the strips of 3 detector are electrically connected it is mandatory that they are aligned to better than their intrinsic position resolution ($\delta x = 10\mu m$ implies $\sim 5\mu m$ for this alignment). A special fixture has been designed (and successfully tested on the test beam prototype) to assemble the *Ladder* to this accuracy [10]. It is shown in Figure 10. The fixture is also mounted on an optical bench, where the location of all the strips can be inspected to an accuracy of $5\mu m$. This fixture provides two basic mechanical references: the plane of all strips, which can be transferred to other structures through the bottom surface of the *Ears*, and the center line of the strips, i.e. the strip corresponding to the central strip of all three detectors. This latter reference can be transferred by means of a dowel pin located in each of the *Ears*.

As indicated above, two bulkheads per barrel are needed to hold the *Ladders* in their

proper position. Each bulkhead will contain a set of ledges where the *Ears* are to be positioned, the surface of the ledges and a precision hole drilled in them allows us to accurately transfer the *Ladder* references. The bulkheads will be carved out of a single piece of Beryllium on a digital mill. A milling routine which allows the ledges to be cut finished without having to remove the piece from the mill bench has been written and tested at Pisa. A pair of bulkheads have been cut from Aluminium using this procedure. A photograph of one is reproduced in Figure 11. These prototypes are presently being evaluated and surveyed at Fermilab. For the final fabrication in Beryllium, where higher rigidity and accuracy are needed, the machining will be done commercially by a firm we have located which specializes in this type of precision machining.

The assembly of the *Ladders* into the bulkhead needs a special fixture also, to ensure the relative positioning of the bulkheads and to allow inspection and survey of the final result. Such a fixture is presently being designed at Fermilab. This assembly can be done at a temperature close to the one at which the SVX will operate.

The existing CDF beam pipe has a 2 inch diameter. The impact parameter resolution of the SVX will improve by about 30% for low momentum tracks and the vertex tagging efficiency will improve by a factor of ~ 1.5 if we decrease the diameter to 1 inch. It is our plan to request help from the accelerator division in order to determine the acceptable minimum size for the beam pipe. In the event there could be a substantial improvement in performance of the SVX we hope to replace the present pipe. We have included the cost of this in the attached SVX budget.

The completed barrels will be inserted around the beam pipe. We plan to scale the present flanges connecting the CDF beam pipe section to the Tevatron beam pipe section down to clear the SVX inner diameter. The SVX will be supported at its outer radius only, by the central VTPC (Vertex Time Projection Chamber) modules. It will not be mechanically coupled to the beam pipe.

It may be necessary to cool the readout electronics. We expect the power dissipation to be less than 100 watts for the entire system. This amount of power dissipation is small, considering the large number of channels involved, but still needs to be removed. If the temperature of the silicon detectors increases, their leakage currents will increase also. Hence, care has been taken in the design to ensure a good thermal connection between the *Ears* and the bulkhead. The *Ears* are in fact made of Alumina, a material which exhibits good thermal conduction properties. Furthermore the bulkhead itself is a good thermal conductor. It is possible to cool the bulkheads by flowing cold water into small pipes which encircle them. Calculations indicate that this appears feasible without the addition of much extra material. In addition, the outer metallic *skin* will partially isolate the SVX from heat generated by the VTPC.

We have evaluated the amount of material present in the SVX. In Figure 12 we plot the number of radiation lengths of SVX material traversed by a particle as a function of its polar emission angle. It appears that the contribution of all the supporting structures is about half of the contribution of the silicon itself. Since most of the area of the SVX is active, the detectors will provide information which can be used to identify conversions and interactions which occur inside them. For example, a conversion in the first layer will show up as double pulse height in all subsequent layers. The bulkhead regions of the

SVX are not active. However, they occupy only $\sim 10\%$ of the length, mostly at the ends. Particles which travel straight up the bulkhead will cross $\sim 3.5\%$ of a radiation length. The amount of dead material present now between the beam and the first sense wire layer of the CTC at 90 degrees is $\sim 2.5\%$ of a radiation length including the beam pipe. Thus, the addition of the SVX adds roughly an equal amount of active material. We believe we are close to the limit on reduction of material given the rigidity and accuracy constraints of the design.

In summary, the assembly of the SVX will proceed as follows:

1. Silicon detectors will be tested for low leakage and sorted by depletion voltage.
2. Readout *Ears* will be fabricated and tested.
3. Detector and *Ears* will be aligned onto the foam supports and glued to form *Ladders*
4. Wire bonds will be made between detectors and readout chips on each *Ladder*. These assemblies will be electrically tested.
5. *Ladders* will be mounted and aligned into the bulkheads and electrically interconnections between *Ears* will be made.

3.2 Electronics

The CDF SVX will contain approximately 40000 individual readout channels within a cylindrical region 8 *cm* in radius and 51 *cm* long. This extremely high channel density makes conventional readout schemes utilizing discrete electronics or cables to carry out individual signals prohibitively difficult. As a result we, as well as other groups designing solid state vertex detectors for colliders, have turned to the use of custom micro-electronics which can be placed at the detector for the readout system. This approach was pioneered at Stanford where a custom VLSI circuit called the Microplex was developed [11]. This device contains 128 charge sensitive amplifiers on a 50 μm pitch, and a multiplexed serial output. Thus many channels could be reduced to a single readout line. The generic readout scheme for a silicon strip detector using a VLSI circuit is indicated in Figure 8.

In our initial work on the design of the CDF SVX we considered using the Microplex circuit in the readout. That circuit was designed to operate at electron-positron colliders and consequently had certain limitations which made it less than optimal for use in a vertex detector at a hadron collider. As a result we undertook to develop a new device which would meet specifications set by the operating environment at the Tevatron collider. The basic requirements were as follows:

1. At the Tevatron, the interaction region is extended longitudinally with a σ of 35 *cm*. This forces us to have rather long silicon strips. Long strips mean large detector capacitances. A basic property of charge sensitive amplifiers is that their electronic noise increases, and gain decreases, with detector capacitance. In order to have good signal size, position resolution, and trackfinding efficiency we wanted the signal to noise ratio of the amplifiers to be greater than 10 with strips having a capacity of 30 *pf*.
2. Because of the large number of readout channels, the potential for large power dissipation exists. To avoid extensive cooling needs, we wanted to keep the power dissipation of the entire vertex detector below 100 watts (2.5 milliwatts/channel).
3. The beam crossing rate at the Tevatron collider is 12 to 100 times larger than at LEP

and the SLC. We wanted the readout speed to be considerably higher than for the Microplex. In addition, the data handling problems of 40000 channels are excessive and so we wanted some local data compaction in the readout chip. This meant that thresholds would have to be set and stored there.

Our development effort began in early 1986 and has resulted in a device which meets the specifications described above. This circuit is known as SVXC and was designed at Lawrence Berkeley Laboratory by Kleinfelder and others [2]. It is our intention to use SVXC as the front end readout of the CDF SVX. Below we will discuss this device in more detail and describe its overall implementation into a readout system for the CDF SVX. Section 3.3 will cover the external data acquisition system which will process data coming from, and send control signals to, the front end components.

The SVXC is a VLSI circuit fabricated in a CMOS process with $3\ \mu m$ minimum feature size. A die photograph is shown in Figure 13. In SVXC analog and digital functions are integrated onto the same chip. In Figure 14 we show a functional diagram of SVXC. The device contains 128 high gain charge sensitive amplifiers, each is followed by a sample and hold stage, a threshold storage stage, a comparator and latch, and digital circuitry to control a serial multiplexed readout. During operation of the device, a threshold is first stored, incoming data is then compared to the threshold and a corresponding latch is set for channels above threshold. When the chip is read out, the digital control circuitry switches sequentially only to those channels which are latched. For each latched channel, the analog voltage stored is connected to a single analog bus and the channel address is simultaneously connected to a 7 bit digital bus. With this built in sparsification feature the readout time of the device is dramatically decreased and is now set by the occupancy rather than the total channel count. An arbitrary number of chips may be daisy-chained together. Options exist also for automatically scanning all channels, or just hit channels plus their immediate neighbors. In the latter case, we can pickup some shared charge which may fall under threshold. Typical readout speed is $1\ \mu s$ per channel when both analog and digital information are required.

We note here that SVXC is the first example of a custom VLSI circuit for high energy physics applications which includes analog functions as well as digital data compression logic on the same chip. This type of device will probably be used extensively at future hadron colliders where event complexity will make full readout too cumbersome and slow.

The specifications discussed above, (1.) and (2.), on noise, gain, and power have been realized in the charge sensitive amplifier stage of SVXC. This circuit is shown in Figure 15. This is a CMOS cascoded inverter with a 0.3 picofarad feedback capacitor, a source follower, and a voltage inverting stage. The last stage limits the bandwidth at the sample and hold capacitor. The fractions indicated by each transistor refer to the dimensions of the gate region (width/length in μm). In the design, these were optimized along with various currents and operating voltages to obtain the desired performance. The amplifier was extensively studied with a circuit simulation program SPICE [12], and a number of prototypes were made before the final configuration was reached. These devices have been studied extensively at Fermilab [13,14] and at LBL. Bench tests have indicated an open loop gain of about 2000 for the SVXC integrator. With a feedback capacitance of 0.3 pf , the integrator has an effective capacitance of 600 pf , far in excess of the silicon strip

capacitance or 30 pf . This is a basic requirement for good charge collection. By varying a test capacitor on the input, the dependence of noise on detector capacitance was studied. The results are indicated in Figure 16 for a double and quadruple sample and hold. In its use, SVXC will probably be operated with the quadruple correlated sample and hold as part of its threshold measurement. This is described in more detail below. The effect of that is to increase the noise by the square root of two. This is indicated in the figure. The most probable charge liberated in a 280 μm thick silicon detector by a minimum ionizing particle (MIP) is ~ 25000 pairs (4 fc). We see that in both cases we are well within the signal to noise specification given above. At this level, the total power dissipation of the device is 1.5 milliwatts per channel, also within the specification. We indicate the basic features of SVXC in Table 2.

In the actual function of SVXC, charge integration would occur for a fixed interval at the time of beam crossing. This time is on the order of 1 μs and is determined primarily by the amplifier response. During the integration time, leakage currents will flow from the silicon detector into the integrator. Normally these are on the order of 3 $nA/strip$ although individual "bad" strips may have currents many times larger than this. In 1 μs we integrate a charge of 3 fc . In a threshold comparison we might expect to set our threshold at a small fraction of a MIP. Thus, our threshold will be of the same order or less than the integrated leakage current. Since these leakage currents can vary from strip to strip we must be able to include the individual strip leakages in the threshold. In order to do this, the SVXC chip has the ability to perform a quadruple correlated sample and hold (as distinguished from the more common double correlated sample and hold which is used widely in collider detector readout systems). The basic procedure is to integrate twice, once with no beam (before a crossing for example), and once with beam. During the first integration, the integrated leakage as well as an injected threshold would be stored on a threshold capacitor. During the second integration, which must be of the exact same duration, the integrated leakage as well as charge from a possible MIP in the detector will be stored on another sample and hold capacitor. The two stored voltages can then be compared at the input to a latch. A more detailed description of the operation and clocking sequences used to operate the circuit in this way is given in Appendix 1.

In addition to the measurements of front end performance described above, SVXC and its earlier iterations have been operated extensively both on the bench and in a beam test, described below in Section 5, to study the total system performance of the circuit. Based on this experience, we feel confident that this device will function well as a readout system for the CDF SVX.

The mechanical configuration of the CDF SVX was described in Section 3.1. The integration of SVXC into a front end readout system for the detector is tightly coupled to the mechanical design. Based upon the number of electrodes at the various radial layers we have allocated a certain number of chips to each detector *Ladder*. These numbers are given in Table 1c. The *Ears* on each *Ladder* will contain the chips, and buswork for distributing various signals to them, as well as certain auxiliary components. The *Ears* will also have interconnections to other *Ears* comprising a readout daisy-chain. Our present plan is to interconnect the four *Ears* on each face of the SVX into a single readout unit, a *Wedge*, subtending 30 degrees of azimuth. This would give us a total of 24 independent readout

units. By distributing the electronics this way, we insulate the system from the failure of any individual chip to a high degree. Each *Wedge* would be served by about 25 separate signal or voltage lines. We intend to minimize the mass in these cables to the extent possible. We have been studying various low mass cable designs, in Copper on Kapton for example, to assess their potential for our needs. Here we are trying to ensure both good signal quality and noise shielding as well.

By placing our front end readout electronics close to the interaction region we increase the potential for damage due to radiation. MOS devices can in principle be highly susceptible to radiation effects. We have estimated the dose likely at the position of our first layer due to charged tracks from beam-beam interactions. Experience gained during the 1987 run of CDF indicate that this should be the dominant source of radiation during stable running. From its minimum bias data, CDF has measured 4 charged particles per unit of rapidity. From these we expect about 350 *Rads* in Silicon in one continuous year of operation assuming one crossing per particle at a given radius. Some of the softer particles may spiral in the SVX while some may scatter out. There will also be a contribution from conversions. To cover these contingencies we estimate a total dose from interactions of 600 *Rads* in the year. Damage from ionizing radiation is most acute for MOS devices under power. The susceptibility can depend strongly on details of the chip fabrication procedure. Consequently it is difficult to make very specific statements about dangerous exposure levels. To this extent, CMOS devices are believed to be safe below a few thousand *Rads* of ionizing radiation. Assuming no catastrophic accidents and also a general power down procedure for the chips during beam injection we believe the CDF SVX readout electronics will be safe. A second source of radiation damage is the interaction of neutrons in the devices. This source is hard to estimate. Neutron effects are generally believed to be secondary to ionizing effects in MOS devices. We plan to perform some neutron dosimetry studies inside CDF during the upcoming run. At present a series of gamma and neutron irradiations of test chips fabricated during the SVXC development are being carried out at Fermilab. We plan to extend these studies to SVXC as well. Should these indicate a potential problem there are a number of design modifications which can be made to the circuit to radiation harden it.

3.3 Data Acquisition

In Section 3.2 we described the use of SVXC, a custom VLSI circuit, as the basic readout element of the CDF SVX. In this section we will discuss the other elements of the data acquisition and control system which will be part of the CDF SVX. The design of this system is currently in progress. We therefore cannot uniquely specify its components. Generically however they are well defined. In addition, we have developed prototype modules for use in the beam test and the design of the full system is being influenced by that work. More detail on the data acquisition system is in a CDF document [15].

Before describing the conceptual layout of the data acquisition system for the SVX we will give an estimate of the average number of words of data expected from the vertex detector. Recall that the SVXC chip performs a local sparsification of the data. Typically we would request all hit channels and their two nearest neighbors. The SVX covers roughly 6 units of rapidity. At CDF we expect 4 charged particles per unit rapidity in a minimum

bias event. Additional multiplicity due to jets in an event might contribute another 25 tracks. This gives us,

$$((6 \times 4) + 25) \text{ particles} \times 4 \text{ layers} \times 3 \text{ channel/hit} = 588 \text{ hit/event.}$$

This is an underestimate because there will be a additional soft component, as well as spiraling tracks to contend with. This component might double the hit numbers. Further, there will be a certain occupancy due to electronic noise fluctuations. This contribution depends upon the S/N ratio as well as the threshold cut we impose on the chip. With a S/N of 13 for a MIP, if we set the threshold at $0.3 \times \text{MIP}$ then we are at 3.9σ on the noise or a fraction of a percent probability. Thus the noise contribution should be negligible. We therefore expect, 1-2K hits per event. Each hit represents 8-10 bits of digitized pulse height plus 16 bits of address indicating the side, the *Wedge*, the chip number, and the channel of the hit. If we take 26 bits total then we expect 3-6 Kbytes per event from the SVX. The present CDF event size is at the 60-100 Kbyte level.

The conceptual layout of the data acquisition system is shown in Figure 17. In this example we have arbitrarily chosen to package certain modules in FASTBUS and place them in the counting room. In actual use, the packaging might be different and certain pieces might instead be in the collision hall. On the other hand, the front end readout components, discussed in Section 3.2, beginning with the cable into the interaction region, are well specified at present.

The basic elements of the data acquisition and control system, as indicated in the figure are as follows.

1. **SEQUENCER:** This module is the master control for the CDF SVX. The various sample and hold functions and resets of the SVXC circuit as well as its data readout require particular digital sequences on up to 12 clocking lines. At different phases of operation, different clock sequences need to be executed. The *Sequencer* is a programmable device which puts out the required patterns and can switch among the various operating phases in response to external interrupt. A prototype device, the SRS (SVX Readout Sequencer), has been built and used to operate the SVX at the beam test. We envision extending some of ideas developed for this to the full *Sequencer*. The entire CDF SVX will require one or two of these modules.
2. **ADC/MEMORY:** The data coming from the CDF SVX will consist of a time sequence of analog voltages and digital addresses corresponding to the pulse height and address of the hit strips. As we are dividing the readout into 24 individual units, there will be 24 such sequences in parallel. The *ADC/Memory* must digitize and store the pulse heights and addresses in a set of associated memories. The ADC will digitize fast enough to handle the readout speed of SVXC (1 MHz) and will be synchronized to the *Sequencer*. For the test beam we built a module using an 8 bit flash ADC and sufficient RAM to buffer the events. In the CDF SVX we will have 24 parallel channels of *ADC/Memory* which will be packaged in some convenient modularity. Note that while in Figure 17 *the ADC/Memory* is indicated as a single module, it will likely be two separate modules for each of the 24 readout units.
3. **REPEATER:** This device is a general interface to buffer, fanout, and multiplex signals going to and from the interaction region. It will be placed as close to the SVX as possible while remaining outside CDF proper.

4. **POWER:** Power is required for the chips (5,6,±12 volts) and for the silicon detector reverse bias (+100 volts). The complication here is that a certain amount of safety interlock is necessary to prevent damage to the readout electronics. If the chips lose power while the detector is biased, leakage current can charge the amplifier inputs up to the bias voltage. These are MOS gates and will be destroyed if breakdown occurs. Thus, the detector bias must be interlocked to the chip power. Furthermore, because of the potential for radiation damage, the chip power must be brought down during injection. We envision a hardware interlock to a gate provided by the accelerator control system.

Design work on the data acquisition system is a subject of current activity.

5. Expected Performance

Simulations of this detector [3],[4],[5], have been performed over the last few years to determine resolutions and efficiencies and to assess its usefulness in sorting out some specific physics processes (see Section 2). A detailed description of the detector was given in the section dealing with the design and assembly of the SVX and in a CDF note [1]. We refer to Figures 4,5, and 6 for an overall view. We will summarize here the results of our studies which were also presented in the cited references.

4.1 Track parameter resolution

The impact parameter resolution, which can be obtained with the combination of information from the CTC and the SVX, is 10–15 μm for tracks of p_t greater than a few GeV/c . For tracks of lower momenta the effects of multiple scattering dominate, and the resolution is degraded to about 60 μm at a p_t of 500 MeV . In Figure 18 we show calculated impact parameter resolution versus p_t . The transverse momentum resolution of the CDF central tracking system is also improved by the introduction of the SVX in CDF, mainly because of the extension of the lever arm. Our studies indicate that more than a factor 2 in p_t resolution can be gained for tracks of $p_t > 15 \text{ GeV}/c$ in all cases in which an average beam position constraint cannot be used (because the track originates from a secondary vertex).

4.2 Trackfinding

The trackfinding algorithm used in this study matched CTC tracks with hits in the SVX. Track finding in the SVX alone has been not so far been considered for two reasons: 1) the redundancy of the SVX is rather marginal (4 measurements and 3 track parameters to determine); 2) due to the short lever of arm of the SVX, fitting for circular tracks without an independent measurement of momentum gives an impact parameter resolution of over 100 μm (when no CTC information is added to the fit).

The computed efficiency for finding tracks in the SVX, as well as the probability to find wrong tracks, may depend significantly on the Monte Carlo event sample used to test the trackfinding algorithm. The high track density in jet cores will lead to lower efficiencies

than in softer events. Furthermore, within these jets, the tracks originating from bottom decays are strongly correlated, and this correlation may make the job of reconstruction even harder. For these reasons we have calculated our trackfinding efficiencies with different samples of ISAJET generated QCD events: $b\bar{b}$ jets of different p_t and $W \rightarrow tb$.

We define the trackfinding efficiency as the fraction of reconstructed tracks out of the total number of “reconstructable” tracks, that is, all tracks which have been found and correctly measured in the CTC and which traverse at least three SVX layers. We also define an error rate, that is, the fraction of tracks which are poorly reconstructed in the SVX, as the fraction of tracks for which the absolute value of the difference between the true and reconstructed impact parameter is larger than three times the calculated statistical error.

Efficiencies and error rates for the various event samples are shown in Table 3: the indicated efficiency is high ($\sim 99\%$) and error rates are low ($\sim 2\%$), independent of the type of event sample chosen.

Current studies of trackfinding in the CTC alone indicate that its efficiency can vary from $\sim 99\%$ in minimum bias events to better than $\sim 70\%$ inside dense high p_t jets (work on this is very much in progress and the number should be expected to improve). Thus the power of the SVX depends to some extent on the quality of tracks found in the CTC. In those cases where we want to tag an isolated lepton, or a B jet (generally lower p_t), the compound efficiency should be good.

4.3 B meson tagging

Our efficiency for tagging B meson decays is determined by a number of effects. As described below, a tag will require three tracks all consistent with a secondary vertex. The first step is to select the track candidates. We say that a decay prong of a B meson is tagged if it is reconstructed in the CTC, it is reconstructed in the SVX, and it has significant impact parameter (i.e., the impact parameter divided by the calculated error is larger than 3). From the results on B meson decay prong tagging efficiencies shown in Table 4 (for 20 GeV/c $b\bar{b}$ jets) and Figure 19, it is clear that there are two dominant effects at this stage. First, the limited detector acceptance, caused by the lower p_t cutoff of the CTC and the restricted z coverage of the SVX relative to the longitudinal size of the interaction region, reduces the initial sample by $\sim 40\%$. Second, the combined CTC+SVX resolution, effected by multiple scattering, reduces it further to the indicated values. These two effects account for the trend seen in Figure 19 of higher efficiencies for higher jet p_t . The hardening of the p_t of the B prongs both increases the CTC acceptance and improves the resolution, because the effect of multiple scattering becomes less significant. We stress here that tracking inefficiencies in the SVX are of negligible importance in this case.

We now come to the problem of tagging B meson decays. Reliable tagging needs at least three reconstructed prongs in the SVX. Indeed, since all the position resolution is in the $R - \phi$ plane, at least three tracks are needed to constrain them as originating from a single vertex. Charm contamination is suppressed by this requirement since the charm decay prong multiplicity is much lower than that of B mesons and the lifetime of charmed mesons is shorter. Contamination from strange particles can be virtually eliminated by

the three track requirement also as well as from the longer decay length. Error rates of one spurious 3 fold vertex out of 10^3 – 10^4 high p_t jet events have been calculated using this tag. Further study and experience with real events may indicate ways to reduce this even further. Note also that the error rate for a double tag is completely negligible. Typical tagging efficiencies (E_3 in the figure) are shown in Figure 20 as a function of the p_t of the $b\bar{b}$ jet sample; separate curves are also shown to separate the effect of physics (E_3 physics in the figure), i.e., the inefficiency due to the fact that some B mesons decay into less than three charged prongs, and that of CTC acceptance (E_3 CTC in the figure). Double tag efficiencies (efficiency to tag both B mesons in the event) are also shown in Figure 21.

5. Test Beam Results

A prototype of the SVX has been assembled, and operated in the CDF test beam during Dec. 1987 through Feb. 1988. The aim of this exercise was to measure signal to noise, efficiency, and resolution, and to gain real-time experience operating the front end readout chip in a full detector system. The prototype consisted of a four layer silicon detector telescope. Each detector was assembled on a stiffened foam *Ladder* in the same way as is intended for the final detector. In this prototype we had one single detector on each *Ladder*, giving a strip capacitance of about 8–10 *pf*. An earlier version of the readout chip, SVXB, was used as front end electronics. This chip had higher noise than SVXC, but otherwise was essentially equivalent functionally. The combination of shorter strips and higher noise made the S/N roughly equivalent to what we expect in the real CDF SVX with 25 *cm* strips and the SVXC readout chip. The front end was read out and controlled by a prototype *Sequencer* and *ADC/Memory* system built for this test. Several thousand 230 *GeV* pion events were collected and analyzed. One of the four layers failed to function properly. In Figure 22 we show a typical event. The three working layers are shown, offset by their relative spacing. A detailed description of the setup and the analysis of the beam test data can be found in a CDF note [6]. We summarize here the results of the analysis.

1. *Pedestals.* Pedestal values were consistent with low leakage currents (in the 1–2 *nA* range) over most of the instrumented area of the detectors. The σ of the pedestal distributions were quite consistent with the estimates obtained assuming 8 *pf* input capacitance and a noise vs. input capacitance curve obtained on the test bench, indicating that noise contributions from other sources were insignificant. The distributions were also remarkably Gaussian as shown in Figure 23.

2. *Charge distributions.* Charge liberated by ionizing tracks in the detectors can be shared by more than one strip. An analysis to determine which contiguous groups of strips (clusters) were hit was therefore performed. A position, based on an optimized centroid calculation algorithm, and a pulse height (sum of all strip charges) were associated with each cluster. We then searched for clusters in the three detectors which lay on the same line within a ± 150 μm window. The cluster charge distribution associated with tracks is shown in Figure 24. The superimposed curve is the fit to a Landau distribution convoluted with a Gaussian. Here, the match between the fit and the expectation is excellent.

3. *Efficiency.* To determine the efficiency on the middle layer we have selected events with only one cluster on the two outer layers and then formed the following table:

Counter	Counts	Fraction of total counts
Total counts	5565	
Bad Spot	122	2 .19%
Base Sample	5443	97 .01%
Tracked	5399	99 .19%
Not Tracked	6	.11%
Not tracked bad	32	.59%
Missed	6	.11%

The entries are defined as follows. *Total Counts* is our base sample. *Bad Spot* indicates those events for which the track position on the middle layer corresponded to a dead strip. Most of these were near the edges of the detectors and were due to the bonding and handling procedures used in the prototype fabrication. The fraction of *Bad Spots* will be much less in the actual device. *Base Sample* is the remaining difference and all subsequent numbers are relative to it. *Tracked* are those events for which a cluster was found in the expected spot. *Not Tracked* are cases where a cluster was found on the middle layer, but not in the right position: a scan of all the events of this category indicated that they consisted mostly of events where at least one of the clusters contained a delta-ray, which produced an offset in the computed centroid of the cluster. *Not Tracked Bad* are the number of cases where the track extrapolated to a bad spot on the middle layer, but an extra cluster was present somewhere else on that layer. This contribution is equivalent to *Bad Spot* and should be eliminated also. Finally, *Missed* are those events for which the position on the middle layer was good but no cluster was found there. This is a true inefficiency. Most of the remaining inefficiency (*Not Tracked*) can in principle be removed by a more sophisticated cluster analysis. The remaining contribution (*Missed*) can be removed only by improving the signal to noise ratio, and can be regarded as the intrinsic inefficiency of the detector.

A similar analysis performed on the other layers yields comparable results.

4. *Resolution*. In Figure 25 we show the distribution of the extrapolated track position minus the cluster centroid on the middle layer. Such distribution has a standard deviation of $10 \mu m$, corresponding to an intrinsic detector resolution of $8 \mu m$.

5. *Alignment*. A final remark must be made on the quality of the alignment between the detectors. The mean value of the residual distributions on each of the three layers is $-3 \mu m$, $3 \mu m$, $-12 \mu m$ respectively, with no geometry correction whatsoever. These values compare very well with our goal of a *Ladder to Ladder* alignment tolerance of $20 \mu m$. Furthermore most of the error comes from problems in construction of the *Ears* used in the prototype, connecting the *Ladder* to the supporting flanges. We have redesigned and mechanically improved the *Ears* which will be used in the real CDF SVX and therefore are confident that the mechanical tolerances will be even better.

6. Schedule and Budget

Our goal is to have the SVX system ready to take data during the 1990 collider run. The system should be assembled at least 5-6 months ahead in order to debug, test, and

gain operating experience with it. The target is therefore that all parts should be assembled by September 1989 (with the possible exception of some DAQ modules).

If we can begin materials procurement in July of 1988, the chart shown in Figure 26 indicates how we will meet that goal. The current status of the items shown is as follows.

1. **Detectors:** All drawings are complete and approved by the detector fabrication firm. The raw silicon has been procured. Processing time is 6–7 months.
2. **Front End Electronics:** We are performing detailed evaluations of the latest version of SVXC and expect to be ready for a final production run soon. Expected processing time is 2–3 months for the chips followed by 2–3 months of mounting and testing.
3. **Mechanical Parts and Tooling:** We are currently drawing the final mounting fixtures and expect most of the work can be completed by the end of 1988.
4. **Ladder Assembly:** This involves many operations, shipping, and testing. We have experience with all of them. We can start as soon as material is procured and the tooling is complete. We expect this phase to last ~ 6 months.
5. **Full System Mounting:** This is a relatively short sequence of operations which however need tooling and instrumentation which we are still designing. We estimate 3 months for the actual mounting process.
6. **DAQ:** The DAQ additions represent a modest increment for CDF. We expect the design to evolve from our experience with a prototype system in the test beam as well as from the general experience with the CDF DAQ system. We should have prototypes early in 1989 and could proceed with production and testing over that year.
7. **Minor Items:** Other operations and construction such as survey, *Ear* fabrication, cable fabrication etc. are omitted from the chart since they are less time consuming and are carried out in parallel with the above.

We have prepared a cost estimate for the SVX and it is given in Table 5. Note that the estimate includes additions to the CDF data acquisition system required for the SVX.

7. Summary and Conclusions

The proposed SVX upgrade of CDF has gone through the preliminary phases of conceptual design, performance simulation, prototype testing, and technical design. At this point the device is ready to be built. This upgrade could open a new range of physics for CDF and offer a new handle for future discoveries. A group within CDF, dedicated to this project, was formed and has acquired much experience and expertise over the past few years of work. An accurate cost assessment has been given. A significant financial contribution on the part of INFN has already be allocated, and we require the additional funds from DOE which are detailed in this proposal to make the SVX operational for the 1990 run of CDF.

Appendix 1: SVXC Circuit Operation

In this appendix we give a more detailed description of the operating procedure for SVXC. A functional diagram of the circuit is given in Figure 14. The active element *A* is the CMOS charge sensitive amplifier. Elements *B*, *C*, *D*, and *E* are CMOS inverters.

Element B also serves to limit the bandwidth seen at the sample and hold capacitor C_S and reduce the noise as described above. When the reset switches on the CMOS inverters are OPEN, the inputs have very large impedance. When the reset switches are CLOSED, the inputs are fixed at a voltage in the middle of the operating range of the inverter, ie. they are connected to a fixed potential. For example, consider the case of R_A OPEN, and R_B , R_S , and R_C CLOSED. At the moment R_B is set OPEN any charge flowing to the input will be integrated and held on C_S and C_C . If R_C is then opened, the voltage stored on C_S will be held fixed from that time onwards. Let the time between R_B opening and R_C opening equal T_{INT} . If R_B is then closed again the charge stored on C_S will be cleared. Opening R_B again allows C_S to again track the input starting from zero. If R_S is then opened a time T_{INT} since the last opening of R_B , the integrated leakage current stored on C_S will equal that stored on C_C from before. The idea then is to inject a threshold during the first integration period and wait for charge from a MIP in the silicon detector to appear during the second. If the voltage across C_S exceeds the voltage across C_C then the output of element C will exceed its reset level.

Elements D and E are a latch which can be used to indicate the state of the comparison to digital logic which follows after appropriate clocking. An example of the cycles described above is shown in Figure 27. Held voltages can be kept until a readout of the chip is initiated. At that point, hit channels can be multiplexed out serially at about 1 MHz.

1. F. Bedeschi et al, CDF-591.
2. S. Kleinfelder et al, Proc IEEE NSS Symposium, Oct. 1987.
3. F. Bedeschi et al, CDF-283.
4. F. Bedeschi et al, CDF-284.
5. F. Bedeschi et al, CDF-601.
6. F. Bedeschi et al, CDF-654.
7. Talk presented by K. Eggert at "Les Rencontres de Physique de la Valle d'Aoste", March 1988
8. F. Abe et al, CDF-494
9. F. Halzen and P. Hoyer, Phys. Lett. **154B** (1985) 324;
A.H. Mueller and P. Nason, Phys Lett. **157B** (1985) 226;
P. Nason et al., Fermilab-Pub-87/222-T (Dec. 1987)
10. F. Bedeschi et al, CDF-592.
11. J.T. Walker et al, NIM **226**, 200 (1984).
12. **SPICE**, University of California, Berkeley, Dept of Elect. Engineering and Computer Science.
13. R. Yarema and T. Zimmerman, "Test Results of the LBL SSD Readout Chip", internal CDF memo, 1987.
14. T. Zimmerman and R. Yarema, CDF-593.
15. C. Haber and F. Kirsten, "A Data Acquisition Primer for the CDF Silicon Vertex Detector", LBL/CDF 88-25, CDF-XXX (to be released).

Figure 1a: Graph for the decay $W \rightarrow tb$ followed by semileptonic t decay.
Figure 1b: Graph for the decay $W \rightarrow tb$ followed by hadronic t decay.
Figure 2: Four jet invariant mass spectrum from $W \rightarrow tb$ followed by hadronic t decay after cuts described in the text.
Figure 3: Number of B jets which can be tagged for $1 pb^{-1}$.
Figure 4: Overall layout of the CDF SVX showing an isometric view.
Figure 5: Quarter view of SVX showing *Ladder* structure.
Figure 6: Quarter view of CDF showing position of SVX.
Figure 7: End view of SVX showing radial layer positions and tilts.
Figure 8: Generic silicon detector readout scheme using custom chip.
Figure 9: Design of *Ladders* for the CDF SVX.
Figure 10: Ladder alignment and fabrication fixture.
Figure 11: Photograph of prototype bulkhead.
Figure 12: Percent radiation lengths contained in the SVX versus polar angle of particle.
Figure 13: SVXC die photograph.
Figure 14: Functional diagram of SVXC circuit.
Figure 15: SVXC front end amplifier.
Figure 16: Noise and S/N for $280 \mu m$ silicon versus detector capacity.
Figure 17: Conceptual layout of the SVX data acquisition system.
Figure 18: Impact parameter measured by the SVX+CTC versus p_t .
Figure 19: Track tagging efficiency for B jets versus jet p_t .
Figure 20: Vertex tagging efficiency for B decays versus p_t .
Figure 21: Double tag efficiency for $b\bar{b}$ events.
Figure 22: Typical event from the SVX beam test.
Figure 23: Individual channel pedestal distribution from beam test prototype.
Figure 24: Pulse height distribution for clusters on tracks.
Figure 25: Distribution of residuals of clusters on tracks for middle layer.
Figure 26: Timescale for SVX fabrication.
Figure 27: Timing cycles for SVXC operation.

Table 1a: Barrel geometrical parameters

	Radius [μm]	Length [μm]
Layer #1	28438	256000
Layer #2	42769	256000
Layer #3	57100	256000
Layer #4	78616	256000

Table 1b: Silicon crystal geometrical dimensions

	Width [μm]	\pm	Length [μm]	\pm	Thickness [μm]	\pm
Layer #1	16040	50	85000	50	280	15
Layer #2	23720	50	85000	50	280	15
Layer #3	31400	50	85000	50	280	15
Layer #4	42930	50	85000	50	280	15

Table 1c: Characteristics of the active area of the detectors

	Width [μm]	Pitch [μm]	Readout strips	Number of chips	Length [μm]
Layer #1	15360	60	256	2	84500
Layer #2	23040	60	384	3	84500
Layer #3	30720	60	512	4	84500
Layer #4	42240	110	384	3	84500

Table 1d: Coverage in polar angle

	Theta \pm	Eta \pm
Layer #1	6.3	2.9
Layer #2	9.5	2.5
Layer #3	12.6	2.2
Layer #4	17.2	1.9

Table 2

Basic Specifications for SVXC Readout Chip

Number of channels/chip = 128.

Power dissipation = 200 mW/chip.

Gain of analog channel = 20-30 mv/fc.

Open loop gain = 2000

Nominal feedback capacitor = 0.3 pf

Nominal value of charge injection capacitor = 0.03 pf.

Range of front end (approx) = 10 MIP.

Signal from MIP in Si detector = 25000 e or 4 fc.

Typical leakage current from 3 Si detectors = 3 na/strip.

Risetime at sample and hold capacitor = 900 ns (10%-90%).

Reset time of charge integrator = 300-400 ns.

Capacitance of strip = 30 pf.

Signal to noise ratio = 13 (quad sample), 18 (double sample) for 30 pf.

Maximum analog readout speed = 1 MHz.

Maximum digital readout speed = 10 MHz.

Risetime of analog output = 400 ns.

Analog supply voltage = 6 VDC.

Digital supply voltage = 5 VDC.

Number of bits digital data = 7 chip addr + 7 chan addr.

Table 3

SVX Trackfinding Efficiency vs Pt of B jets

A= % of track not found

B= % of tracks with $ABS(\text{true} - \text{reconstruct impact parameter})/\sigma > 3$
 where sigma is the fit error on the impact parameter

Sample size of good tracks (found in CTC and cross > 3 SVX layers = 1000

Pt Jet	A	B
5 GeV/c	2.4	0.8
10 GeV/c	1.2	2.5
20 GeV/c	1.7	2.2
100 GeV/c	1.3	2.4
W-->tb	1.6	2.0

Table 4

SVX B jet Vertex Tagging Efficiencies

Sample of 20 GeV Pt B jets, Nbp = Number of B charged prongs = 500
 Beam pipe diameter = 2 inches

%CTC = #B decay tracks reconstructed in the CTC / Nbp

%SVX = #B decay tracks reconstructed also in the SVX / Nbp

%TAG = #B decay tracks reconstruct in SVX with visible i.p. / Nbp

where i.p. means impact parameter and "visible" means that the impact parameter is greater than 3 times its fit error.

Conditions	%CTC	%SVX	%TAG
No multiple scattering and bunch length sigma = 1 cm.	64.	64.	46.
Multiple scattering ON and bunch length sigma = 1 cm.	64.	64.	32.
Multiple scattering ON and bunch length sigma = 20 cm.	62.	51.	24.

Table 5
CDF SVX Budget Estimate

Item	R&D FNAL	Equip FNAL	INFN-Pisa
Silicon Detectors:			
Silicon detector prototypes			13.0
Silicon wafers for detector fab			60.0
Drafting for masks			5.0
Prototype AC coupled detectors			29.0
Mask fabrication			23.0
Production detectors			700.0
Mechanical:			
SVX mechanical model:			
Cut dummy silicon	2.0		
Model Ears and pins	3.0		
PHI mounting fixture		45.0	
Misc. mechanical R&D	20.0		10.0
Final mech construction		30.0	
Cooling		10.0	
New beam pipe		100.0	
Front End Electronics:			
Ear board prototypes	5.0		
Ear board preliminary	10.0		
Radiation damage tests	5.0		
SVXC chip tests	5.0		
Custom cables R&D	20.0		
Production of SVXC chip		40.0	
Production/test of Ear boards		40.0	
Detector power supplies		10.0	
Custom cables production		30.0	
Data Acquisition:			
DAQ Sequencer development	15.0		
Sequencer construction		30.0	
DAQ ADC development	10.0		
ADC construction		37.0	
Memory modules		125.0	
FASTBUS scanners		20.0	
Segment Interconnects		10.0	
Crates and power supplies		32.0	
Cables		37.0	
<hr/>			
Subtotals	95.0	596.0	840.0
Contingency (25% on US)	24.0	149.0	
Contingency (25% on Italy)		210.0	
EDIA (on US contribution)		143.0	
<hr/>			
Subtotals	119.0	1098.0	840.0
Total US	= 1217.0		
Total Italy	= 840.0		
<hr/>			
Total	= 2057.0		

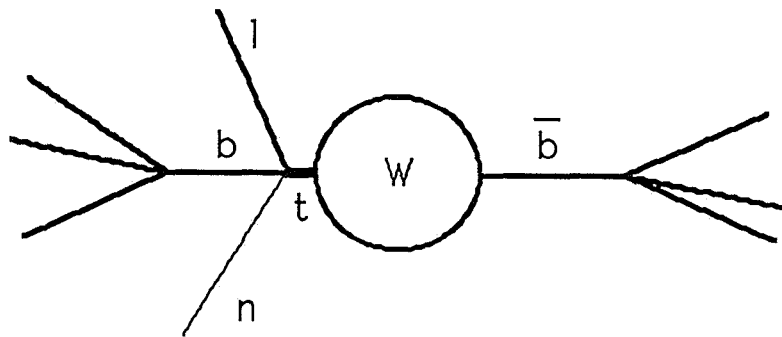


Figure 1a

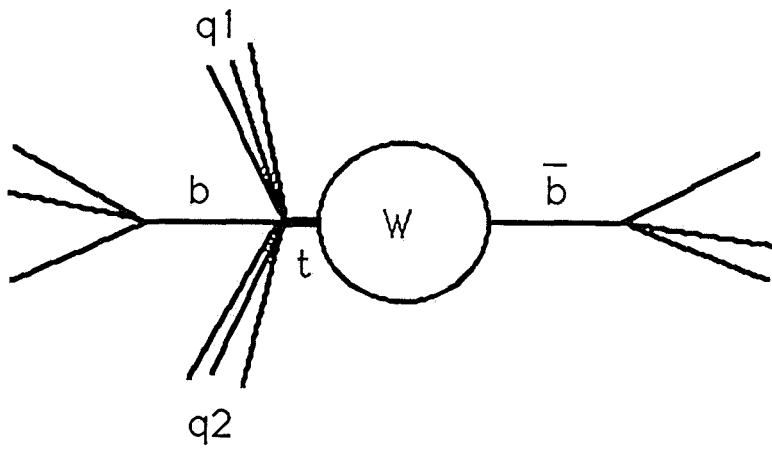


Figure 1b

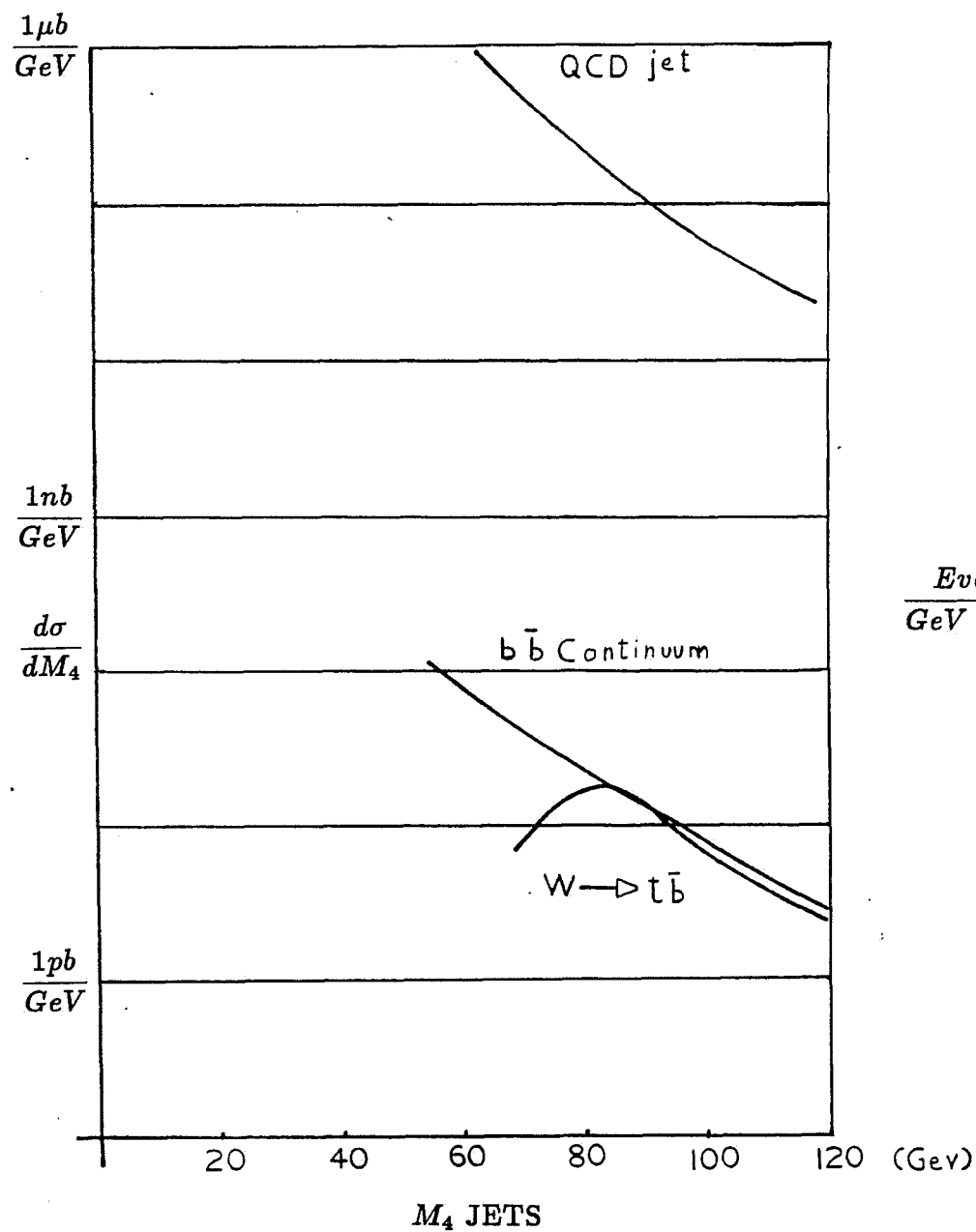


FIGURE 2

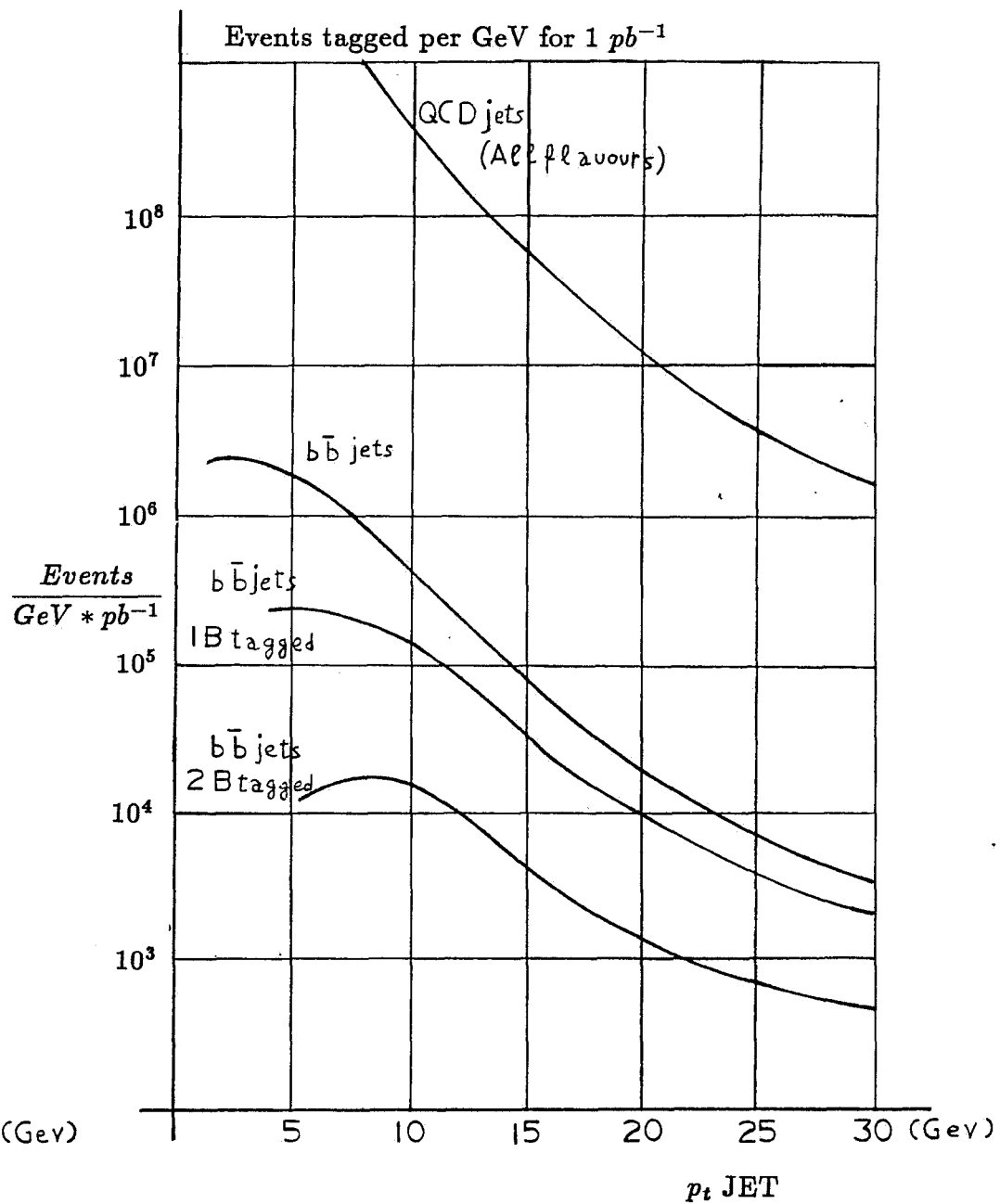


FIGURE 3

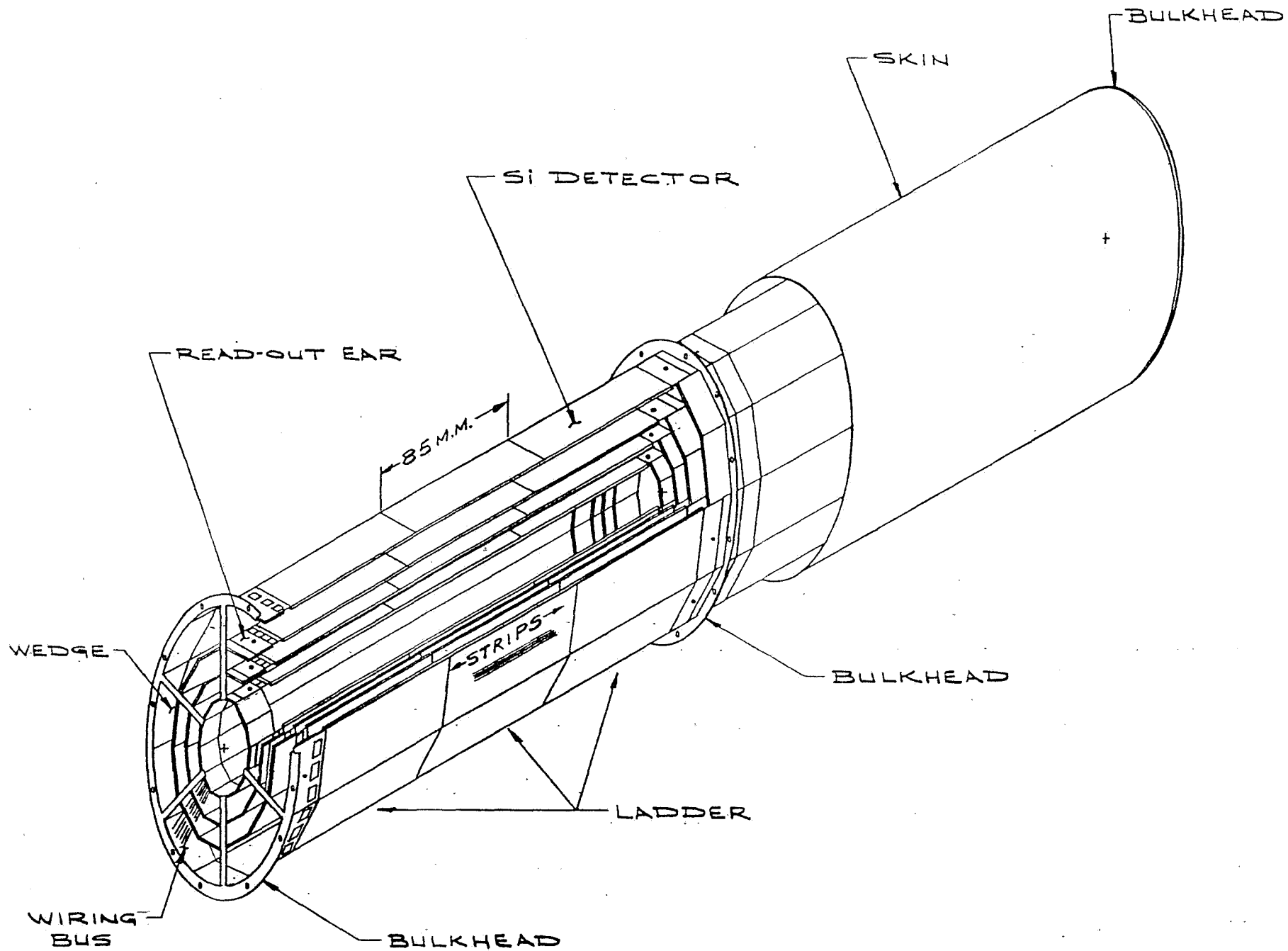


FIGURE 4

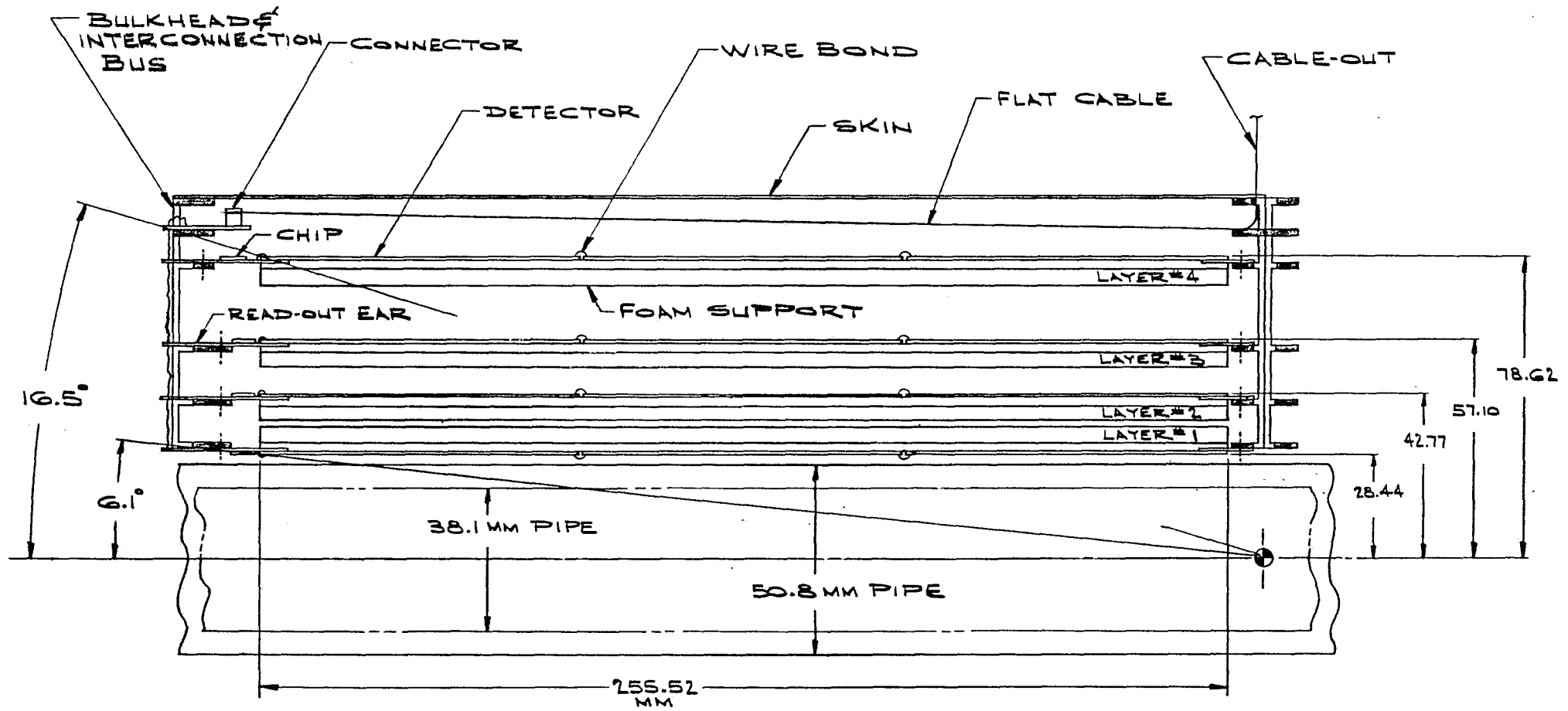


FIGURE 5

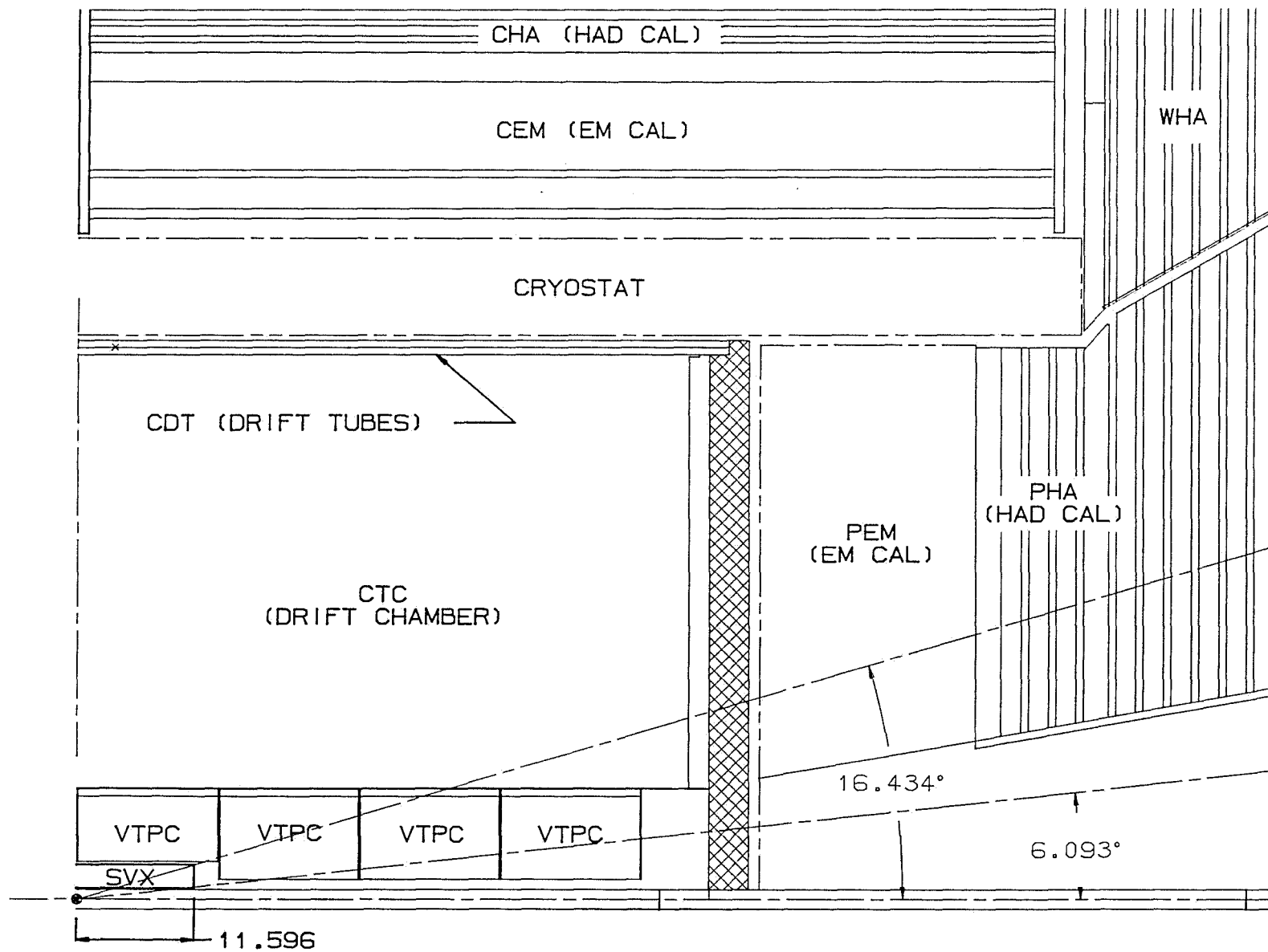


FIGURE 6

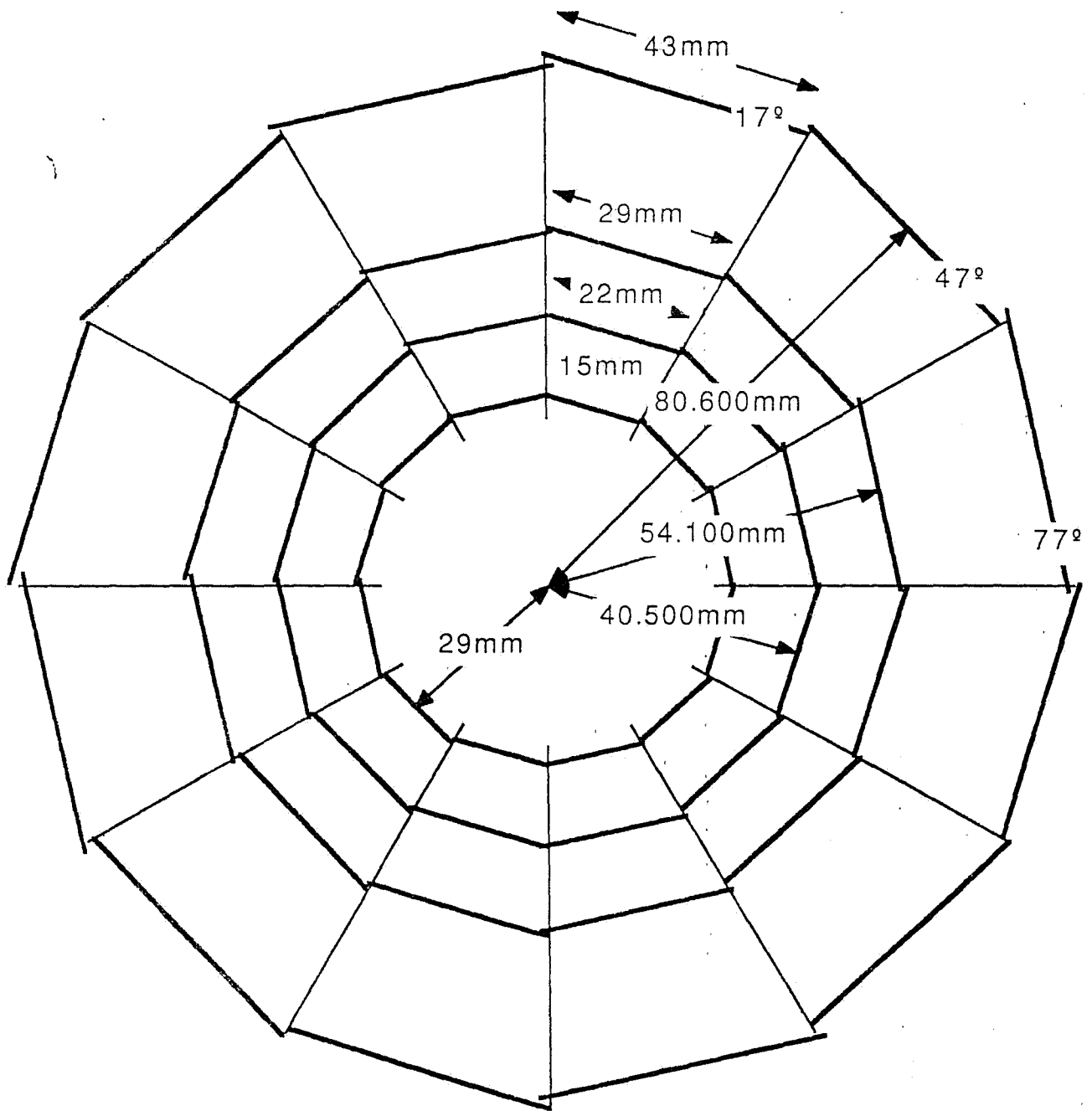


FIGURE 7

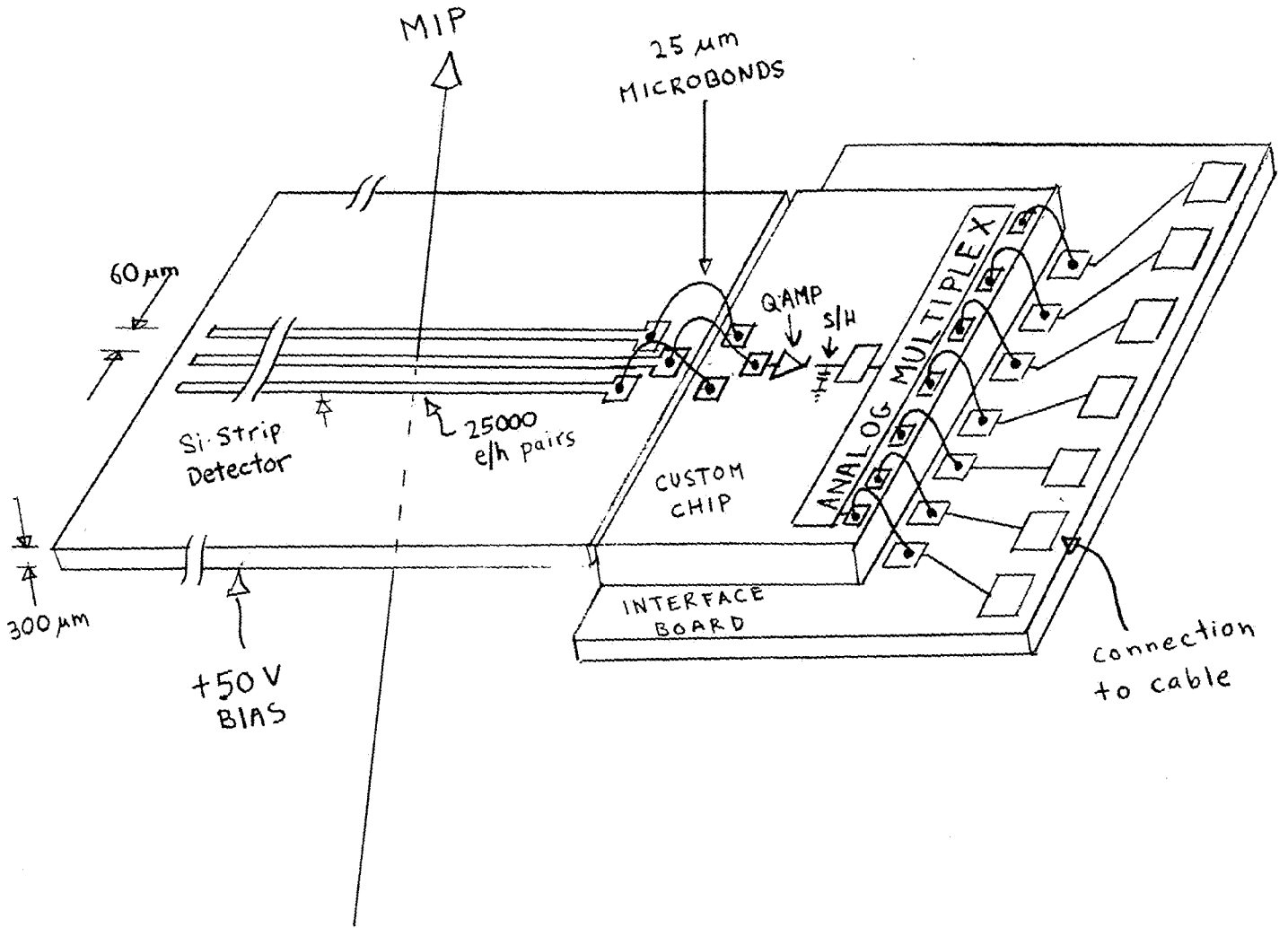
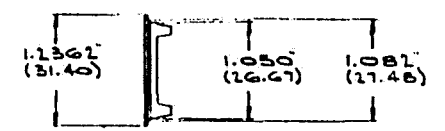
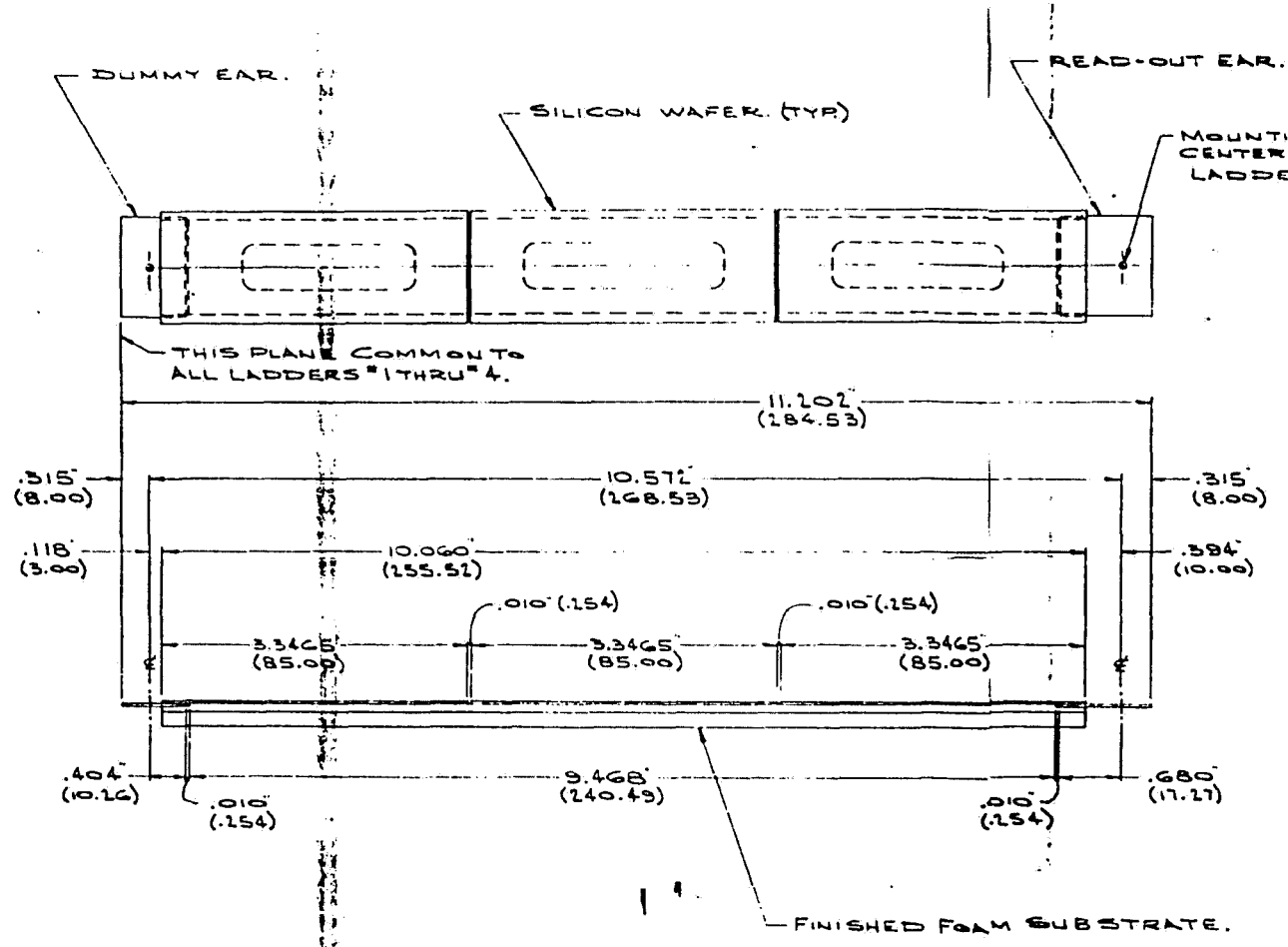
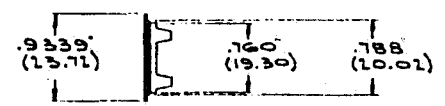


FIGURE 8

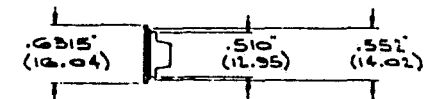
REV.	DESCRIPTION	DRAWN	DATE
		APPD.	DATE



LADDER #3



LADDER #2



LADDER #1

ITEM NO.	PART NO.	DESCRIPTION OR SIZE	QTY.	REQ.
PARTS LIST				
UNLESS OTHERWISE SPECIFIED		ORIGINATOR		
FRACTIONS	DECIMALS	ANGLES	DRAWN	D. TOUSIGNANT
1	2	2	CHECKED	
1. BREAK ALL SHARP EDGES 1/64 MAX.			APPROVED	
2. DO NOT SCALE DWG.			USED ON	

FIGURE 9

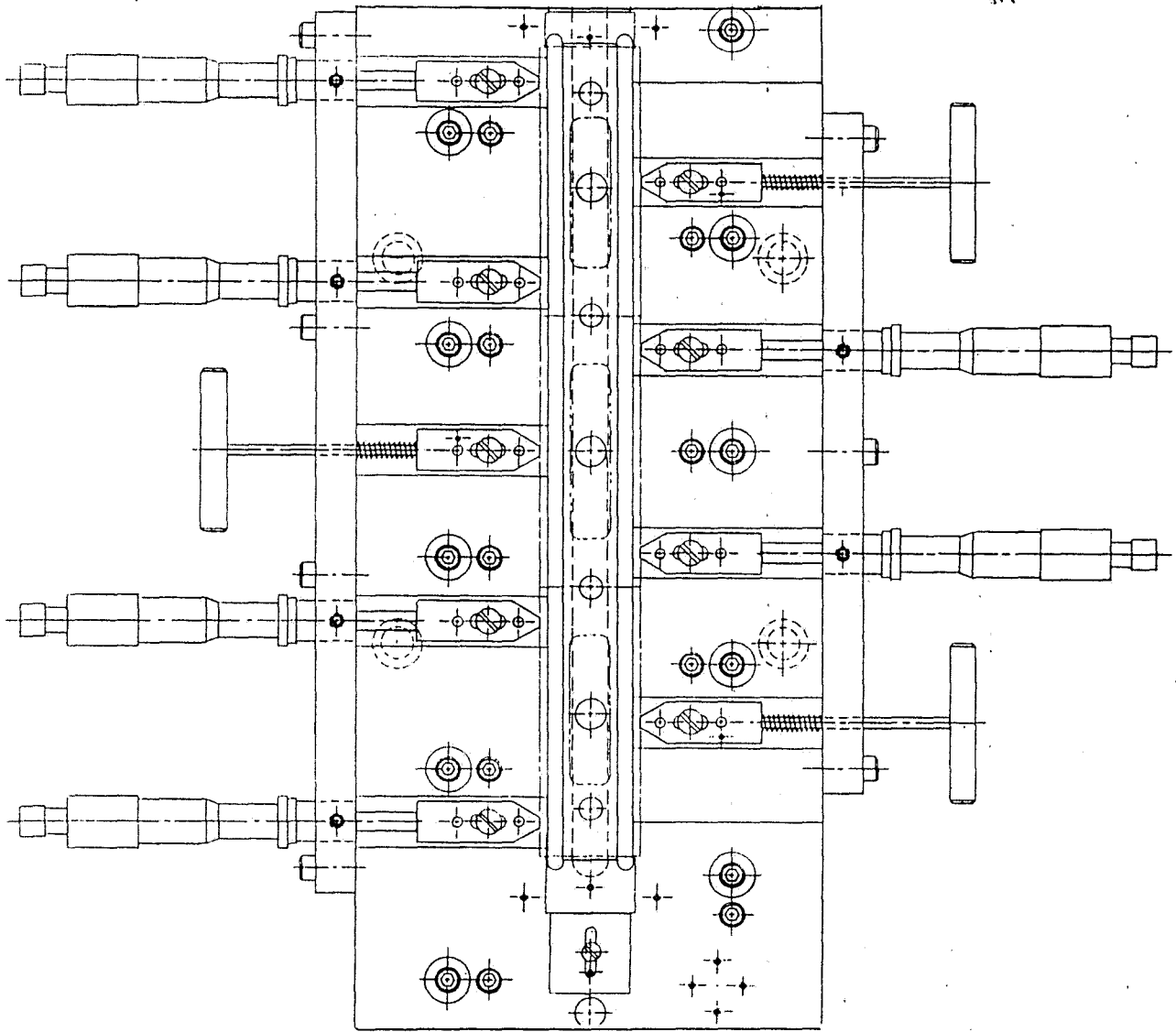


FIGURE 10

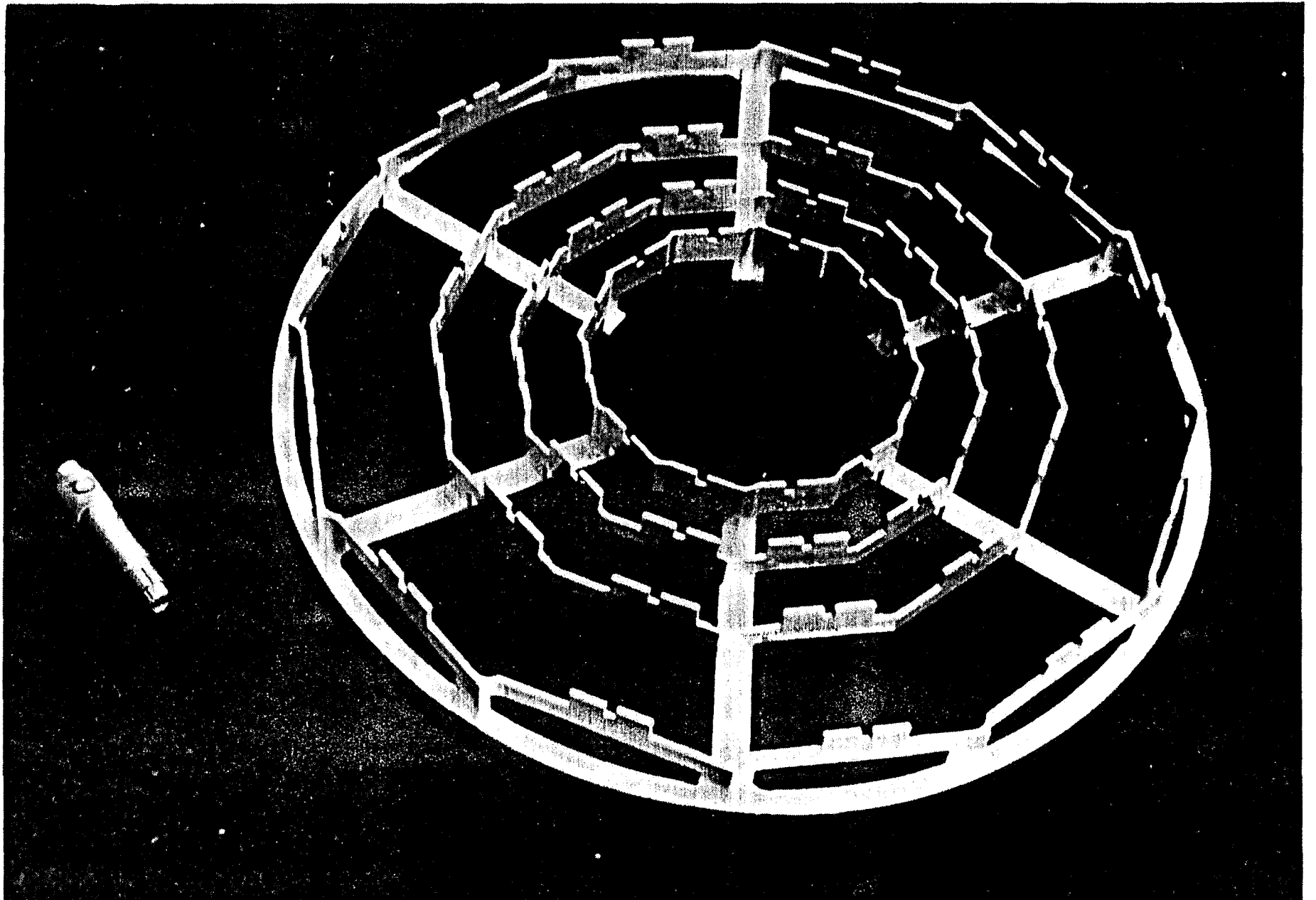


FIGURE 11

Summary SVX material

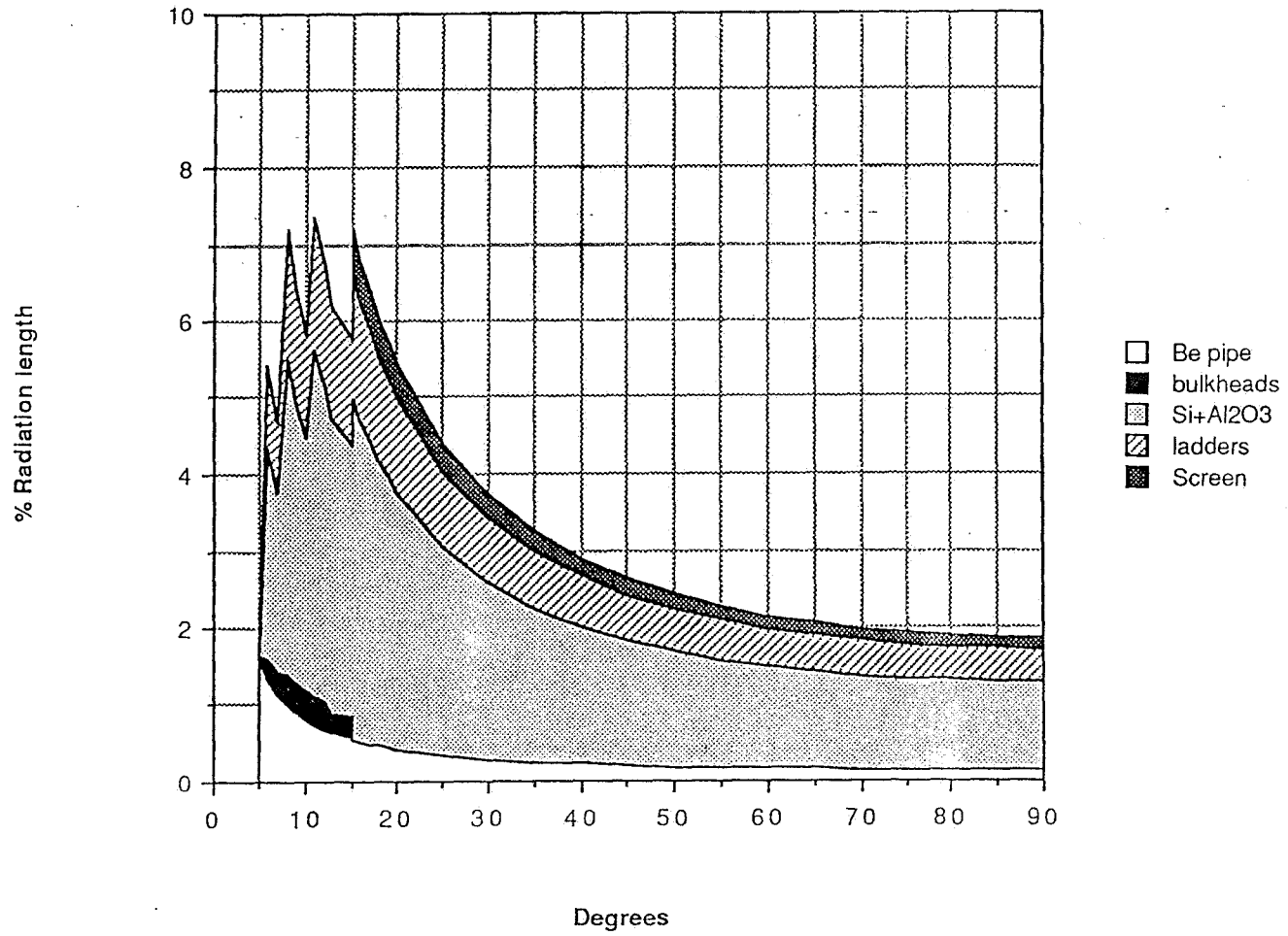


FIGURE 12

GR AC AG CA NE AP DG EN FO AT 46 AS AM AS AZ AI AP NE HE HL PI TN AO AQ DP NE AP BI AC AG GR

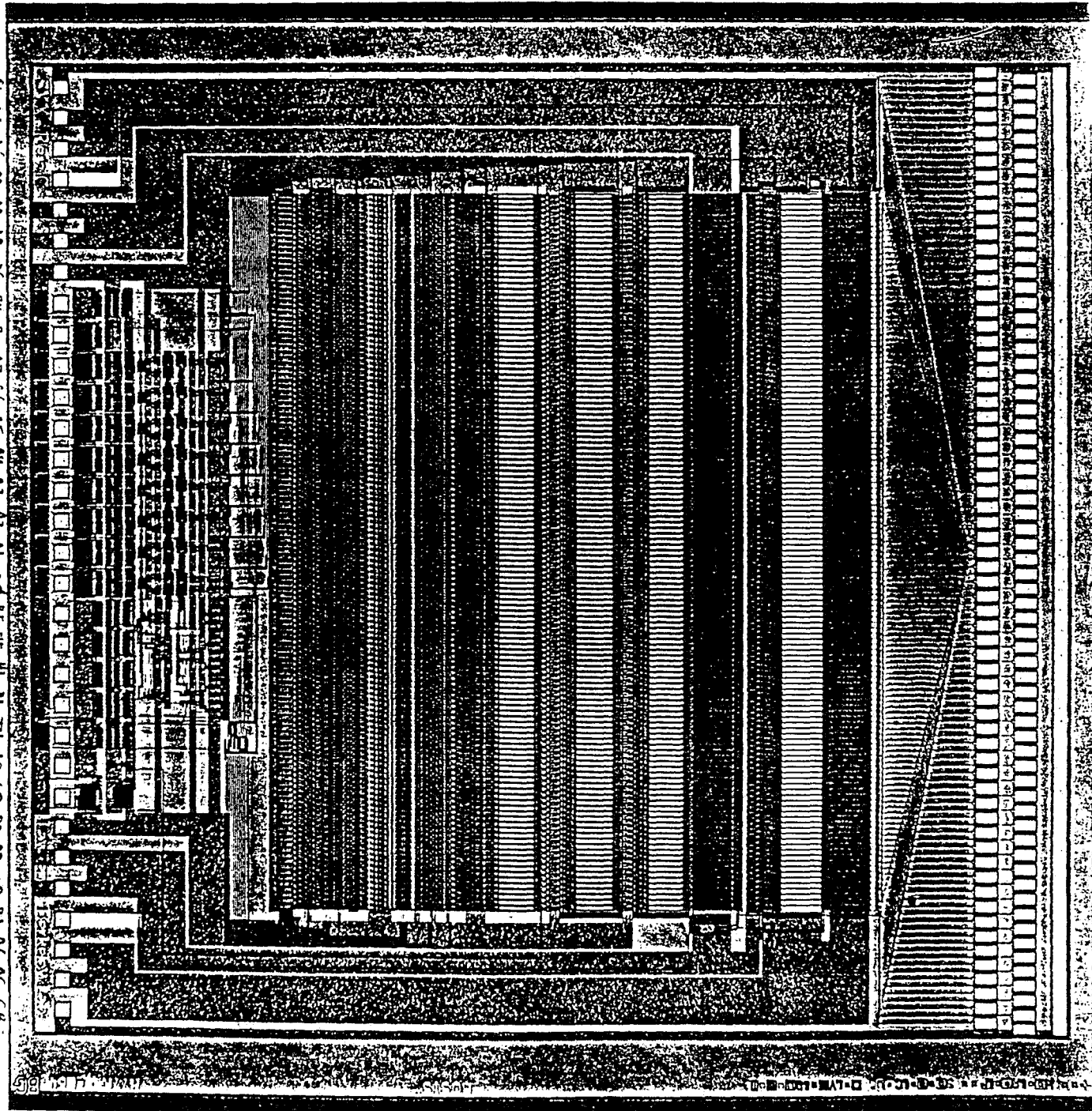


FIGURE 13

SVXC Functional Diagram

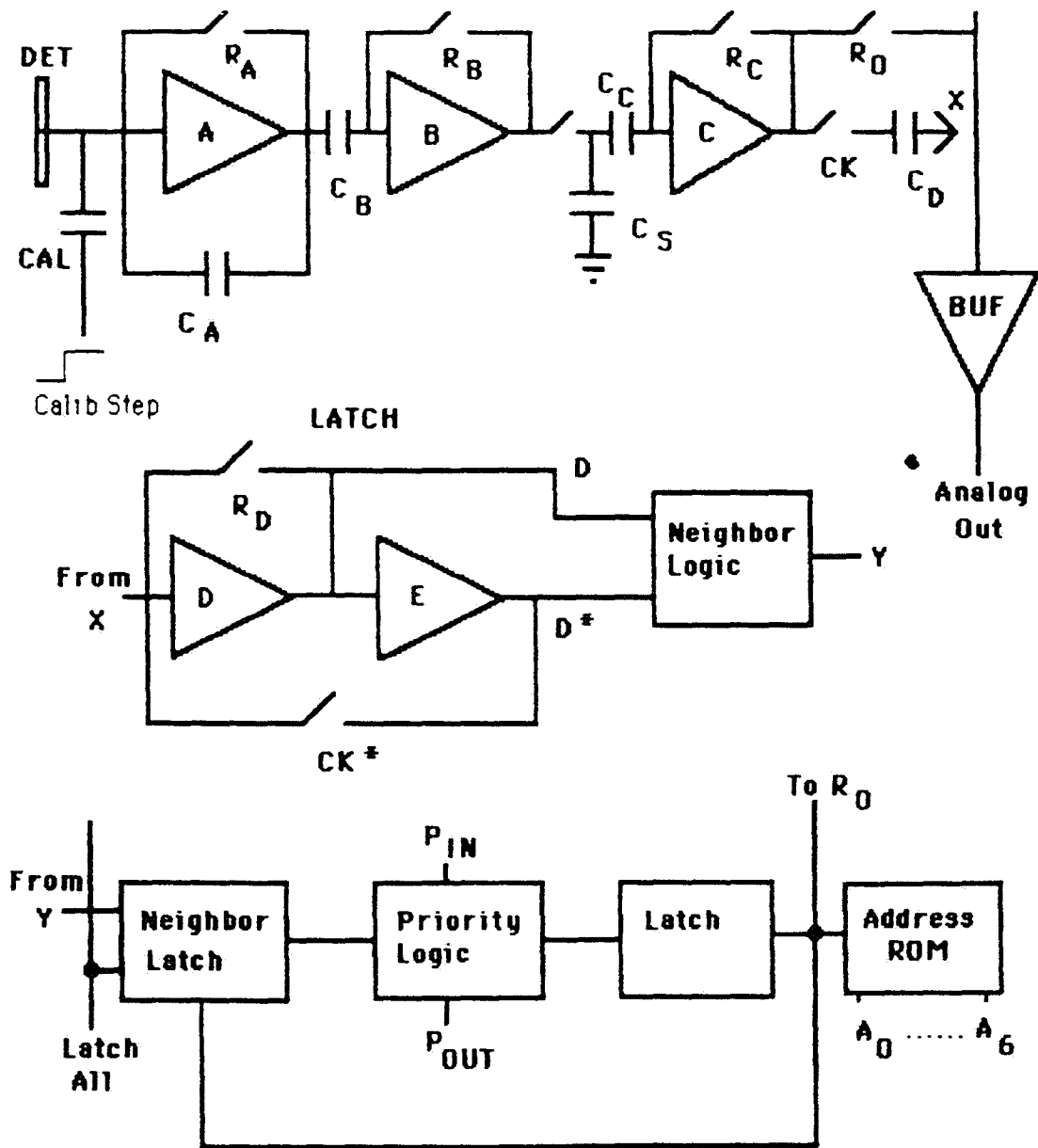


FIGURE 14

SVXC
FRONT END

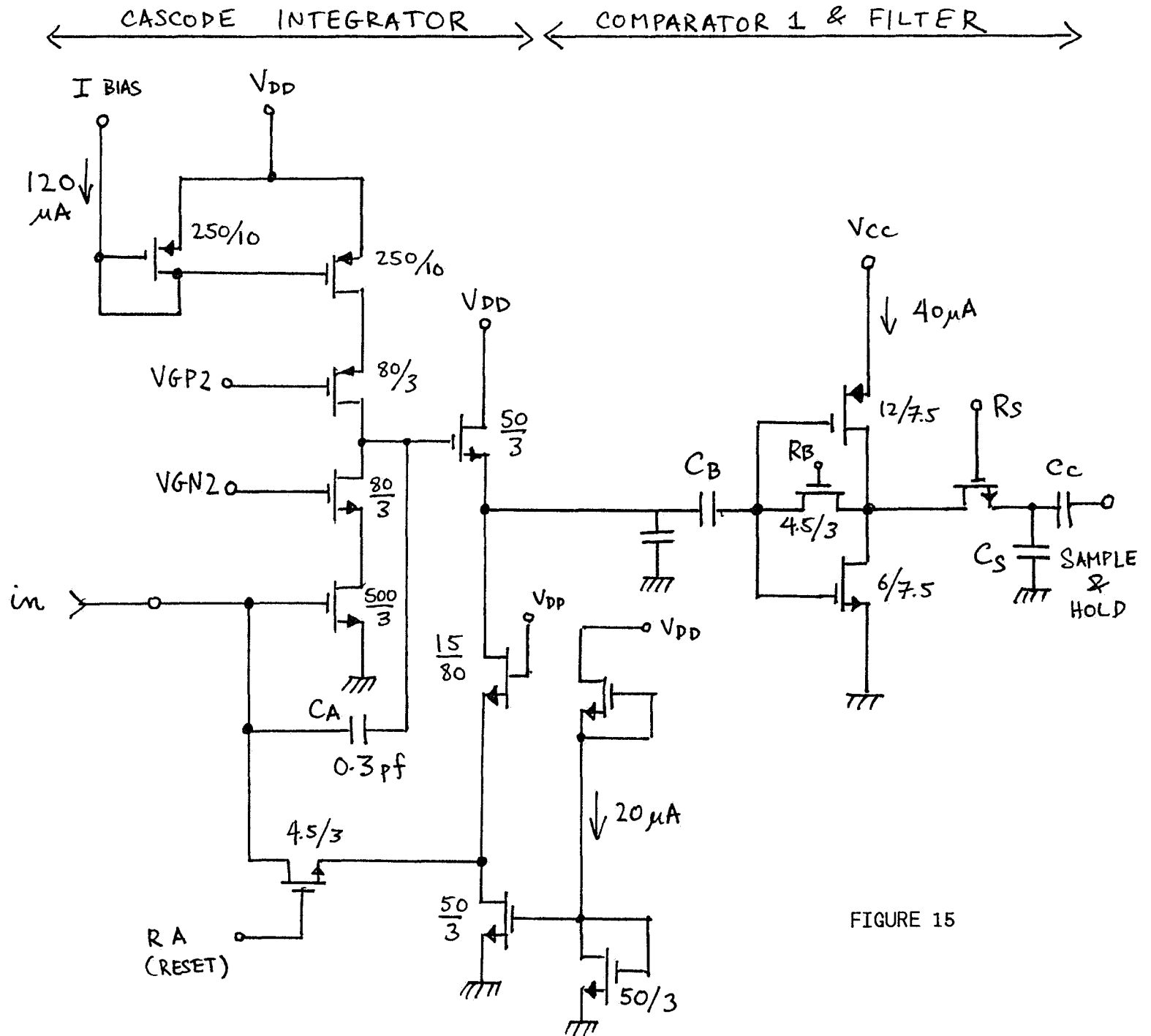


FIGURE 15

Noise vs Cdet

CDF SUXC amplifier

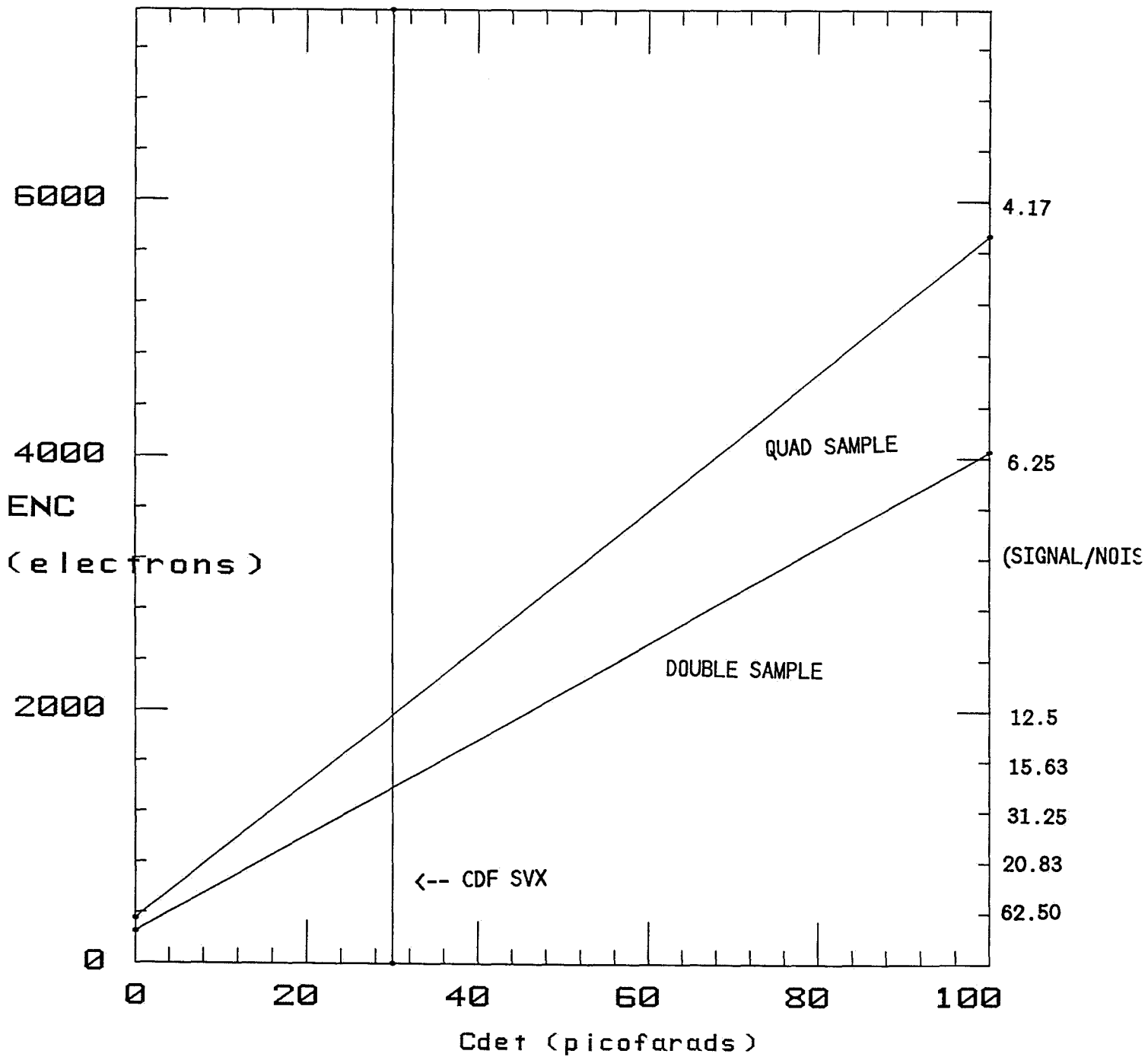
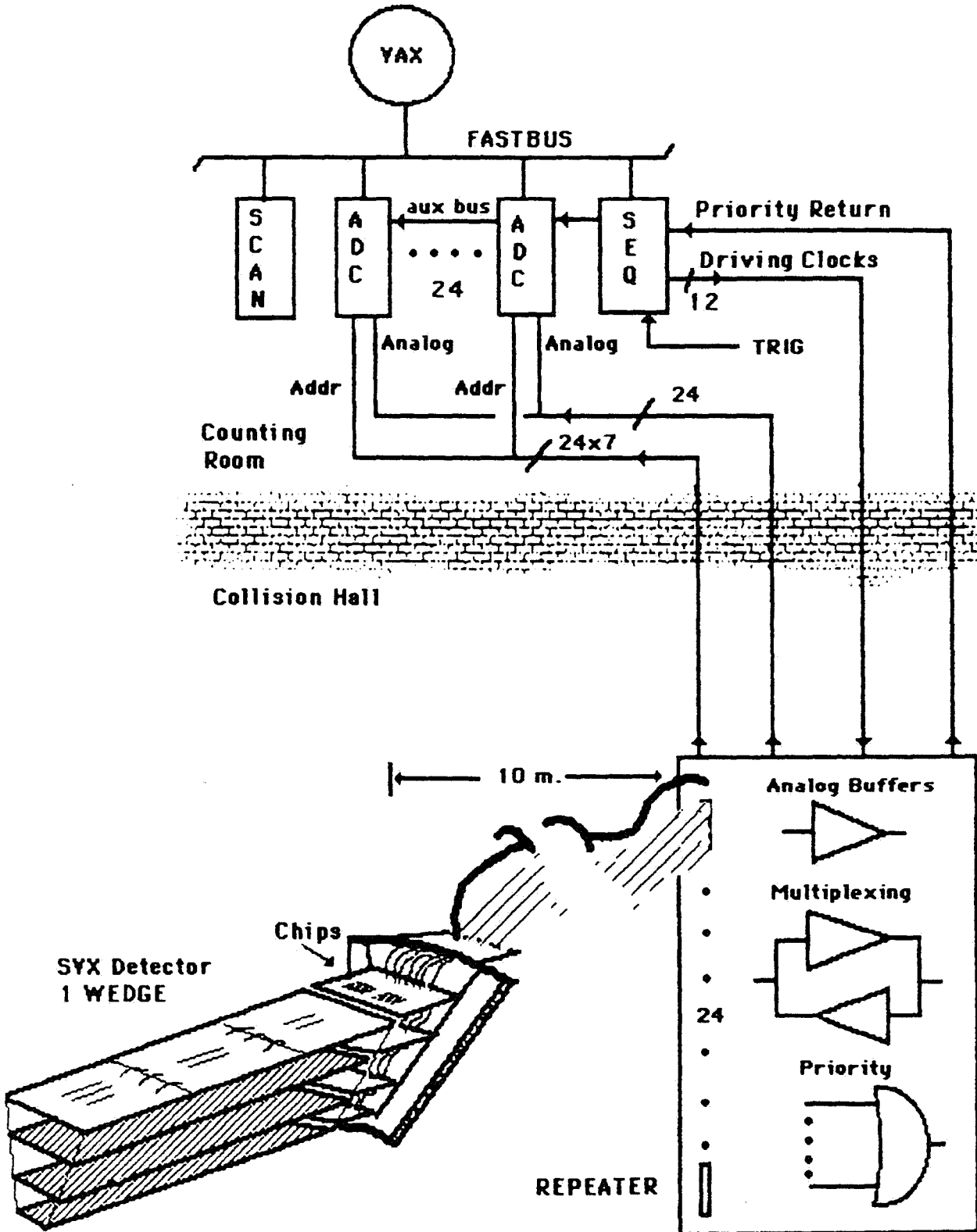


FIGURE 16

FIGURE 17

CDF SVX: Possible DAQ Configuration



Impact parameter resolution

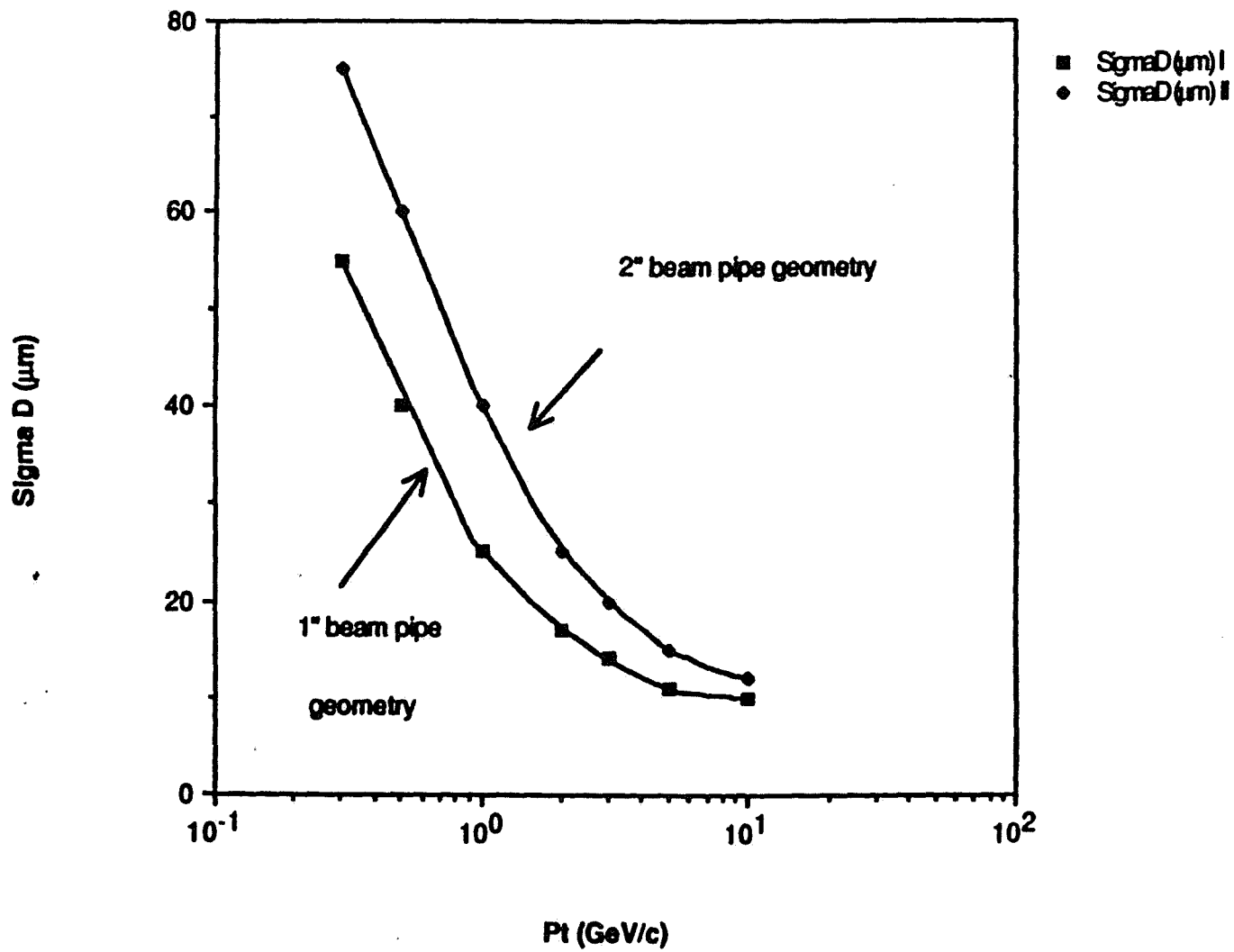


FIGURE 18

BEAUTY TRACKS TAGGING EFFICIENCY

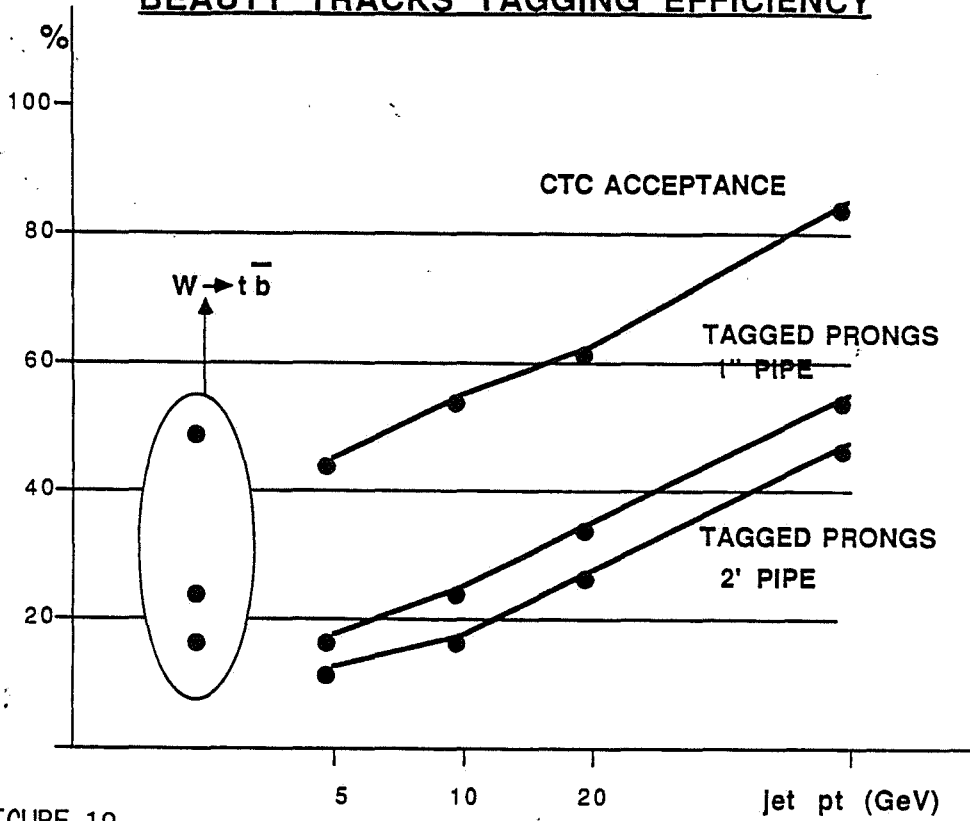


FIGURE 19

VERTEX TAGGING EFFICIENCY SUMMARY

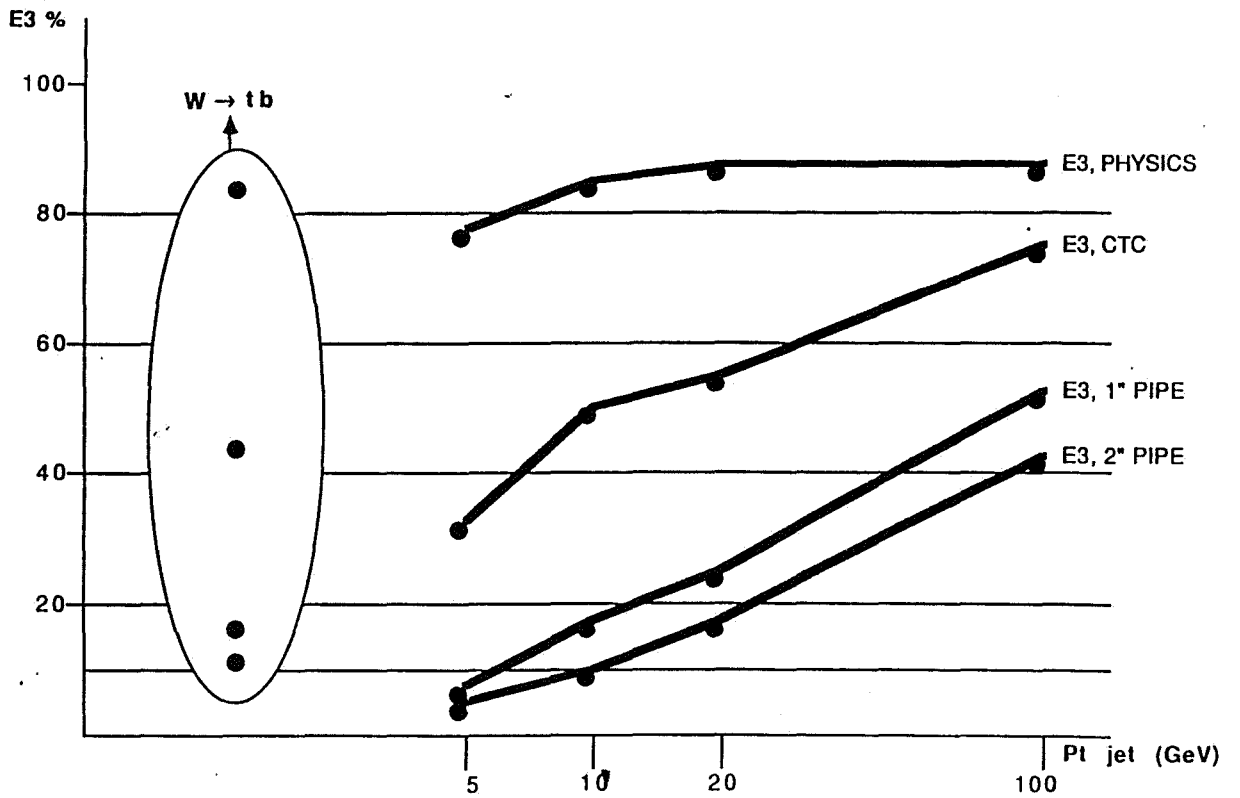


FIGURE 20

DOUBLE TAG EFFICIENCY

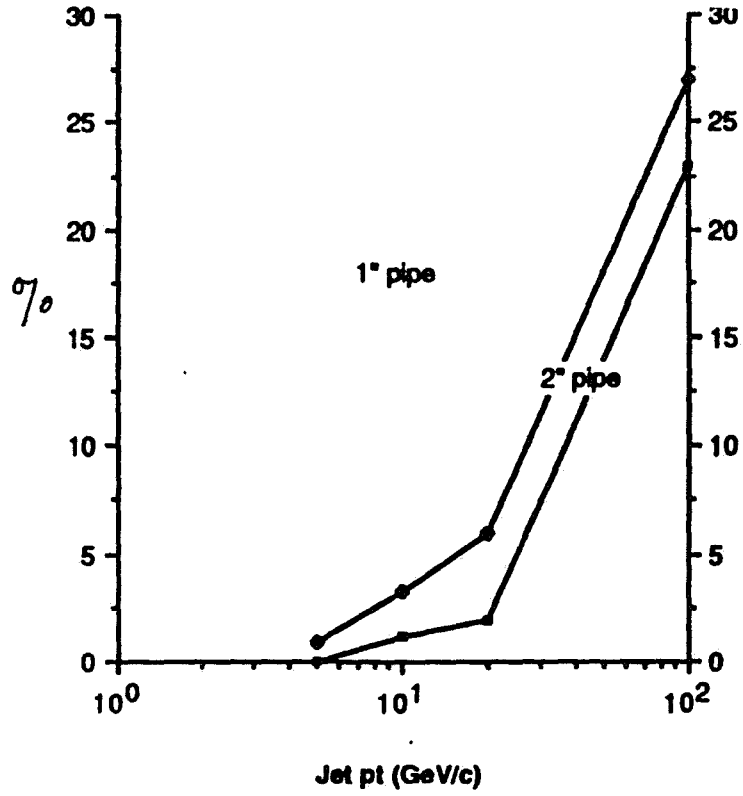


FIGURE 21

CDF SUX Test Beam Event: 230 Gev Pion

(pulse height is offset by relative detector spacing)

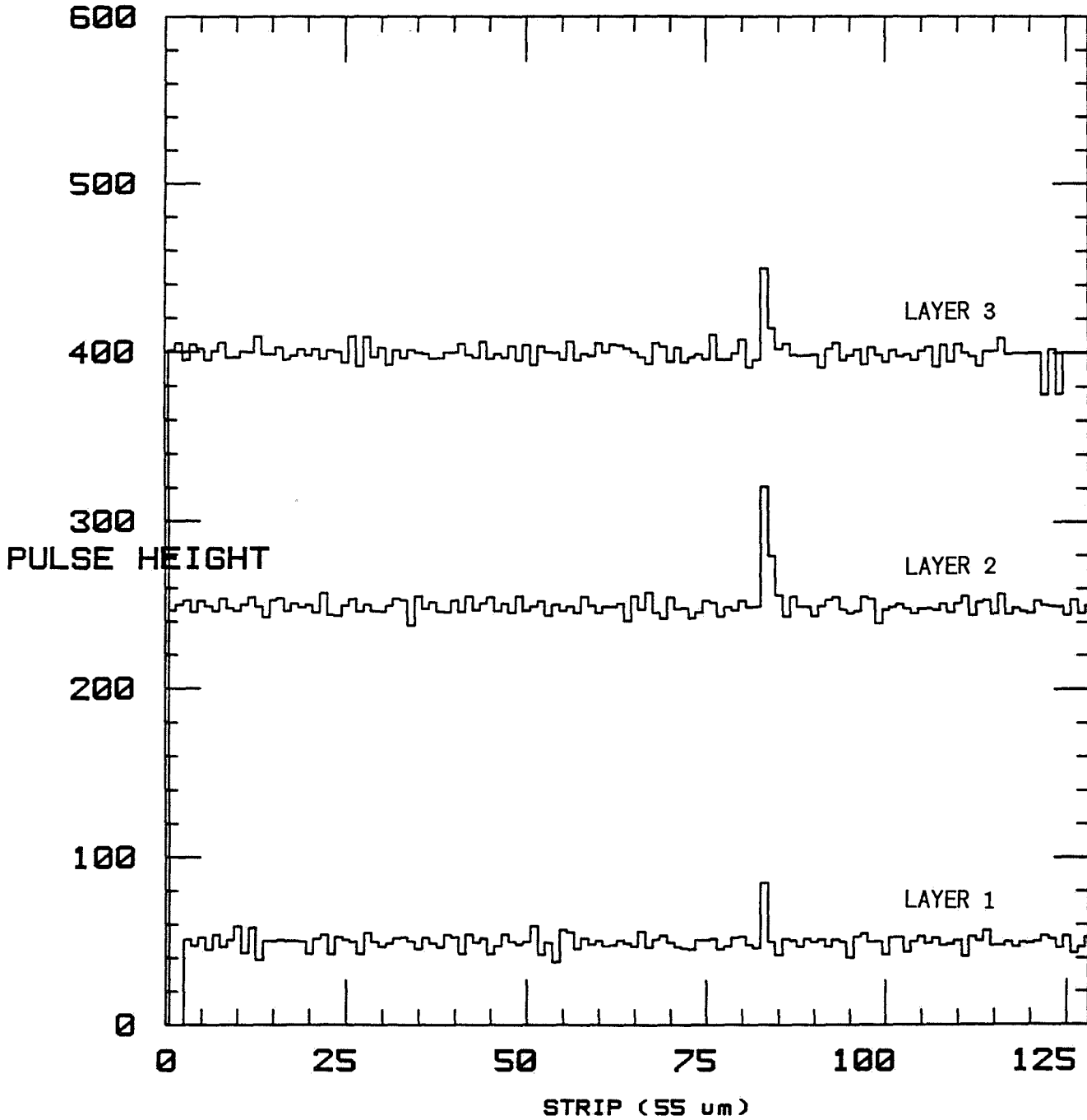


FIGURE 22

INDIVIDUAL CHANNEL PEDESTAL DISTRIBUTION

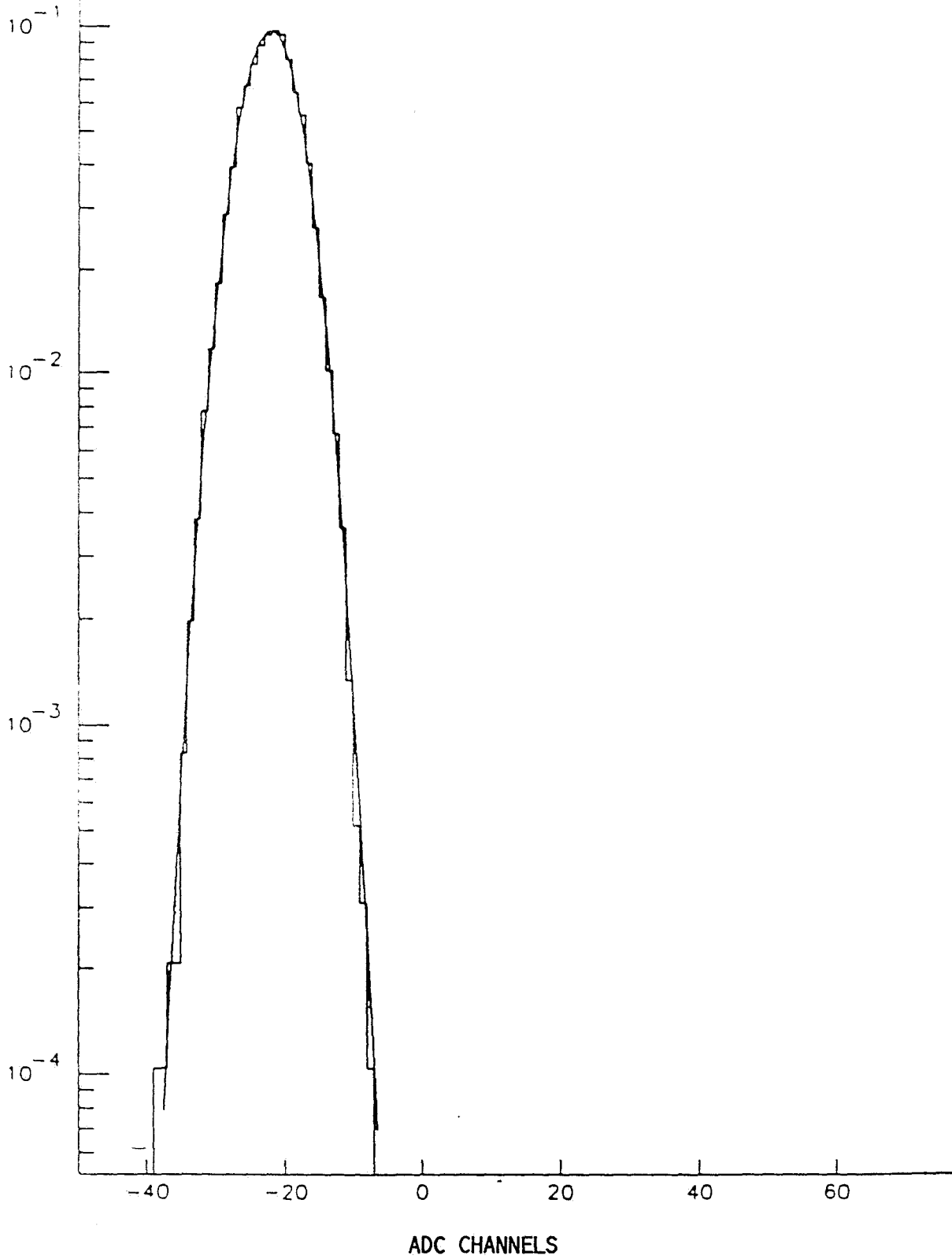


FIGURE 23

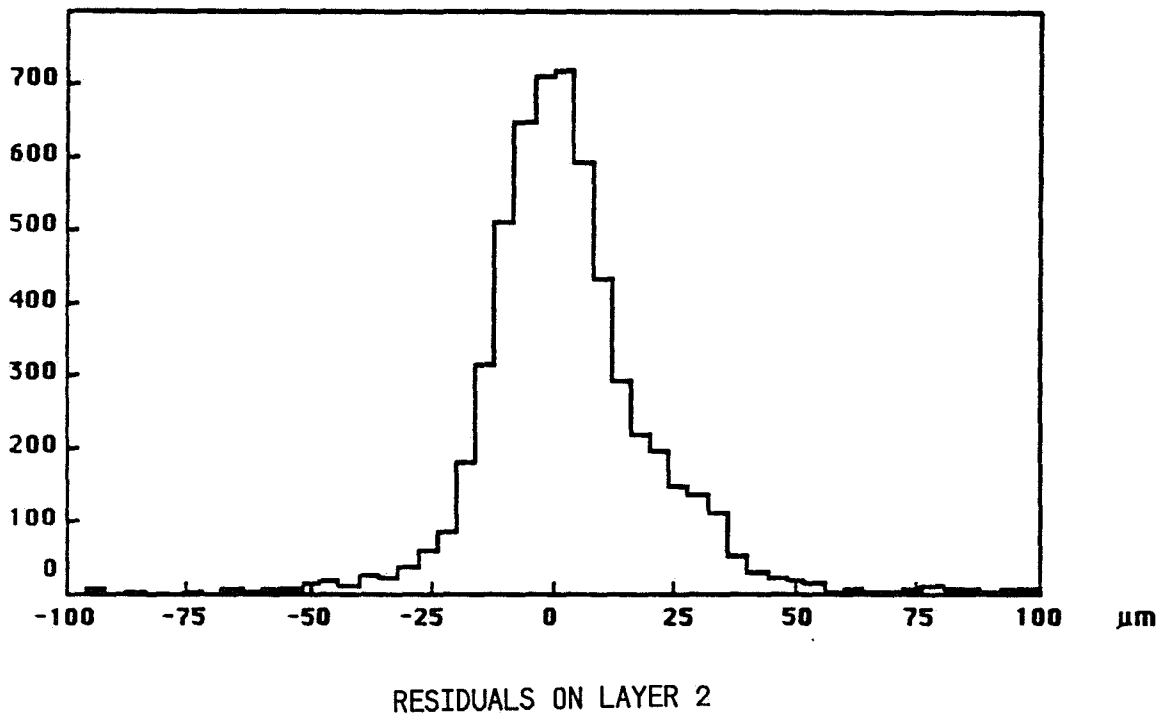
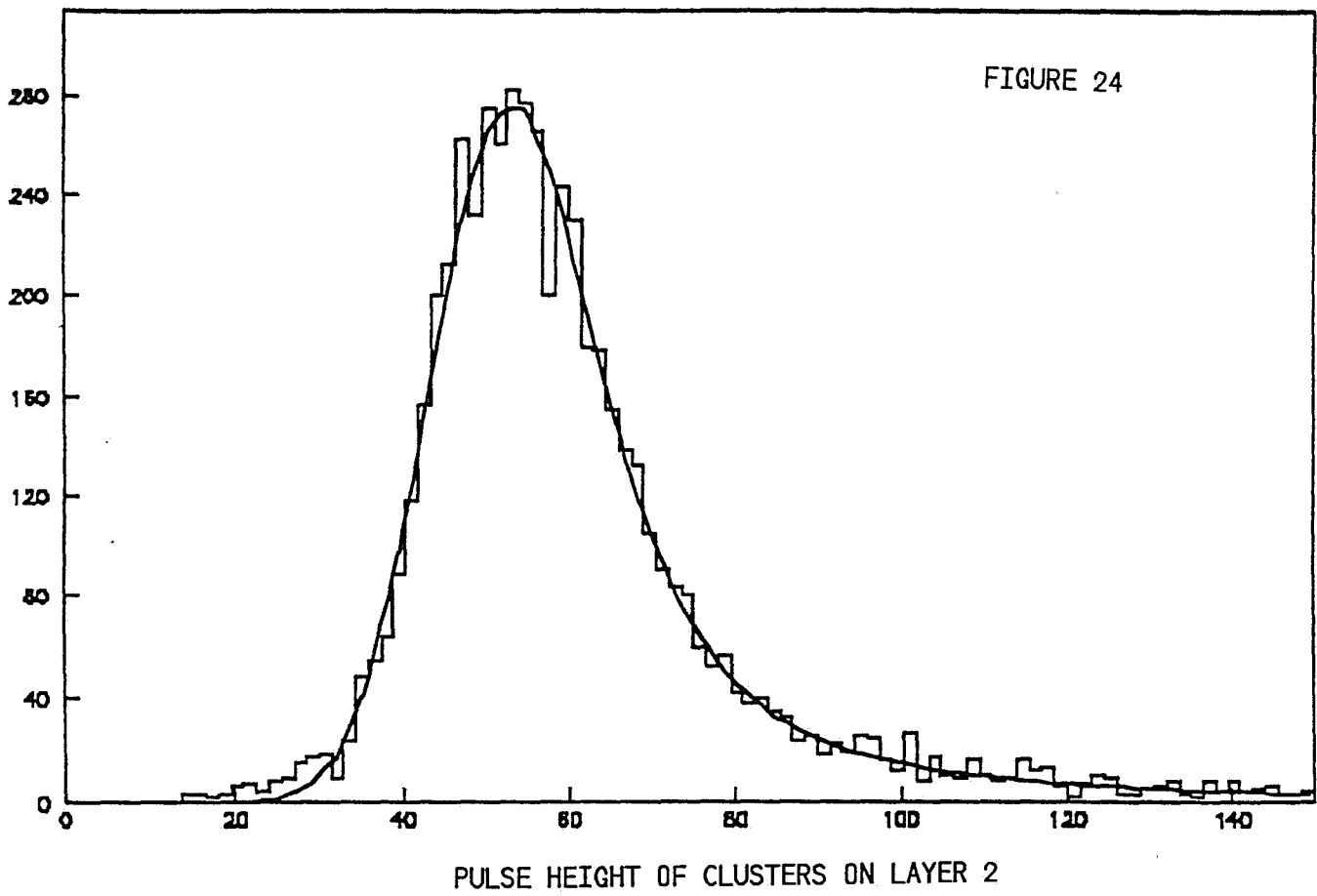
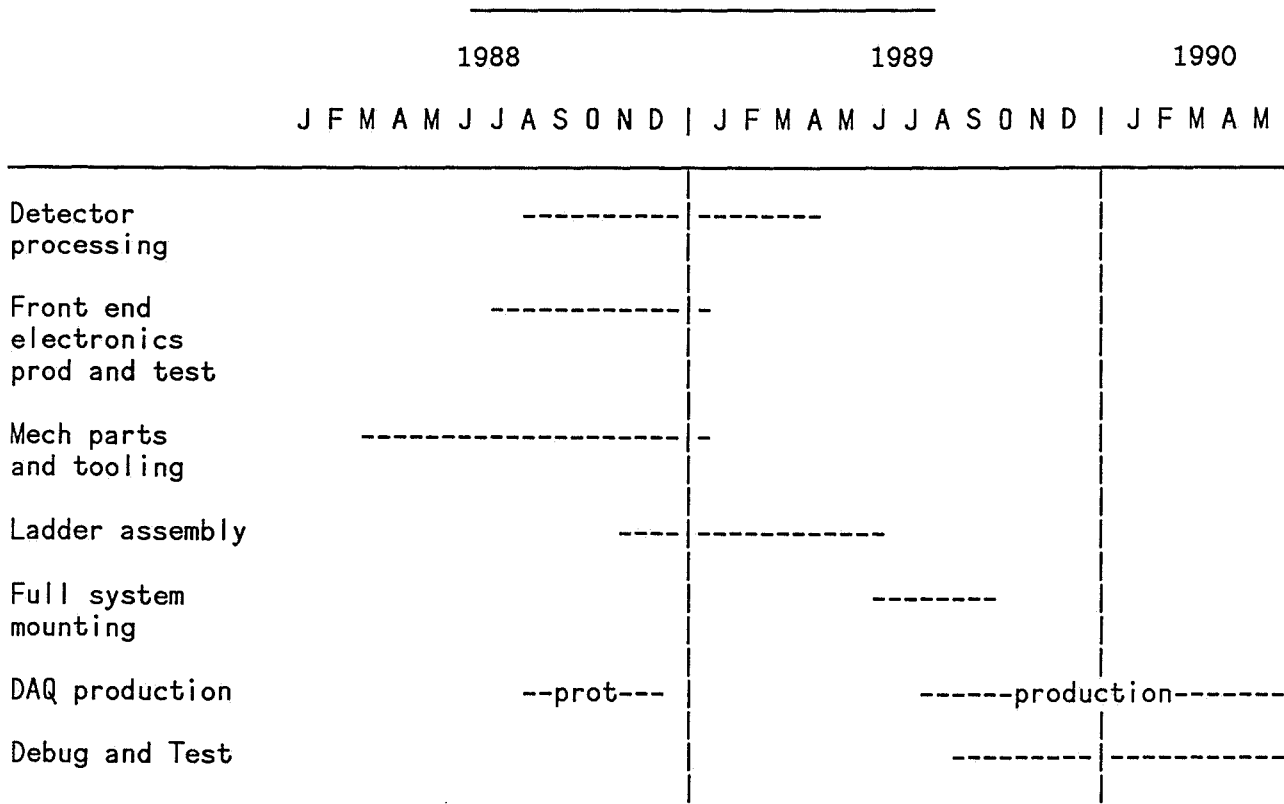
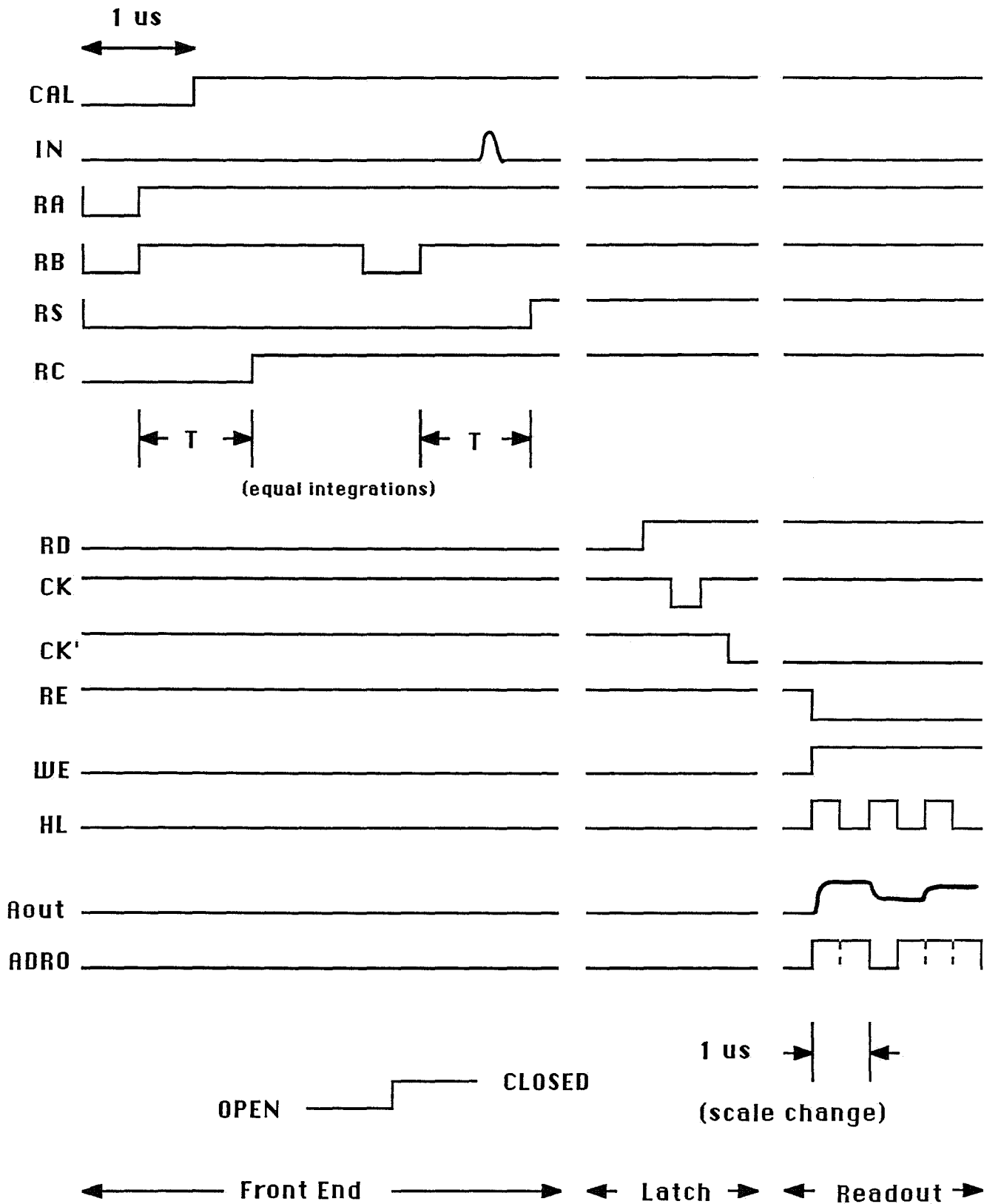


FIGURE 25

Figure 26

CDF SVX Construction Schedule





SXHC Timing Cycles

FIGURE 27

**Fermilab**

October 19, 1988

TO: T. Yamanouchi
FROM: M. Shochet, A. Tollestrup
SUBJECT: Muon Upgrade Proposal for CDF Detector

The enclosed proposal is for an upgrade of the CDF Muon system. T. Liss will describe this system in detail at his PAC presentation. This upgrade will significantly improve our angular coverage for muons and thereby greatly increase our acceptance for dileptons. The added steel in the central region also eliminates the problem of hadron punch through, an improvement important for triggering on leptons in a very high luminosity environment.

We need Stage 1 approval in order to utilize the resources presently available in the Collaboration. The muon work as well as the electronic improvements needed for the luminosities expected in the next two runs can be carried out within the Laboratory's fiscal guidelines.

MS:AVT/cip

A Proposal to Upgrade the CDF Muon System

George Brandenburg
Harvard University

Steve Errede, Lee Holloway, Tony Liss
University of Illinois at Urbana-Champaign

Umesh Joshi, Dennis Theriot
Fermi National Accelerator Laboratory

Kuni Kondo
University of Tsukuba

Lee Pondrom
University of Wisconsin at Madison

Introduction

The current CDF muon system covers the regions $55^\circ \leq \theta \leq 90^\circ$, and $4^\circ \leq \theta \leq 17^\circ$ with respect to both the proton and antiproton directions. This leaves a large gap in zenith angle from 17 degrees to 55 degrees. This is a region of crucial importance for studying the leptonic decay channels of heavy particles. In addition, the CDF central muon system, which covers the region $55^\circ \leq \theta \leq 90^\circ$, has an average of only 5.4 pion interaction lengths between it and the event vertex. This presents serious problems both online and offline. Online, the single muon trigger rate is dominated by interacting and non-interacting hadronic punch through. Offline, the identification of muons in or near jets is compromised by non-interacting punch through.

The CDF muon upgrade consists of four parts: central muon upgrade, central muon extension, end wall chambers and intermediate toroids. Figure 1 shows an elevation view of the CDF detector including the layout of the proposed chambers and additional steel. The central muon upgrade consists of an additional 60 cm of steel behind the current central muon system, followed by a second set of muon chambers. The central extension covers the region from $42^\circ \leq \theta \leq 55^\circ$ with chambers mounted on the surface of a cone for 270° in azimuth, while the 90° quadrant at the bottom of the detector will be distorted to accomodate the floor in the collision hall. The conical arrangement of these chambers can be seen in the top view of the detector shown in figure 2. The distortion necessary for the bottom quadrant is shown in the beam's eye view of figure 3. The region $30^\circ \leq \theta \leq 42^\circ$ is covered by chambers mounted in a circle on the end wall calorimeter. In the region $17^\circ \leq \theta \leq 30^\circ$, one can no longer use the central tracking chamber in the trigger to measure muon momentum, so this region is covered by the intermediate toroids, employing one meter thick magnetized iron instrumented by drift chambers. In figure 4 we show the number of absorption lengths as a function of θ at $\phi = 0^\circ$ before and after the upgrade. Each of the systems is described in detail below, and a summary of the cost of each system is given in Appendix A.

Physics Motivation

The motivation for the upgrade as a whole has two logical parts: extended coverage and additional central steel. The former is an issue of muon acceptance, while the latter is an issue of trigger rates and background. We will frequently make use of the example of $b\bar{b}$ decays to illustrate various points in this document. This is not by any means because this is the only physics we are interested in, but rather because the difficulties in studying $b\bar{b}$ decays are rather generic. They include the desire to have good dimuon acceptance and to be able to identify muons near hadronic activity.

• Central Upgrade

Muon physics in the central region is of the utmost importance because heavy particles tend to decay centrally. For instance, from ISAJET Monte Carlo studies we find that 44% of the decay leptons from a 60 GeV top quark will be in the region $55^\circ \leq \theta \leq 90^\circ$ (note that when we speak of a region in θ we will always mean that angle with respect

to both the proton and antiproton directions). Similarly, for bottom quark decays, 25% of the decay leptons will be in the same region. Because the present CDF central muon system has an average of just 5.4 pion interaction lengths between it and the interaction point, about 1 in 220 hadrons traverses the calorimeter without interacting, thereby faking a muon. A detailed study of hadronic punch through in the central region has been done and is attached as Appendix B. This is a serious problem for the physics of non-isolated muons, such as those from semi-leptonic b decays, and also muons from other processes which typically contain significant amounts of hadronic activity.

To illustrate this difficulty, we take the case of b decays. In figure 5 we show the transverse momentum distribution of charged tracks inside jets with $E_t \geq 20\text{GeV}$ and $40^\circ \leq \theta \leq 90^\circ$. A track is considered to be inside the jet if it is contained in a cone of size

$$\Delta R = \sqrt{\Delta\eta^2 + \Delta\phi^2} \leq 0.7$$

about the E_t weighted centroid of the calorimeter cluster. If one is interested in muons above 5 GeV we see that there are typically 1.2 such tracks per jet. This means that 0.5% of jets above 20 GeV will contain a non-interacting hadron, i.e. a fake muon. The cross section for the production of $b\bar{b}$ pairs with $40^\circ \leq \theta \leq 90^\circ$ and with a minimum P_t of 20 GeV is 44 nb at the Tevatron [1]. The probability for one of these bottom quarks to decay semi-leptonically to a muon with $P_t \geq 5.0\text{GeV}$ is 0.075. Thus the cross section for observing a 5 GeV muon from b decay in an event with a 20 GeV jet is 3.3 nb. On the other hand, the inclusive jet cross section integrated above 20 GeV is approximately $1 \mu\text{b}$ at CDF [2] for $40^\circ \leq \theta \leq 90^\circ$. Using our 0.5% probability of non-interacting hadrons in these events, we find that the cross section for this type of QCD background is 10 nb. This simple argument gives a signal to background of $1/3$ *from punch through alone*.

Another important source of background to muon events is the decay in flight of pions and kaons. The probability for decay in flight to muons is $.027/P_t$ for pions and $.127/P_t$ for kaons. Using the UA5 particle mix of 21% kaons, 58% pions and 21% protons, we get a decay in flight probability of a given charged particle of $.042/P_t$. This is equal to the probability of non-interacting punch through at 90° for $P_t=6.4$ GeV. Since the probability of non-interacting punch through is, to first order, independent of P_t , it becomes the dominant source of background to the prompt muon signal at even moderate P_t .

The second concern which motivates the central upgrade is that of triggering on medium P_t muons. This is important for the study of bottom as well as for an understanding of the backgrounds contributing to any new physics signatures involving muons, for example top. The central muon trigger cross section out of Level 2 is $1.5\mu\text{b}$ (1.5 Hz at $\mathcal{L}=10^{30}\text{cm}^{-2}\text{s}^{-1}$) with a P_t threshold of 6 GeV. At Level 3 this can be reduced to no less than $0.3\mu\text{b}$ without losing a significant fraction of real muons. Above 6 GeV, the rate is dominated by interacting and non-interacting punch through. Current hardware limitations constrain the rate out of Level 2 to a maximum of 10 Hz which must be split amongst a mix of many different triggers. Similarly, the rate out of Level 3 is constrained by the tape writing speed to be about 1.5 Hz. It is clear that if we are to be able to continue to trigger on inclusive

muons at medium P_t at luminosities much above $10^{30}\text{cm}^{-2}\text{s}^{-1}$, we must significantly reduce the background contribution to the trigger rate.

The central muon upgrade, averaged over zenith angle, adds 3.0 pion interaction lengths of steel to the central region. This will reduce the background from hadronic punch through by a factor of 20. Some help is also given to the less serious background from π and K decays in flight by the additional absorption lengths which increase the minimum muon momentum from 1.3 GeV to 1.8 GeV, and the magnetized return yoke above and below the detector which provides a crude second momentum measurement. By adding the chamber hits outside the extra absorber as an extra road requirement in Level 2, we will reduce the Level 2 central muon trigger rate by more than an order of magnitude. This will allow us to keep trigger conditions stable and to continue to trigger on medium P_t muons as the Tevatron luminosity climbs above $10^{30}\text{cm}^{-2}\text{s}^{-1}$.

Similar gains are achieved in offline analysis. The signal to background ratio for all muon signals in the central region will improve by a large factor since the backgrounds to most are now dominated by punch through. This will have a very significant effect on our ability to do heavy flavor physics. This includes top, where the cross section may be very small and the events typically have a lot of hadronic activity, and bottom, where the dimuon analysis in the central region becomes essentially free of punch through background, and, with enough data and suitable cuts the single muon analysis becomes feasible. Similar gains in sensitivity are made in terms of searching for a fourth generation of heavy quarks and leptons.

• Extended Coverage

The gap in muon coverage between 17° and 55° causes 50% of $W \rightarrow \mu\nu$ events to be lost. The losses are even more serious for dimuon physics. Figure 6 shows, as a function of pseudo-rapidity interval covered by a muon upgrade, from 0.65 where our central muon system ends to 2.0 where our forward muon system begins, the acceptance for di-muons from Z_s , $b\bar{b}$ and 60 GeV $t\bar{t}$ production, assuming that we trigger on the entire system. The minimum P_t for triggering each of the parts is assumed to be 3 GeV for central, central extension and endwall chambers, 5 GeV for the intermediate toroids and 6 GeV for the forward toroids. This shows that in all three cases the dimuon acceptance is increased by approximately a factor of four. The very small acceptance for $b\bar{b}$ is a result of the P_t cut. Fortunately the cross section is quite large.

Another way of looking at this is to ask how the di-muons are distributed about the five different regions. Taking, again, $b\bar{b} \rightarrow \mu^+\mu^-X$ as an example, we show, at the top of the next page, a two dimensional array where each entry gives the fraction of detectable di-muons, i.e. those which pass the above P_t cuts, which are found in the corresponding pair of regions. Using this table, we find that 22.1% of the di-muons are found with the current central-forward combination. If we add the central extension, we gain another 21.2%, almost a factor of two. Adding, then, the endwall chambers gives another 33.8%. Finally, completing the coverage with the intermediate toroids yields the remaining 23.0%. Note that the increase in acceptance when adding a given region is sensitive to how much is covered when that section is added. For instance, if we first add the end wall chambers to the central-forward combination, we gain 26.0% rather than 33.8%. This makes it clear

	Central	Cent Ext	End Wall	Int Toroids	For Toroids
Central	16.3%	7.7%	9.0%	4.6%	2.1%
Cent Ext	7.7%	3.4%	3.9%	2.1%	1.2%
End Wall	9.0%	3.9%	4.4%	2.3%	1.8%
Int Toroids	4.6%	2.1%	2.3%	1.6%	1.7%
For Toroids	2.1%	1.2%	1.8%	1.7%	1.6%

Table 1: Distribution of di-muons from $b\bar{b}$ decays in the five components of the upgraded CDF muon system

that leaving any sizeable gap in the overall muon coverage causes a large loss of di-muon events.

Finally, one can ask for more than fractions. Is the number of events accumulated sufficient to do physics? To answer this question we show the series of figures 7-10, giving the number of dimuon events observed in one inverse picobarn of data at $\sqrt{s} = 1800\text{GeV}$ from $b\bar{b}$ with one muon in the central region and one in each of the other four detector regions. In each figure, the abscissa is the P_t of the central muon, and the family of curves corresponds to different P_t cutoffs in the region of the second muon. A $b\bar{b}$ cross section of $25\mu\text{b}$ and a $b \rightarrow \mu$ branching ratio of 11.7% have been used in making these plots. Similar numbers of events are observed in other combinations of regions. It is quite clear that, with complete coverage, an extremely rich sample of di-muons is obtained.

Having complete coverage for muons is also very important for measurement of muon asymmetry in the electroweak decays of $W \rightarrow \mu\nu$ and $Z^0 \rightarrow \mu^+\mu^-$. This is a difficult measurement to make in the electron channel because we can only measure electron charge to about $\theta = 30^\circ$ with the central tracking chamber. In contrast, with the toroids, we can measure muon charge to very small angles.

An additional purpose of the muon upgrade will be to provide a passive (Level 3 and/or offline) veto for cosmic ray induced bremsstrahlung events. This will be useful for helping reduce these backgrounds in searching for large E_t isolated gamma events, such as might be observed from SUSY photino decays. At present, the muon coverage is such that an appreciable fraction of cosmic ray induced bremsstrahlung events have no accompanying track in the existing muon chambers, due to many holes in the coverage [3]. The extended coverage will obviously fill many of these gaps, while the central upgrade will cover the many ϕ cracks and the $\theta = 90^\circ$ crack in the central detector.

•Effect of Tevatron Intensity Upgrade

The present muon system and proposed muon upgrades will function reliably and be triggerable up to luminosities of a few 10^{30} . At a luminosity of 10^{31} the di-muon and di-lepton triggers are still working but we are beginning to have problems with the present central muon system for single muon triggers. There is simply too much punch through and the trigger rates become excessive. The central muon upgrade, if implemented, will give us an additional factor of 20 in the reduction of punch through and thus will allow us

to trigger on single isolated muons at luminosities of several 10^{31} .

There is a complication when the number of bunches exceeds six in addition to the generic CDF electronics problem. The drift cells in the central muon system have a maximum drift time of about 700 ns. When the time between bunch crossings becomes of the order of $1 \mu\text{s}$ or less then an additional level of trigger, say level 1/2, will have to be implemented. This can be achieved technically in several ways, for example, a plane of scintillators or by requiring a radial track in the last two superlayers of the CTC. We will start the necessary R and D as soon as we know the plans of the Laboratory.

Scenarios for operating the forward intermediate muon trigger above 10^{30} luminosity depend on the bunch spacing. The maximum drift time in either system is $1 \mu\text{s}$. If the $3.5 \mu\text{s}$ bunch spacing (six bunch operation) is retained, a luminosity of 10^{31} would result in a forward plus intermediate trigger rate out of level 3 of about 0.3 hz, or 30% of the tape, with no P_t cut. This rate is acceptable, depending on physics priorities for space on the output tape allocated to various triggers. The TDC's used in the toroid muon system are digital devices which are capable of pipelining the data for bunch spacings less than $1 \mu\text{s}$. It would be necessary to devise a pre-trigger so that hits from the correct bunch crossing could be selected from the TDC's, but the basic hardware can survive multibunch operation.

Central Muon Upgrade

The central upgrade consists of adding a second set of muon chambers behind an additional 60 cm of steel in the region $55^\circ \leq \theta \leq 90^\circ$. The return yoke of the CDF solenoid already provides the necessary steel above and below the CDF central detector so that it is only necessary to add additional steel on the two sides. At this point we do not plan to magnetize the additional steel.

The central upgrade chambers will be standard single wire drift cells. Four chamber layers are required with one pair of chambers with the wire direction perpendicular to the other pair. There is 22 cm of available space between the top of the CDF solenoid return yoke and the bottom of the cable tray. For four chamber layers, this leaves us 5 cm per layer. To keep the 3:1 aspect ratio of the chambers, necessary for easy field shaping, we will build drift cells of 5 cm x 15 cm cross section. This gives a maximum drift time of approximately $1.4 \mu\text{s}$.

Three different lengths of chamber are required. The chambers which cover the return yoke on the top and the bottom of the detector will have wires running in the Z and X directions (Z is parallel to the beam and X is out of the ring). The return yoke is split into two pieces, both on top and on bottom, each of which is 640 cm in Z and 286 cm in X. The X chambers will therefore be 286 cm extrusions. 43 chambers per layer per yoke piece will be required for full coverage or a total of 344 X chambers for two layers. The Z chambers will be 640 cm long extrusions. 19 chambers per layer per yoke piece are required for full coverage or a total of 152 Z chambers for the yoke.

To cover the side walls we need again the Z chambers described above, and in addition a third length chamber with wires in the Y direction. The Z chambers must cover a total length of 1024 cm, so 68 Z chambers per layer per side wall are needed for a total of 272 more Z chambers. For the Y chambers, 1024 cm is probably too long for a single chamber, so we will break this up into two chambers of 511 cm length. To cover the total length of 640 cm, we will need 86 Y chambers per layer per side wall for a total of 344 Y chambers.

Because of the arrangement of orthogonal layers, only a single TDC is required for each channel. It is not necessary to use these chambers in the Level 1 trigger because they cover the same pseudo-rapidity region as the current central muon chambers, and the level one trigger rate is acceptable at low P_t . However, as described above, a Level 2 trigger using the upgrade chambers is required when the Tevatron luminosity exceeds $10^{30} \text{cm}^{-2} \text{s}^{-1}$ in order to keep the Level 2 trigger rate at a manageable level without having to raise the P_t threshold to an uncomfortable point. This can easily be done by adding hits in the upgrade chamber as an additional road requirement of a Level 2 central muon trigger.

Design Parameters of the Central Upgrade

Pseudo-rapidity coverage	$ \eta \leq 0.7$
Cell size	5cm x 15cm
Max drift distance	7.5cm
Max drift time	1.4 μ s
Number of X chambers (286cm long)	344
Number of Y chambers (511cm long)	344
Number of Z chambers (640cm long)	424
Total number of channels	1112
Total additional iron required	630 tons
Pion interaction lengths at $\theta = 90^\circ$	7.8
Minimum detectable muon P_t	1.8 GeV
Multiple scattering at $\theta = 90^\circ$	15cm/P

Central Muon Extension

The central extension consists of 'pinwheels' of drift cells around each end of the central detector. The pinwheels extend from 42° to 55° . At 55° they slightly overlap the coverage provided by the central muon system. These cells extend the pseudorapidity coverage of the muon system from 0.65 to 1.0. No additional steel will be added for this detector. However, as seen in figure 4, the large angle through the hadron calorimeter yields considerably more material on average than protects the current central muon system.

The drift cells will be arrayed as a logical extension of the central system. In particular, there are four layers of twelve cells for each 15° ϕ sector. Successive layers are offset to eliminate ambiguities. In a given layer every cell overlaps the previous one at the inner edge so that simple rectangular cells can be used in a circular geometry.

The upper three quarters of the pinwheel are tilted to increase its acceptance. The section which extends 45° on either side of the vertical at the bottom is more problematic, as can be seen from Fig. 1. This section must be inserted between the central detector and the floor and requires the use of both vertical and horizontal cells. An end view of the pinwheel is shown in Fig. 3.

A standard drift cell has dimensions 180cm long by 15cm wide by 3cm thick. For the bottom section, cells of shorter lengths are needed. Each cell contains a single sense wire and is run in the limited streamer mode. They will be fabricated from aluminum extrusions. The inside faces of the cells are lined with a circuit board which provides a relatively uniform gradient out to the edges of the cell. The circuit board has strips etched parallel to the sense wire and these strips are biased to 2 kV while the outside strips are connected to the grounded outer edges of the cells.

The total number of cells required for the central extension is $2(\text{ends}) \times 4(\text{layers}) \times 24(\text{sectors}) \times 12(\text{cells}) = 2304$. Including spares, the total to be fabricated is approximately 2400. It is possible to have these delivered to Fermilab in time for installation prior to the 1990 CDF run.

As is done in the current central system, each pair of cells have their sense wires joined at one end and then have a single TDC - double ADC combination for readout. This will give a rough position along the wire using charge division and an accurate position transverse to the wires. The maximum drift time is approximately $1.5\mu s$ which is adequate for six bunch running; as in the rest of the muon system, more than six bunch operation will require a Level 1/2 pre-trigger. The entire extension will require 144 TDC/ADC RABBIT muon boards and 96 trigger boards. These in turn require an additional 12 RABBIT crates.

Design Parameters of the Central Extension

Pseudo-rapidity coverage	$0.7 \leq \eta \leq 1.0$
Cell size	3cm x 15cm
Max drift distance	7.5cm
Max drift time	$1.5 \mu s$
Total number of channels	2304
Pion interaction lengths at $\theta = 55^\circ$	6.2
Minimum detectable muon P_t	1.4 GeV
Multiple scattering at $\theta = 55^\circ$	13cm/P

End Wall Chambers

A primary consideration in the design of the endwall muon chambers has been to use them for triggering purposes in combination with the central track processor. These chambers will extend from 30° to 42° in zenith angle and will have 2π coverage in azimuth. A track at a zenith angle of 30° will traverse four superlayers of the central tracking chamber (CTC) so that a good match of the muon hits with tracks from the CTC is possible. In addition to a good identification of muons, such a match also imposes a P_t cut. Since the CTC has very good ϕ resolution, it is important that the endwall chambers have a resolution no worse than multiple scattering.

The endwall chambers will be segmented in ϕ and operate in the limited streamer mode like the central muon chambers. A big advantage of this is that the electronics need not be re-designed. There will be in all 48 modules of muon chambers, one per endwall calorimeter module. Each module has four layers of staggered ϕ planes as shown in figure 11. The staggering helps to resolve the left-right ambiguity. Zenith angle information is obtained by means of charge division. A typical ϕ cell in a chamber is shown in figure 12. It consists of 2 I-beams at an angle so that the cross-section is rectangular, 2.0cm deep with the width varying from 4.2cm at the top to 2.8cm at the bottom. Because of the geometry chosen, a graded field is necessary to maintain the necessary field of 19 kV/mm at the wire for streamer mode operation. This can be accomplished using resistor chains. The field throughout the cell will be greater than 1 kV/cm so that the drift velocity is saturated and uniform throughout.

Design Parameters of the Endwall Chambers

Pseudo-rapidity coverage	$1.0 \leq \eta \leq 1.3$
Cell size	2cm x 4.2cm to 2cm x 2.8cm
Max drift distance	2cm
Max drift time	400ns
Total number of channels	2016
Pion interaction lengths at 42°	7.0
Minimum detectable muon P_t	1.6 GeV
Multiple scattering at 42°	14cm/P

Intermediate Toroids

Figures 1 and 2 show the intermediate toroids located between the forward tracking chambers (FTC) and the forward electromagnetic calorimeter (FEM). The toroid iron is centered at 5.2 m from the IP and is 1 m thick. The toroids are 7.6 m in diameter with a 2.6 m diameter hole in the middle, adequate for access to the small angle detectors and the FTC. The toroids must be split for access to the end plug calorimeter. The magnetic field in the iron will be saturated at an average value of 1.8 T, with a momentum resolution of 25% dominated by multiple scattering. For comparison the present forward toroid system has a momentum resolution of 18%. Like the forward toroids, the intermediate trigger will be self contained, based on the tracking of a muon through the toroid to determine the transverse momentum. A correction to the trigger road must be made for the vertex position.

It is useful to discuss the forward and intermediate toroids together when considering high luminosity trigger strategies. The present measured Level 1 trigger cross section in the forwards is $0.1\mu\text{b}$ dominated by trigger roads which are in fact not tracks. Level 2 has no effect on the stand alone muon trigger. Tracking is done at Level 3, which results in an output of $0.02\mu\text{b}$ and a distribution of muons which peaks around $3\text{ GeV}/c P_t$. Extra rejection can be gained by a P_t cut at Level 3. The spectrum is dominated by $\pi \rightarrow \mu$ and $K \rightarrow \mu$ decays in flight for P_t less than $10\text{ GeV}/c$. Prompt muons are about half of the yield at $10\text{ GeV}/c$, and increase in fraction as the P_t increases. Non-interacting hadronic punch through is not a problem in the toroid systems.

The rapidity bite of the intermediate toroids is $1/3$ that of the forwards, but the solid angle is about 50% larger. While rapidity is a better measure for light particles, solid angle is more appropriate for the heavy ones. Light particle decays dominate the rate for tracks, but the Level 1 trigger is largely non-track garbage. If one takes the intermediate level 1 cross section to be $0.1\mu\text{b}$ then the level 3 output of tracks should be around $0.01\mu\text{b}$ or 0.01 hz at 10^{30} luminosity. The implications of higher rates have been previously discussed.

The drift chambers for the intermediate toroids are patterned after the forward chambers. The chamber area is slightly smaller (37m^2 vs 45m^2 per ring of chambers), and the middle chamber in the forward system is mounted behind the toroid in the intermediate one, there being no room along the beam to split the toroid and its coils. Thus the intermediate measurement will be input and output slopes of the track. A total of 24 extra 96 channel digital TDC units are required, along with the associated trigger cards and Fastbus crates. The pads in the present forward chambers are read out with RABBIT, but we are investigating the possibility of using Fastbus readout for the intermediate pads. We are also studying the implementation of a track finder at level 2 for both the forward and intermediate toroids to further decrease the rates into level 3.

Design Parameters of the Intermediate Toroids

Pseudo-rapidity coverage	$1.3 \leq \eta \leq 1.9$
Cell size	2.0cm x 10.0cm
Max drift distance	5cm
Max drift time	$1\mu\text{s}$
Field Integral	1.8 T-m
Total number of channels	2304
Pion interaction lengths at $\theta = 30^\circ$	11.6
Minimum detectable muon P_t	2.5 GeV
Multiple scattering at $\theta = 30^\circ$	18cm/P

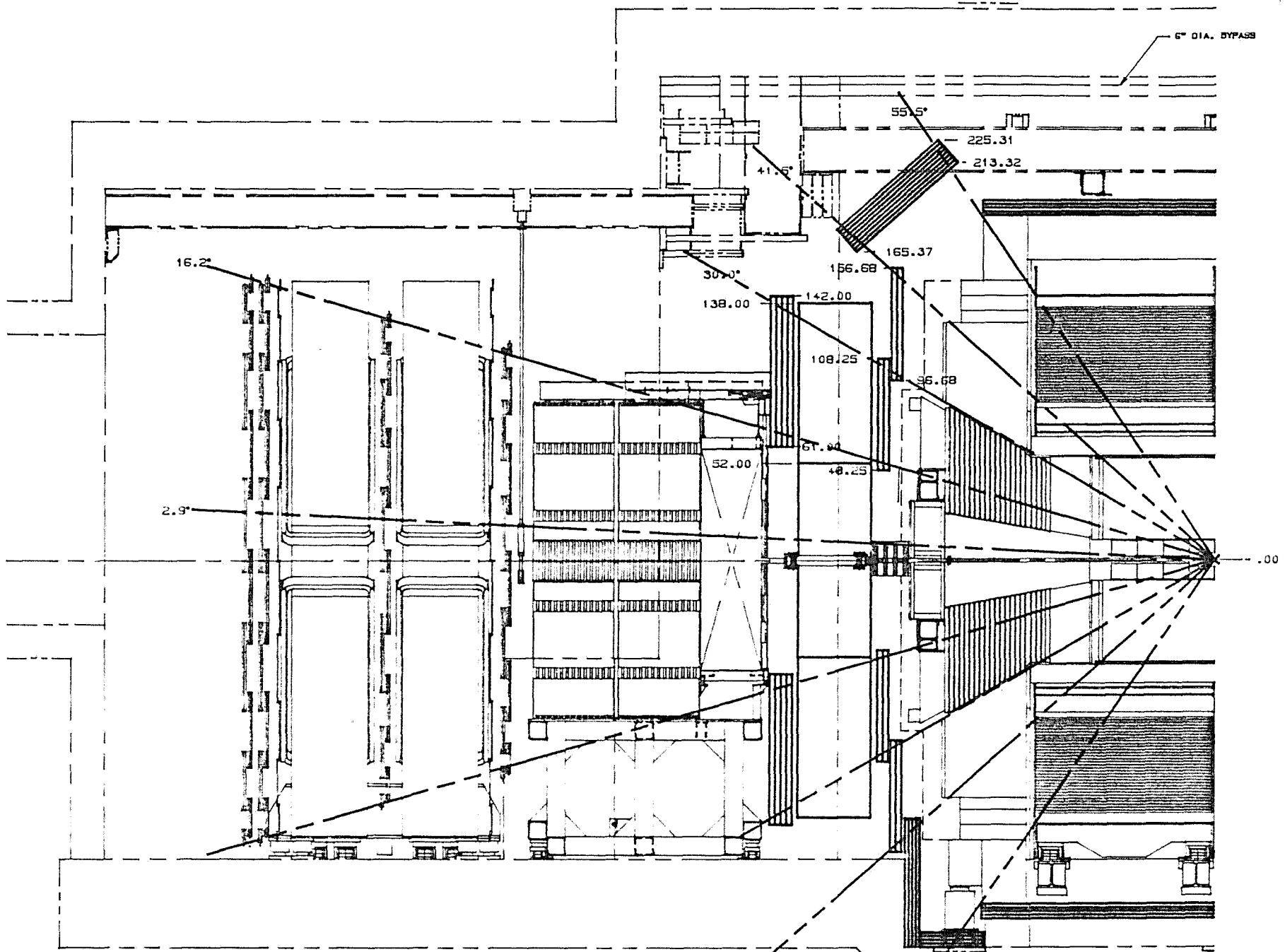
We would like to express our gratitude to Jon Rosner, Lynne Orr and Waikwok Kwong for providing most of the dimuon distributions, and to George Redlinger who provided the plot of transverse momentum distribution in jets.

References

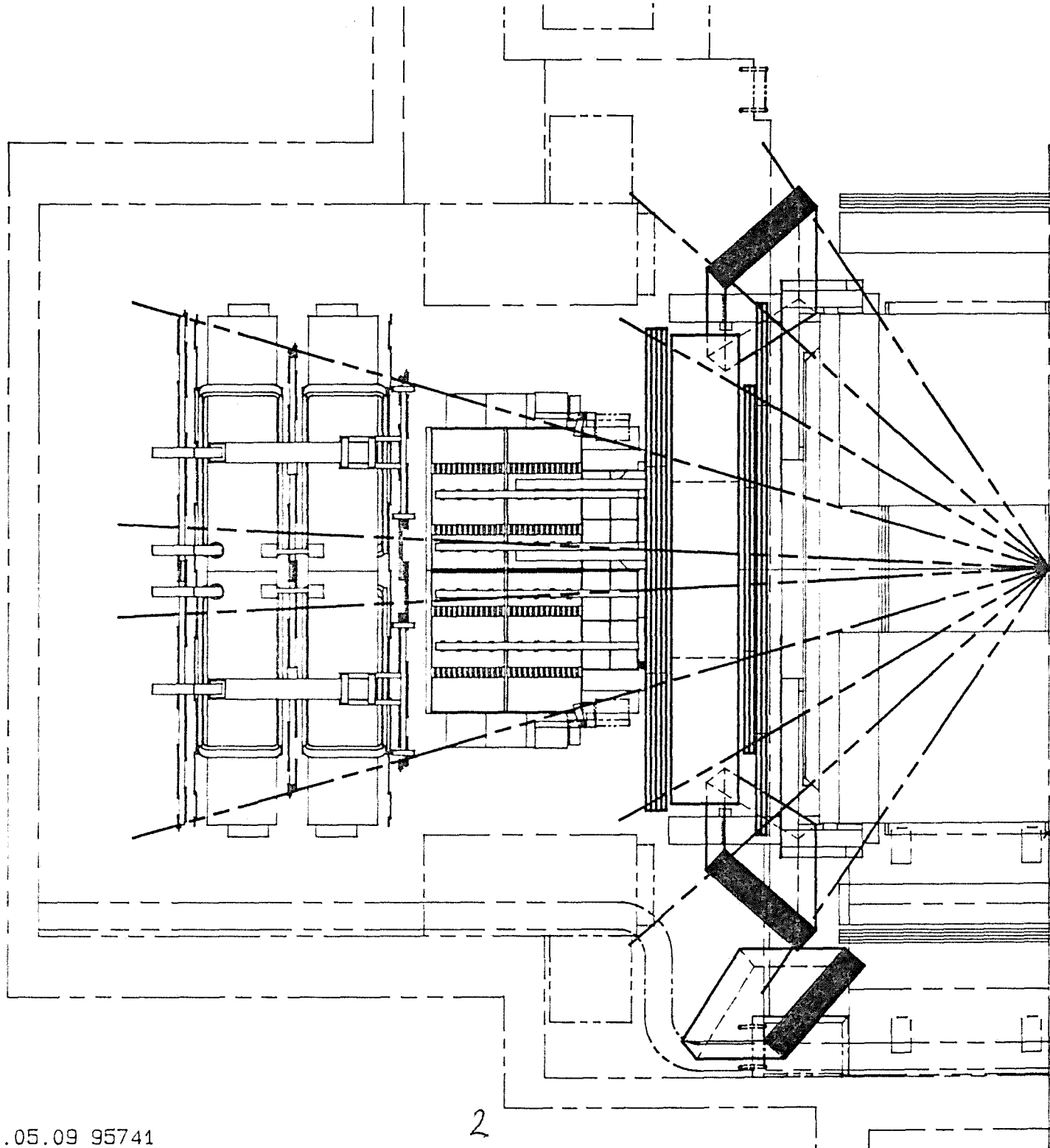
- [1] E. L. Berger, *Heavy Quark Production in Hadron Collisions*, Proceedings XXII Rencontre de Moriond, Les Arcs, France (1987) .
- [2] F. Abe et al., *Measurement of the Inclusive Jet Cross Section at the Tevatron $p\bar{p}$ Collider*, CDF Note 746 Submitted to Phys. Rev. Lett.
- [3] T. Kamon and S. Mikamo, *Rate Estimation of Cosmic Ray Backgrounds to Isolate Gamma Ray Events in the CDF Calorimeter*, CDF Note 624 .

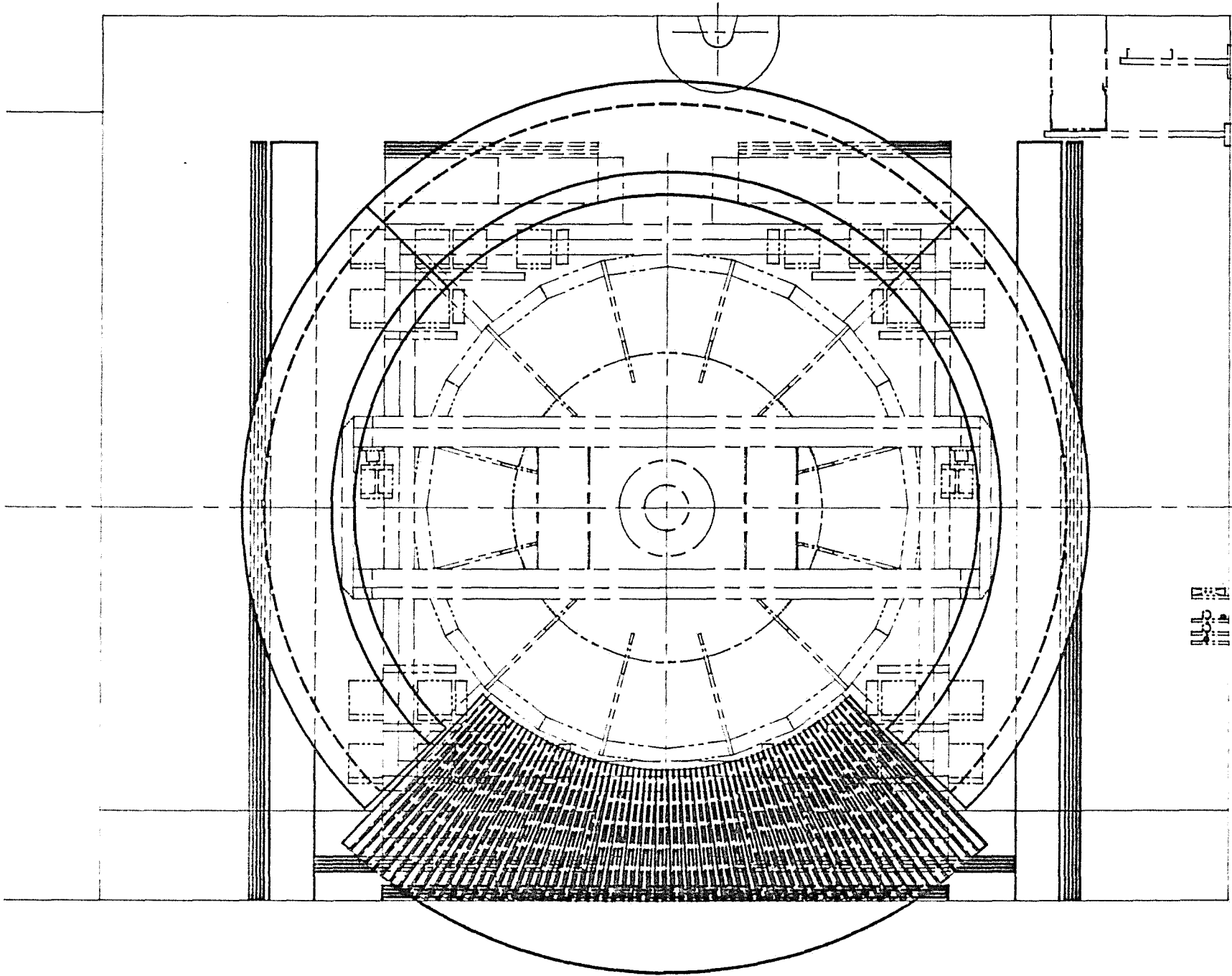
Figure Captions

1. Elevation view of the CDF detector showing the proposed muon upgrade chambers.
2. Top view of the CDF detector showing the proposed muon upgrade chambers including the steel walls at the sides of the detector.
3. End view of the CDF detector showing the bottom 90° of the central extension.
4. Number of absorption lengths between the beam-beam vertex and the point where muons are identified. The abscissa is the polar angle, θ , from the beam axis. The dashed curve represents the current situation, with forward muon coverage from 3° to 17° and central coverage from 55° to 90°. The solid line indicates the addition of steel in the central region and the intermediate toroids. The curves indicate the thickness at azimuthal angle, $\phi=0$.
5. The number of charged tracks per jet as a function of transverse momentum.
6. Dimuon acceptance as a function of pseudo-rapidity (η) interval covered by a muon upgrade for $b\bar{b}$, $t\bar{t}$, and Zs. The left most point corresponds to the present situation with just central and forward muon coverage and the right most point corresponds to filling the entire gap from $\eta=0.65$ to $\eta=2.00$ with a triggerable muon system.
7. Number of dimuon events in 1 pb^{-1} from $b\bar{b}$ as a function of P_t cutoff with one muon in the central and one in the central extension. The abscissa is the P_t cut applied to central and each curve corresponds to a different P_t cutoff in the central extension.
8. Same as Fig. 7 but with the second muon in the endwall chambers.
9. Same as Fig. 7 but with the second muon in the intermediate toroids.
10. Same as Fig. 7 but with the second muon in the forward toroids.
11. Typical end wall chamber module.
12. Typical ϕ cell of the proposed end wall chambers.



TOROID PROPOSAL BETWEEN END PLUS
AND FORWARD SHOWER (LOOKING NORTH)
SCALE: 1/32
DATE: APRIL 20, 1988





三
三
三

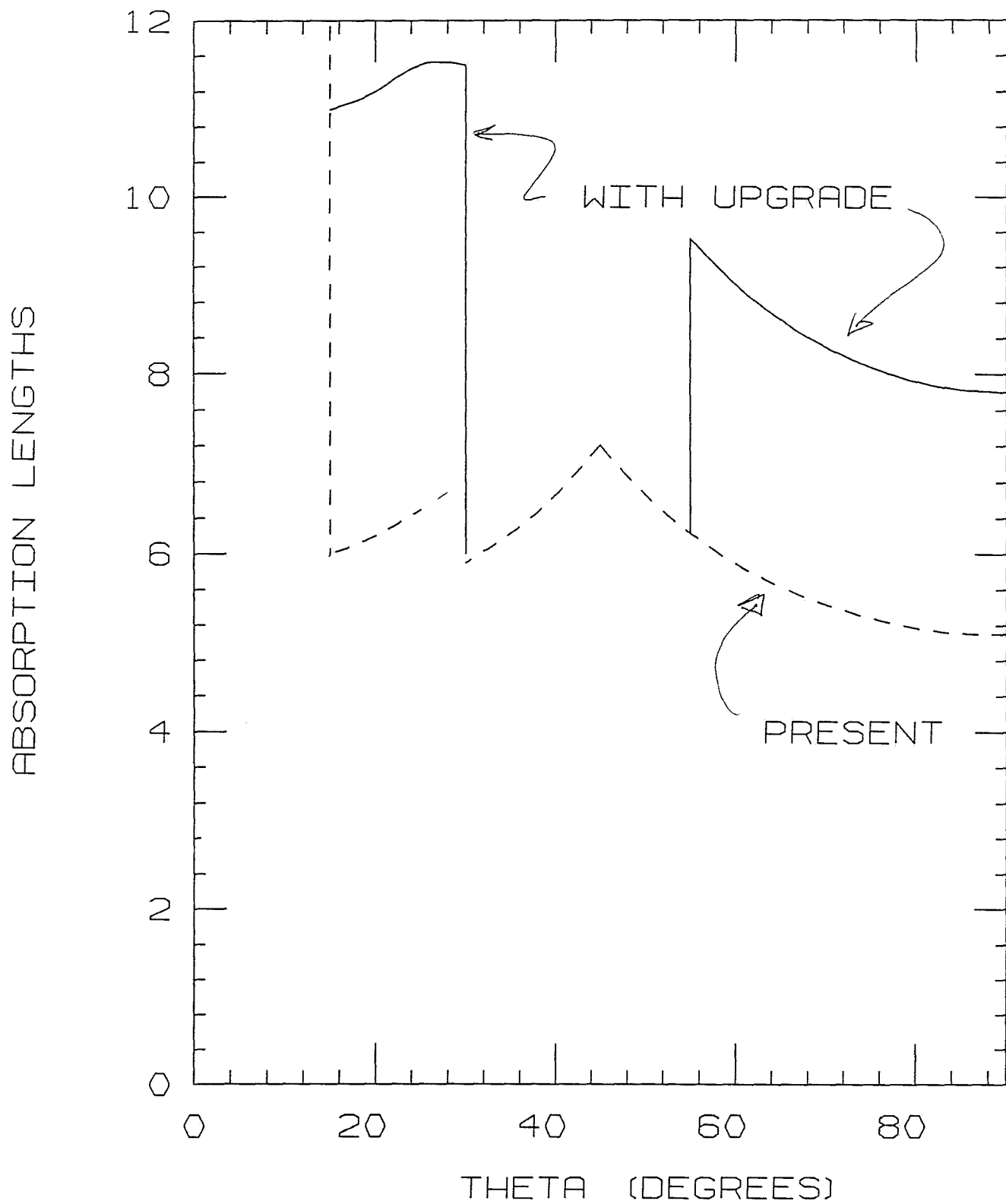


Fig. 4

DN/DpT In Jets

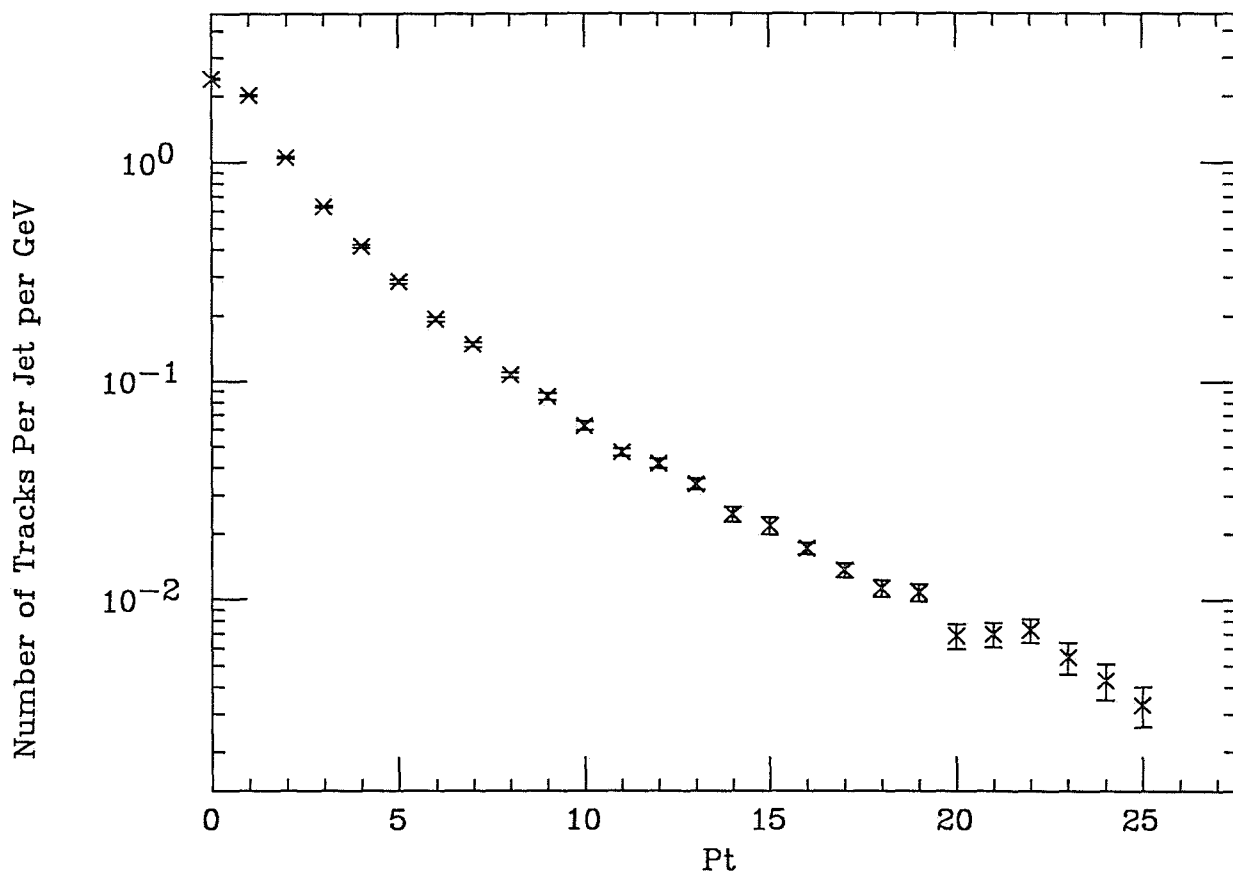


Fig. 5

Di-Muon Acceptance

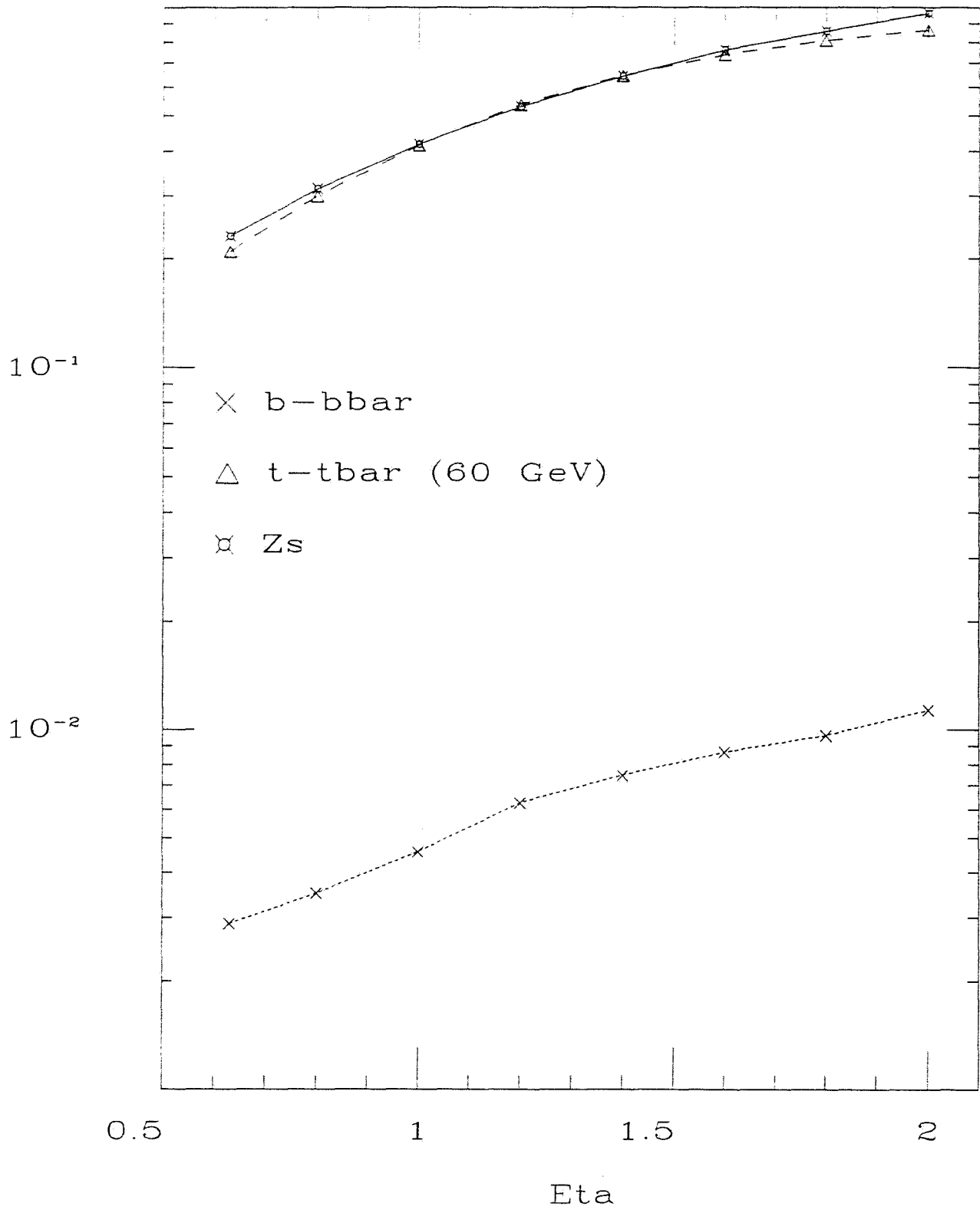


Fig. 6

DIMU CENTRAL, CENTRAL EXTENSION

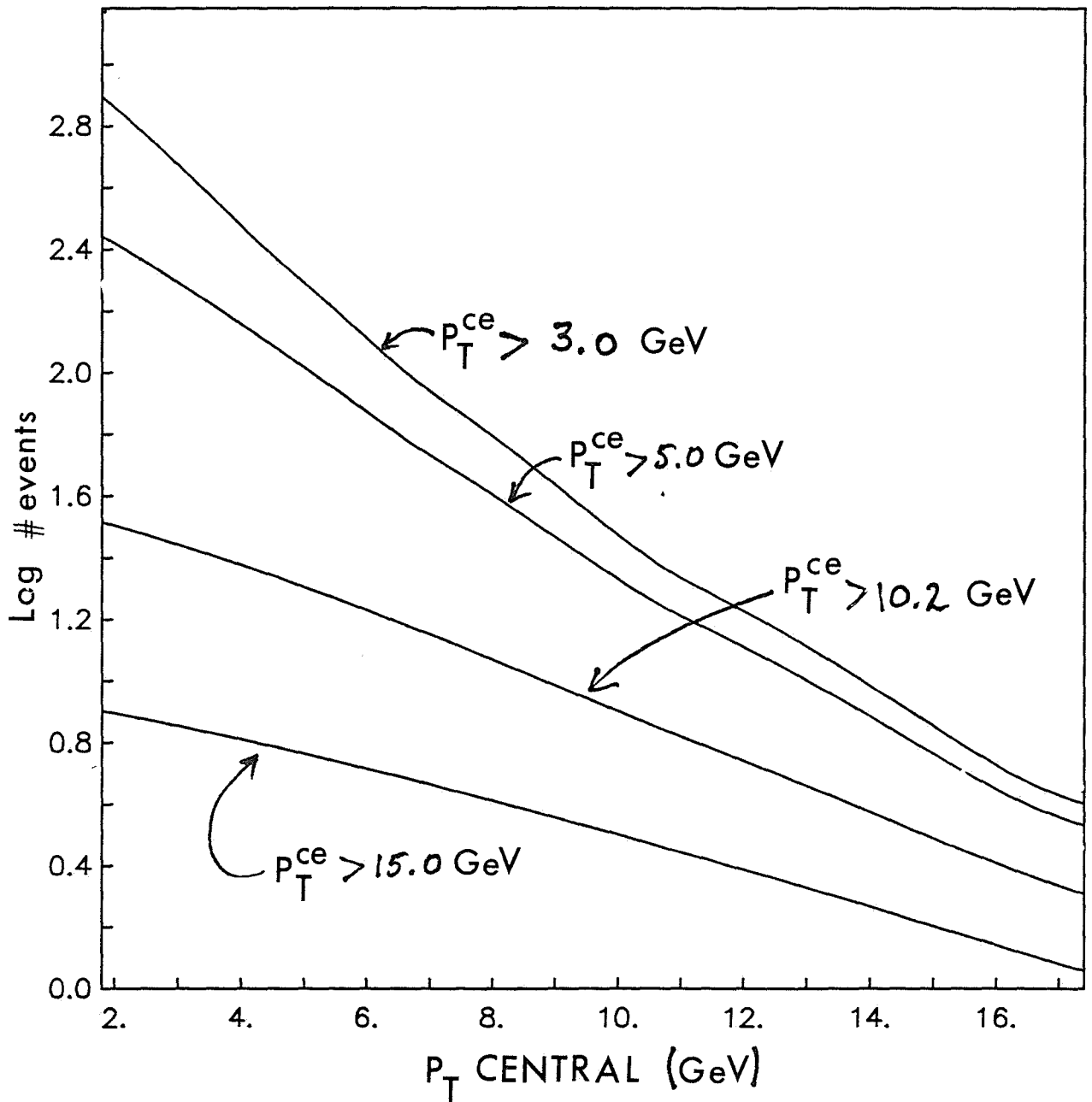


FIG 7

DIMU CENTRAL, ENDWALL

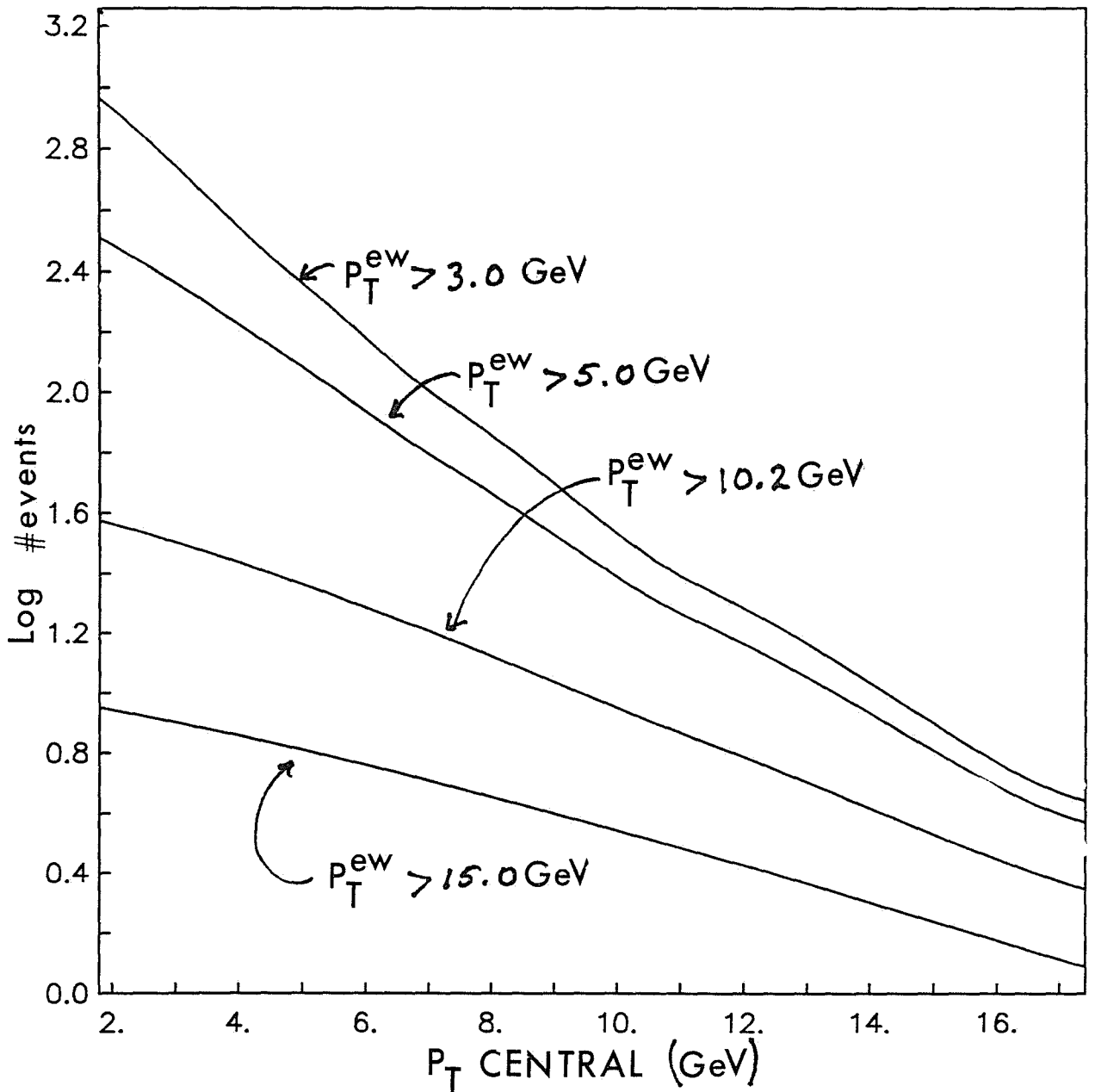


FIG 8

DIMU CENTRAL, INT. TOROIDS

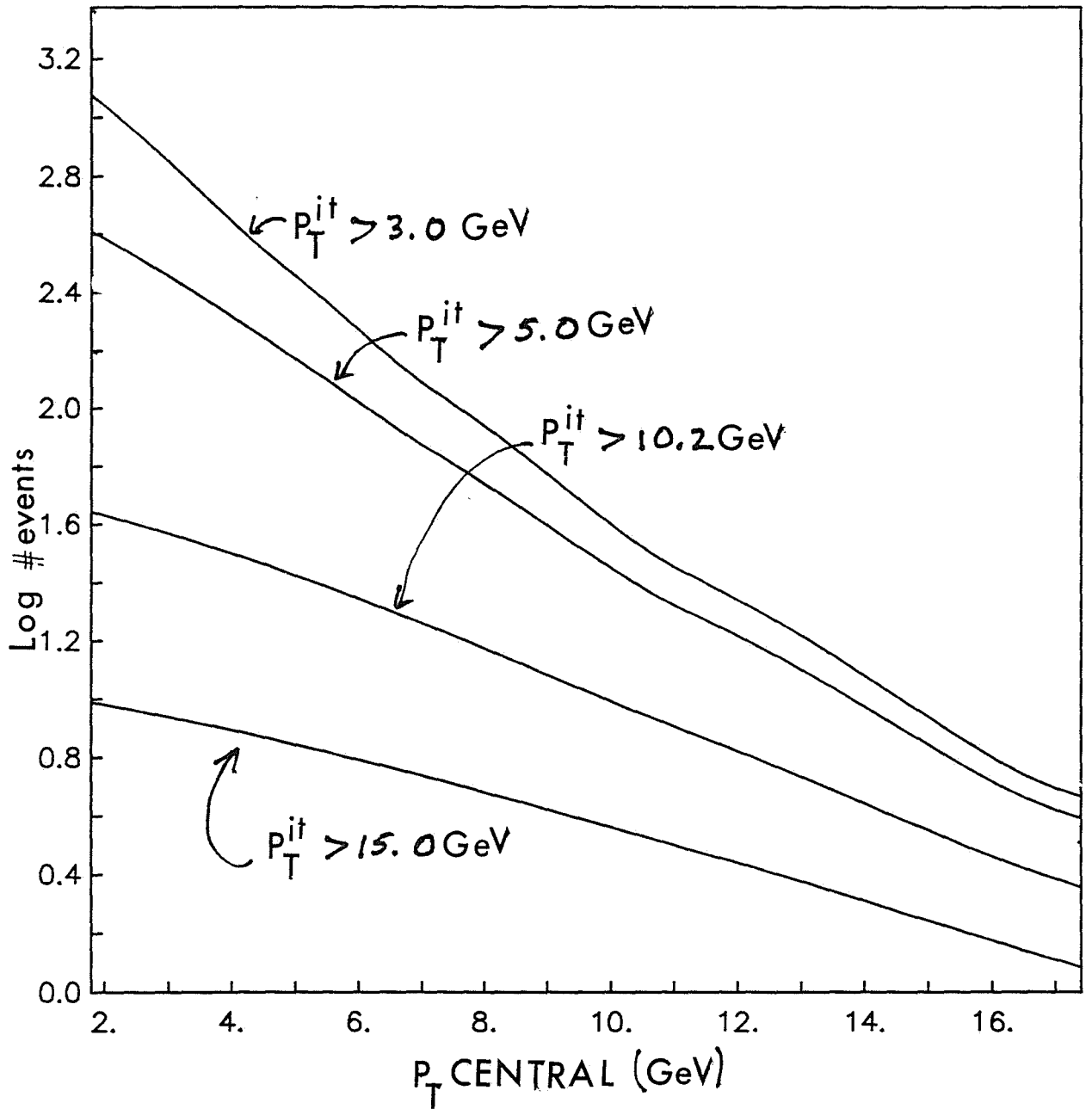


FIG 9

DIMU CENTRAL, FORWARD

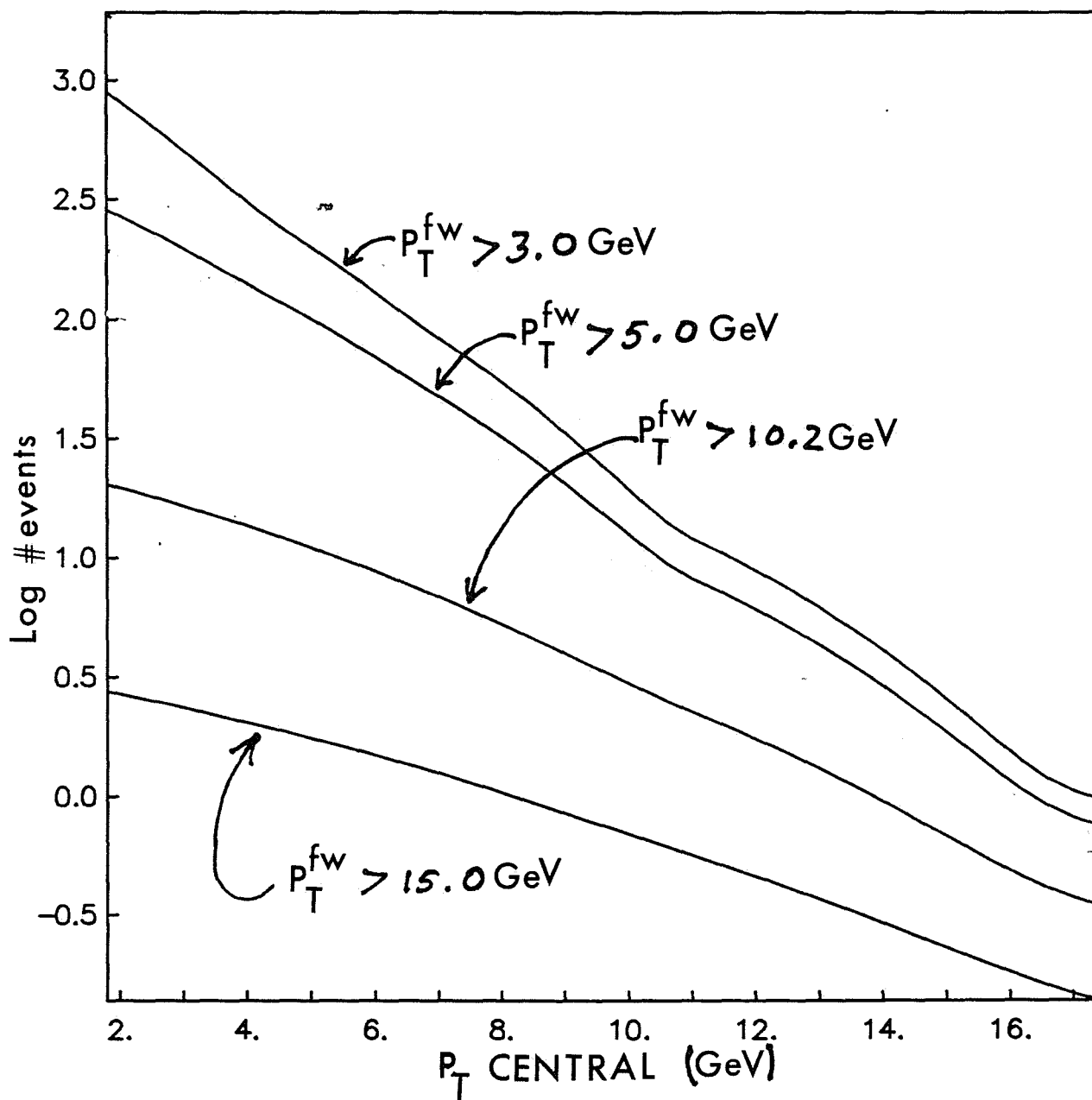


FIG 10

A PLANE OF END WALL MUON CHAMBER

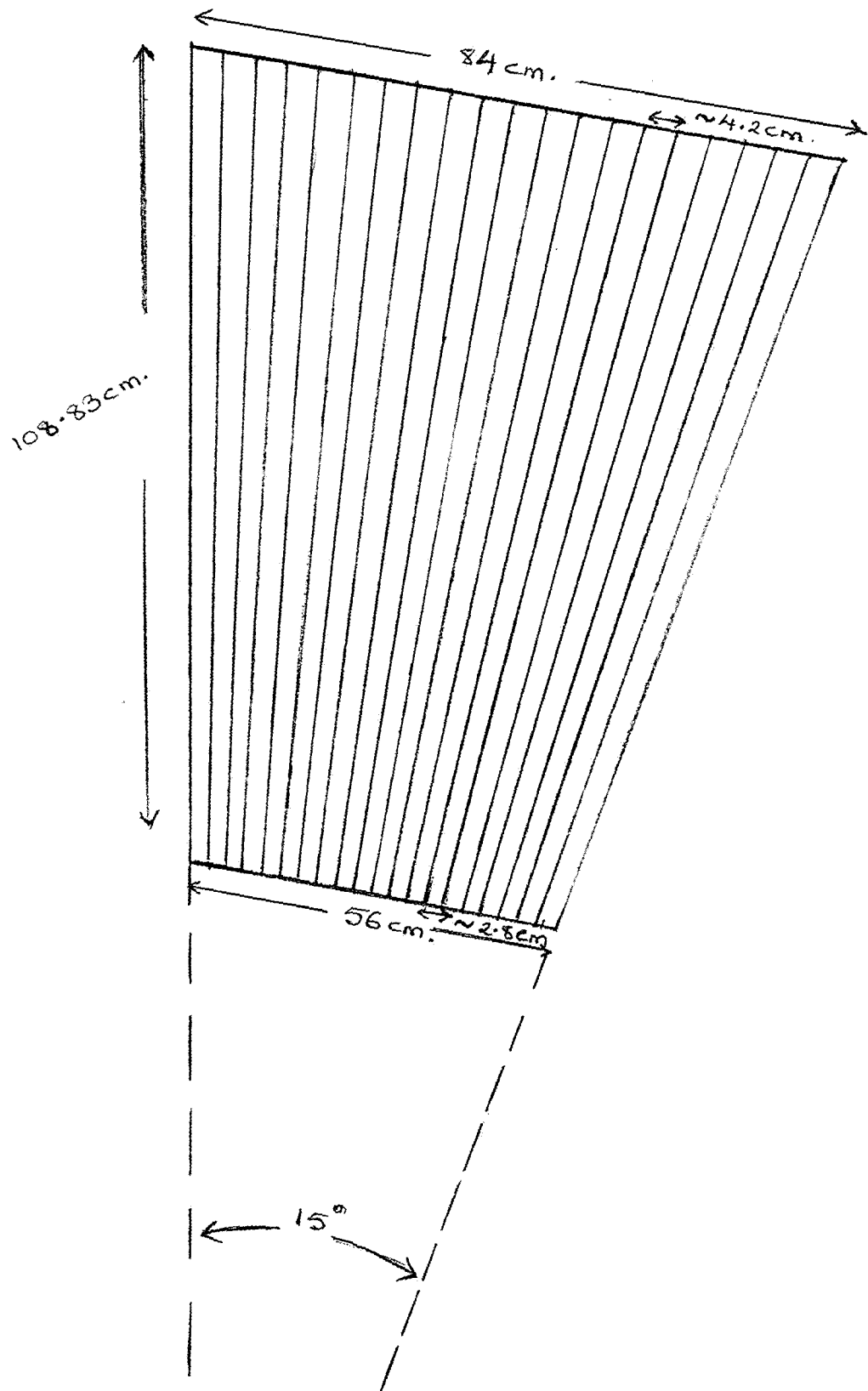


FIG. 11

A CELL IN ENDWALL MUON CHAMBER.

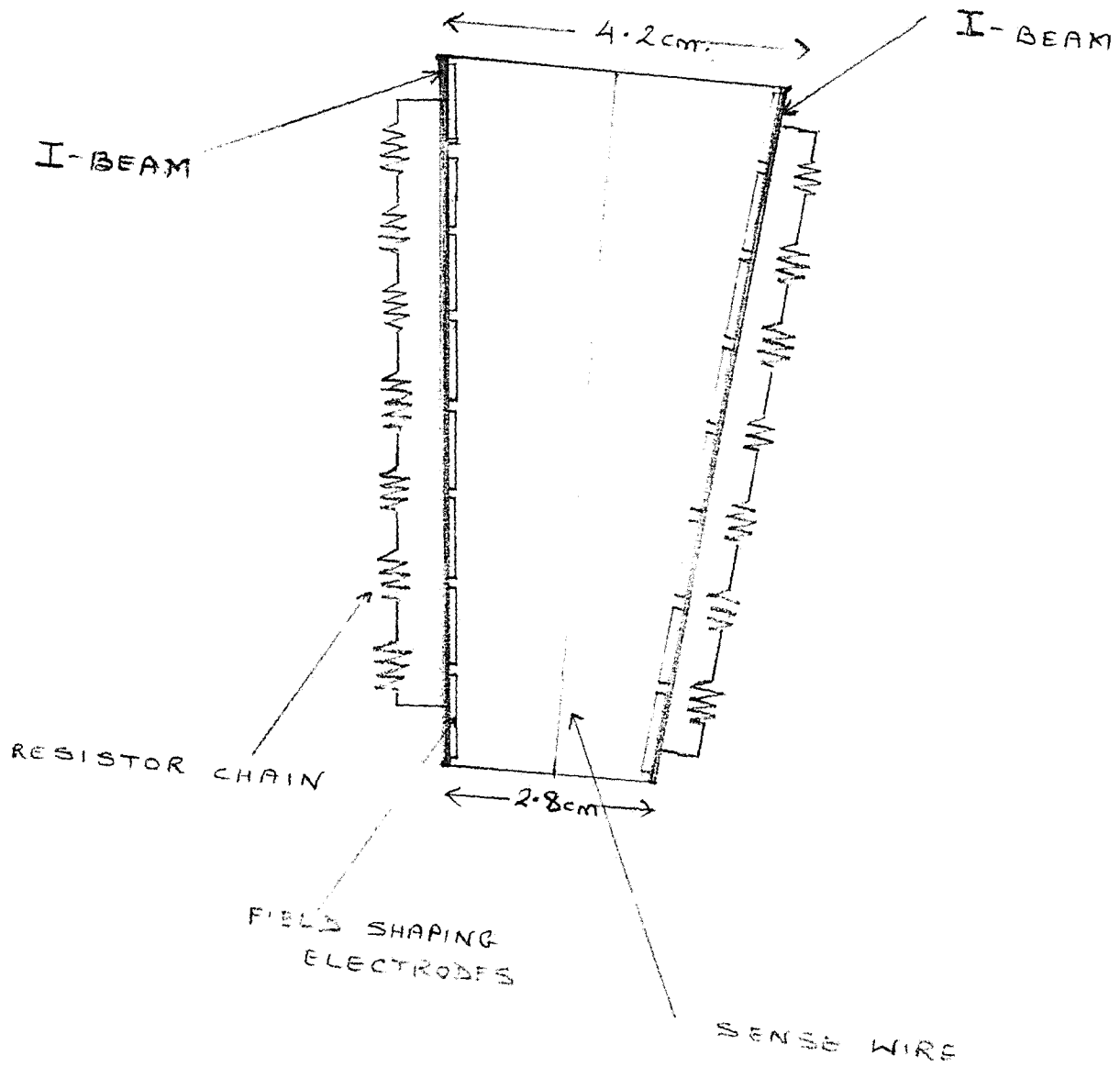


Fig. 12

CDF Muon Upgrade

A. Extension of Central Muon Chambers

Extends central muon coverage from 55 to 45 degrees
Consists of pinwheels of drift tubes around each end of the central detector

Materials Costs for tubes		125
Labor Costs to assemble tubes		200
Stands		100
Electronics	2304@\$200	460
Trigger		100
	Harvard Labor Contrib	-150
	Subtotal	835
	25% Contingency	184
	15% SWF	153
	System total	1172

B. Upgrade of Central Muon Coverage

Adds two steel walls to sides of central detector
Instruments new steel walls and top and bottom of magnet yokes with drift chambers

Steel	630 tons @ \$750	500
Chambers		1000
Labor to assemble chambers		200
Electronics	1112 @ \$200	222
Trigger		50
	Japanese Contribution	-986
	Subtotal	986
	25% Contingency	247
	15% SWF	185
	System total	1418

C. Intermediate Muon Toroids

Adds two steel toroids with chambers to cover 15 to 30 degrees

Toroids: Designed and fabricated by PSL		
	Design and drafting	113
	Steel	212
	Machining steel	213
	Coils	144
	Bases	165
	Mounting for Chambers	50
	Engineering supervision at FNAL	32
	Subtotal	929
Chambers: Fabricated by U of Wisconsin		
	Chambers	200
	Labor to assemble	100
	Electronics and HV	210
	TDC and Fastbus	190
	Subtotal	700
Assembly at FNAL		213
	Grand Subtotal	1842
	25% Cont	461
	15% SWF	345
	System Total	2648

D. Endwall Muon Chambers

Consists of drift chambers covering the region between 30 and 45 degrees

Chambers		250
Labor to assemble		200
Electronics	2016@\$200	403
	Subtotal	853
	25% Cont	213
	15% SWF	160
	System Total	1226

Grand Total - All systems 6464

Pion Punchthrough Probability in the Central Calorimeter

David A. Smith, University of Illinois
Hans B. Jensen, Fermi National Accelerator Laboratory

Abstract

The number of absorption lengths traversed by pions, kaons, protons, and antiprotons in a central wedge is calculated as a function of the incident hadron momentum. The momentum dependence is strong, resulting in 3 times as many non-interacting pions at low momentum as compared to high momentum. Fits and a fortran function are provided to ease calculations of backgrounds to muon signals. Corrections are made for the energy loss of the particle in the wedge. An overall punchthrough probability using the UA5 charged particle mix is shown. The fact that K^+ 's have a smaller absorption cross section than K^- 's leads us to the prediction of a charge asymmetry in the non-interactive hadron punchthrough background to the inclusive central muon spectrum.

1 Motivation

Two principal backgrounds confuse a study of prompt muons in the CDF central region. These are muons from pion and kaon decay, and hadrons that don't shower in the calorimeter. This note concerns the latter category. A charged hadron leaves a minimum-ionizing trail in the calorimeter until it showers. If it never showers, it is indistinguishable from a muon. The probability \mathcal{P} for an incident hadron not to interact after traversing a distance x of material is

$$\mathcal{P} = e^{-\Lambda} = e^{-x/\lambda_{abs}} \quad (1)$$

or $1/165$ for $\Lambda = 5.10$. The absorption length λ_{abs} depends on the absorption cross section,

$$\lambda_{abs} = \frac{A}{N\rho\sigma_{abs}}, \quad (2)$$

where A is the atomic number of the material, N is Avogadro's number, ρ is the density of the material, and σ_{abs} is the absorption cross section. Hence one need only know the depths and cross sections for the different materials in the calorimeter, and Λ comes from simple arithmetic.

The difficulty is in knowing the cross sections accurately. The Particle Data Booklet (PDB) only tabulates values for proton interactions in different materials at high energy, $E > 50$ GeV, and the PDB cross section curves are only for hadrons incident on proton targets. The cross section for hadrons on heavier targets obeys a power law,

$$\sigma_{abs} = \sigma_0 A^\alpha \quad (3)$$

Hadron	σ_0	α
K^+	20.37 ± 0.80	$0.791 \pm .01$
K^-	22.56 ± 0.90	$0.779 \pm .01$
π^+	25.64 ± 1.00	$0.764 \pm .01$
π^-	25.86 ± 1.00	$0.762 \pm .01$
p	37.99 ± 1.48	$0.719 \pm .01$
\bar{p}	43.50 ± 1.73	$0.698 \pm .01$

Table 1: Parameters for the power-law fit to the A -dependence of the absorption cross-section for 60 GeV/c particles [Carroll].

and simple scaling from the proton values to the pion values is complicated by the fact that α varies significantly amongst hadron species. Hence, the literature has to be probed beyond a cursory reference to the data booklet. Table 1 shows how the power law for the inelastic cross section varies for different mesons.

One last motivating remark: a rough, 10% estimation of Λ based on naive scaling will result in a 50% error in the rate for non-interacting punch through's. That is, the error in the rate is

$$\frac{\delta \mathcal{P}}{\mathcal{P}} = \left(\frac{\delta \Lambda}{\Lambda}\right) \Lambda$$

and $0.1 \times 5.1 = 51\%$. A survey of the literature indicates that about 3% accuracy in Λ is obtainable, lowering the error in the rate to 15%. Hence a small improvement in the Λ calculation yields a big gain in the rate estimate, and it is worth going into detail.

2 Sources

To get our numbers we have compared different sources:

- Published A -dependence of absorption cross sections, found in the PDB references and references therein [Carroll, Roberts, Denisov];
- π -iron absorption lengths measured during detector calibrations in other experiments [CDHS, CIFT];
- Particle Data Booklet cross section plots (see figures 1 and 2) ¹;
- CDF central wedge testbeam data. This only provides limits on the final values, for reasons discussed below.

Figure 3 shows a compilation of the various cross section measurements for pions in iron. Some explanations are in order:

¹Thanks to Bill Carithers for obtaining Vax files of the cross section data from the Particle Data Group.

Meson-Proton Cross-Sections

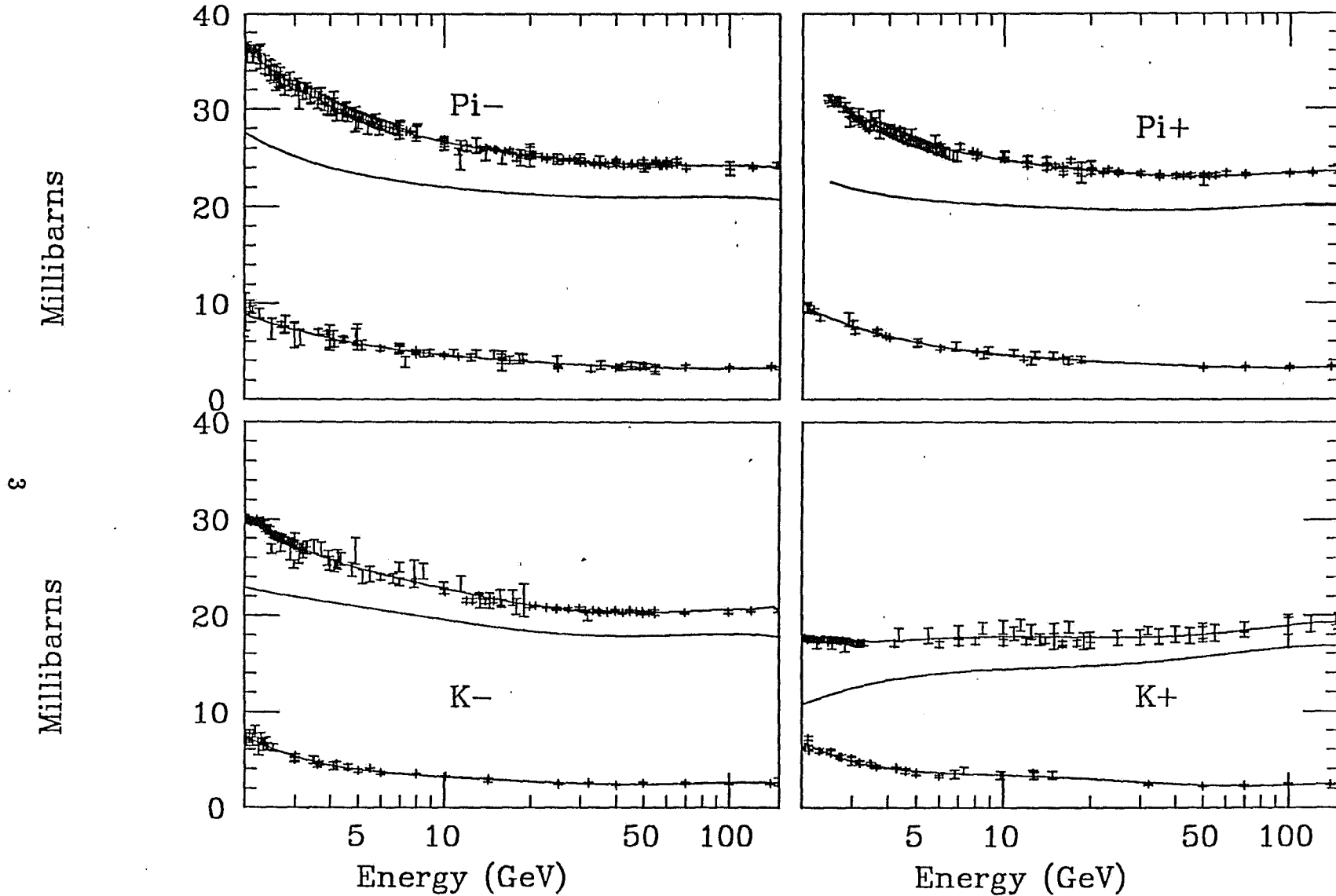


Figure 1: Meson-proton cross sections as a function of meson energy, taken from the Particle Data Group. In each plot, the top curve is σ_{total} , the bottom curve is $\sigma_{elastic}$, and the third curve comes from subtracting the fits to the first two, $\sigma_{inelastic} = \sigma_{total} - \sigma_{elastic}$.

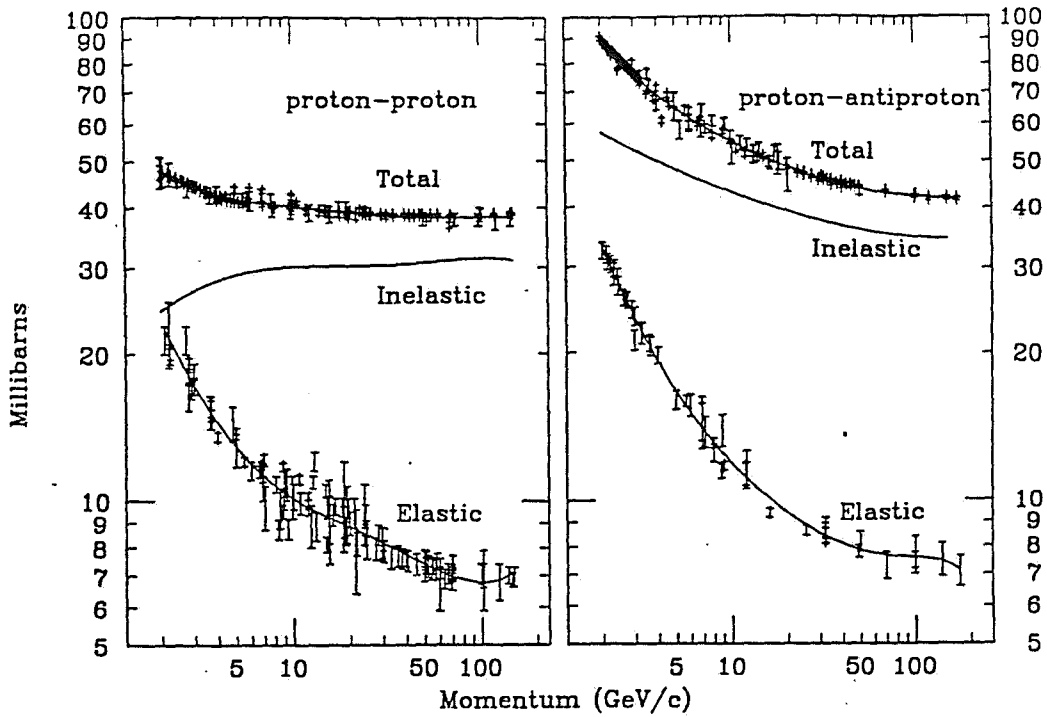


Figure 2: Proton-proton (left) and antiproton-proton (right) cross sections as a function of energy, taken from the Particle Data Group. Curves are as in figure 1.

- The values listed in the PDB Table of Nuclear Properties are weighted averages from Carroll and Roberts. Since Roberts only studies incident neutrons, and Carroll only descends to 60 GeV, Denisov is included to learn how to scale to lower energies.
- The solid curve is the average of the π^+ and the π^- inelastic cross sections on protons taken from the fits in figure 1, scaled to match Denisov at $p_\pi = 30$ GeV/c. We use the average since the material in the wedge contains roughly equal proportions of protons and neutrons, and the data booklet curves (or, alternatively, isospin symmetry) show that $\sigma_{\pi^+p} \simeq \sigma_{\pi^-n}$ and $\sigma_{\pi^-p} \simeq \sigma_{\pi^+n}$.
- CDHS [6] measures an effective absorption length for their iron/scintillator combination, which is then corrected to obtain a value for pure iron. Their result is somewhat lower than the other values.
- CITF [5] measures the non-interaction probability \mathcal{P} , which is then converted to a cross section for comparison.

The main point of figure 3 is that thin-target measurements of the absorption cross section yield the same results as measurements of interaction probabilities made using thick, complex calorimeters. That is, the data in figure 3, obtained by a variety of different methods, yield consistent results. Hence we can use the published values of the absorption cross sections covering a broad range of target materials, particle types and energies to calculate the number of absorption lengths in a wedge.

Carroll et al [1] provide the most recent, comprehensive set of absorption cross sections. Our method, then, is to use Carroll's values at 60 GeV/c to calculate high energy values of the number

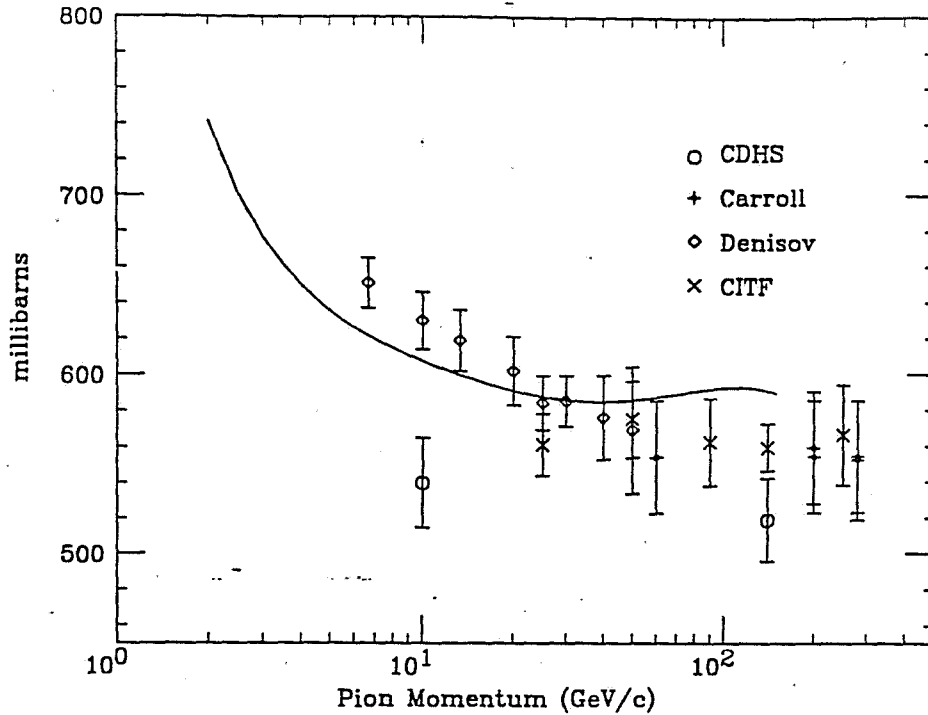


Figure 3: Pi-iron inelastic cross sections, as measured by the various authors[1-6]. Where absorption lengths (CDHS) or interaction probabilities (CITF) were measured, they have been converted to a cross section for comparison. The solid curve is $(\sigma_{\pi+p} + \sigma_{\pi-p})/2$ from figure 1, to allow for the equal proton and neutron mix in iron, scaled to match Denisov at 30 GeV.

of absorption lengths in a wedge, and then scale the curves from the Particle Data Group (the $\sigma_{inelastic}$ curves of figures 1 and 2) to extrapolate to lower energies. Table 2 lists Carroll's cross sections for the different target materials present in the central wedges and for the different particle types, at 60 GeV/c, as well as the absorption lengths calculated from equation (2).

The method just described introduces a small systematic error into our calculation. The absorption cross section,

$$\sigma_{abs} = \sigma_{total} - \sigma_{elas} - \sigma_{quasi}, \quad (4)$$

is different from the inelastic cross section,

$$\sigma_{inelas} = \sigma_{total} - \sigma_{elas}, \quad (5)$$

by σ_{quasi} , the quasi-elastic scattering cross section². The difference is less than 3% over the energy range covered by Denisov et al [3]. We use σ_{abs} to calculate the number of absorption lengths in wedge at high energy, but σ_{inelas} to extend to low energy. A systematic error arises to the extent that the energy dependence of σ_{abs} is different from that for σ_{inelas} . We consider this error to be negligible.

Central wedges contain two types of scintillator. The hadron calorimeter uses plexiglas (also called Lucite or acrylic) while the shower counter has polystyrene. (CDHS [6] uses plexipop, which

²This is Carroll's nomenclature. Unfortunately, the data booklet defines σ_{inelas} to be exactly what we have called σ_{abs} .

	K^+	K^-	π^\pm	p	\bar{p}
Target	<i>Absorption Cross Sections (mb)</i>				
Lead	1360 ± 42	1414 ± 45	1479 ± 44	1730 ± 52	1805 ± 56
Iron	491 ± 28	518 ± 29	554 ± 34	685 ± 38	721 ± 41
Alu	280 ± 9	299 ± 9	324 ± 10	409 ± 12	439 ± 13
Carbon	144 ± 4	153 ± 5	169 ± 5	222 ± 7	242 ± 7
	<i>Absorption Lengths (cm)</i>				
Lead	22.3 ± 0.7	21.4 ± 0.7	20.5 ± 0.6	17.5 ± 0.5	16.8 ± 0.5
Iron	24.0 ± 1.4	22.7 ± 1.3	21.3 ± 1.3	17.2 ± 1.0	16.3 ± 0.9
Alu	59.3 ± 1.9	55.5 ± 1.7	51.2 ± 1.6	40.6 ± 1.2	37.8 ± 1.1
Plexi	114 ± 3	107 ± 3	97 ± 3	74 ± 2	67 ± 2
Poly	128 ± 4	120 ± 4	109 ± 3	83 ± 3	76 ± 2

Table 2: Absorption cross sections, in millibarns, for 60 GeV/c hadrons incident on different targets (from Carroll et al [1]). The absorption lengths are calculated using the cross section values and equation (2). (The central hadron calorimeter uses plexiglas and central EM uses polystyrene.)

is doped plexiglas and has the same absorption length.) Since both plastics are predominantly carbon, we scale from the data booklet values for the absorption length according to

$$\lambda = \lambda^{PDB} \times \frac{\sigma_{carbon}^{PDB}}{\sigma_{carbon}^{Carroll}}$$

3 Central Calorimeter Test Beam Data

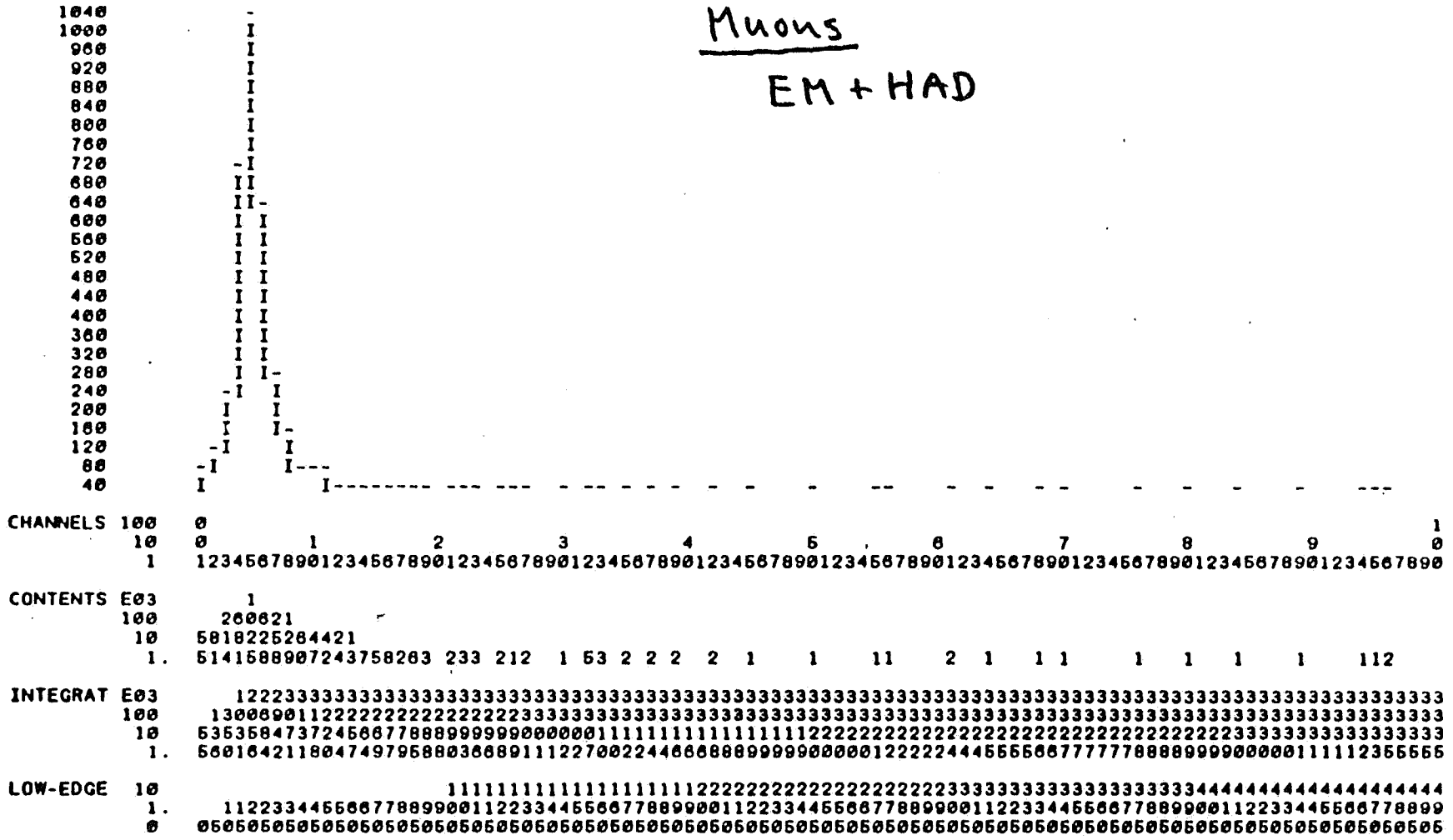
3.1 Data Sample

Test beam data taken in M-Test on February 12, 1988 has been used for an analysis of the non-interactive pion punchthrough probability. A 57.1 GeV π^+ beam was directed at the center of tower 2 of wedge #30³. The data consists of 18482 events (run 10516). A 10 inch by 10 inch scintillator counter placed behind an additional 9 feet of steel behind the wedge served as a muon tag. The counter efficiency (for charged particles) was measured with 190 GeV pions to be 54897/56869 or 96.53% \pm 0.08% (statistical error only). The efficiency of the muon tag must be less than or equal to this number (multiple scattering and interactions in wedge and additional steel will reduce the efficiency):

$$\text{Muon tag efficiency} \leq 96.53\% \pm 0.08\%$$

³Thanks to Barry Wicklund and Fumi Ukegawa for making a short, special format disk file of this data!

Muons
EM + HAD



• ENTRIES = 3436 • ALL CHANNELS = 0.3336E+04 • UNDERFLOW = 0.9200E+02 • OVERFLOW = 0.9000E+01
 • BIN WID = 0.5000E+00 • MEAN VALUE = 0.2731E+01 • R . M . S = 0.2946E+01 • ABNDR CHA = 0.0000E+00

0

50 GeV

Figure 4: Total (EM + Hadron) pulse height distribution of 57.1 GeV μ^+ 's at tower 2 center (coarse binning). Note the 92 underflow entries.

3436 events are tagged as muons. Their pulse height distribution (EM + HAD) is shown in figures 4 and 5. The energy scale has been determined using the assumption that the beam energy of 57.1 GeV is correct, and then following the standard CDF calibration procedure. The muon pulse height distribution looks Landau-like with an average of about 2.45 GeV. There is a long tail towards large pulse heights. 56 events (1.6%) for instance, have (EM + HAD) > 10 GeV. It is conceivable that some of these events are overlaps of two beam particles, a muon and a pion for instance. The muon efficiency with a cut of (EM + HAD) < 5 GeV is then at least (figure 4):

$$\frac{(3178+92 \text{ (underflows)})}{3436} = 95.2\% \\ \text{(57.1 GeV } \mu^+ \text{'s at tower 2 center)}$$

We are interested in measuring the non-interactive pion punchthrough probability. We will now define this to be the probability that the (57.1 GeV) π^+ gives a pulse height (EM + HAD) of less than 5 GeV. To obtain a "clean" pion sample, we begin with a total of 18482 events, followed by the following cuts:

1. Remove 3436 events tagged as muons
2. Remove 278 events tagged as having late particle hits
3. Remove 27 events for which the total pulse height exceeds 85 GeV.
4. Remove 70 events tagged as electrons by the beam Cerenkov counter
5. Remove 189 events, untagged by the (inefficient) Cerenkov tag, but electron-like in that they have EM > 50 GeV and HAD < 3.3 GeV.

This leaves 14482 "pion" events. Note that cuts 3-5 don't remove non-interactive punch-through candidates.

3.2 Analysis for (EM + Hadron)

The pulse height histogram (EM + HAD) for these pions is shown in figure 6. There are 223 events with $0 < \text{EM} + \text{HAD} < 5$ GeV and 52 underflows. The muon pulse height histogram with the same binning is shown in figure 5. The ratio between the two is plotted bin-by-bin in figure 7 (left). Apart from the underflow bin, the ratio looks fairly constant in the range 0 - 5 GeV at a value of (223 pion events/3178 muon events) = 0.070. It seems reasonable then to count only $0.070 \times 92 = 6$ of the pion underflow events as real, and disregard the remaining $52 - 6 = 46$ events in the pion data (maybe there was no real beam particle in these events?). In summary then, there are $223 + 6 = 229 \pm 15$ events or 1.6% of the pion events which have (EM + HAD) < 5 GeV:

$$\text{Fraction of muon-like events} = 1.6\%$$

Some of these events must be muons which were untagged because of the muon tag inefficiency. There should be at least

$$3436 \times \frac{(1.0 - 0.9653)}{0.9653} = 124 \pm 4$$

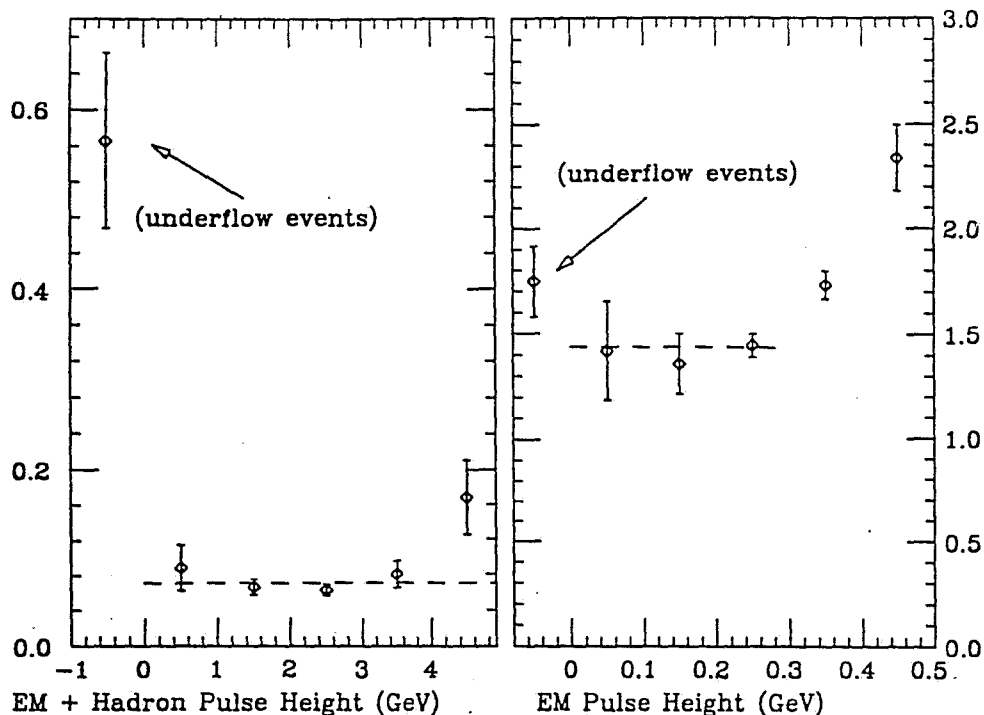


Figure 7: Ratio $\frac{\pi}{\mu}$ of pion-to-muon events per bin. Left-hand plot is for the total pulse height (EM + Hadron) taken from figures 5 and 6. Right-hand plot is for the EM pulse height taken from figures 7 and 8. For low pulse heights, and neglecting the underflow bins, the ratios are fairly constant.

such untagged muon events, leaving at most $(229 \pm 15) - (124 \pm 4) = 105 \pm 15$ non-interacting pions. The non-interactive pion punchthrough probability is therefore at most

$$\frac{105 \pm 15}{14482 - 124} = 0.73\% \pm 0.1\%$$

for 57.1 GeV π^+ 's at the center of tower 2 (corresponding to $\Lambda_{wedge} \geq 4.92 \pm 0.14$).

3.3 Analysis for the EM Shower Counter

A similar analysis can be performed to determine the pion interaction probability in the EM calorimeter alone. Figure 8 shows the pulse height distribution in tower 2 (EM only) for muons, while figure 9 shows the same distribution for pions. The bin-by-bin ratios are shown in figure 7 (right). The ratio is approximately constant in the pulse height interval 0 - 0.3 GeV with an average value of $2092/1455 = 1.44$. The total number of pions with a muon-like pulse height is therefore $3436 \times 2092/1455 = 4940$. Correcting for the muon tag inefficiency, we therefore find that the probability that a pion is muon-like in the EM calorimeter is

$$\frac{4940 - 124}{14482 - 124} = 33.5\% \pm 0.5\% \quad (\text{statistical only})$$

This number is surprisingly small. It would correspond to the EM calorimeter being 1.09 absorption lengths for these pions ($e^{-1.09} = 0.336$), which is more than calculated from the materials (see below).

Material	# layers	layer thickness	total thickness	π abs lengths
Coil sim ¹⁾			6.4 cm	0.125
Front plate			0.9525	0.019
Pb	30	2.54/8 = 0.3175	9.525	0.465
Al cladding	30	2 × 0.15 × 2.54	2.286	0.045
Str. chmbr.				0.022 Λ_p^2)
Polystyrene	31	0.5	15.5	
Mylar	1	0.4 × 2.54	1.016	
All plastic ³⁾			18.034	0.165
Total				0.841 ⁴⁾

Table 3: Material thicknesses and numbers of absorption lengths for the components of the central electromagnetic shower counter. Notes are given in the text.

4 Λ_{wedge} Calculations

Given the absorption lengths in table 2, we can add up the different materials to obtain a value for Λ for a central wedge, for 60 GeV/c particles. This section demonstrates the method for the pion case.

4.1 Central Hadron

Fe: (32 layers) × (2.54 cm/layer) ÷ (21.3 cm) = 3.82 ± 0.23 abs lengths

Scin: (32 layers) × (1.0 cm/layer) ÷ (97 cm) = 0.33 ± 0.01 abs lengths

Spring retainers: 0.7 cm Fe → 0.03 absorption lengths

$$\Lambda_{CHA} = (4.18 \pm 0.2) / \sin \theta \text{ absorption lengths for 60 GeV/c pions.}$$

4.2 Central EM

The shower counter contains a wider variety of material than the central hadron calorimeter: aluminum cladding on the lead, strip chambers, etc. Table 3 summarizes the contributions from the different materials to the total absorption length. The total is

$$\Lambda_{CEM} = (0.84 \pm 0.3) / \sin \theta \text{ absorption lengths for 60 GeV/c pions.}$$

We can now compare our result with the test beam value for tower 2,

$$\begin{aligned} \Lambda_{CEM}(\text{tower2}) &= 0.84 / \sin(72.2^\circ) \\ &= 0.88 < 1.09 \quad (\text{test beam result, see §3.3}). \end{aligned}$$

<i>Absorption Lengths per Wedge</i>				
K^+	K^-	π^\pm	p	\bar{p}
4.35 ± 0.20	4.60 ± 0.21	5.02 ± 0.23	6.09 ± 0.28	6.45 ± 0.29

Table 4: Total number of absorption lengths per wedge, Λ_0 , such that $\Lambda = \Lambda_0/\sin(\theta)$, for 60 GeV/c hadrons.

Notes for table 3:

1. The coil simulator has roughly the same number of absorption lengths as the outer tracking and coil;
2. The strip chamber thickness is given in proton absorption lengths, taken from reference [7]. The correction for pion lengths is negligible;
3. Summing all listed layers gives 1.52 cm less than the actual stack height. This 'leftover' material is treated as plastic;
4. The lead stack thickness varies from tower to tower, to maintain a constant number of radiation lengths, but to a good approximation the actual number of absorption lengths traversed by a track with angle θ relative to the beam axis is obtained from $0.841/\sin\theta$. (The totals for each tower, in proton absorption lengths taken from the data booklet, are tabulated in the CEM NIM paper [7].)

4.3 Entire Wedge

To compare with the testbeam result we use $\theta = 72.2^\circ$ for tower 2, and find

$$\Lambda(\text{tower 2}) = 4.18/\sin(72.2^\circ) + 0.86 = 5.25 \pm 0.24,$$

compared to the lower limit, 4.92 ± 0.14 , obtained in the test beam.

Then for 60 GeV/c pions incident on a central wedge, there are $(4.18 + .84) = 5.02 \pm 0.23$ absorption lengths in front of the muon chambers. Similar analyses for the other hadrons yield the results listed in table 4.

5 Low Energy Extrapolation

With the high energy values in hand (see table 4), we scale the PDB curves for σ_{inelas} from figures 1 and 2, in order to extrapolate to lower energy.

The PDB curves are for proton targets, whereas the wedges consist of roughly equal numbers of protons and neutrons. Hence some care is needed. As stated earlier, for pions we use the average inelastic cross section

$$\sigma_\pi = (\sigma_{\pi+p} + \sigma_{\pi-p})/2 \tag{6}$$

Particle	P0	P1	P2	P3	P4	P5
π	8.492	-4.713	2.968	-0.9973	0.1679	-0.0110
K^+	1.718	2.161	-0.533	-0.0925	0.0555	-0.0057
K^-	6.676	-1.832	1.326	-0.6193	0.1337	-0.0103
p	3.814	1.442	0.2904	-0.4478	0.1200	-0.0100
\bar{p}	12.440	-3.137	0.7221	-0.1178	0.0121	-0.0004

Table 5: Fit parameters for the momentum dependence of Λ_0 , where $\Lambda = \Lambda_0/\sin(\theta)$ is the number of absorption lengths traversed by a hadron track with angle θ relative to the beam axis. A fortran function C\$MUO:CMWINT is available to calculate Λ_0 using these parameters.

since $\sigma_{\pi+p} \simeq \sigma_{\pi-n}$ and $\sigma_{\pi-p} \simeq \sigma_{\pi+n}$ (see data booklet curves). However, kaons require a separate curve for K^+ ($u\bar{s}$) and for K^- ($\bar{u}s$), since the anti-up quark can annihilate with up quarks in the nucleon N so that $\sigma_{K-N} > \sigma_{K+N}$. Now since neutrons have fewer up quarks it is also true that $\sigma_{K-p} > \sigma_{K-n}$ and hence for a composite target we should use some sort of average of the K^+N or the K^-N cross sections. Unfortunately, those measurements are unavailable in our energy domain so we content ourselves with using the shapes of the σ_{K+p} and σ_{K-p} curves, and scale them to match the high energy values from the previous section. This compromise contributes to our final systematic error.

Figure 10 (dashed lines) shows the extrapolations of the high energy values of the number of absorption lengths for particles at normal incidence on a wedge down to 2.5 GeV. The curves from the particle data book (figures 1 and 2) are scaled to match the values in table 4 at 60 GeV/c. The curves in figure 10 are six parameter polynomial fits in $\log(E)$. That is,

$$\Lambda(E) = \sum_{n=0,5} P_n (\log E)^n \quad (7)$$

where the values of the parameters P_i are listed in table 5. ⁴

A correction can be applied to the curves in figure 10. Since a minimum ionizing particle traversing a wedge loses about 1.3 GeV, ⁵ the inelastic cross section will vary as E changes. That is, one can calculate

$$\Lambda_{effective} = \frac{\int \Lambda(E) dE}{\int dE}. \quad (8)$$

This correction is included in figures 10, 11, and 12. The effect in figure 11 is as much as 20% for 4.5 GeV π^- 's.

The fortran function C\$MUO:CMWINT in the development area of the CDF offline analysis package uses the polynomial fits and applies the $\frac{dE}{dx}$ correction to provide the user with Λ , given the particle species and energy.

⁴Thanks to John Filaseta and Jim Wiss of E687 for providing the fitting routine.

⁵1.3 GeV is an average over the η range of the muon chambers. The most probable value varies from 1.2 GeV in tower 0 to 1.6 GeV in tower 6.

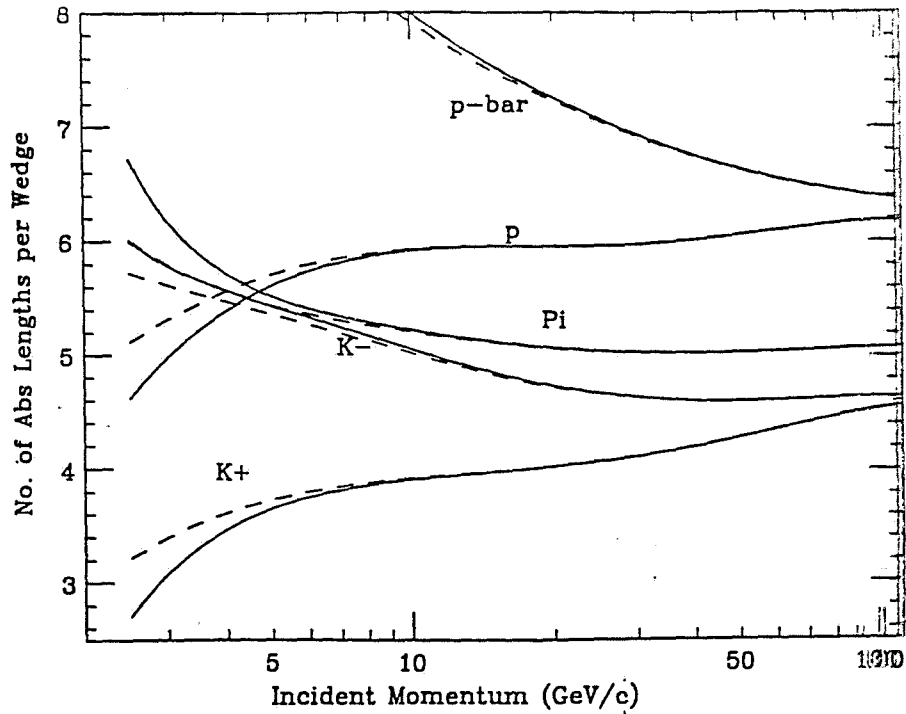


Figure 10: Number of absorption lengths at normal incidence on a central wedge for kaons, pions, protons, and antiprotons. The shape of the curve comes from the fit to the Particle Data Group cross section curves, and the absolute values are scaled to match the values in table 4 at 60 GeV/c. Solid curves are corrected for $\frac{dE}{dx}$ losses, dashed curves are uncorrected. Error bars on the curves are about 3%.

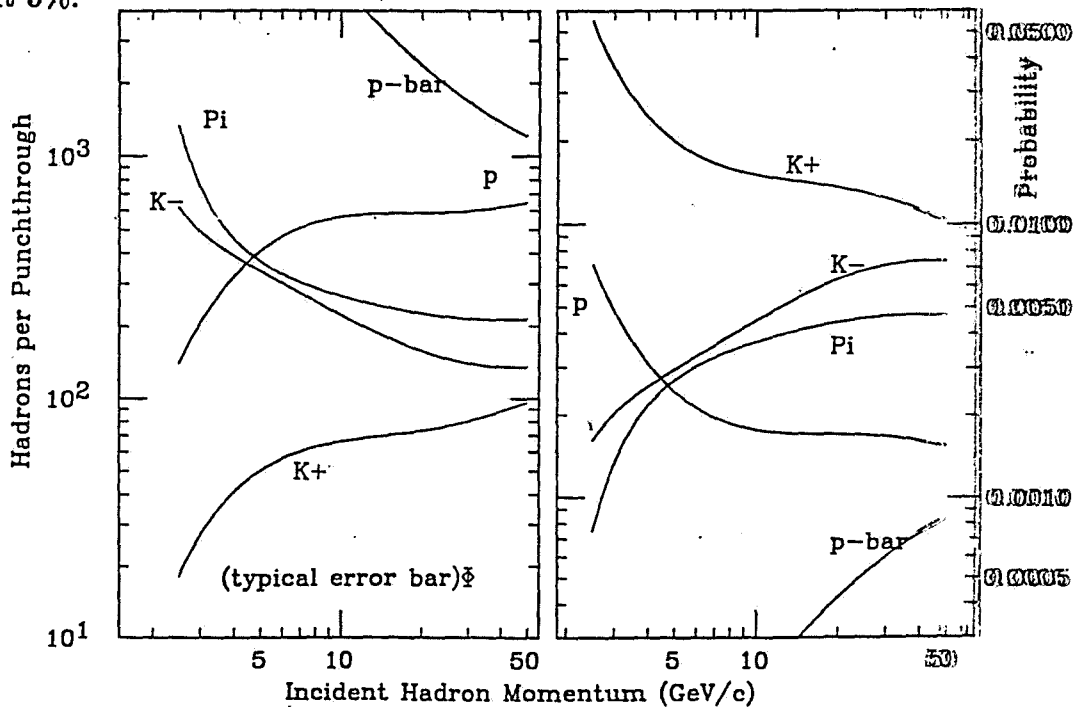


Figure 11: Non-interacting punch-through probability (right-hand plot) and inverse probability (left-hand plot) for hadrons incident on a central wedge, averaged over the η coverage of the central muon chambers. Included in the curves is the change in $\Lambda(E)$ due to the $\frac{dE}{dx}$ losses by the hadron.

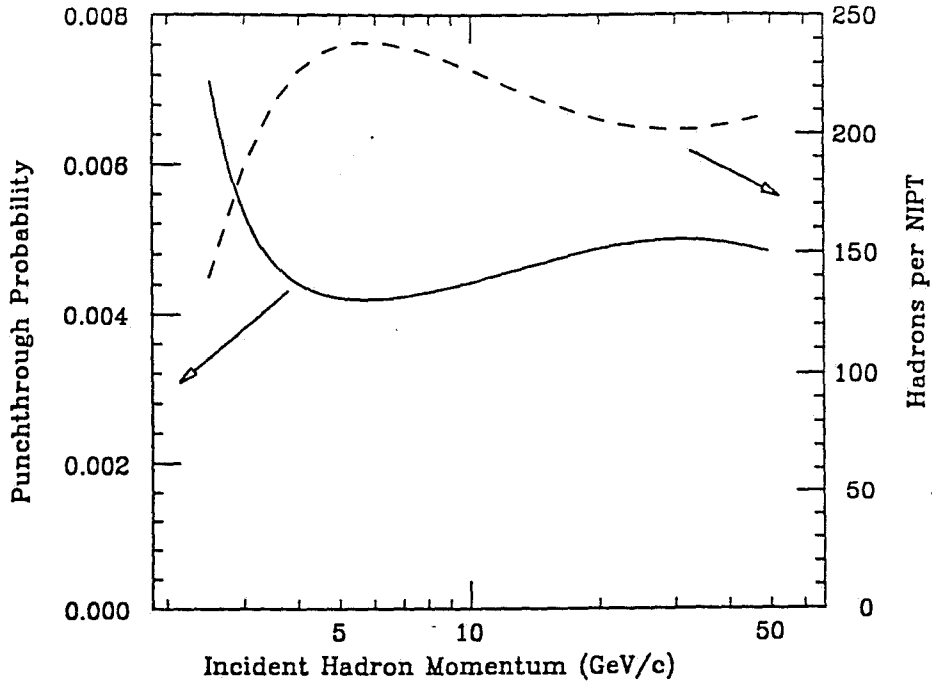


Figure 12: Using the UA5 mix of 58% pions, 21% kaons, and 20% protons and antiprotons, the curves from figure 5 are averaged to give an overall non-interacting punchthrough probability, as a function of energy (solid curve) [10]. For convenience, the inverse probability (dashed curve) is also shown.

Since the η distribution of mesons from ‘generic’ events is flat in the region covered by the central muon chambers, it is convenient to calculate the average value of Λ for that region,

$$\Lambda_{avg} = \frac{\int \Lambda(\eta) d\eta}{\int d\eta}. \quad (9)$$

Here, $\Lambda(\eta)$ comes from $\Lambda(\theta) = \Lambda_0/\sin \theta$, where θ is the track angle relative to the beam axis, and $\eta = \cot(\log \frac{E}{2})$ is the pseudorapidity. Figure 11 shows $e^{\Lambda_{avg}}$ and $e^{-\Lambda_{avg}}$ as a function of momentum. It shows that 1 out of 25 positive 3 GeV K^+ 's will not even notice the calorimeter as they sail through, as compared to 1 in 700 for π 's.

6 Muon Background Charge Asymmetry

There are two backgrounds to the inclusive direct muon spectrum in the central region (CMU): Pion and kaon decay, and non-interactive hadron punchthrough. There is no difference between the signature in the detector for direct muons at a given p_t and non-interactive charged hadrons of the same p_t . Decays, on the other hand, can sometimes be rejected because the decay muons have, on the average, lower momentum than the parent hadrons. The reconstructed p_t in the CTC is therefore on the average lower for the decay muons, the decay muons will suffer more multiple scattering in the calorimeter (leading to a less accurate track matching), and some of them will range out before reaching the muon chambers. This effectively reduces the decay background (due to the steeply falling p_t spectrum). Some kaon decays can also be rejected due to observable

kinks in the CTC. Kinks that effectively straighten the CTC tracks without being rejected, can, on the other hand, significantly increase the decay background (again due to the steeply falling p_t spectrum). We will assume in the following that this effect is not dominant.

Let us define the background charge ratio $R(p_t)$ as the ratio of positives to negatives at a given p_t :

$$R_{backgr}(p_t) = \frac{\text{Positives}(p_t)}{\text{Negatives}(p_t)} = \frac{1 + \frac{N_K P_{K^+ + \epsilon_K D_K}}{N_\pi P_\pi + \epsilon_\pi D_\pi} + \frac{N_p P_p}{N_\pi P_\pi + \epsilon_\pi D_\pi}}{1 + \frac{N_K P_{K^- + \epsilon_K D_K}}{N_\pi P_\pi + \epsilon_\pi D_\pi} + \frac{N_{\bar{p}} P_{\bar{p}}}{N_\pi P_\pi + \epsilon_\pi D_\pi}} \quad (10)$$

where P_π , P_{K^+} , P_{K^-} , P_p , and $P_{\bar{p}}$ are the pion (charge independent), kaon (charge dependent), proton and antiproton non-interactive punchthrough probabilities, $\epsilon_\pi D_\pi$ and $\epsilon_K D_K$ the (charge independent) decay probabilities to $\mu\nu$ multiplied by the probabilities for non-rejection, and N_π , N_K , $N_p = N_{\bar{p}}$ the (charge independent) numbers of particles at the given p_t .

The charge ratio for punchthrough alone (i.e. ignoring decays) represents an upper limit for the (punchthrough + decay) charge ratio. A lower limit for the charge ratio can be obtained by overestimating the number of retained decay events, for instance by completely ignoring the fact that some decay events can be rejected. This allows us to write

$$\frac{1 + \frac{N_K P_{K^+ + D_K}}{N_\pi P_\pi + D_\pi} + \frac{N_p P_p}{N_\pi P_\pi + D_\pi}}{1 + \frac{N_K P_{K^- + D_K}}{N_\pi P_\pi + D_\pi} + \frac{N_{\bar{p}} P_{\bar{p}}}{N_\pi P_\pi + D_\pi}} < R_{backgr}(p_t) < \frac{1 + \frac{N_K P_{K^+}}{N_\pi P_\pi} + \frac{N_p P_p}{N_\pi P_\pi}}{1 + \frac{N_K P_{K^-}}{N_\pi P_\pi} + \frac{N_{\bar{p}} P_{\bar{p}}}{N_\pi P_\pi}} \quad (11)$$

where again the limits correspond to $\epsilon = 1$ and $\epsilon = 0$, respectively. These limits are illustrated in figures 13 a and b for two different assumptions about the particle ratios (representing reasonable limits on the heavy particle fractions):

- a) $N_K/N_\pi = N_{(p+\bar{p})}/N_\pi = 0.10$ independent of p_t
- b) $N_K/N_\pi = N_{(p+\bar{p})}/N_\pi = 0.36$ independent of p_t (the UA5 mix).

The decay probabilities times branching ratios have been calculated using a radius of 215 cm (the interface between the EM and hadron calorimeters), pion and kaon masses of 0.13957 and 0.49367 GeV/c² and $c\tau$ for pions and kaons of 780.4 and 370.9 cm:

$$D_\pi = 1 - e^{-0.03845/p_t} \text{ for pions}$$

$$D_K = 0.635(1 - e^{-0.2862/p_t}) \text{ for kaons}$$

where 0.635 is the branching ratio for $K \rightarrow \mu\nu$.

A significant deviation from 1.0 is observed in all cases at low p_t . The inclusive CMU charge ratio for B0 data should therefore provide a useful handle on the punchthrough background (we expect a charge ratio of 1.0 both for the direct muon signal and for the decay background). Once observed, this charge ratio deserves a more careful calculation.

What about dimuons? Whereas it is generally believed that the inclusive (single) CMU rate at low p_t is dominated by background (so that the charge asymmetry calculated above should be observable), the dimuon rate may be dominated by signal (for which the $\pm\pm$ ratio is 1.0). The $\pm\pm$ ratio for the background should instead be the square of R calculated above. The $\pm\pm$ ratio in B0 data, compared to the \pm ratio for single muon candidates, should therefore be a good indicator of background in the dimuon sample.

Punchthrough Charge Asymmetry

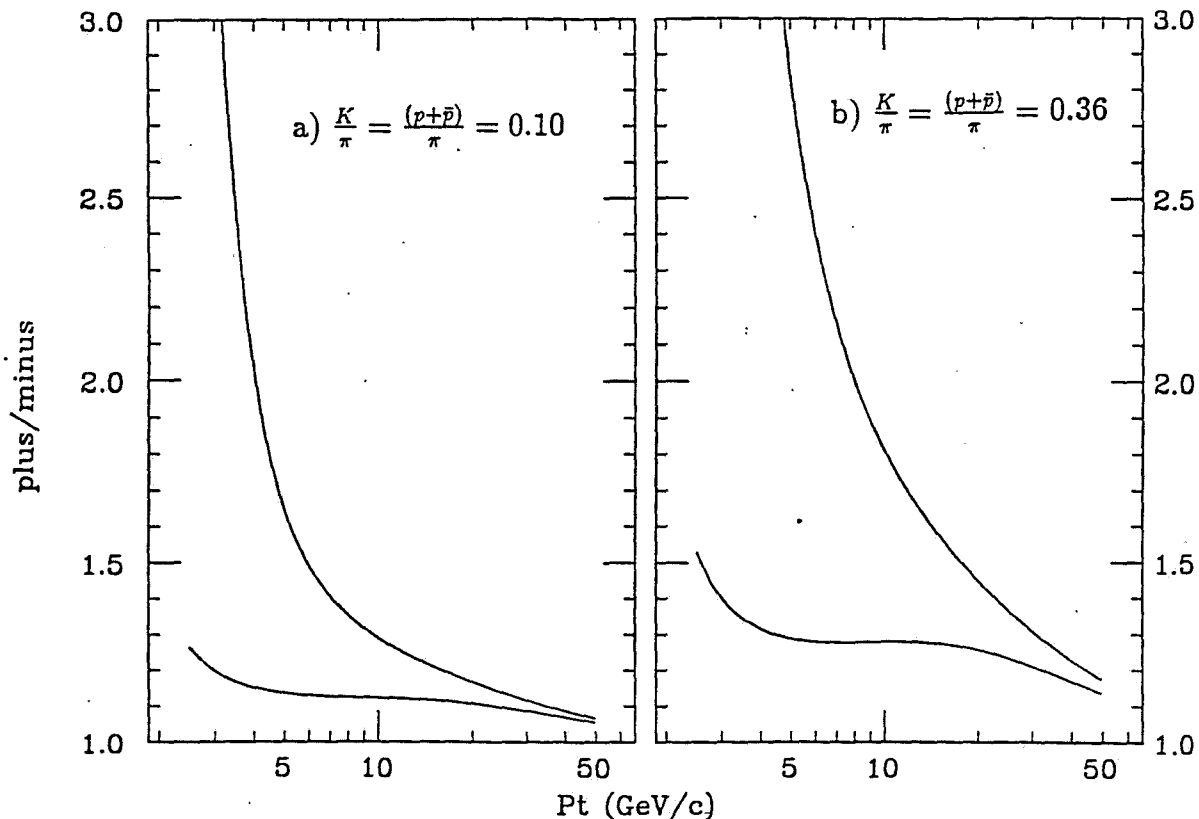


Figure 13: Ratio of the number of positive-charge tracks to the number of negative-charge tracks observed in the central muon chambers, as a function of transverse momentum (relative to the beam axis). The upper curves are calculated assuming no contribution from decay-in-flight, while the lower curves come from the assumption that all secondary muons would pass the muon identification cuts. a) Lower bound on the heavy particle mix, $\frac{K}{\pi} = \frac{(p+\bar{p})}{\pi} = 0.10$, b) upper bound on the particle mix, $\frac{K}{\pi} = \frac{(p+\bar{p})}{\pi} = 0.36$.

7 Conclusion

The rate for non-interacting hadron punch-through's in the central muon chambers is sensitive to both the energy dependence of the inelastic cross section and the derivative of the dependence. Protons turn out to make a non-negligible contribution to the rate, and the varying amounts of material traversed by particles with different pseudorapidity η also changes the rate. Hence the calculation is fairly complex and there are a number of systematic uncertainties that can fudge the final answer.

Even so, we have presented a method for calculating the rates and the error on the rate, and first indications are that agreement with the data is reasonable. One consequence of our results is that we expect to see a charge asymmetry amongst the tracks reaching the central muon chambers. This excess of positively charged tracks arises from the small absorption cross section for K^+ 's.

References

1. Carroll et al, "Absorption Cross Sections of π^\pm , K^\pm , p , and \bar{p} on Nuclei Between 60 and 280 GeV/c", *Phys Lett* **80B** (1979) 319.
2. Roberts et al, "Neutron-Nucleus Inelastic Cross Sections from 160 to 375 GeV/c", *Nucl Phys* **B159** (1979) 56.
3. Denisov et al, "Absorption Cross Sections for Pions, Kaons, Protons, and Antiprotons on Complex Nuclei in the 6 to 60 GeV/c Momentum Range", *Nucl Phys* **B61** (1973) 62.
4. Bellettini et al, "Proton-Nuclei Cross Sections at 20 GeV", *Nucl Phys* **79** (1966) 609.
5. John Yoh, "A Study of the Effects of Leakage in the CDF Calorimetry Using E616 (CITF) Hadron Test Data", CDF-110 (1981). (Thanks to John Yoh for providing data beyond that presented in the paper.)
6. CDHS Internal Report, "Measurement of Hadronic and Electromagnetic Shower Development Between 10 GeV and 140 GeV by an Iron-Scintillator Calorimeter", Emlyn Hughes. (Thanks to Adam Para for clarifying the contents of this paper.)
7. Balka et al, "The CDF Central Electromagnetic Calorimeter", *Nucl Instr and Meth* **A267** (1988) 272.
8. Ascoli et al, "The CDF Central Muon Detector", *Nucl Instr and Meth* **A268** (1988) 33.
9. "Kaon Production in $p\bar{p}$ Collisions at a Centre-of-Mass Energy of 540 GeV", G.J. Alner et al (UA5 collaboration) *Nucl Phys* **B258** (1985) 505.

April 19, 1990

Dr. John Peoples, Director
Fermilab

Dear John,

Here is the current draft of the CDF upgrade proposal. As you requested, we are forwarding it to you now for use in Fermilab long term planning. You will see that for some of the upgrades, most notably the forward calorimeters, we have not yet made a final choice of technology. In order to make that decision, we need the results of studies which will take place in the test beam this spring and early summer. We expect to produce the final version of the proposal by the fall and then present it to the PAC at its October meeting.

We are also enclosing a copy of the CDF reprints for the year ending January, 1990.

Regards,



Mel Shochet

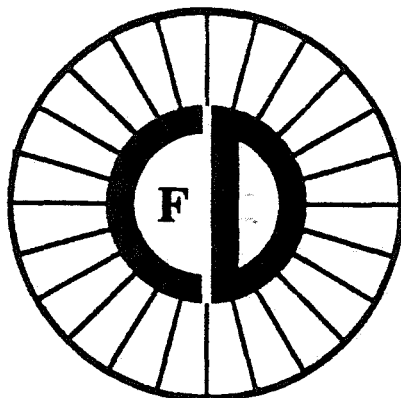


Alvin Tollestrup

for the CDF Collaboration

enclosure

cc: Ken Stanfield
Peter Garbincius
Hugh Montgomery
Physics Advisory Committee



Proposal For an Upgraded CDF Detector

The CDF Collaboration

Draft: April 19, 1990, Preliminary Version

Abstract

A major upgrade is proposed for the CDF detector in order to exploit fully the physics opportunities of high luminosity running at the Fermilab Collider.

Contents

1	Introduction	7
2	Physics Accomplishments	15
2.1	The 1987 Run	15
2.2	The 1988-89 Run	21
3	Planned Physics Program	27
3.1	Electro-Weak Physics	27
3.2	Heavy Quark Physics	39
3.3	QCD Physics	47
3.4	B Physics	55
3.5	Exotic Physics	61
3.6	Rare Processes	63
4	Hardware Upgrades	66
4.1	Tevatron Upgrade	70
4.2	Plug and Forward Calorimeters	72
4.2.1	Plug Scintillation Calorimeter	72
4.2.2	Gas Calorimeters	84
4.3	Central Drift Chamber	87
4.4	Vertex Time Projection Chambers	88
4.5	Silicon Vertex Detectors	90
4.6	Muon Systems	93
4.7	Data Acquisition Electronics	102
4.8	Level 3 Trigger: Online Analysis and Event Filtering	113
4.9	Online Computing: RUN_CONTROL	119
4.10	Offline Computing	121
4.11	Miscellaneous Systems	124
5	Cost Projections	125
5.1	Budget: Plug Calorimeter	125
5.2	Budget: Silicon Vertex Detector	129
5.3	Budget: Muon Detectors	130
5.4	Budget: Data Acquisition System	131
5.5	Budget: Online Computing	135
5.6	Budget: Miscellaneous	136

5.7	Budget Summary	137
5.8	Funding Profile	138
5.9	Budget: Offline Computing and Data Storage	139
6	Participating Institutions and Physicists	141

List of Figures

1-1	Schematic of Proposed CDF Detector Evolution	11
1-2	Evolution of $\eta - \phi$ coverage for electrons	12
1-3	Evolution of $\eta - \phi$ coverage for muons	13
1-4	Evolution of Tracking Coverage for Triggers vs. θ	14
2-1	Inclusive Charged Particle Cross Section vs. P_T	17
2-2	$dN_{ch}/d\eta$ at $\eta = 0$	17
2-3	Inclusive Jet Cross Section	18
2-4	Inclusive K_s^0 Cross Section	18
2-5	D^* Production in Jets	19
2-6	Jet-Broadening Parameter, Q_T	19
2-7	Two Jet Differential Cross Sections	20
2-8	Jet Fragmentation	20
2-9	$Z^0 \rightarrow e^+e^-$ Invariant Mass Plot for Calorimeter Data	23
2-10	$Z \rightarrow \mu^+\mu^-$ Invariant Mass Plot for Tracking Data	23
2-11	$W^\pm \rightarrow \mu^\pm\nu$ Transverse Mass Plot	24
2-12	$W^\pm \rightarrow e^\pm\nu$ Transverse Mass Plot	24
2-13	Transverse Mass Plots for the $e^\pm + \text{jets}$ Top Quark Search	25
2-14	$P_t(\mu)$ vs. $E_t(e)$ for the $e^\pm\mu^\pm$ Top Quark Search	25
2-15	Transverse Momentum Distributions for the Gauge Bosons	26
2-16	Transverse Momentum Distribution for Jets	26
3-1	Constraints on M_{top} by M_W	29
3-2	Forward-Backward Asymmetry in $Z \rightarrow e^+e^-$	32
3-3	Predicted M_{top} Dependence of $\sin^2\theta_W^{afb}$	33
3-4	Charge Asymmetry in $W \rightarrow \ell\nu_\ell$	34
3-5	Total Cross Section for High-Mass Z' Production	35
3-6	Limits on Quark-Lepton Compositeness from Drell-Yan Cross Section	37
3-7	Top Quark Production at 1.8 TeV vs. Top Mass	39
3-8	Expected number of $t\bar{t} \rightarrow e\mu$ events	40
3-9	Expected number of events from $t\bar{t} \rightarrow e^+e^-$ and $t\bar{t} \rightarrow \mu^+\mu^-$	41
3-10	Expected number of events for $t\bar{t} \rightarrow \text{lepton} + \text{jets}$	43
3-11	CDF Efficiency for Detecting $t\bar{t}$ With b Tagging	44
3-12	The branching ratio for $t \rightarrow W + b$ for charged Higgs Models	46
3-13	Inclusive Jet Cross Section	48
3-14	Jet Cross Section vs. Clustering Cone Radius	49
3-15	Comparison of Jet Cross Section with Leading Order QCD	49

3-16 High Energy End of Inclusive Jet Cross Section	50
3-17 Dijet Invariant Mass Spectrum from CDF	51
3-18 Cross Section for High-Mass Dijet Resonances	51
3-19 Highest E_T Direct Photon Candidate	52
3-20 Direct Photon Cross Section	53
3-21 Integral Cross Section for Direct Photons	53
3-22 P_T Distribution for W Compared to Theory	54
3-23 P_T Distribution for Z Compared to Theory	54
3-24 Invariant Mass Spectrum $K^-\pi^+$ ($K^+\pi^-$)	56
3-25 Invariant mass spectrum for $e^-K^-\pi^+$ ($e^+K^+\pi^-$)	56
3-26 B^0 Mixing Distributions vs. B Momentum	59
3-27 B^0 Mixing Distributions vs. Lepton Momentum	60
4-1 A cutaway view of the CDF detector for 1993	69
4-2 Side View of Existing CDF Detector	73
4-3 Side View of Upgraded CDF Detector	74
4-4 Plug Segmentation in $\eta - \phi$	76
4-5 Scintillating Tile With Waveshifting Optical Fiber	80
4-6 Drawing of SVX detector.	90
4-7 Expected SVX Impact Parameter Resolution.	91
4-8 Muon Toroid Resolution vs. Polar Angle	94
4-9 Muon Toroid Structure: Radial-Axial Diagram	96
4-10 Muon Toroid Resolution vs. Momentum	100
4-11 DAQ System Overview Block Diagram	104
4-12 Diagram of Calorimeter Front-End Electronics	107
4-13 Block Diagram of DAQ Connections to Level-3 (1989)	115
4-14 Block Diagram of DAQ Connections to Level-3 (1991)	116
4-15 Diagram of a Level-3 Silicon Graphics Box (1991)	117
4-16 Block Diagram of DAQ Connections to Level-3 (1993)	118

List of Tables

3-1	Projected Uncertainties in the $W \rightarrow e \nu$ Mass Measurement	28
3-2	Projected Uncertainties in the $W \rightarrow \mu \nu$ Mass Measurement	28
3-3	Projected Uncertainties in the R_e Measurement	30
3-4	Projected Uncertainties in the R_μ Measurement	31
3-5	Projected Uncertainties in the $\text{Sin}^2\theta_W^{AFB} Z^0 \rightarrow e^+e^-$ Measurement	32
3-6	Projected Uncertainties in the $\text{Sin}^2\theta_W^{AFB} Z^0 \rightarrow \mu^+\mu^-$ Measurement	33
3-7	Z' Total and Partial Cross Sections	36
3-8	Gauge Boson Pair Total Cross Sections	38
4-9	CDF Detector Systems Channel Count	68
4-10	Tevatron Bunch Spacing Parameters	70
4-11	Overview of Proposed Calorimeter Upgrade	76
4-12	Features and Benefits of Proposed Calorimeter Upgrade.	84
4-13	CDF Muon System Coverage	93
4-14	Dimuon triggers: $t\bar{t} \rightarrow \mu^+\mu^- + X$	95
4-15	Muon Toroids: Bend Angles and Sagittas	99
4-16	Muon Toroids: Trigger Rates	99
4-17	Level-3 Parameters	113
5-18	Tile Scintillator Plug Budget	126
5-19	Plug Pre-Radiator Costs	127
5-20	Plug Position detector Costs	128
5-21	Silicon Vertex Detector Costs	129
5-22	Forward Muon Budget	130
5-23	Data Acquisition Electronics Budget	132
5-24	Level 1,2 Budget	133
5-25	Level 3 Budget	134
5-26	Online Computing Budget	135
5-27	Budget for Miscellaneous Items	136
5-28	CDF Upgrade Budget Summary	137
5-29	CDF Upgrade Budget Profile	138
5-30	Offline Computing Budget for the 1991 Run	139
5-31	Offline Computing Budget for the 1993 Run	140
5-32	CDF Offline Computing Budget Profile	140

1 Introduction

The Collider Detector at Fermilab (CDF) has been used to exploit the unique physics opportunities of the Fermilab Tevatron I project, where counter-rotating beams of protons and antiprotons collide at 1.8 TeV in the center-of-mass. Until the next millenium, this will likely remain the highest energy for particle physics experiments at an accelerator.

Fermilab has an ambitious program of improvements to the Tevatron which will upgrade its performance and extend its physics reach during the coming years. In order for CDF to exploit the opportunities provided by accelerator improvements, a number of its systems must be substantially upgraded - detectors, electronics, data acquisition (DAQ) and analysis facilities. This document presents the motivation for such an upgrade, its scope for each subsystem, and the resources needed to accomplish it.

CDF, a powerful, general purpose detector system, has been operated during three periods of collider operation. In October, 1985, a brief test at very low luminosity yielded the first detected collisions at the Tevatron. During 1987, an engineering run produced $\sim 25nb^{-1}$ of integrated luminosity and a variety of physics results. During a year-long run starting in June, 1988, the Tevatron surpassed its design luminosity, reaching $\sim 2 \times 10^{30}/\text{cm}^2\text{-sec}$, and CDF wrote $\sim 4500 nb^{-1}$ of data to magnetic tape. At this writing, early results of the analysis of these data are being presented at conferences and published in journals. These are discussed in Section 2.

The projected improvements in the luminosity of the Tevatron collider, $\mathcal{L} \sim 5 \times 10^{30}/\text{cm}^2\text{-sec}$ or higher in 1991 and $\mathcal{L} \sim 5 \times 10^{31}/\text{cm}^2\text{-sec}$ or higher by 1995, offer CDF considerably extended physics reach. A definitive search for the top quark will be possible. Either it will be found and its properties studied, or far-reaching revisions in the standard model will be necessary. Further improvements in our measurements of the mass, width and decays of the W^\pm will also provide stringent tests of the Standard Model. All four electro-weak bosons, W^\pm , Z^0 and γ can be used to probe the short-range behavior of partons. Limits will be extended on parton compositeness and the existence of supersymmetric and other exotic particles. Section 3 describes the physics goals for future CDF operation in more detail.

In order to confront the combined challenges of the upgraded Tevatron and the physics opportunities it offers, CDF must undergo a staged improvement program.

At present, in the configuration used for the 1988-89 run, the detector consists of electromagnetic and hadronic calorimeters covering nearly 4π solid angle around the interaction region in a tower geometry. A large, superconducting solenoidal magnet containing drift chambers measures the momentum of charged particles and gives visual reconstruction of the event. Muon chambers around the perimeter of the central detector and iron-toroidal magnets at each end identify muons. Details of the detector design, construction and performance can be found in the original design report¹ and in published papers.²⁻²⁶

Upgrades in progress for the 1991 run are described in Ref. 27. Some are required for CDF to function at $\mathcal{L} \sim 5 \times 10^{30}/\text{cm}^2\text{-sec}$ and others will improve its physics capabilities by extending the kinematic region covered, by increasing the detector's resolving power and

background rejection and by enhancing its reliability. The modifications include extensive front end electronics changes, replacement of the Vertex Time Projection Chamber, and implementation of the Silicon Vertex Detector which was part of the original CDF design. The central muon upgrade (CMUP) will improve rejection of hadron punch-through in the region already covered ($0 \leq |\eta| \leq 0.7$), and the muon coverage will be extended (CMEX) to cover the region $0.7 \leq |\eta| \leq 1.1$. The cause of breakdown problems at the edges of the plug gas calorimeters has been identified and they are being repaired. This will improve coverage for electrons in the region $1.1 \leq |\eta| \leq 1.3$. Pre-radiators will be added to the central electromagnetic calorimeters to improve identification of γ 's and π^0 's. The Central Tracking Chamber will be operated at lower gain to extend its lifetime and some changes to the pre-amps may be needed. A segment processor (CPT) for track-finding in the CTC will be implemented to add to the Level 2 trigger capabilities. A higher rate of throughput will be needed in the DAQ system. This means replacing the prototype wire-wrap Event Builder used in 1988-89 with a printed-circuit version which incorporates a number of improvements based on operating experience. The Level 3 online computer farm is undergoing a major upgrade to deal with higher rates and additional tasks imposed on it. Increases in online computing power for control and monitoring are needed, as well as a substantial increase in offline analysis capacity.

This proposal is concerned principally with the 1993 run. The overview at the end of this section lists the upgrades proposed for that time scale. Some subsystem upgrades are mandated by the shorter bunch spacing (395 nsec) of the upgraded Tevatron. Others are necessary because of further improvements in luminosity up to $\mathcal{L} \sim 5 \times 10^{31}/\text{cm}^2\text{-sec}$, which is a key ingredient in extending the Tevatron Collider's physics capability. The proposed detector upgrades will undergo extensive evaluation in this year's test beam run.

Figure 1-1 shows schematically the evolution of the detector from 1989 to 1991 and proposed changes for 1993. Figures 1-2 (for electrons) and 1-3 (for muons) show the improvements in detector and trigger coverage in the form of $\eta - \phi$ plots. Figure 1-4 shows the θ coverage for various trigger levels for the three runs. Section 4 contains more detailed discussions of each of the proposed hardware upgrades. The budget and a list of participating institutions and physicists are presented in Sections 5 and 6.

Beyond the 1993 run, the Tevatron luminosity is expected to increase further, and consideration is being given to an even shorter bunch spacing - ~ 200 nsec. The 1993 upgrade plans for scintillation calorimeters, muon detectors and the digital portions of the DAQ system take this into account, and these systems should function well in 1995 and beyond. The front end electronics described below are designed for 395 nsec bunch spacing. We estimate roughly \$4M added cost to change the presently planned front end electronics capability from 395 nsec to ~ 200 nsec bunch spacing. Some present systems which require no upgrade for 1993 may run into problems thereafter. For example, the central tracking drift chamber and vertex time projection chamber may require substantial modification or replacement for runs in 1995 and beyond. This is particularly true if the ~ 200 nsec bunch space option is adopted. Additional fast signals from the detector will be made available to the Level-2 trigger to improve background rejection. As Tevatron upgrade plans become clear, CDF upgrade plans will proceed apace.

The design, construction and operation of this facility are being carried out by a consortium of physicists from the following institutions in the United States, Italy and Japan: Argonne National Laboratory; Brandeis University; University of Chicago; Fermilab; Laboratori Nazionali di Frascati; Harvard University; University of Illinois; Johns Hopkins University; KEK, Tsukuba; Lawrence Berkeley Laboratory; University of Michigan; University of Pennsylvania; University and Scuola Normale Superiore of Pisa; Osaka University; Purdue University; University of Rochester; Rockefeller University; Rutgers University; Texas A&M University; University of Tsukuba; Tufts University; University of Wisconsin. The collaboration will continue expanding.

OVERVIEW

The modifications needed for CDF to address the physics accessible with higher Tevatron luminosity are summarized below.

1. Upgrade the plug and forward calorimeters to accommodate the higher luminosity and shorter bunch spacing.
2. Move the muon toroids closer to the central detector and build new muon chambers and electronics. to increase muon coverage.
3. Upgrade the silicon vertex detector for operation at higher luminosity and shorter bunch spacing.
4. Replace pre-amplifiers in the central tracking chamber.
5. Upgrade front-end electronics, trigger and data acquisition system to allow efficient operation at 395 nsec bunch spacing.
6. Expand the bandwidth into and computing capacity of the Level 3 online event processing farm.
7. Increase offline computing capacity to ~ 2000 mips.

Schematic of Proposed CDF Detector Evolution

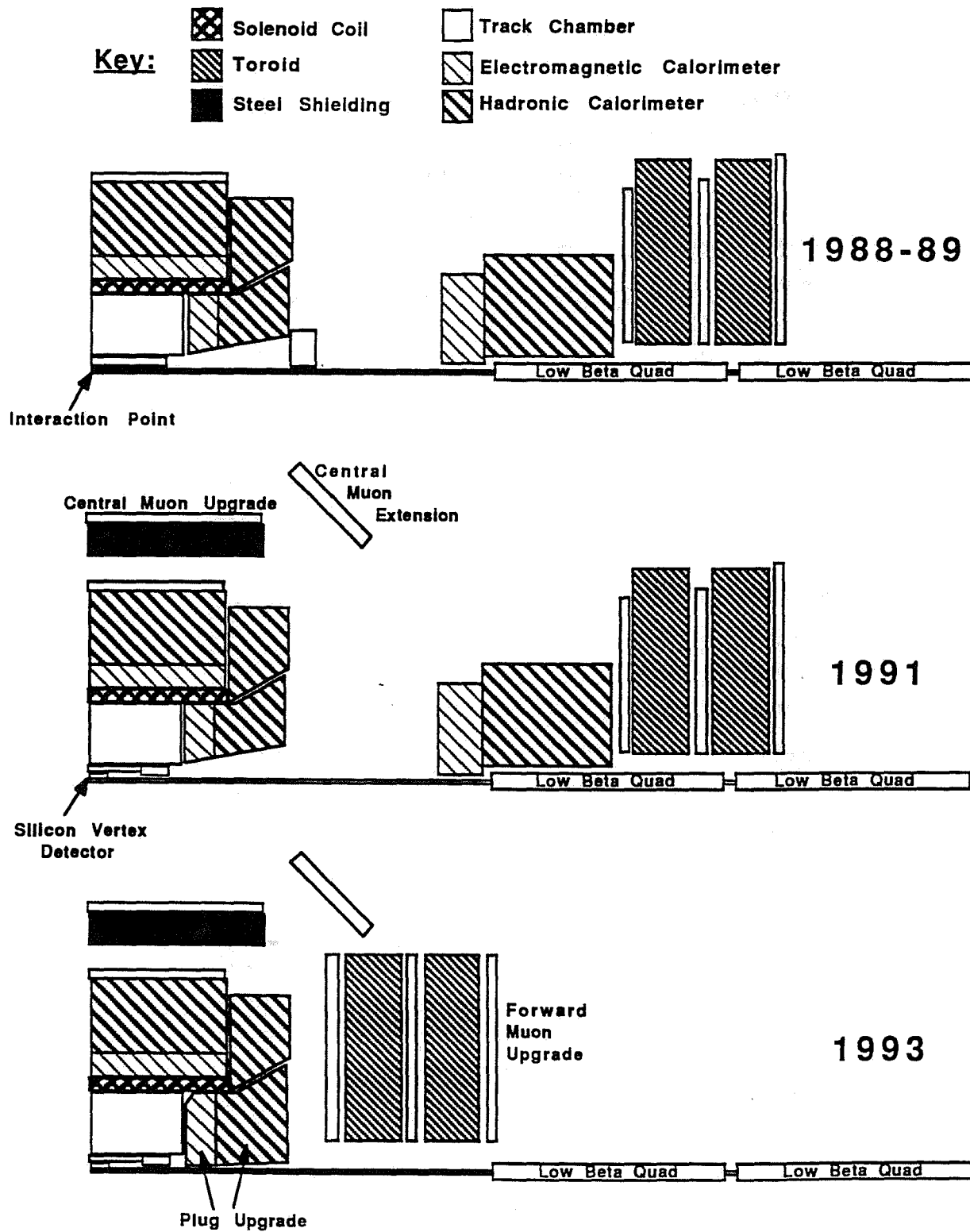






Figure 1-1: Schematic of Proposed CDF Detector Evolution

CDF Electron Coverage Upgrades

Trigger Threshold based on:

-  EM Cluster Only
-  EM Cluster, Track without p, shower max strip match
-  EM Cluster, Track Momentum, shower max strip match
-  EM Cluster, Track Momentum, shower max strip match, pre-radiator detector

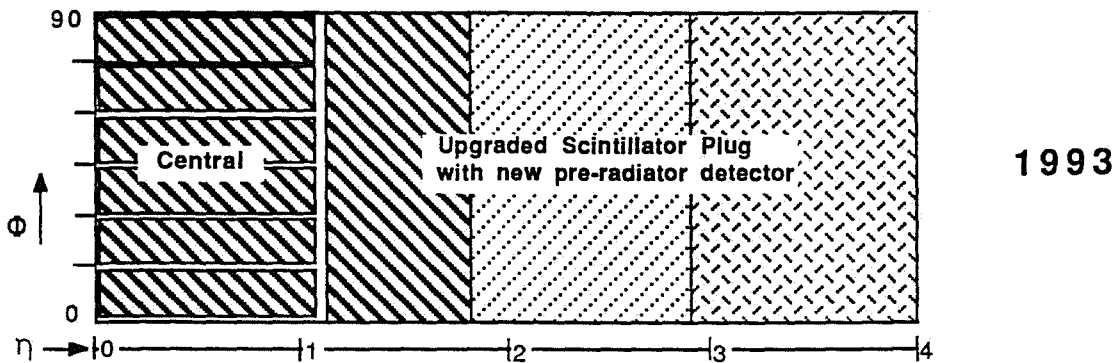
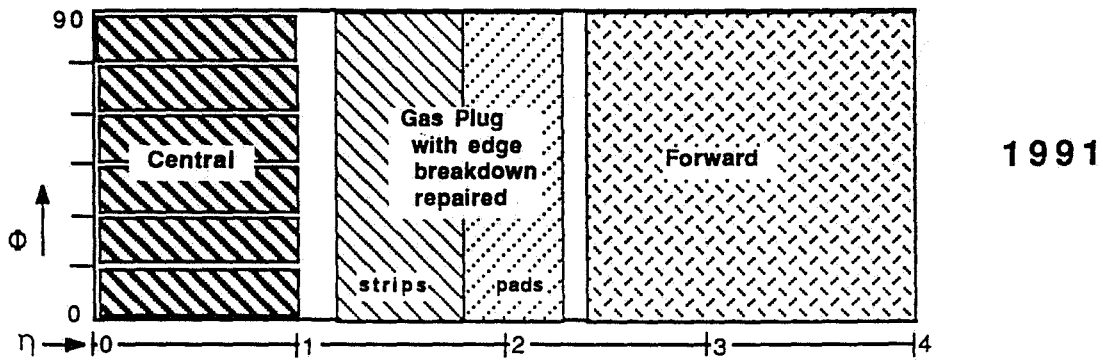
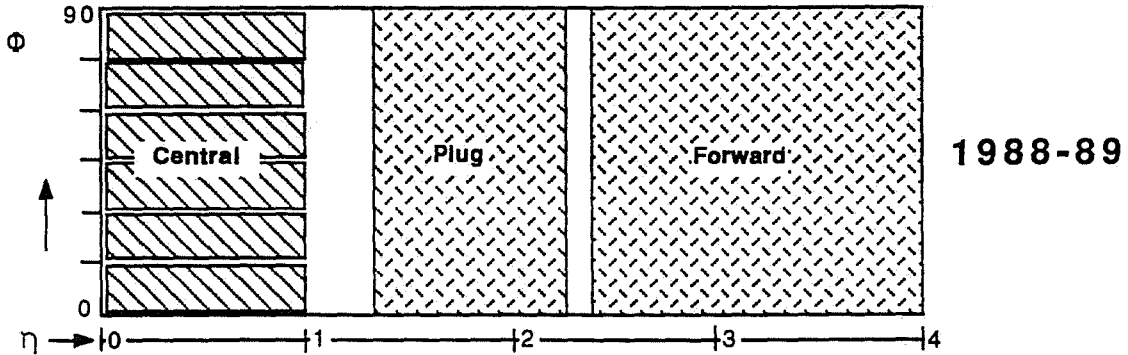






Figure 1-2: Evolution of $\eta - \phi$ coverage for electrons

CDF μ Coverage Upgrades

- Trigger Threshold based on:
-  No trigger, tag offline (or Level 3) only
 -  Muon Chambers + track momentum information
 -  Muon Chambers (+extra steel) + track momentum
 -  Muon Chambers + track momentum + Scintillator for fast trigger

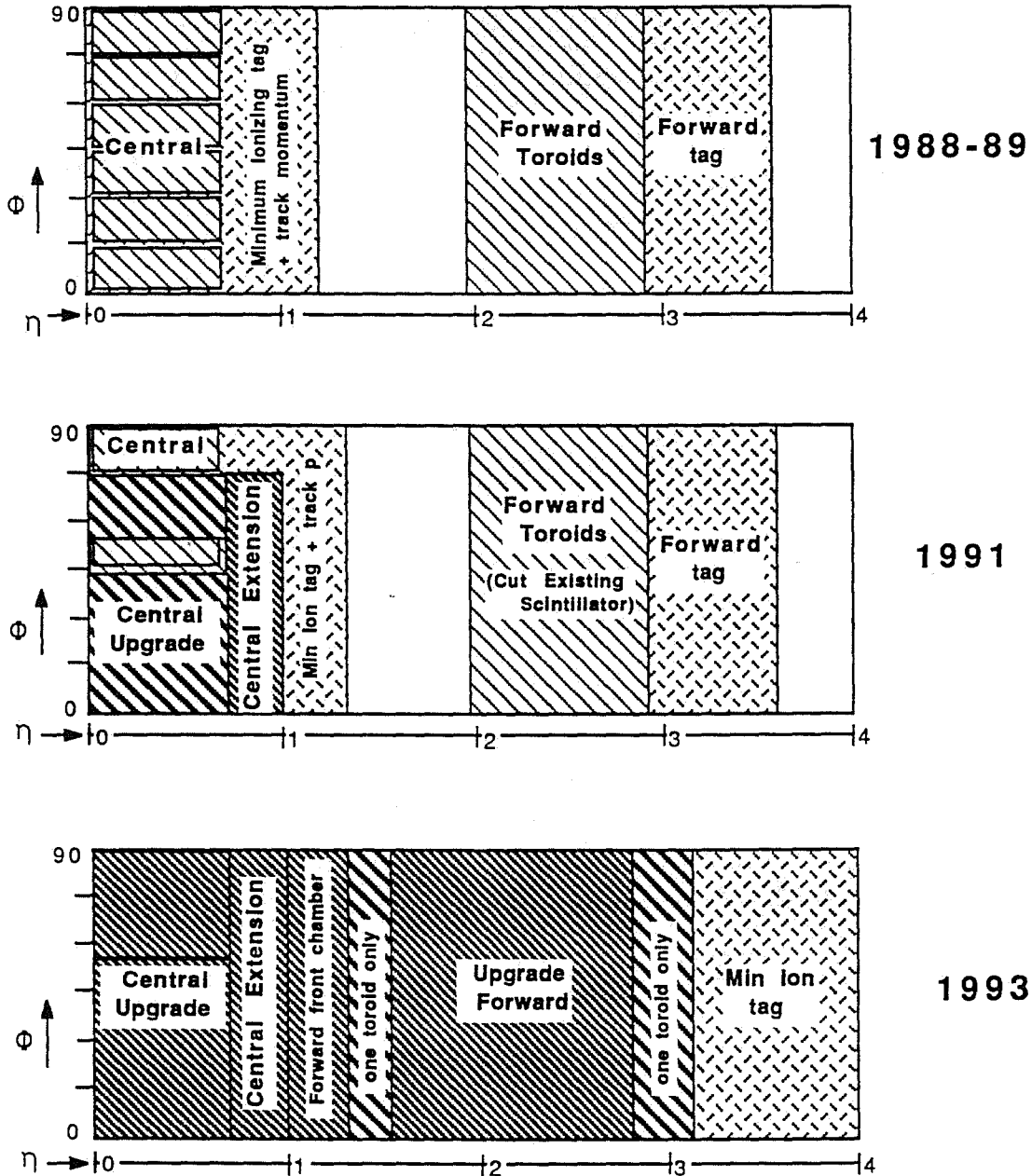







Figure 1-3: Evolution of $\eta - \phi$ coverage for muons

CDF Tracking Coverage Upgrades

-  Track with p, resolution $dP/Pt = 3\% \cdot Pt$
-  Track with p, resolution $dP/Pt = 0.7\% \cdot Pt$

Track Information:

-  Tracks associated with the primary vertex, $dP/Pt = 0.11\% \cdot Pt$
-  Tracks associated with the proper primary OR secondary vertex, and $dP/Pt = 0.11\% \cdot Pt$
-  Track associated with proper primary vertex, but no momentum information

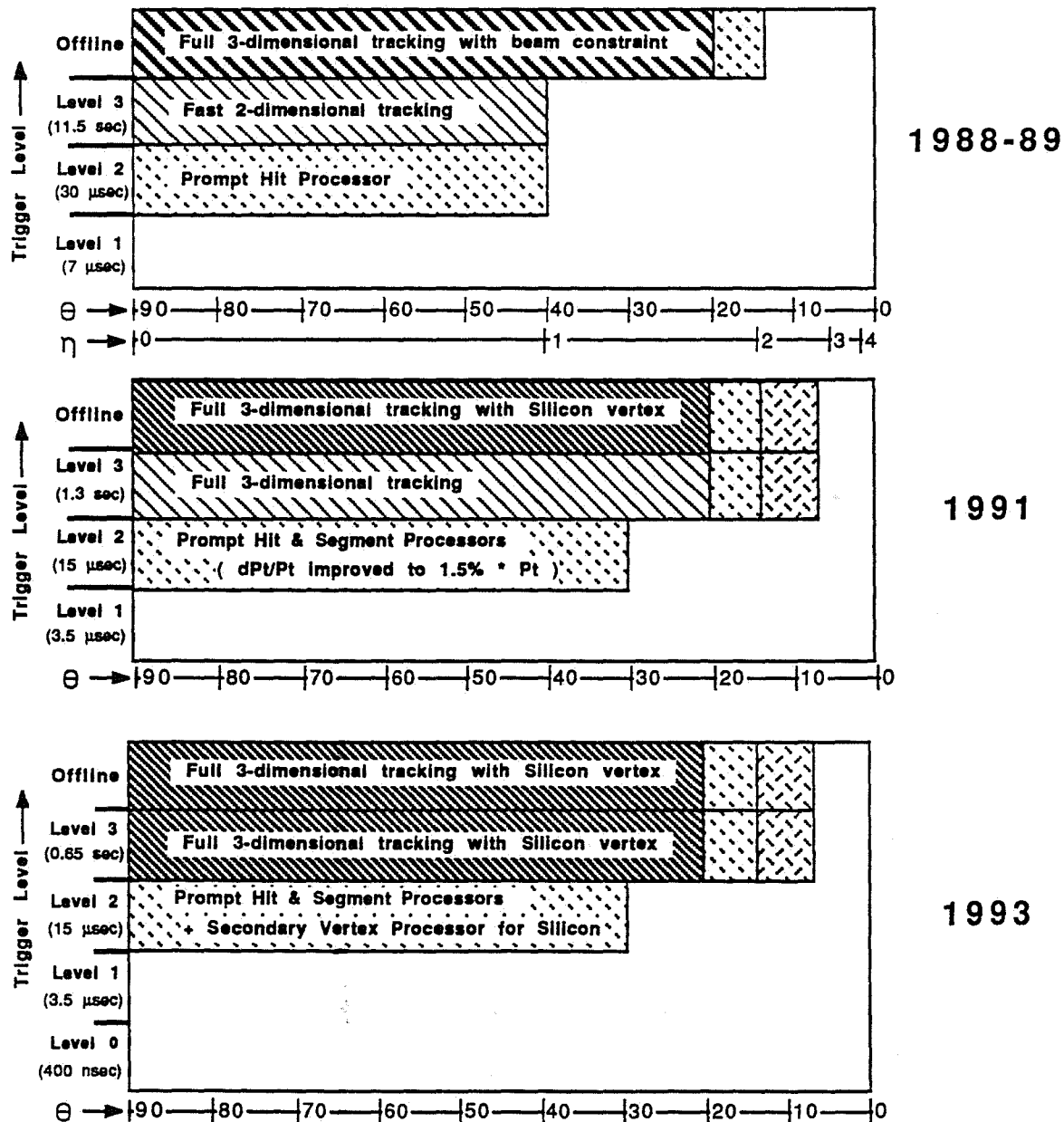


Figure 1-4: Evolution of tracking coverage for various trigger levels for various ranges of θ in the the 1988-89, 1991 and 1993 runs.

2 Physics Accomplishments

2.1 The 1987 Run

The operation of CDF during 1987 was intended as an engineering run, and it achieved its objectives of bringing into operation most of the major detection systems, the Level-1 trigger, and most of the data acquisition system. Operational procedures, calibration techniques and safety systems were refined as their strengths and weaknesses were observed under "battle conditions".

Approximately 25 nb^{-1} of integrated luminosity were accumulated and 250 tapes of data written. This data set allowed CDF to confront and solve most of the problems of analyzing these complex events: maintenance of large databases for calibrations and run conditions, development and tuning of Monte Carlo programs, and integration of data from a variety of complicated subsystems into a unified analysis.

A much more important product of the 1987 run was a rich yield of unique physics results from 1.8 TeV $p - \bar{p}$ collisions which are described in a number of Ph. D. theses and papers, both published and in preparation. These include:

1. Measurements of the transverse momentum distribution²⁸ (Fig. 2-1) of charged particles produced at $\sqrt{s} = 630$ and 1800 GeV. The average P_T increases more rapidly than $\log s$.
2. A measurement of the pseudorapidity distributions of charged particles produced at $\sqrt{s} = 630$ and 1800 GeV.²⁹ This data, combined with lower energy data, show a growth faster than $\log s$ at $\eta = 0$. (See Fig. 2-2.)
3. The inclusive jet cross section was measured. Jets were seen up to $p_T = 250 \text{ GeV}/c$, higher transverse momentum than ever before observed.³⁰ The predictions of Quantum Chromodynamics (QCD) assuming pointlike partons were consistent with the distribution (Fig. 2-3). Fits to the distribution assuming non-pointlike partons placed a lower limit of 700 GeV on the compositeness parameter. This implies that quarks and gluons are pointlike down to distances of order 3×10^{-4} fermis.
4. The production and subsequent decay for $W^\pm \rightarrow e^\pm \nu$ in 1.8 TeV $\bar{p}p$ collisions was measured to be $\sigma \cdot B = 2.6 \pm 0.6 \pm 0.5 \text{ nb}$, in good agreement with theory and extrapolation from lower energy data.³¹
5. A search for supersymmetric particles was performed. Assuming the simplest versions of SUSY models, it was established that the masses of squarks and gluinos, if they exist, must be greater than 75 GeV.³²
6. The dijet angular distribution was measured, and it confirmed the predictions of QCD. This distribution also tested the pointlike parton hypothesis and placed a lower limit on the compositeness parameter of 330 GeV.³³

7. A measurement of the transverse momentum distribution of K_s^0 mesons.³⁴ (See Fig. 2-4.)
8. A search was performed for heavy, stable charged particles.³⁵ It set cross section and mass limits in the context of specific models.
9. Identification of D^* states in jets produced at CDF.³⁶ Fig. 2-5 shows the observed signal for this state.
10. A measurement of the two-jet invariant mass spectrum.³⁷
11. Measurement of the jet-broadening parameter, Q_T , as a function of jet- E_T .³⁸ This parameter is sensitive to the ratio of 3-parton to 2-parton final states, and is free of divergences which plague other global parameters. (See Fig. 2-6.)
12. Measurement of Two Jet Differential Cross Sections $d^3\sigma(\bar{p}p \rightarrow J_1 + J_2 + X)/dE_T d\eta_1 d\eta_2$ averaged over $|\eta_1| \leq |0.6|$ is in agreement with QCD predictions.³⁹ (See Fig. 2-7.)
13. A study of jet fragmentation.⁴⁰ Figure 2-8 shows the distribution of charged particle fractional momentum, Z , within jets, summed over all jet energies. Studies of the Z -distribution as a function of di-jet invariant mass show that it becomes more steeply falling with increasing $M(j-j)$ from 60 to 200 GeV/ c^2 as expected from scale breaking in QCD.

Many of these analyses led to Ph.D. theses at the participating institutions. Among these are:

- Berkeley: Rob Harris, Brad Hubbard
- Chicago: George Redlinger, Y. Tsay, Rick Snider
- Harvard: Rick St. Denis, Dave Brown, Rob Carey
- Illinois: Dave Smith, Tom Westhusing
- Penn: Marshall Miller
- Pisa: Simone Dell'Agnello, Marco Incagli
- Purdue: Martin Schub, Aesook Byon, Steve Kuhlmann
- Rutgers: Brenna Flaughner
- Tsukuba: Yohei Morita, Maki Sekiguchi, Aki Yamashita, Masa Shibata
- Wisconsin: John Skarha

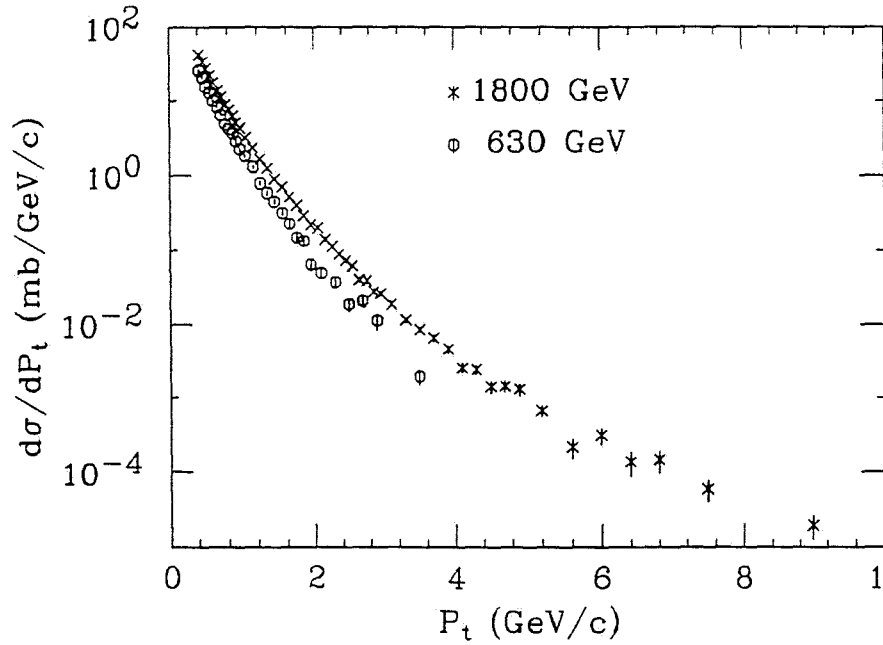


Figure 2-1: Inclusive charged particle cross section vs. P_T for rapidity $|y| < 1.0$ at $\bar{p}p$ energies of 630 and 1800 GeV.

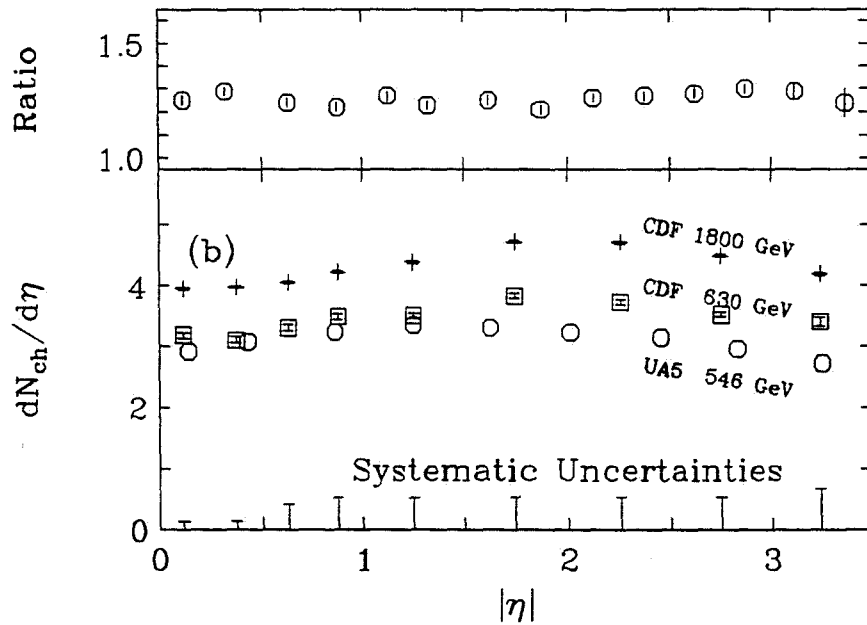


Figure 2-2: A plot of the charged-particle distribution, $dN_{ch}/d\eta$, at $\eta = 0$ measured by CDF and UA5^{41,42,43}. The upper plot shows the ratio of the distribution at 1800 GeV to that at 630 GeV.

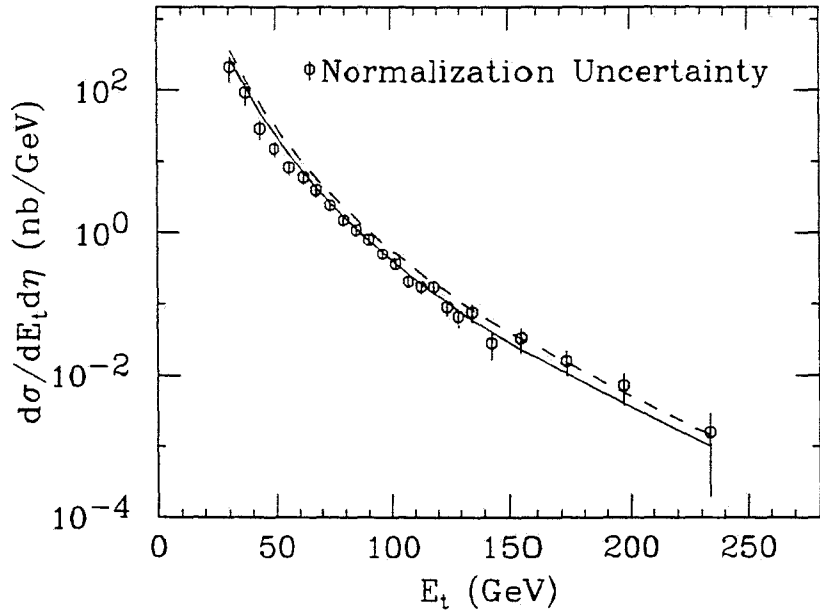


Figure 2-3: Inclusive jet cross section as a function of transverse energy, E_T at $\sqrt{s} = 1.8$ TeV compared to a range of QCD predictions described in Ref. 30. Error bars include statistical uncertainty and the E_T -dependent part of the systematic uncertainty. There is an overall normalization uncertainty of 34%.

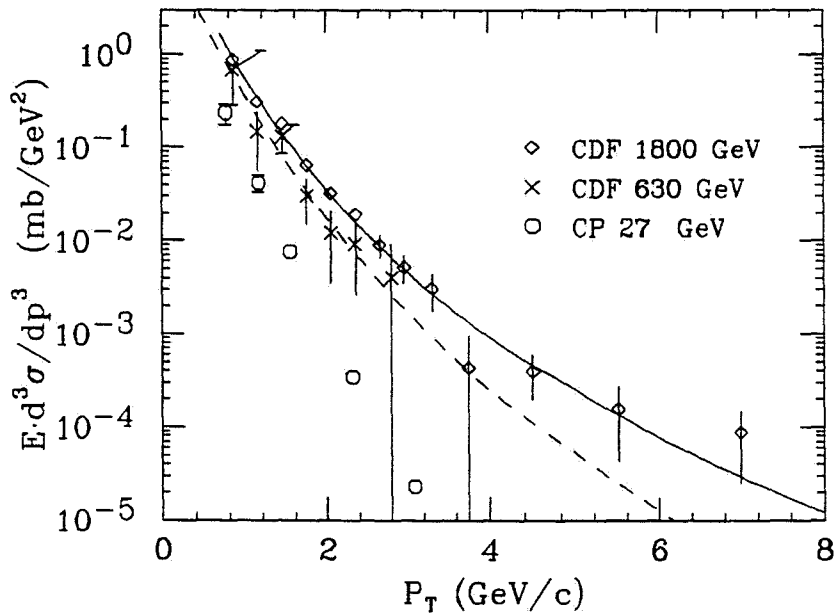


Figure 2-4: Inclusive K_s^0 Cross Section from CDF for rapidity $|y| < 1.0$ $\bar{p}p$ at $\sqrt{s} = 630$ and 1800 GeV. Also plotted are K production data from the Chicago-Princeton group,⁴⁴ pp at $\sqrt{s} = 27$ GeV. The dashed curve is a fit to data from UA5,⁴⁵ $\bar{p}p$ at $\sqrt{s} = 546$ GeV. The solid line represents a fit to the 1800 GeV data with a function of the form $A p_0^n / (p_T + p_0)^n$ where p_0 is fixed at 1.3 GeV/c and $n = 7.7 \pm 0.2$.

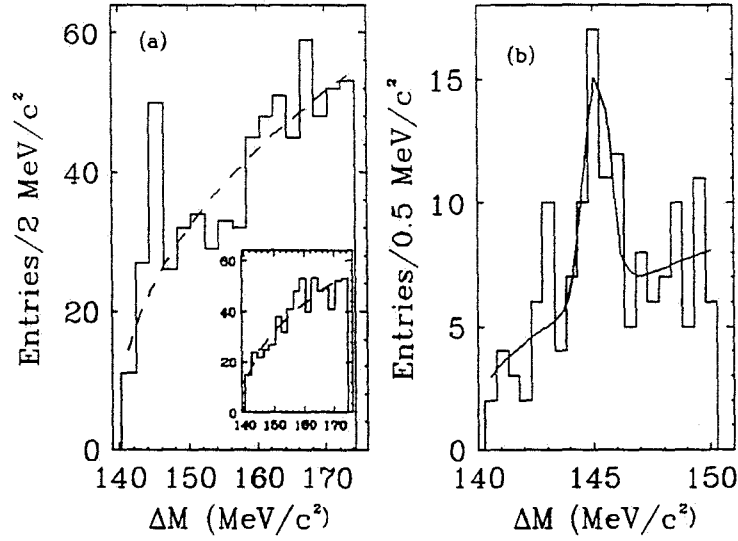


Figure 2-5: (a) The mass difference, $\Delta M \equiv M_{K\pi\pi} - M_{K\pi}$ after all cuts. The dashed line is a fit to the background. The inset shows the mass difference after all cuts for the wrong-sign mass combination, i.e. where one tries to form a D^{*+} with the combination $K^+\pi^-\pi^+$ instead of $K^-\pi^+\pi^+$. (b) The region of the peak in finer detail.

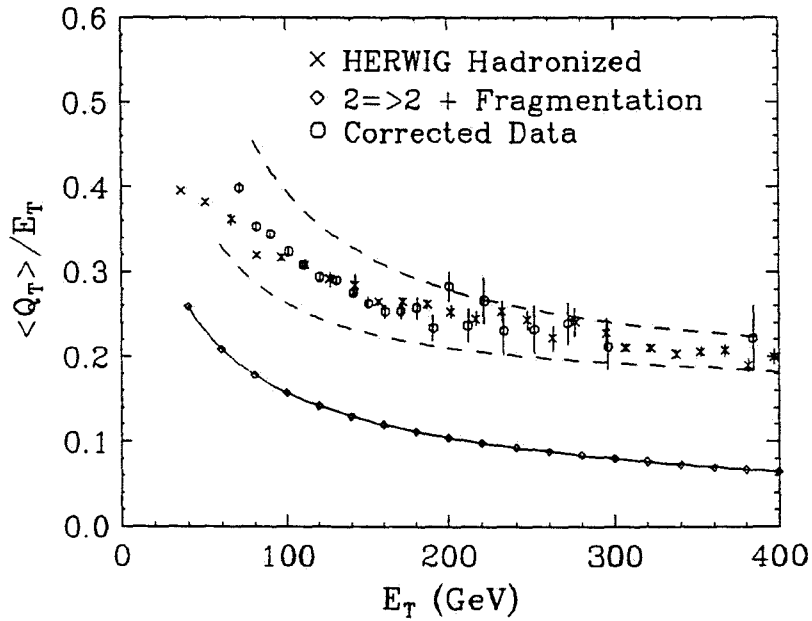


Figure 2-6: A plot of the ratio $\langle Q_T \rangle / E_T$ vs. E_T in the range $|\eta| < 1.1$ compared with a high-order QCD calculation done with the Herwig Monte Carlo program. The dashed curves above and below the corrected data points show the systematic uncertainty limits. A fragmented $2 \rightarrow 2$ calculation was done to show how much of the broadening is due to soft processes without hard bremsstrahlung. The solid curve is a spline fit joining these calculated points.

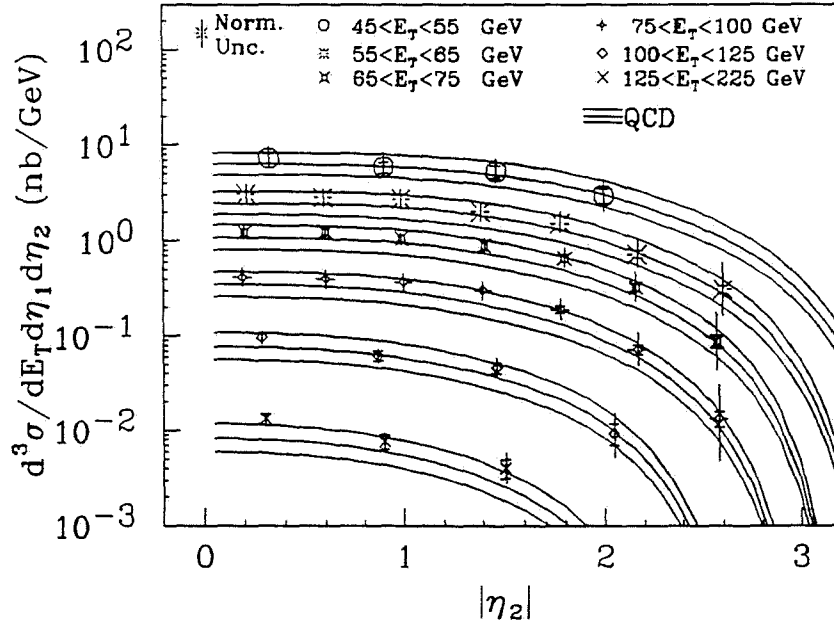


Figure 2-7: Two Jet Differential Cross Sections averaged over $\eta_1 \leq |0.6|$ compared with QCD predictions where η_1 (η_2) is the rapidity of the first (second) jet. The inner error bars are statistical, and the outer error bars include the statistical uncertainty and the E_T and η_2 dependent part of the systematic uncertainty. The $E_T - \eta_2$ independent normalization common to all points is $1.00^{+0.41}_{-0.30}$.

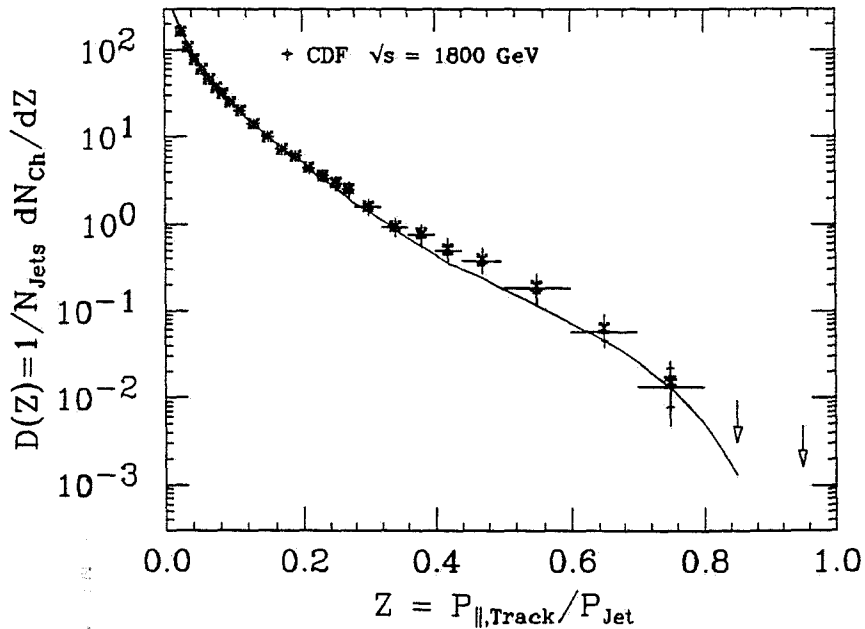


Figure 2-8: A plot of the charged fragmentation function, $D(Z)$. The CDF data have statistical and systematic errors as indicated. The curve is a prediction of the HERWIG 3.2 Monte-Carlo program.

2.2 The 1988-89 Run

For the run beginning in June, 1988, all of the CDF components were brought up to full strength. The forward calorimeters were fully instrumented. The far forward section was fully instrumented with new silicon detectors and drift chambers down to small angles to measure the total cross section. The Level-2 and Level-3 trigger systems were brought on line. Faster and more useful control room displays of events and detector performance were installed. Substantial improvements had been made to all aspects of operations based on the earlier running experience.

The primary emphasis of this run was physics, and major resources were devoted to offline analysis to enable it to keep up with the production of data. Approximately 4.4 pb^{-1} of integrated luminosity were written to 5000 magnetic tapes during the year-long run. The first-pass offline processing of the complete data set was finished within a month after the run ended, and the various physics groups began to work with the full data set. At this writing (April 19, 1990), the following physics topics are in various stages of completion:

1. From samples of $Z^0 \rightarrow \mu^+\mu^-$ and $Z^0 \rightarrow e^+e^-$ the mass of the Z^0 has been measured to be $M(Z^0) = 90.9 \pm 0.3(\text{stat.} + \text{syst.}) \pm 0.2(\text{scale}) \text{ GeV}$.⁴⁶ (See Figs. 2-9 and 2-10.)
2. From samples of $W^\pm \rightarrow \mu^\pm\nu$ and $W^\pm \rightarrow e^\pm\nu$ the mass of the W^\pm has been measured to be $M(W^\pm) = 79.83 \pm 0.44$. (See Figs. 2-11 and 2-12.) The value of $\sin^2 \theta_W$ is thus determined to be 0.230 ± 0.009 . (Preliminary result.)
3. A search for the top quark through the decay channel: $t\bar{t} \rightarrow e + \text{jets}$.⁴⁷ The existence of a standard-model top quark is excluded in the mass range 40 to 77 GeV/c^2 at the 95% confidence level. (Figure 2-13).
4. A search for the top quark or fourth-generation b quark (b') through the decay channel: $t\bar{t} \rightarrow e\mu$.⁴⁸ (Figure 2-14). The existence of a standard-model top quark or b' in the mass range 28 to 72 GeV/c^2 is excluded at the 95% confidence level.
5. Further analysis of other di-lepton signatures has been done, e.g. $t\bar{t} \rightarrow e^+e^-$, $t\bar{t} \rightarrow \mu^+\mu^-$, and $t\bar{t} \rightarrow e + \text{soft}\mu$. A preliminary combined result of all di-lepton modes places a lower limit on the top mass of 89 GeV/c^2 at the 95% confidence level.
6. We have measured $R = [\sigma \cdot B(W \rightarrow e\nu)] / [\sigma \cdot B(Z \rightarrow ee)]$, the cross-section-branching-fraction ratio, to be $R = 10.2 \pm 0.8(\text{stat.}) \pm 0.4(\text{syst.})$.⁴⁹ Combining this with other measurements, we find the width of the W^\pm to be $\Gamma(W) = (2.19 \pm 0.20) \text{ GeV}$.
7. From a measurement of the forward-backward asymmetry in the decay $Z^0 \rightarrow e^+e^-$, we have determined $\sin^2 \theta_W = 0.232 \pm 0.016$. This result does not include corrections for radiative loops. (Preliminary result.)
8. We have put 95% confidence level lower limits on the masses of a heavy W or a heavy Z at 380 GeV and 400 GeV , respectively. (Preliminary result.)

9. We have searched for a light Higgs Boson in the process $Z^0 \rightarrow Z^0 + H^0$ with the H^0 decaying to two light charged particles (e^+e^- , $\mu^+\mu^-$, $\pi^+\pi^-$). At the 95% confidence level the existence of such a particle with standard model couplings is excluded in most of the mass range below 1 GeV/c².⁵⁰
10. Measurement of the transverse momentum distributions of the electro-weak gauge bosons (Figure 2-15).
11. Measurement of the transverse momentum distribution of jets. Analysis of the full data sample should allow tests of parton compositeness to an energy scale of 1500 GeV.
12. Three-jet distributions and tests of QCD. (See Fig. 2-16.)
13. The search for SUSY particles has been extended, and no evidence for their existence is found at masses up to 150 GeV.

Many of these analyses are the subjects of Ph.D. theses, completed or in progress, by students at the participating institutions. Among these are:

- Brandeis: Milciades Contreras, Luc Demortier, Les Nakae
- Chicago: Aaron Roodman, Paul Derwent
- Harvard: E. Kearns, W. Trischuk, C. Jessop, J. Ng,
- Illinois: Phil Schlabach, Vic Scarpine, Peter Hurst, Hovhannes Keutelian, Ray Swartz, Chris Luchini, Dave Kardelis
- Berkeley: Brian Winer, Bob Drucker
- Penn: Dave Connor, John Walsh, Tim Rohaly
- Pisa: Giovanni Punzi, Sandra Leone
- Purdue: B. T. Huffman, J. I. Tonnison
- Rutgers: Ping Hu
- Texas A&M: Tim Hessing
- Tsukuba: Fumi Ukegawa, Toshi Mimashi, Shun-ichi Kanda, Satoru Ogawa, Mikio Takano, Mariko Ninomiya, Yoshi Seiya, Takashi Ino, Masa Yokoyama
- Wisconsin: Karen Byrum, Lee Markosky, Rich Markeloff, Jodi Lamoureux

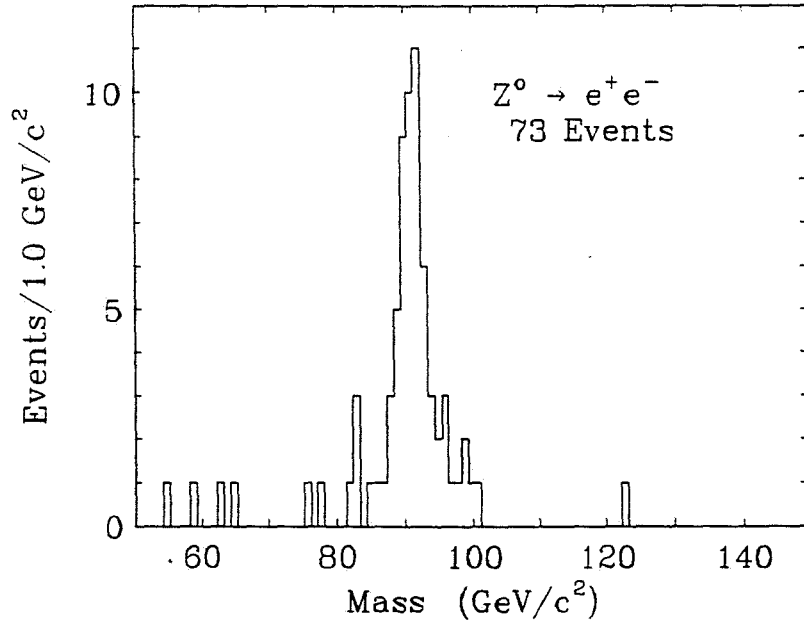


Figure 2-9: Calorimeter-based invariant mass plot for electron-positron events.

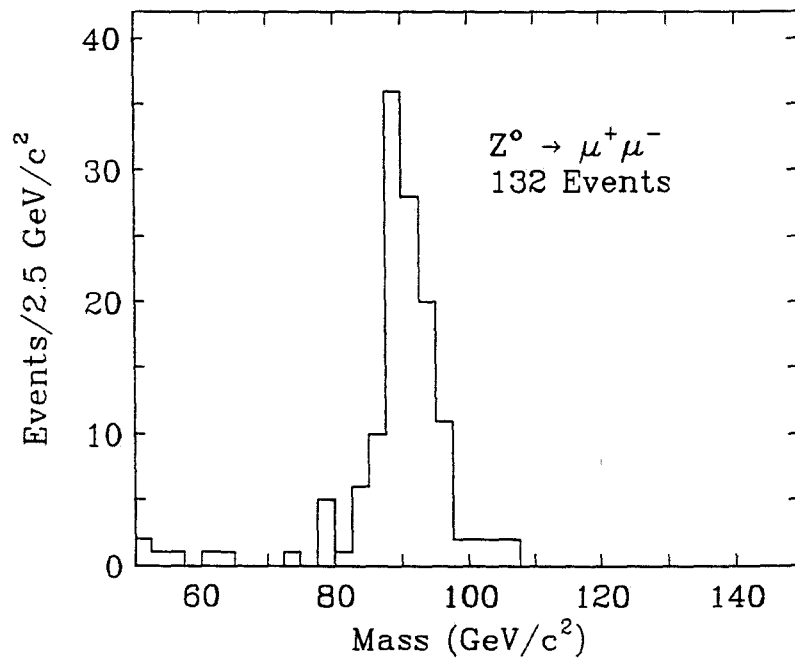


Figure 2-10: Invariant mass plot for $Z \rightarrow \mu^+\mu^-$ based on tracking data.

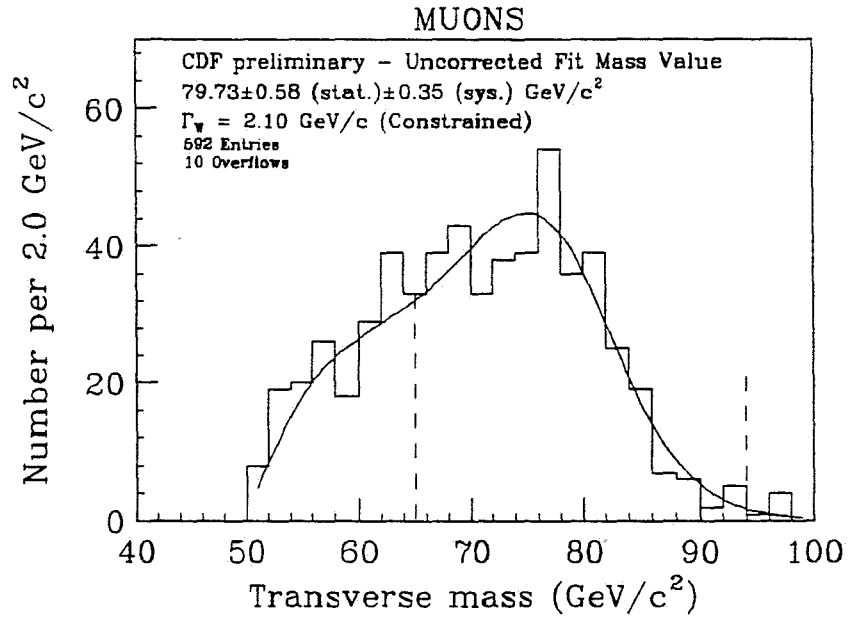


Figure 2-11: Transverse mass plots for $W^\pm \rightarrow \mu^\pm \nu$.

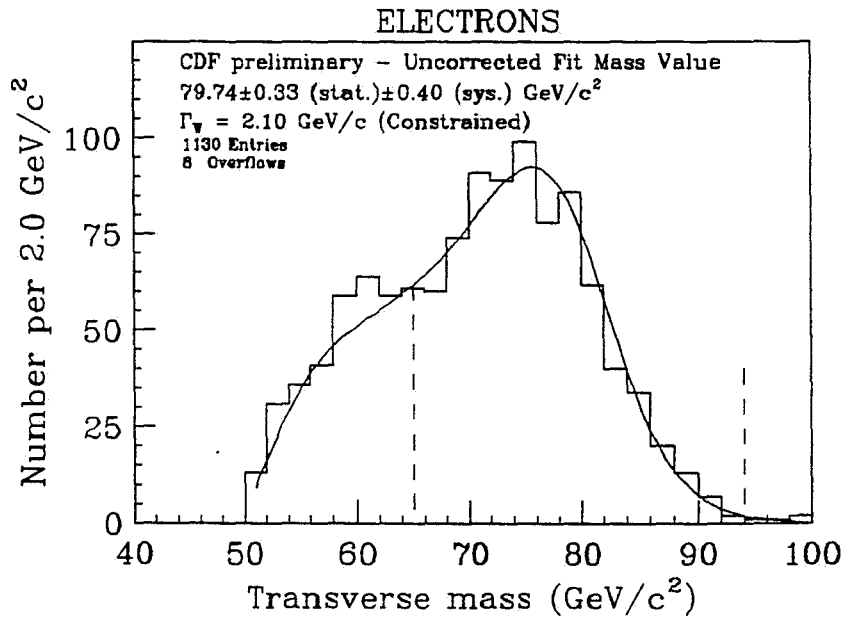


Figure 2-12: Transverse mass plots for $W^\pm \rightarrow e^\pm \nu$.

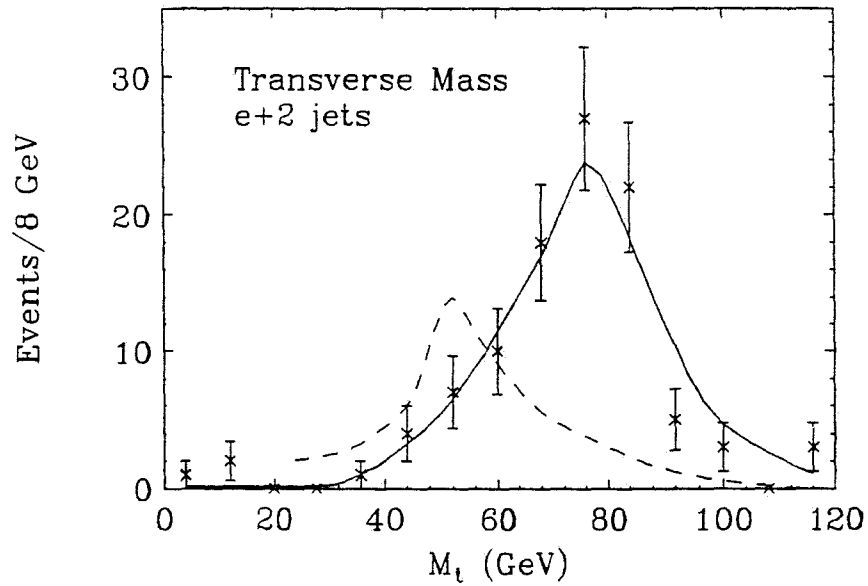


Figure 2-13: The transverse mass ($M_T^{\nu\nu}$) distributions for the $e^\pm + 2$ jets data (points), $W + 2$ jets (solid curve), and $t\bar{t}$ production with $M_{top} = 70$ GeV/c² (dashed curve).

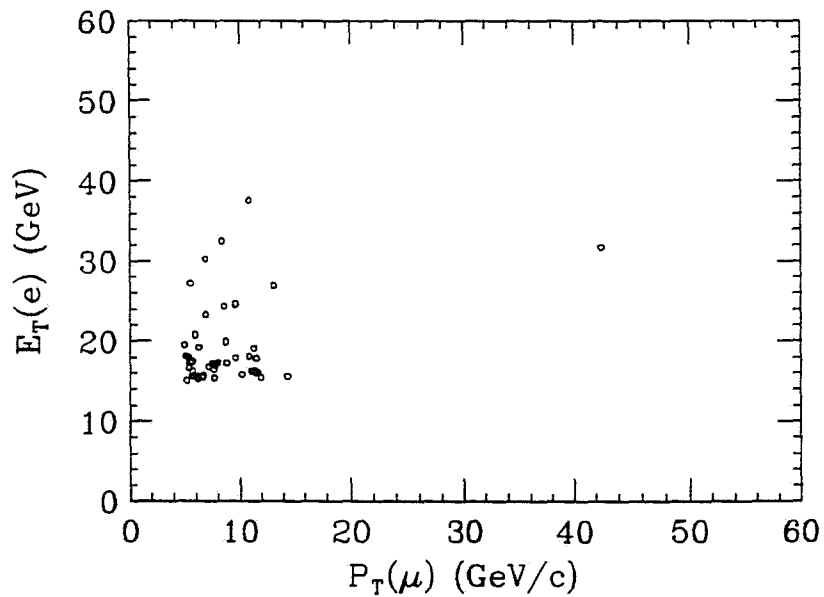


Figure 2-14: Electron transverse energy vs muon transverse momentum for the CDF data with an integrated luminosity of 4.4 pb^{-1} . Approximately seven events would be expected in the region $p_T(\mu) > 15$ GeV/c and $p_T(e) > 15$ GeV/c if the top quark mass is 70 GeV/c².

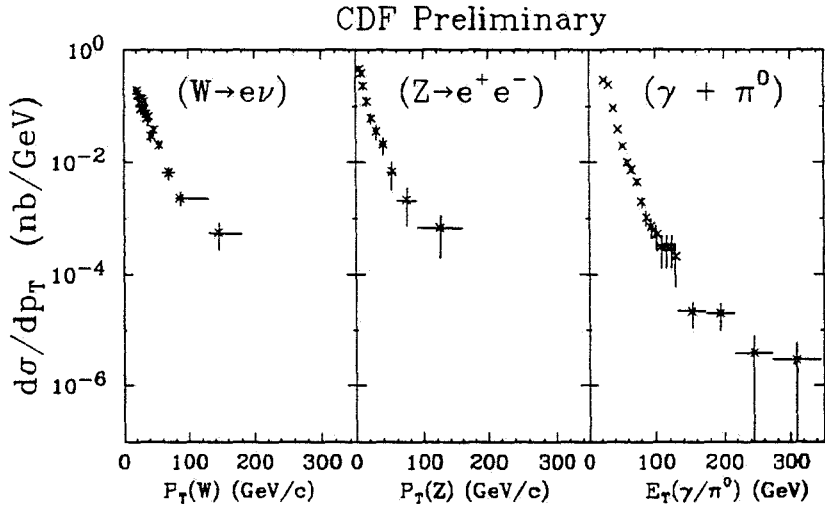


Figure 2-15: Transverse momentum distributions for W^\pm , Z^0 and γ . The W and Z distributions have been divided by the branching fraction for the observed decay mode. Since isolated photons cannot be distinguished from isolated π^0 's above 32 GeV in the 1989 CDF detector configuration, the γ spectrum above that E_T is contaminated by π^0 's.

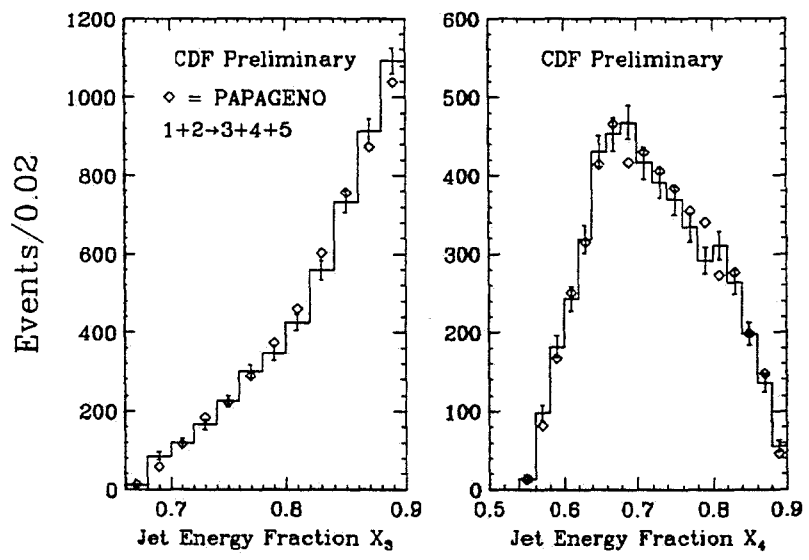


Figure 2-16: Three-jet final states are a measure of the parton processes $1 + 2 \rightarrow 3 + 4 + 5$ where the final state partons fragment into the observed jets. In the rest system, the jet energies are E_i ordered $E_3 > E_4 > E_5$. We define $x_i = 2E_i/M$ where $M = E_3 + E_4 + E_5$. The x_3 and x_4 Dalitz plot projections are plotted along with the QCD predictions.

3 Planned Physics Program

3.1 Electro-Weak Physics

The minimal Standard Model (SM) of $SU(2) \times U(1)$, surprising in its elegant simplicity, has been extraordinarily successful in describing weak and electromagnetic phenomena over the full reach of experimental observation. The model, with the exception of the Higgs sector of the theory, is completely determined by three input parameters. Two are known to very high precision, albeit at low energy and momentum transfers: the fine structure constant, α and the Fermi constant, G_F from muon decay. The third parameter enters through the weak bosons, W and Z^0 . Until recently, the most precise measurements were of the electroweak mixing angle, $\sin^2\theta_W$ as determined from deep inelastic neutrino scattering experiments. With the model so fixed, all other parameters – the W and Z^0 masses in particular – are determined up to radiative corrections from loop diagrams associated with the gauge boson masses and running the input coupling constants to a common kinematic regime.

The picture has recently changed with the operation of the SLC and LEP e^+e^- colliders. The Z^0 mass has supplanted $\sin^2\theta_W$ as the most precisely known weak boson parameter, thus properly becoming input to the SM.

It is now the task of the Fermilab Collider to make improvements on precision measurements of the W mass, the W width and $\sin^2\theta_W$ to confront the newly determined SM predictions. The Z^0 sector will continue to be the domain of electron-positron colliders. The precision measurements of the Z^0 parameters from LEP experiments have secondary benefits for W physics at Fermilab. They provide a calibration point to control some of the systematic uncertainties that have previously limited the precision of W measurements at hadron colliders, and also help to refine predictions for Z^0 production cross sections at the Tevatron - important for improvements in *e.g.* the W/Z^0 cross section ratio and W width measurements.

The proposed improvements in CDF lepton coverage result in significant improvements for both W and Z^0 physics. For example, the proposed upgrade for the muon system, extending the triggerable muon coverage out to $|\eta_\mu| < 2.8$, provides roughly a twofold increase in trigger acceptance for both $W \rightarrow \mu\nu$ and $Z^0 \rightarrow \mu^+\mu^-$ over that expected for the 1991 collider run. For electrons, the proposed improvements for enhanced coverage in the region $1.1 < |\eta_e| < 3.0$ for the 1993 run, in terms of hermeticity, triggerability, enhanced electron identification and background rejection in turn implies enhanced statistics and greater cleanliness for both $W \rightarrow e\nu$ and $Z^0 \rightarrow e^+e^-$ data samples.

We discuss the ramifications of the proposed improvements to the CDF lepton coverage on various electroweak physics topics - contrasting expectations for two scenarios, 50 pb^{-1} and 500 pb^{-1} of integrated luminosity to that of the present experimental situation (5 pb^{-1}), with particular attention given to those systematic effects which limit the precision of various measurements. In these discussions we have assumed that the Z^0 parameters are known from the LEP experiments to essentially infinite precision.

The W Boson Mass

Unlike the Z^0 , the W invariant mass cannot be reconstructed from its leptonic decays since the neutrino is not detected. Rather, the transverse components of the neutrino energy are inferred from the missing transverse energy (\cancel{E}_T) in the event. The transverse mass, M_T (the three-vector analog of the invariant mass) is used to extract the W mass. Unfortunately, the shape of the M_T distribution is influenced by a number of other effects such as the \cancel{E}_T resolution, lepton energy/momentum resolution, lepton subtraction from the underlying event, the W width and also structure function uncertainties. Our estimates for the uncertainties are given in Tables 3-1 and 3-2 for the electron and muon W decay channels.

Category	$5 pb^{-1}$	$50 pb^{-1}$	$500 pb^{-1}$
W Statistics	340	95	40
Energy Scale	310	90	40
Structure Functions	100	50	25?
Resolutions, $W P_t$	120	35	10
Electron Subtraction	170	35	10?
Background	50	20	10?
Fitting	50	30?	20?
Overall	520	155	70?

Table 3-1: Projected Uncertainties in the $W \rightarrow e \nu$ Mass Measurement

Category	$5 pb^{-1}$	$50 pb^{-1}$	$500 pb^{-1}$
W Statistics	520	110	50
Energy Scale	160	50	20
Structure Functions	100	50	25?
Resolutions, $W P_t$	190	55	10
Muon Subtraction	205	60	10?
Background	50	20	10?
Fitting	50	30?	20?
Overall	625	160	65?

Table 3-2: Projected Uncertainties in the $W \rightarrow \mu \nu$ Mass Measurement

The uncertainty associated with each of these systematic effects is a product of the partial derivative of the fitted W mass with respect to the parameter of interest, times the uncertainty in the parameter itself. For example, consider the \cancel{E}_T resolution:

$$\text{Systematic uncertainty on } M_T = \sigma_{M_T} = \frac{\partial(M_T)}{\partial(\sigma_{\cancel{E}_T})} \cdot \Delta(\sigma_{\cancel{E}_T}) \quad (1)$$

The derivative $\partial(M_T)/\partial(\sigma_{\cancel{E}_T})$ is determined by Monte Carlo simulation. The uncertainty in the \cancel{E}_T resolution, $\Delta(\sigma_{\cancel{E}_T})$ is extracted from the data. We have, perhaps optimistically,

assumed that enough computing power will be available so that the Monte Carlo part is never a limiting factor. The uncertainty in a parameter can be itself limited by statistics, as is the case for the \cancel{E}_T example above. For such parameters, the uncertainty, though systematic, will scale like the square root of the integrated luminosity. Others, such as the proton structure function, may not. Combining the two W decay channels to obtain a single measurement of the W mass, and using the world-average Z^0 mass to set the mass scale, the overall uncertainty in the W mass for integrated luminosities to tape of 5, 50, and 500 pb^{-1} is estimated to be ± 450 , ± 115 , and $\pm 50 MeV/c^2$, respectively.

In Fig. 3-1, we show the W mass (combined e and μ W decay channels) and uncertainties for the three scenarios as a function of the top quark mass, with the Higgs mass as a parameter. For illustration, we assume the central value of the W mass remains at its present value, $79.80 GeV/c^2$, and the uncertainties scale according to Tables 3-1 and 3-2. The current situation ($4.4 pb^{-1}$) imposes rather crude constraints on the the top quark mass. However, for 50 and 500 pb^{-1} the top quark mass would be constrained to lie within a $\pm 25 GeV/c^2$ and $\pm 15 GeV/c^2$ mass range at the 1-sigma level, respectively for Higgs masses between $50 \leq M_H \leq 1000 GeV/c^2$.

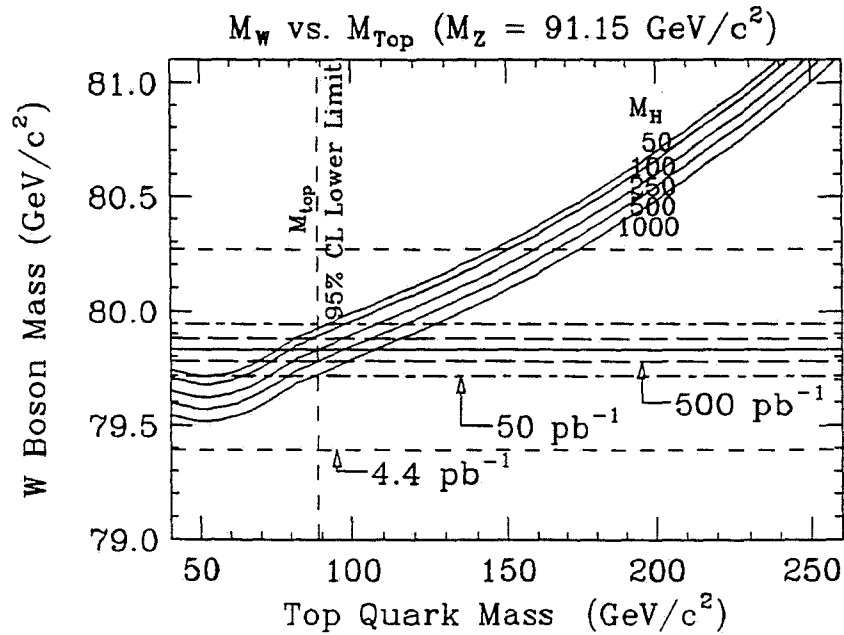


Figure 3-1: Constraints on M_{top} by measurements of M_W . Uncertainties are given for several values of integrated luminosity. Example given is for the current best measurement of M_W .

With 50 pb^{-1} of data, a direct search for the top quark should have a discovery limit of $M_{top} \sim 140 GeV/c^2$ and thus would not be in conflict with the W mass constraints. With 500 pb^{-1} the top mass limits from the W mass are compressed slightly. However, the discovery limit for a direct top quark search in this latter scenario is much larger, exceeding

200 GeV/c^2 . If the top quark were not discovered at this level of integrated luminosity, the SM would be proven inadequate.

Alternatively, the top quark may be found. Suppose the top quark mass were $\sim 120 GeV/c^2$ and thus discoverable with 50 pb^{-1} of data. The measured rate alone is enough to constrain the top quark mass to $\sim 10\%$. In this scenario, improved knowledge of both the W mass and top quark mass may begin to give us a hint of the Higgs mass. With 500 pb^{-1} of data, the situation becomes even more interesting in this regard.

R , the Ratio of W to Z^0 Production and Leptonic Decay

The ratio R is the ratio of W / Z^0 production cross sections \times leptonic decay branching ratios:

$$R = \frac{\sigma(\bar{p}p \rightarrow W X) B(W \rightarrow \ell \nu_\ell)}{\sigma(\bar{p}p \rightarrow Z^0 X) B(Z^0 \rightarrow \ell\ell)} = \frac{\sigma(\bar{p}p \rightarrow W X) \Gamma(W \rightarrow \ell \nu_\ell) \Gamma(Z^0)}{\sigma(\bar{p}p \rightarrow Z^0 X) \Gamma(Z^0 \rightarrow \ell\ell) \Gamma(W)}$$

The advantage of dealing with ratios is the cancellation of many systematic effects in both the experimental measurement and the theoretical calculations. The ratio of the total cross sections and the leptonic partial widths can be calculated to rather high precision. Moreover, recent precision measurements of the Z^0 width from SLC and LEP experiments rule out a fourth family of light neutrinos. Thus a precise measurement of R yields the total W decay width. The W width is sensitive to anything which can couple to the W and would be the only practical way to detect objects that so couple and then decay without a distinctive signature. We consider an example below.

We show the expected statistical and systematic uncertainties for R in Tables 3-3 and 3-4 for the W and Z^0 electron and muon decay channels. In contrast to the case for the W mass, the overall uncertainty in R is statistics-limited (by the total number of Z^0 's) until the 500 pb^{-1} scenario. The W width should be determined to 1-2%.

Category	5 pb^{-1}	50 pb^{-1}	500 pb^{-1}
$Z^0 \rightarrow e^+e^-$ Statistics	300 events 6.0 %	4000 events 1.6 %	50,000 events 0.5 %
W Backgrounds	0.7 %	0.5 %	0.3 %
Z^0 Backgrounds	1.5 %	1.0 %	0.5 %
Efficiencies	3.0 %	1.0 %	≤ 0.5 %
Acceptances	2.0 %	1.0 %	0.5 %
S.M. Input Parameters	0.5 %	≤ 0.4 %	≤ 0.3 %
Overall	7.1 %	2.4 %	1.1 %

Table 3-3: Projected Uncertainties in the R_e Measurement

As noted above, the R ratio is an inclusive technique for searching for objects which couple to the W and Z^0 but have masses that are kinematically allowed for the W and

Category	5 pb ⁻¹	50 pb ⁻¹	500 pb ⁻¹
Z ⁰ → μ ⁺ μ ⁻ Statistics	200 events	3500 events	45,000 events
	7.3 %	1.8 %	0.5 %
W Backgrounds	0.7 %	0.5 %	0.3 %
Z ⁰ Backgrounds	1.5 %	1.0 %	0.5 %
Efficiencies	3.0 %	1.0 %	≤ 0.5 %
Acceptances	2.0 %	1.0 %	0.5 %
S.M. Input Parameters	0.5 %	≤ 0.4 %	≤ 0.3 %
Overall	8.3 %	2.6 %	1.1 %

Table 3-4: Projected Uncertainties in the R_μ Measurement

forbidden for the Z^0 . The top quark in the mass range 45 to 80 GeV/c² is a familiar example. If the top decay were dominated by a charged Higgs and a b quark, $t \rightarrow H^+ + b$, direct observation of the top quark would be very difficult. Estimates of the W branching ratio into a top quark in this mass region range up to 16% which is easily observable in measurements of R .

Asymmetry in Leptonic Z⁰ Decays: $\sin^2\theta_W^{AFB}$

The angular distribution of leptonic Z^0 decays (where the decay angle $\hat{\theta}$ is defined as the angle between the positron and the proton in the Z^0 CM system) shows a forward-backward asymmetry due to interference between the vector and axial-vector components of the electroweak neutral current. The vector part is proportional to $(0.25 - \sin^2\theta_W^{AFB})$, so the asymmetry is a sensitive measure of the deviation of $\sin^2\theta_W^{AFB}$ from 0.25. Note that $\sin^2\theta_W^{AFB}$ is not the same as $\sin^2\theta_W^{MS}$, which is defined in terms of the W and Z^0 boson masses:

$$\sin^2\theta_W^{MS} \equiv 1 - (M_W/M_Z)^2$$

which is sensitive to radiative corrections associated with *e.g.* fermion loops involving top quarks. On the other hand, $\sin^2\theta_W^{AFB}$ is more closely related to intrinsic couplings as defined at the Z^0 pole. The relation between $\sin^2\theta_W^{MS}$ and $\sin^2\theta_W^{AFB}$ is given by:

$$\sin^2\theta_W^{MS} = \sin^2\theta_W^{AFB} / (1 - \Delta R')$$

where the radiative correction factor $\Delta R'$ is a function of the gauge coupling constants g and g' and decay constants f and \bar{f} evaluated at the W and Z^0 mass scales. The current CDF data for the Z^0 forward-backward asymmetry are shown in Fig. 3-2. By definition, the asymmetry is the rate difference for the transformation $\cos\hat{\theta} \rightarrow -\cos\hat{\theta}$. This transformation is identical to the transformation $\ell^- \rightarrow \ell^+$. Therefore the detector acceptance will be symmetric in the angular distribution if it is charge symmetric. Electron (positron) identification is dominated by the calorimetric information, which cannot distinguish charge. For muons, the systematics of the CDF detector are such that it is very nearly charge independent. This is a long-winded

way of saying that the asymmetry measurement is remarkably free of systematic effects due to irregularities in detector acceptance.

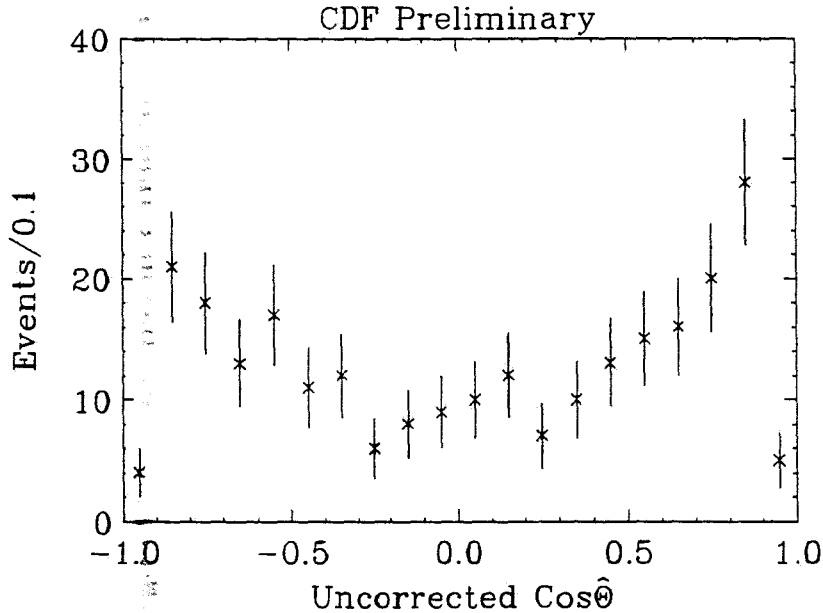


Figure 3-2: Forward-Backward Asymmetry in $Z \rightarrow e^+e^-$

We have examined the statistical and systematic uncertainties in our three standard scenarios and the results are shown in Tables 3-5 and 3-6. Notice that the overall uncertainty in $\sin^2\theta_W^{AFB}$ is statistics-limited until the total data set approaches $500 pb^{-1}$. The dominant systematic uncertainty comes from imprecise knowledge of the structure functions. The systematic uncertainty in Tables 3-5 and 3-6 represents the extreme variations to a wide choice of structure function parameterizations. Our optimism that these variations will decrease in the future is based on the expectation that the structure functions will become better known from other measurements (see *e.g.* the following section).

Category	$5 pb^{-1}$	$50 pb^{-1}$	$500 pb^{-1}$
$Z^0 \rightarrow e^+e^-$ Statistics	0.0160	0.0048	0.0016
Structure Functions	0.0020	0.0010	0.0010
Detector Efficiency	≤ 0.0010	-	-
Overall	0.0160	0.0049	0.0019

Table 3-5: Projected Uncertainties in the $\sin^2\theta_W^{AFB} Z^0 \rightarrow e^+e^-$ Measurement

Category	5 pb^{-1}	50 pb^{-1}	500 pb^{-1}
$Z^0 \rightarrow \mu^+ \mu^-$ Statistics	0.0260	0.0054	0.0016
Structure Functions	0.0020	0.0010	0.0010
Detector Efficiency	≤ 0.0020	-	-
Overall	0.0260	0.0055	0.0019

Table 3-6: Projected Uncertainties in the $\text{Sin}^2\theta_W^{AFB} Z^0 \rightarrow \mu^+ \mu^-$ Measurement

We show the combined e and μ results for the three scenarios and a comparison with the SM prediction in Fig. 3-3. Since the Z^0 forward-backward asymmetry essentially measures the ratio of the coupling constants g_A/g_V at the Z^0 pole, the result for $\text{sin}^2\theta_W^{AFB}$ depends very weakly on the top quark mass. Therefore the measurement is a direct test of the SM alone. Also, since this process has a $q\bar{q}$ initial state, the asymmetry depends on the weak charges of the quarks and is, thus, different from the lepton asymmetry measurements at LEP.

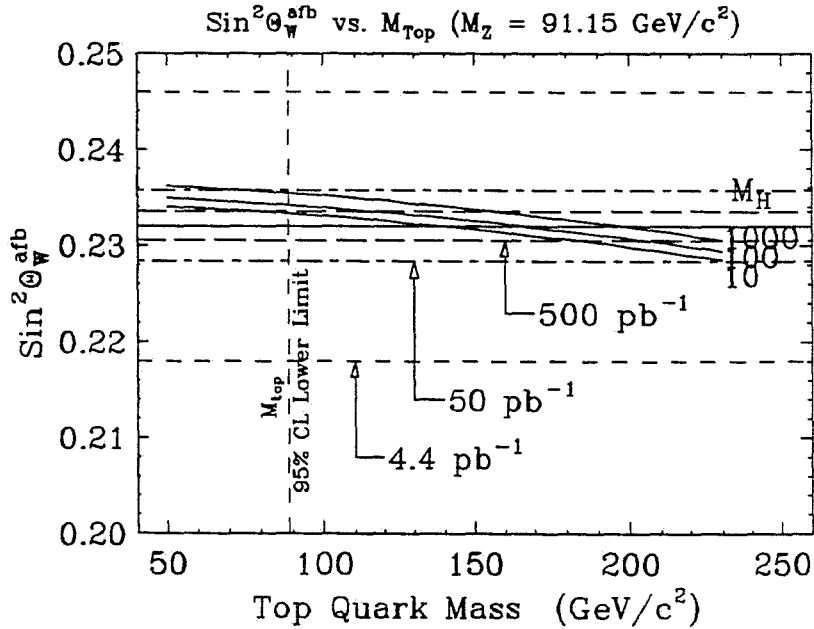


Figure 3-3: Predicted M_{top} dependence of $\text{sin}^2\theta_W^{afb}$ from the combined results of forward-backward asymmetry measurements in $Z \rightarrow e^+e^-$ and $Z \rightarrow \mu^+\mu^-$. Uncertainties are given for several values of integrated luminosity. Example given is for current CDF measurement.

Charge Asymmetry in Leptonic W Decays

The charge asymmetry in leptonic W decays, *e.g.* $W \rightarrow e\nu$ and $W \rightarrow \mu\nu$ while interesting in its own right as a fundamental measurement of the V-A structure of the charged current weak interactions, also yields important information on the ratio of d/u quarks at a $Q^2 \simeq M_W^2$. Along with other structure function information obtained at the Tevatron collider from QCD jet and direct-photon production, this information can be fed-back into other analyses such as the W mass and R measurements, in order to help reduce systematic uncertainties due to imperfectly known structure functions. At the present time, we use various sets of structure functions fit to parton distributions measured at much lower Q^2 values. These must be evolved to the W and Z^0 mass scales. With the present 4.4 pb^{-1} CDF has analyzed $W^\pm \rightarrow e^\pm\nu_e$ and $W^\pm \rightarrow \mu^\pm\nu_\mu$ events in the pseudo-rapidity ranges $|\eta_e| < 1.0$, and $|\eta_\mu| < 0.6$ respectively. Analysis in progress is extending the asymmetry measurements for $W^\pm \rightarrow e^\pm\nu_e$ into the range $1.0 < |\eta_e| < 1.7$. Sensitivities due to acceptance and different choices of structure functions are shown in Fig. 3-4. There are significant gains in structure function sensitivity with improved muon coverage.

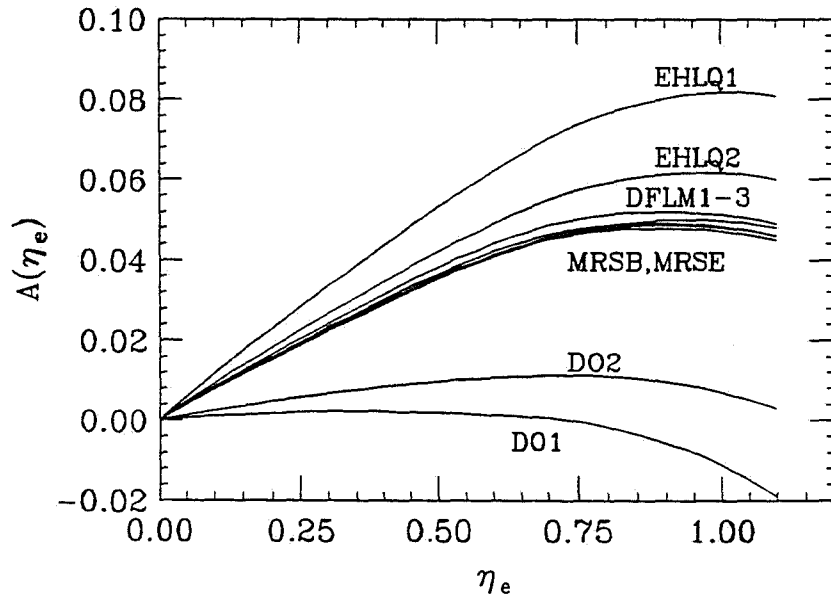


Figure 3-4: Charge Asymmetry in $W \rightarrow \ell\nu_\ell$

Search for Sequential Z' Bosons

Having considered several precision tests of the SM, we turn now to one possible extension of the model – sequential Z' . Sensitivity to a high mass Z' will be unique to Fermilab. We have investigated the prospects for detecting a high-mass Z' decaying into lepton pairs. Assuming SM couplings for the Z' width, the Z' branching ratios are the same as those of the Z^0 . The calculations for the total and partial cross sections are given in Table 3-7 and shown in Fig. 3-5.

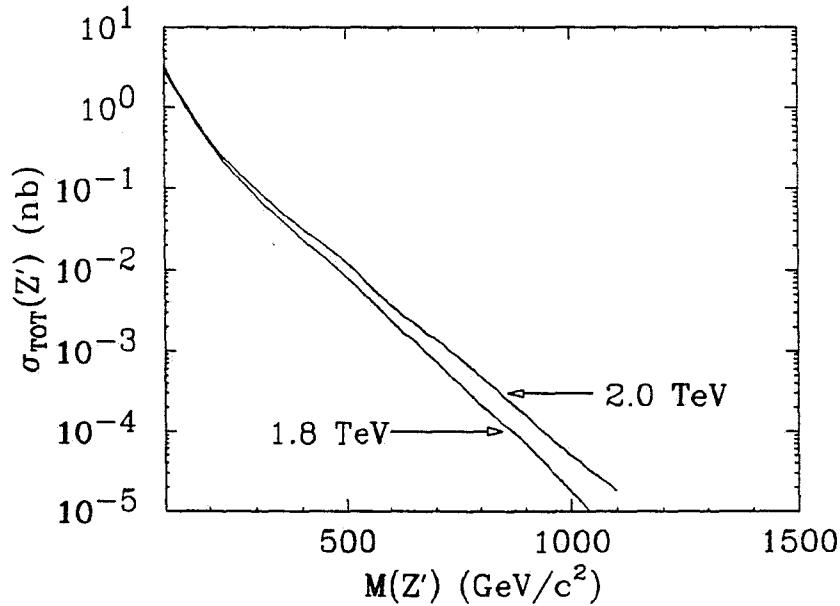


Figure 3-5: Total Cross Section for High-Mass Z' Production

Before translating the cross section into discovery limits, the mass resolution must be investigated to determine the signal-to-background ratio. The inherent signal-to-background (Z' versus Drell-Yan) is the same as that at the Z^0 according to our assumption of SM coupling constants. However, for muon pairs, the muon momentum resolution gets worse at much higher P_T . Some resolution degradation can be recouped at high P_T by using the constraint on the total E_T as measured by the calorimeters. For example, if the vector sum of the E_T in all calorimeter towers were zero (i.e., no \cancel{E}_T) then the two muon P_T 's in the event are constrained to balance within the calorimetric resolution. This constraint leads to a relative mass resolution which is better than 20%, even at a Z' mass of 500 GeV/c^2 . This mass resolution is completely adequate for a Z' peak to stand out over the Drell-Yan background.

We show the calculated total cross section as a function of the Z' mass in Fig. 3-5. We estimate the discovery limits based on the production of 10 events of either Z' into an

Z' Mass (GeV/c^2)	500	750	1000
$\sigma_{Z'} (pb) \bar{p}p \sqrt{s} = 2.0 TeV$	10	0.6	0.03
$\sigma_{Z'} \cdot BR(Z' \rightarrow \ell^+ \ell^-) (pb)$	0.33	0.02	0.001

Table 3-7: Z' Total and Partial Cross Sections

e-pair or Z' into a μ -pair. The discovery limit for 500 pb^{-1} at $\sqrt{s} = 2.0 TeV$ is 750 GeV/c^2 . The proposed upgrades to the muon coverage for CDF will also play a crucial role here, doubling the acceptance over that of the 1991 muon detection system. Improvements to the hermeticity, triggerability and background rejection of the electron coverage will also improve the sensitivity for the detection of Z' production and decay into e^+e^- pairs.

The expected rate for production of W' and subsequent decay to electron-neutrino or muon-neutrino is roughly ten times that for Z' at a given mass for the conditions in Fig. 3-5.

Search for Quark-Lepton Compositeness

The search for sequential Z' bosons requires a measurement of the Drell-Yan lepton pair continuum beyond the Z^0 pole. If quarks and leptons are composite objects with a compositeness scale Λ_{QL} , then the differential and integral $d\sigma/dM_{pair}$ distributions beyond the Z^0 pole will deviate from the D-Y predictions, with a dependence set by the contact interaction scale Λ_{QL} , as shown in Fig. 3-6 for different contact Λ_{QL} 's. Here again, the proposed upgrade, which doubles the (triggerable) muon coverage plays a crucial role. Improvements to the hermeticity, triggerability and background rejection of the electron coverage will also significantly improve the sensitivity for the detection of high-mass e^+e^- pairs. The present CDF limits from di-electron data on a left-left pseudoscalar contact term in the interaction Lagrangian are:

$$\begin{aligned} \Lambda_{QL}(-) &> 1.7 TeV \text{ at } 95 \% \text{ CL for } \eta = -1 \\ \Lambda_{QL}(+) &> 1.3 TeV \text{ at } 95 \% \text{ CL for } \eta = +1 \end{aligned}$$

These limits can be increased to more than 3.0 TeV for the upgraded CDF detector as proposed for the 1993 run, with 500 pb^{-1} integrated luminosity for both e and μ pair channels.

Detectability of Gauge Boson Pairs

The study of pair production of vector bosons probes the gauge structure of the SM since these processes are sensitive to tri-linear gauge couplings. For example, the process $\bar{p}p \rightarrow W + \gamma$ probes the magnetic moment of the W boson, for which the SM makes very definite predictions. In W pair production, gauge theory predicts cancellation of diagrams to produce good behavior at high energies. The process $\bar{p}p \rightarrow Z^0 + \gamma$ is a good test of Z^0 boson compositeness, since its cross section is enhanced by more than an order of magnitude in some composite models.

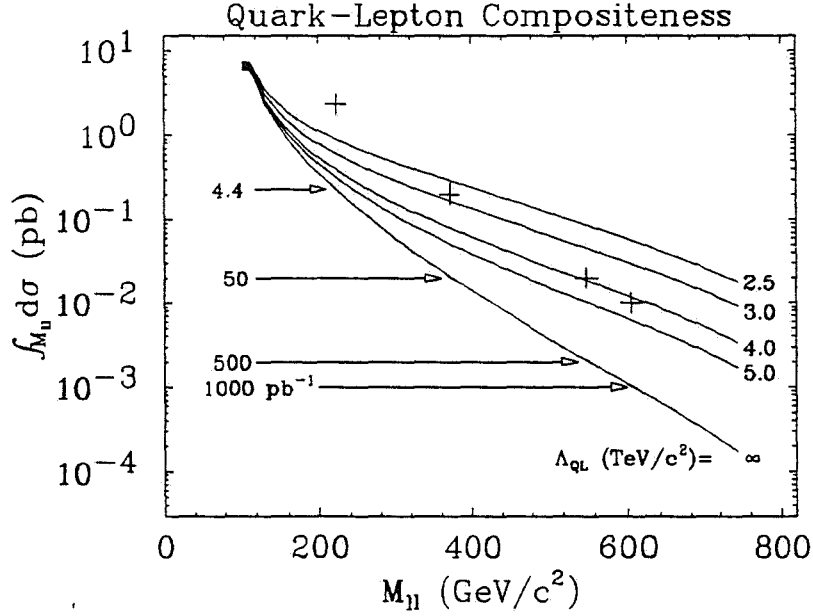


Figure 3-6: A plot of the integral of the di-lepton cross section above a given di-lepton invariant mass for various assumptions about the compositeness scale parameter, Λ_{QL} . Limits on Quark-Lepton Compositeness from Drell-Yan Cross Section are indicated by the crosses. For each assumed value of the integrated luminosity, these show a contribution from the contact potential of ten events at a di-lepton mass where the pure Drell-Yan contribution is one event.

At the Tevatron, the SM predictions for the gauge boson pair production cross sections are not large. (See Table 3-8.) Based on preliminary results from the present run as well as on theoretical expectations, a search for heavy gauge-boson pairs with one of W or Z^0 decaying to hadrons will be obscured by background from single boson production in conjunction with QCD jets. In practice, such searches will likely be limited to the doubly-leptonic decay channels, with considerable reduction in rate. Furthermore, for W pair production, there are potential backgrounds from top pair production and decay if the top quark mass is within the mass range of $90 \leq M_{top} \leq 130 \text{ GeV}/c^2$. For these reasons, the predicted event yields for doubly-leptonic decays of $W W$, $W Z^0$ or $Z^0 Z^0$ boson pairs are expected to be too low for detailed studies beyond rough cross section measurements. This will, however, provide good sensitivity to anomalous boson pair production, either a failure of the diagram cancellation in the Standard Model or the presence of di-boson resonances as predicted in some models. The outlook for $\bar{p}p \rightarrow W + \gamma$ or $\bar{p}p \rightarrow Z^0 + \gamma$ is much more favorable due to suppression of the event yield by only one factor of the W or Z^0 leptonic branching ratio. With an integrated luminosity of 500 pb^{-1} a test of the standard model prediction of the W magnetic moment appears feasible, by studying the angular distribution of the γ 's in $\bar{p}p \rightarrow W + \gamma$. It also appears feasible with an integrated luminosity of 500

pb^{-1} to measure the cross section for $\bar{p}p \rightarrow Z^0 + \gamma$ to an accuracy of $\sim 6\%$, and, if found in agreement with the SM prediction, to place constraints on composite models of W and Z^0 bosons. The gauge boson pair event yields are summarized in Table 3-8, summed over all $e - \mu$ final state combinations.

Gauge Boson Pair Process	Total Prod'n Cross Section (pb)	$5 pb^{-1}$ Event Yield	$50 pb^{-1}$ Event Yield	$500 pb^{-1}$ Event Yield
$W W$	6.0	0.7	10	130
$W Z$	1.2	0.1	0.5	8.0
$Z Z$	0.7	0.0	0.1	0.2
$W \gamma$	10.0	5.6	75	990
$Z \gamma$	9.0	1.4	20	280

Table 3-8: Gauge Boson Pair Total Cross Sections. The W - W , W - Z and Z - Z entries are summed over all μ - e final state combinations. The $W\gamma$ and $Z\gamma$ yields assume that the photon passes an E_T cut of 10 GeV.

3.2 Heavy Quark Physics

A primary goal of CDF in the coming runs is to discover the top quark and to study its properties. The current CDF top search places a preliminary lower limit on the top quark mass (M_t) of 89 GeV at 95% confidence level.^{47,48,51} Standard model calculations based on the world averages for various electroweak parameters indicate that M_t should be less than 200 GeV.⁵² This offers the Tevatron a unique window for top physics in the next decade. A t-quark search using the CDF detector will be sensitive enough to discover the standard model t-quark if it lies within this allowed mass interval with as little as 100 pb^{-1} , and with a data sample of 500 pb^{-1} will be able to do more detailed studies of its properties.

Figure 3-7 shows the $p\bar{p} \rightarrow t\bar{t}$ production cross section at $\sqrt{s} = 1.8 \text{ TeV}$, as a function of M_t .^{53,54} From the experience gained during the last run, the CDF collaboration

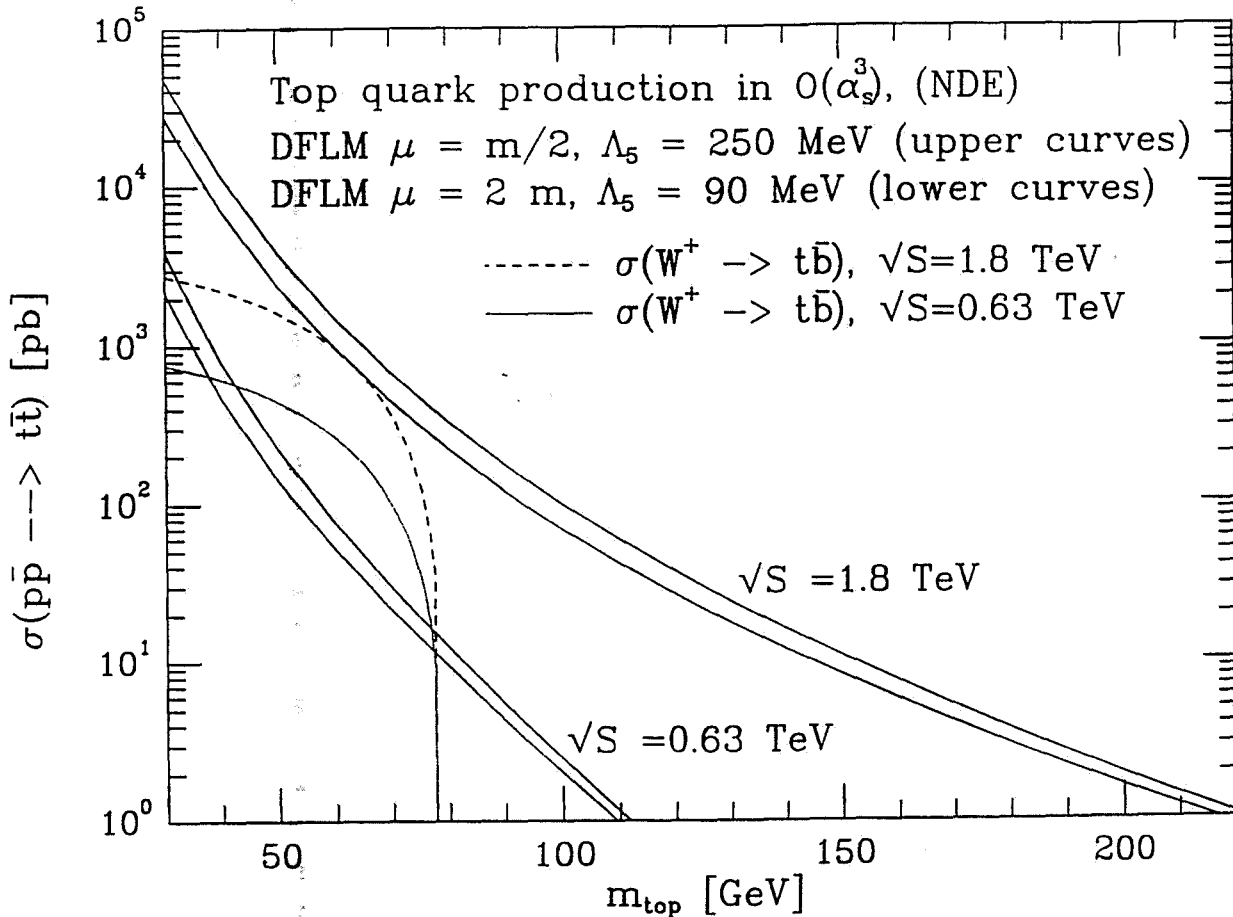


Figure 3-7: Production of $t\bar{t}$ as a function of top mass in $p\bar{p}$ collisions at 1.8 TeV.

is focusing its search on two specific decay topologies. The first is the dilepton channel, where each t-quark decays semileptonically, producing $e + \mu$, $e + e$, or $\mu - \mu$, plus \bar{A}_T and two B's. The second channel is the electron or muon + jets mode, where only one of the t-quarks is required to decay semileptonically. Other potentially sensitive channels are being

investigated, such as multi-jet events with large \cancel{E}_T , with and without leptons such as τ 's. Another tool in the search for top is B tagging in top events with an upgraded CDF. Finally, there is physics to be done with the top sample once the t-quark is discovered. These issues are discussed in the subsections which follow.

Dilepton Production

The 1988-89 CDF data displays the importance of good lepton identification in the top search. The search for top in the $e + \mu$ channel will have as its dominant background production of two vector bosons, which has a cross section comparable to 160 GeV $t\bar{t}$ production.⁴⁷ The background from the process $p\bar{p} \rightarrow Z \rightarrow \tau^+\tau^-$ is potentially quite large but can be rejected by making cuts on the lepton acollinearity, energy and \cancel{E}_T . We therefore expect little or no background in the $e + \mu$ channel with cuts that are relatively efficient for $t\bar{t}$ up to $M_t \approx 160$ GeV.

The primary benefits of the CDF upgrade to the di-lepton search are in the increase in the solid angle coverage of the lepton identification systems. The completion of the muon systems will extend the triggerable muon coverage out to $|\eta| < 2.8$. Electron coverage in the region $1.1 < |\eta| < 3.0$ will also be enhanced by improving its hermeticity, triggerability, and background rejection. With these improvements, the increase in acceptance in the $e + \mu$ channel for 130 GeV $t\bar{t}$ events is calculated to be 30% over the CDF detector of the 1991 run. Figure 3-8 shows the expected rate of $e + \mu$ events from $t\bar{t}$ vs. M_t in the $e + \mu$ channel. Also shown is the expected rate for $t\bar{t}$ events with the additional requirement of two detected

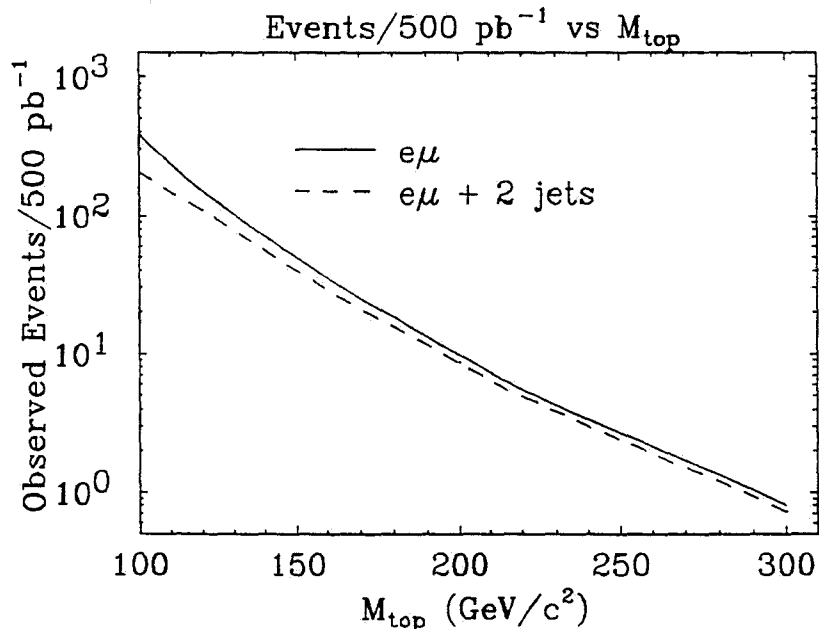


Figure 3-8: Expected number of observed $t\bar{t}$ events for $t\bar{t} \rightarrow e\mu$ as a function of top mass.

jets. This requirement rejects most of the divector boson background and keeps this channel relatively background free compared to the signal rates for top masses well above 200 GeV.

The other sources of backgrounds, such as Z 's produced with additional jet activity, where the Z decays to two τ 's, can be suppressed with cuts on the lepton-pair opening angle.

The dilepton channels resulting from the semileptonic decay of both heavy quarks into either electron or muon pairs have also been used in the current CDF top search and will be used in t -quark searches in the upcoming runs. The sum of these two channels has the same product branching ratio (2.5%) as the $e + \mu$ final state. The primary background in these channels comes from Z production and decay into lepton pairs. However such events are easily rejected with a cut on lepton pair masses consistent with the Z mass, and by requiring $\cancel{E}_T > 20$ GeV to reject the remaining Drell Yan events. We find that the addition of these two channels increases the acceptance for top by 65% over that which one gets from the $e + \mu$ channel alone. The proposed CDF upgrade will increase the $\mu - \mu$ (e - e) acceptance over that expected in the 1991 run for 130 GeV top by 50% (20%). Figure 3-9 is similar to Fig. 3-8 but for the e - e and $\mu - \mu$ rather than the $e + \mu$ channel. The dominant

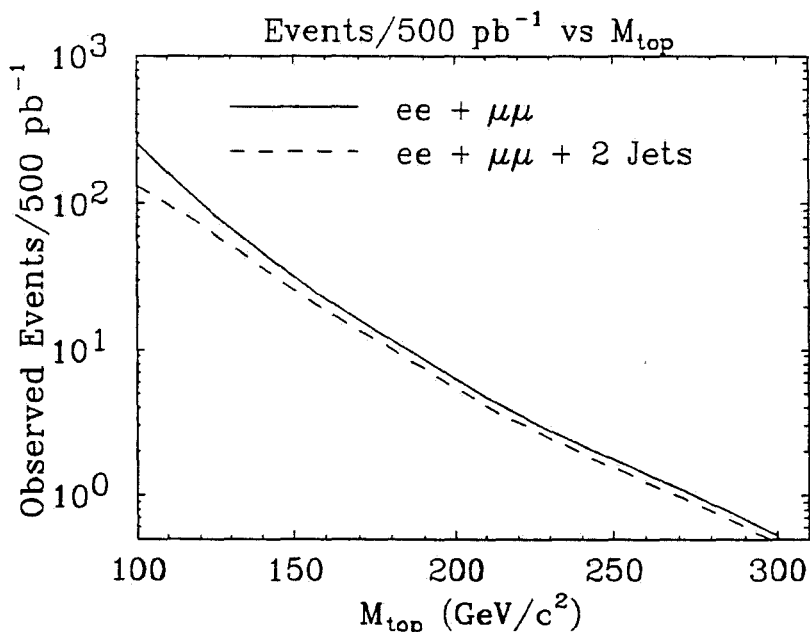


Figure 3-9: Expected number of observed events for $t\bar{t} \rightarrow e^+e^-$ and $t\bar{t} \rightarrow \mu^+\mu^-$ vs. M_{top} .

background in these channels is likely to be Drell Yan or mismeasured Z 's with sizable P_t and mismeasured MET. To suppress this background we can cut on MET significance and MET isolation. The background rates in the e - e and $\mu - \mu$ modes is expected to be small compared to expected top signals for top searches up to 200 GeV.

We expect to be able to claim discovery of top with an excess of 10 events over small expected backgrounds in the $e + \mu$ sample and a comparable excess in the e - e and $\mu - \mu$ channels combined. With 500 pb⁻¹, this puts our discovery reach well in excess of $M_t = 200$ GeV. This ignores the search for top into lepton + jets, which will be equally sensitive to top when combined with b -tagging techniques.

The Lepton + Jets Channel

The CDF t-quark search also exploits the second $t\bar{t}$ decay topology where one quark decays semileptonically to yield an energetic electron or μ , a ν plus a b jet, and the other quark decays to three jets. This decay topology represents about 30% of the total t-quark rate, making it a factor of six more copious than the sum of the di-lepton channels. We are confident that QCD backgrounds generating fake lepton candidates and large \cancel{E}_T will not be the primary source of background events. (Note the 1%-2% rate of such backgrounds in our inclusive W sample). However, there is a sizable background rate from W's produced with associated multijet activity (referred to as W+jets).

None the less, CDF has successfully used the e + jets mode to first rule out top below 77 GeV using a transverse mass analysis to subtract this background. We have subsequently used both the e +jets and the μ + jets samples to extend the sensitivity of the t-quark search by requiring, in addition, a b-quark tag. This analysis combined with the results of the di-lepton search have been used to increase the lower M_t limit to 89 GeV.⁴⁸ Reliable estimates of the size of the W+jets background to a heavier t-quark search are difficult to make due to the fact that the background results from higher-order QCD diagrams that in practice are difficult to calculate. However, with reasonable assumptions and using our existing W+jet data as a guide, we anticipate that this background can be handled even above $M_t = 200$ GeV.

The planned upgrade of lepton coverage will increase the acceptance for the μ + jets channel by 25% and e + jets by 10% over that expected for the CDF detector in the 1991 run. These modest increases reflect that fact that the partons produced in heavy t-quark decays tend to be isotropic. We also expect better rejection of non-electron background in the range $1.1 < |\eta| < 3.0$ resulting from both the improvements in tracking and in the calorimeters in this region. Figure 3-10 shows the yield vs. M_t for an e + \cancel{E}_T + 4-jet analysis, where the jet E_T thresholds have been varied to optimized signal-to-noise at each mass. For example, we expect about 550 detected events from a 150 GeV top in the combined e + 4-jets and μ + 4-jets channels for 500 pb⁻¹ of data. In the current CDF data sample, we observe no events passing this event selection, which implies, with 95% confidence, a lower limit on the expected signal-to-background ratio of about 1-to-1. There are additional kinematic variables, such as P_T of the W, which we can exploit to further reject W+jets and further enhance the signal-to-noise in this channel. However, we believe that the b tagging techniques discussed below will provide the cleanest way of separating top from the W+jets background while maintaining modest efficiency for top.

B Tagging With the Upgraded CDF Detector

We believe that regardless of the decay topology used to detect events resulting from t-quark production, the most convincing piece of evidence that we do see top decay is an enhanced rate of b-quarks in the final state above the rate expected from other sources. This implies that B meson tagging will have a crucial impact on CDF's ability to both detect t-quarks and study them. We have considered two ways of tagging b-quarks: tagging the low-energy

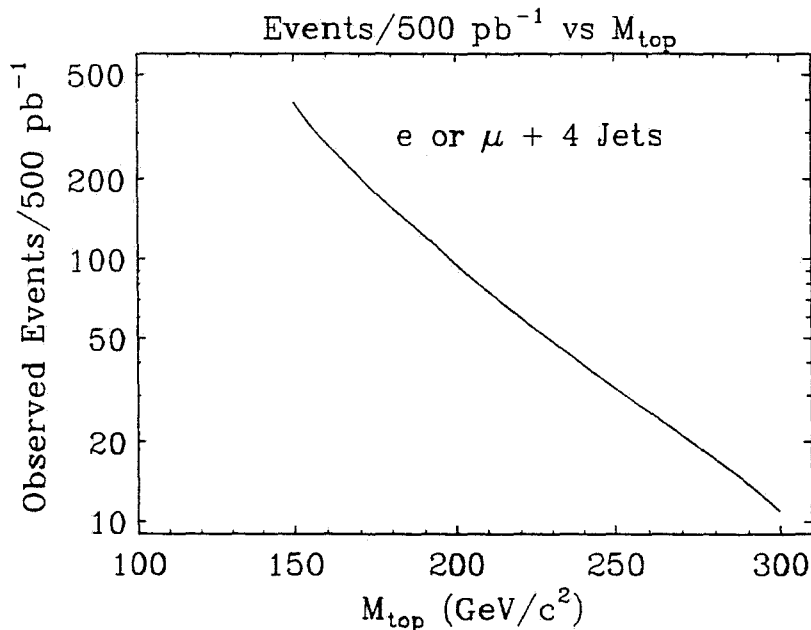


Figure 3-10: Expected number of observed events for $t\bar{t} \rightarrow \text{lepton} + \text{four-or-more jets}$ as a function of top mass.

lepton resulting from the semi-leptonic decay of the b-quark and the use of the SVX to tag secondary vertices resulting from the finite b-quark lifetime.

In the search for top with the current CDF data, we have tagged b-quark decays using the presence of a low energy muon. At least one such muon will be produced in 36% of $B\bar{B}$ pairs. The current CDF detector has an 12% efficiency for detecting these muons in $t\bar{t}$ events that are in our lepton + jet sample. The 1991 CDF upgrades to the central muon detector (CMU) and the addition of the central muon extension (CMX) will provide a substantial increase in the low energy muon detection because of the increase in muon system acceptance and the overall reduction in the rate of punch-through backgrounds allowing us to make looser cuts on the muon candidates. The proposed 1993 upgrade will further improve muon detection by increasing the solid angle covered by the forward muon toroid system (FMU). In addition, we are currently developing a low energy electron-finding algorithm that exploits the excellent performance of the central electromagnetic strip chambers.

In the proposed CDF upgrade, the B meson lepton-tagging efficiency will be further increased by the improvement in the electron identification in the plug region. We estimate roughly a 20% increase in B-tagging in both the muon and electron modes over our projected capabilities in the 1991 run.

We believe that the silicon vertex chamber (SVX) will be the primary method by which b-quarks will be tagged in $t\bar{t}$ events. We have estimated the SVX tagging efficiency for b-quarks produced in the t-quark decays using the ISAJET Monte Carlo. The proposed B tag is based on the number of tracks in a jet that have large impact parameters relative to the primary vertex. We require that at least three tracks have impact parameter (with respect

to the beam line) greater than three times the extrapolated impact parameter resolution. Backgrounds to this tag from charm and accidentals are estimated to be about 5%.

The kinematics of t decay present a favorable situation for tagging. For example, approximately 65% of the b-quark jets in a $t\bar{t}$ event with a M_t of 120 GeV are within $|\eta| < 1.0$. The mean P_T of the B jets is 30 GeV. Thus the majority of these jets will have relatively long B flight paths, will have the B meson daughters contained in the CTC tracking volume, and will have small impact parameter uncertainties from multiple Coulomb scattering. The complete CTC + SVX acceptance and efficiency for the 3 track tag is 29%. The probability of tagging at least one B jet in an event is 49%.

The B tagging efficiency vs. M_t is shown in Fig. 3-11. For $M_t > \sim 100$ GeV, the

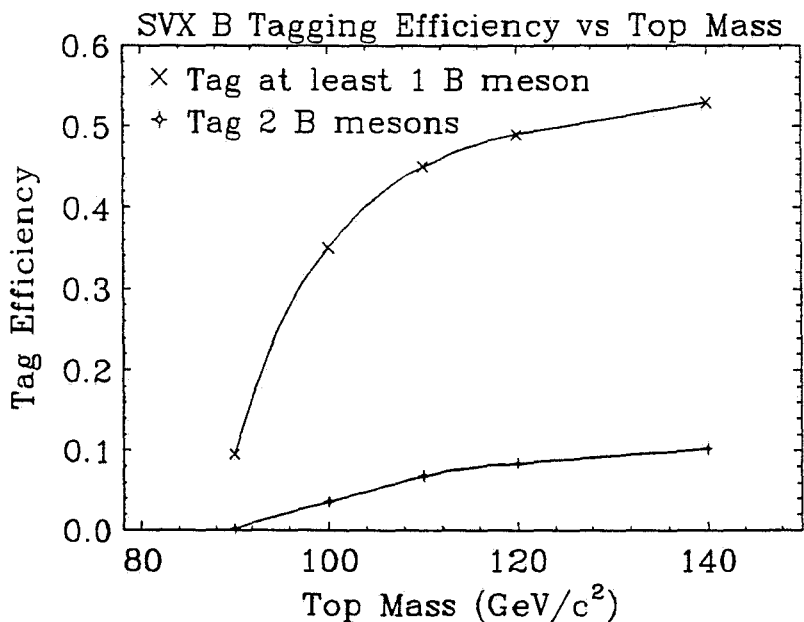


Figure 3-11: CDF Efficiency for Detecting $t\bar{t}$ through b tagging as a function of top mass.

SVX tagging rate is substantial. Note that our B tag requirement of three tracks with 3σ impact parameters is rather conservative. With more experience we hope to develop more efficient tags with equivalent background rejection. With 500 pb^{-1} of data, for example, we expect to use events containing a Z and significant jet activity as a control sample in order to develop tags that efficiently isolate the top signal from the quite similar W+jets background.

Using the leptonic and secondary vertex tags, we expect to tag a substantial fraction of the B's in both the dilepton and lepton + jets sample. A fully functioning SVX is a critical tool for this. It provides additional background rejection, with high efficiency for the top signal, which is needed to exploit the higher rate for top found in the lepton + jets channel.

Physics Opportunities with a Top Sample

The most important physical parameter of the t -quark is its mass. Assuming the Standard Model, the Electroweak parameters (most notably the W mass) vary with M_t as a result of radiative corrections. A fairly precise measure of M_t is, therefore, one of the most important tests of the Standard Model available to us in the 1990's.

There are three ways CDF will attempt to measure M_t . The first is by the observed rate of top candidates. Since the cross section for top is falling rapidly (Fig. 3-7, and the theoretical uncertainty in this rate is not large ($\pm 30\%$), a measure of the top rate alone constrains M_t . For example, if M_t is 150 GeV, we expect to measure M_t to within 10-15 GeV using the rate of observed dilepton events.

The mass can also be extracted directly from the dilepton and lepton + jets top candidate sample. Baer et al.⁵⁵ suggest ways of determining M_t using the dilepton + 2 jet sample. They claim a measurement of M_t to within 10 GeV is possible using as few as 10 events, for M_t in the range of 150 GeV.

The lepton + jet sample seems to be the obvious place to try to reconstruct M_t , because one of the top decays does not involve a neutrino. It is complicated, however by combinatorics, initial-state radiation, and jet overlap. Here B tagging can help to reduce the combinatorics. Others have studied mass resolution in the lepton + jet events and find promising results.⁵⁶ A CDF study of our mass resolution in this channel is underway.

Beyond measuring M_t , it will be important to confirm that this quark decays according to the minimal standard model. Extensions of the standard model that include charged Higgs particles predict rather large changes in the relative rate of single and multi-lepton final states from a $t\bar{t}$ event. Observation of such unusual decay rates will therefore be suggestive of the presence of a charged Higgs.^{57,58} If the top is heavier than the W (which seems likely on the basis of our 1989 data), then the relative rate of $t \rightarrow bW$ is quite often comparable to the rate of $t \rightarrow h + b$. Figure 3-12 shows the branching ratio for $t \rightarrow bW$ for $M_t = 150$ GeV for a particular two-Higgs doublet model,⁵⁷ as a function of the Higgs mass and the ratio of Higgs doublet vacuum expectation values (often expressed as $\tan\beta$). Except for a narrow range of $\tan\beta$, where the standard model charged current decay is totally suppressed, it is reasonable to expect to discover the top with a 500 pb^{-1} sample via its decay $t \rightarrow W + b$.

There are three measurements CDF can make with an upgraded detector which will rule out or discover a charged Higgs in a finite range of Higgs masses and $\tan\beta$. First, we can compare M_t as measured by rate with M_t measured directly from the kinematic features of the candidate events. A mass (as inferred from the rate) larger than that measured directly could be an indication that the t -quark has a significant non-charged current decay rate. If the t -quark decays to h^+b , the h^+ has two significant decay modes ($h^+ \rightarrow c\bar{s}$ and $h^+ \rightarrow \tau^+\nu$) whose relative rate is a function of $\tan\beta$. Significant decay rates into charged Higgs may therefore drastically change the rate of τ decays from top. We expect to be able to search for τ 's in the inclusive lepton samples and look for top candidates where one top decays to e or μ and the other to τ . Drastic deviations from the Standard Model prediction of the

$$m_t = 150 \text{ GeV}/c^2$$

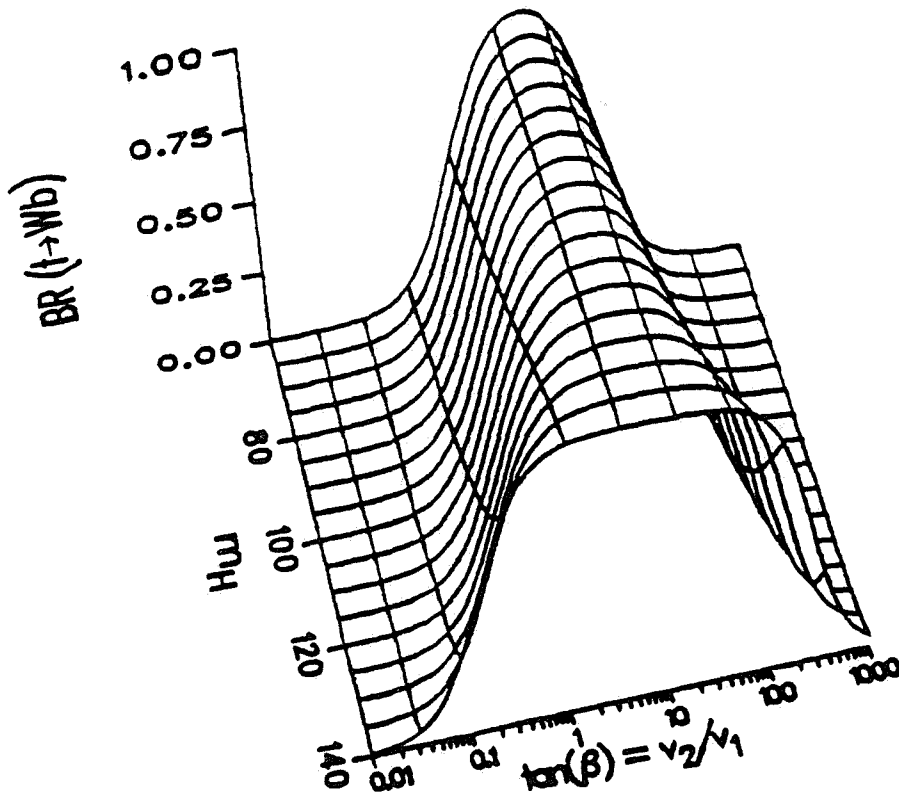


Figure 3-12: The branching ratio for $t \rightarrow W + b$ for $M_t = 150 \text{ GeV}$ for a particular two-Higgs doublet model,⁵⁷ as a function of the Higgs mass and the ratio of Higgs doublet vacuum expectation values ($\tan \beta$).

number of τ 's from top are predicted for certain Higgs masses and $\tan \beta$ values. The relative rate of dileptons and single lepton events is also sensitive to non-charged-current top decays. Significant departures from the Standard Model rate of $1/6$ are possible if the t -quark decays via $t \rightarrow h^+ b$. We also expect to be able to search for τ 's in the multi-jet plus \bar{A}_T sample as a signature of $t \rightarrow h^+ b$.

If M_t is roughly 150 GeV , and there exists a charged Higgs between the W mass and M_t , with 500 pb^{-1} of data CDF is likely to observe departures from the Standard Model predictions in the top sector.

3.3 QCD Physics

In the study of hadron collisions, QCD processes are, and will continue to be the baseline against which all new processes will be measured. The luminosity upgrades to the Tevatron, and specifically, the main injector will extend the studies of QCD into a substantially higher energy regime where many new phenomena may be found. In addition, new calculations and improvements in the understanding of detector performance will increase the precision of the tests of QCD. To illustrate the reach in energy gained by the upgrade, the following processes will be discussed along with the discovery potential in each channel: a) jet cross section, b) direct photons, c) high P_t W's and Z's. High invariant mass Drell-Yan events were discussed in Sec. 3.1.

Jet Cross Section

The measurement of the inclusive jet cross section ($p\bar{p} \rightarrow \text{Jet} + X$) is well defined to all orders of perturbation theory. At any fixed total transverse energy, two jet production dominates the final state over all other cross sections. In particular, because of the large cross section, jet production explores the highest Q^2 available. For example, the highest invariant mass seen at the Tevatron to date is above 1 TeV. Recently, the inclusive jet cross section has been calculated⁵⁹ to order α_s^3 . This calculation greatly reduces the theoretical uncertainty associated with the variation in renormalization scale associated with α_s and with the evaluation of the parton distribution functions.

Figure 3-13 shows, as a function of jet E_t , the jet cross section measured by CDF, based on an integrated luminosity of 4.2 pb^{-1} . The most outstanding feature is the large range (≈ 7 orders of magnitude) over which the cross section has been measured, and the highest transverse energy reached (420 GeV). The solid line, indicating the predictions of leading order QCD, appears to already provide a fairly good description of the data.

The new calculations to order α_s^3 have the additional feature that the jet cross section depends on the effective radius in the η - ϕ metric used for clustering. This is because at the theoretical level, gluon radiation can escape the jet clustering cone. This aspect of the calculation does not exist at leading order where only two partons are emitted in the final state. Figure 3-14 shows the variation in the jet cross section with cone radius at 100 GeV E_t , and compared to the predictions of Soper *et al.* There is some expectation that the prediction would steepen with calculations performed at still higher orders.

The jet cross section can be used as a probe of effects which appear with large coupling strengths. The best known example is the effect of quark substructure on the shape of the jet E_t spectrum at the high end. If quarks were composed of smaller objects, a structure function for the quark would exist, which would modify the scattering at short distances. This effect can be parameterized by adding a contact term to the QCD Lagrangian with an effective distance scale defined by the parameter Λ_{comp} .⁶⁰ Figure 3-13 shows the effect of a Λ_{comp} of 950 GeV as a dashed line. This is the current best lower limit (95 % CL), derived from CDF data.

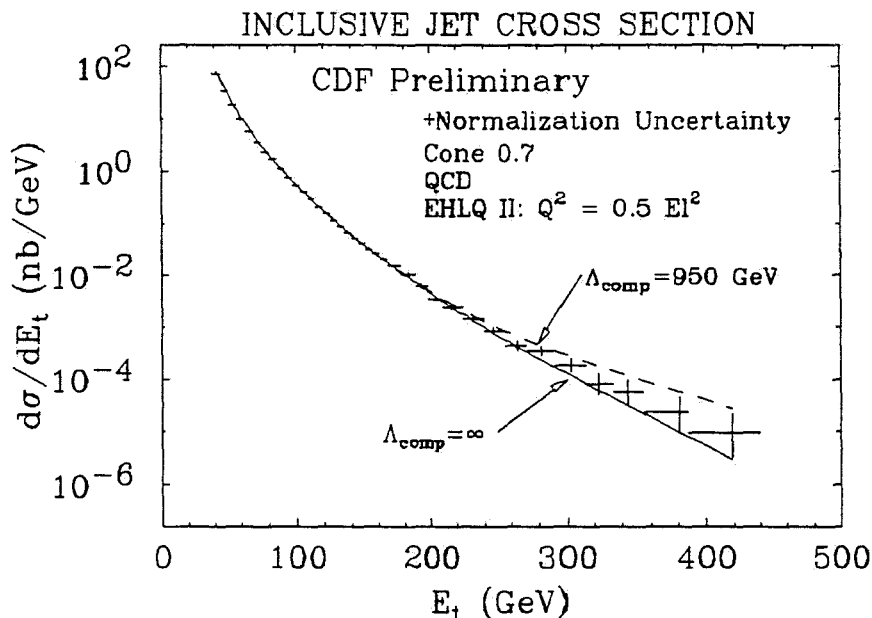


Figure 3-13: The inclusive jet cross section measured by the CDF detector. The solid line is the prediction of leading order QCD, where the curve has been normalized to the data in the region $70 \leq E_t \leq 200$ GeV. The dashed curve shows the effects on the cross section of compositeness with scale parameter of 950 GeV.

Figure 3-15 shows the jet cross section on a linear scale, normalized to leading order QCD in the region $70 \leq E_t \leq 150$ GeV. Because of the way energy corrections are handled, in order to compare to α_s^3 calculations, no correction was used for energy out of the jet clustering cone. This effect is not in the leading order calculation, and has a size roughly indicated by the dotted line. At the high end, there appears to be a small excess of events relative to QCD. This excess varies between 2.5 and 3.5 σ (stat. errors only), and for now is a curiosity. One thing this does indicate is the need for understanding the high x end of the structure functions at high Q^2 .

Figure 3-16 shows the high energy end of the inclusive jet cross section, and the E_t reach for different amounts of integrated luminosity. The arrows indicate the potential reach in cross section for several integrated. From this, it can be shown that that the ultimate reach, e.g. from two runs of 500 pb^{-1} , will correspond to a Λ_{comp} of approximately 1.8 TeV. It is important to point out that in the event of no signal, this measurement plays a role in tying down the high x end of the parton distribution functions. For example, if an excess is eventually observed at the SSC, the results of a Tevatron measurement at high x should provide the basis for understanding whether the excess lies in the structure functions or in some new effective interaction.

The two-jet invariant mass spectrum is likewise sensitive to heavy objects pro-

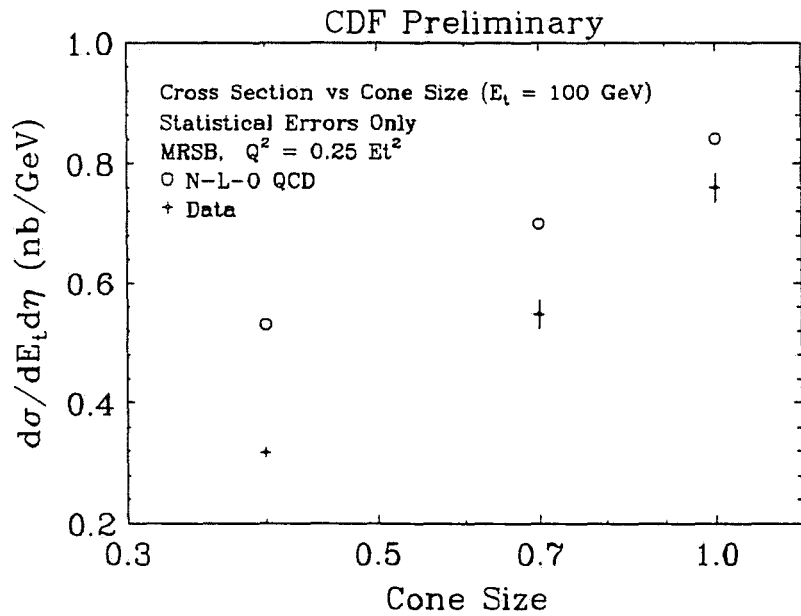


Figure 3-14: The variation in the jet cross section with the clustering cone radius at fixed transverse energy (100 GeV). The predictions are those of Soper *et al.*

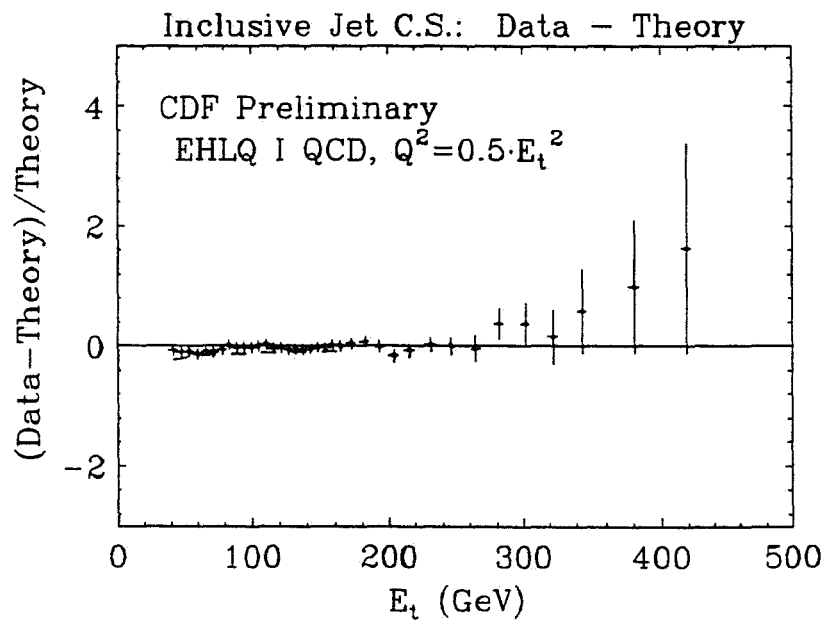


Figure 3-15: Jet cross section from CDF, plotted on a linear scale, and compared to leading order QCD.

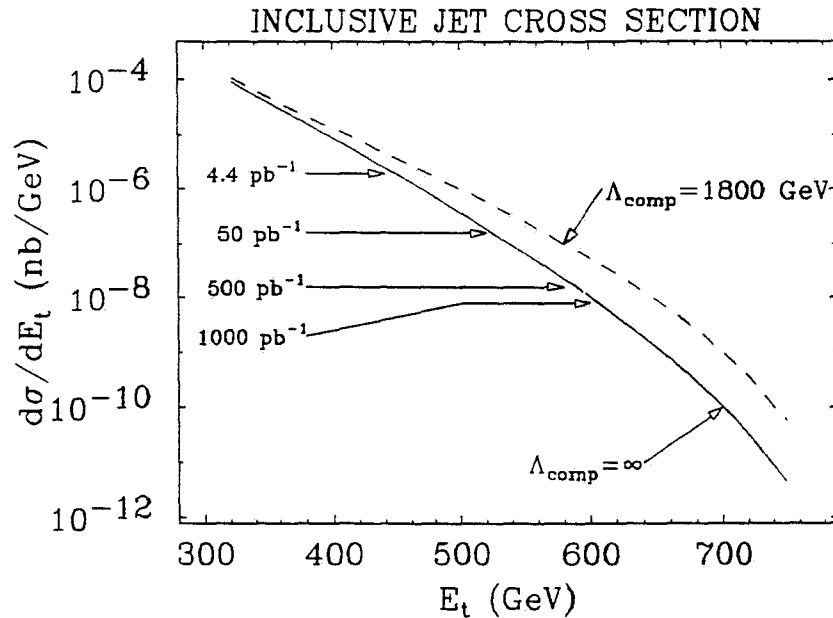


Figure 3-16: High energy end of the inclusive jet cross section. Arrows indicate the expected reach in jet E_t for different amounts of integrated luminosity.

duced with a strong coupling. In chiral color models⁶¹, a massive octet of gluons is predicted which would lead to a broad resonance in the two-jet invariant mass spectrum above 150 GeV. This resonance, because of its strong coupling, would produce a sizable enhancement in the dijet mass spectrum above the QCD background. Figure 3-17 shows the two jet mass spectrum from approximately 25 nb^{-1} of data. The leading order QCD predictions again provide a good description of the data, allowing the axigluon to be excluded in the mass range $120 \leq M_a \leq 210 \text{ GeV}$ for $\Gamma_A = .09M_A$. The most current data set includes events with invariant masses in excess of 900 GeV, allowing a substantially higher sensitivity to such objects. For the eventual reach of the Tevatron luminosity, 1 fb^{-1} of data, the discovery limit for axigluons should extend well above 1 TeV. This is shown in Fig. 3-18 where the predicted signal is shown above a QCD background for different masses.

Direct Photons

As with jets, direct photons provide both a probe of QCD and a signature for interesting new physics processes. Figure 3-19 shows the highest E_t (300 GeV) direct photon candidate observed to date in the CDF detector. Direct photons in QCD probe the quark-gluon vertex, and are sensitive to the gluon structure function at low x . At high energies, they provide a good test of vector boson couplings ($W\gamma$) and don't involve losing rate because of the branching fraction.

Figure 3-20 shows the most recent direct photon cross section from CDF. This

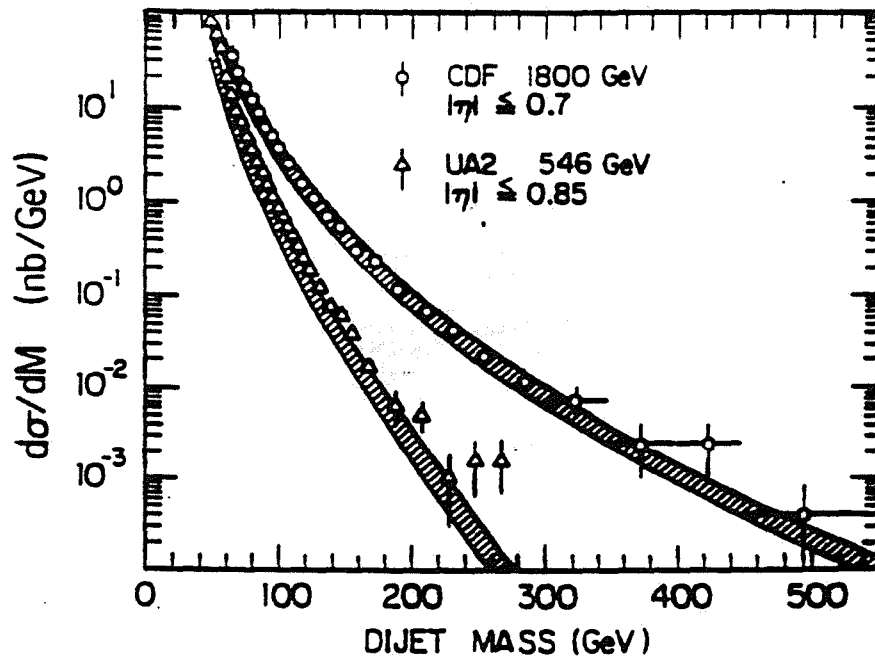


Figure 3-17: Two jet invariant mass spectrum from CDF data, along with a band representing the range of leading order QCD predictions. New CDF data exists, increasing the reach in invariant mass to above 900 GeV.

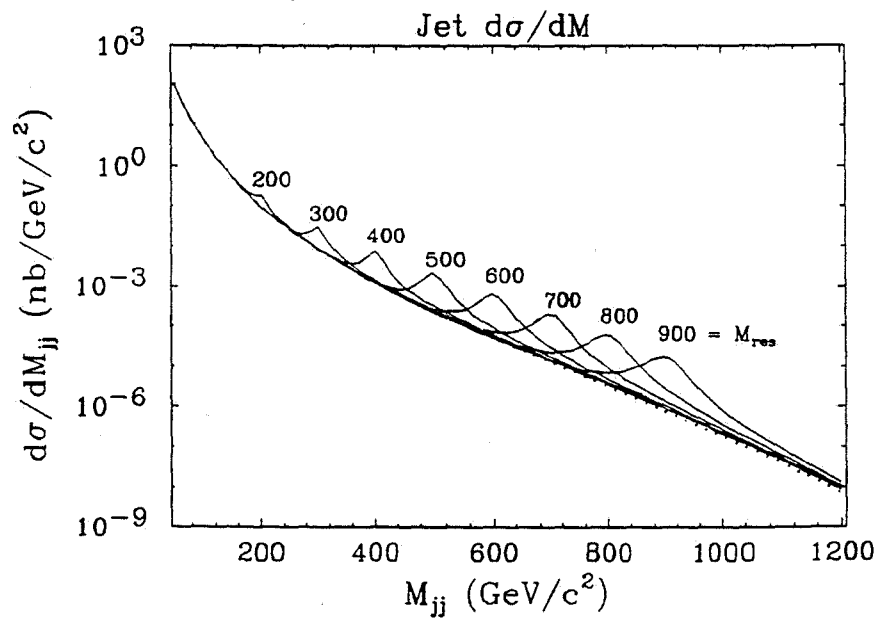


Figure 3-18: Expected cross section for the two jet invariant mass up to 1.2 TeV. Sensitivity to possible new strongly interacting particles would show up as resonances, with a sensitivity reaching 1 TeV.

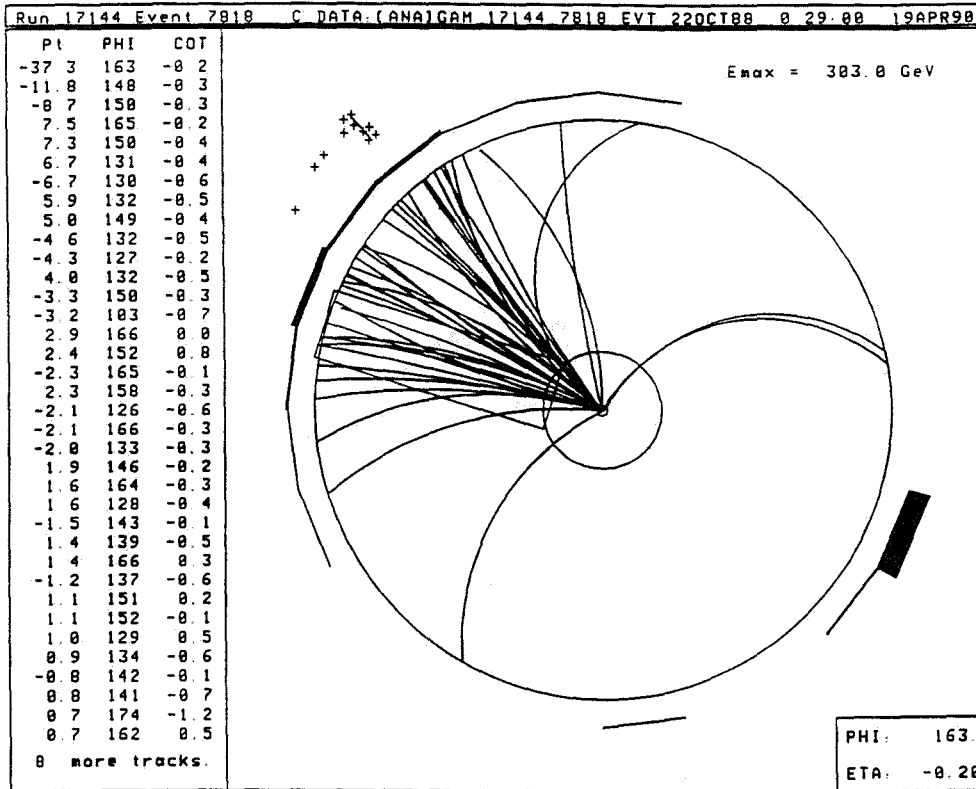


Figure 3-19: The highest E_t direct photon candidate observed in the CDF detector, having over 300 GeV transverse energy.

is compared to a leading order QCD calculation. Recent calculations exist at the next-to-leading order level, and work is in progress to make more precise comparisons to these. In Fig. 3-21 the expected cross section is shown as an integral cross section above a fixed E_t . From this, it is apparent that the reach in E_t will be up to 400 GeV for this process. For 1 fb^{-1} , one might expect roughly 40 $W\text{-}\gamma$ events where the W decays into leptons, and 120 $Z\text{-}\gamma$ events where the Z decays into leptons; this is requiring an invariant mass of 200 GeV between the boson and the direct photon.⁶²

High E_t W and Z production

High P_t W and Z production are analogs to direct photon production, and form the background for other processes, such as heavy top. Other, non-standard processes, such as a techni-rho would appear as an enhancement in the P_t spectrum.⁶³ Recently, calculations have been performed at order α_s^2 for the P_t spectra of the W/Z .⁶⁴ These calculations reduce the theoretical uncertainty in the cross section. Figures 3-22 and 3-23 show these predictions for the cross section along with CDF data. Clearly there is a reasonable agreement between theory and experiment. With 1 fb^{-1} , the P_t reach for W 's should allow a significant measurement out to 250 GeV.

Processes involving technicolor-type models could produce heavy particles decaying to W pairs. The exact nature of such couplings are not certain, but do provide some impetus to examine the potential discovery limits. From different scenarios, and depending on the coupling, it may be possible to detect techni-rho's with masses up to 250 GeV.

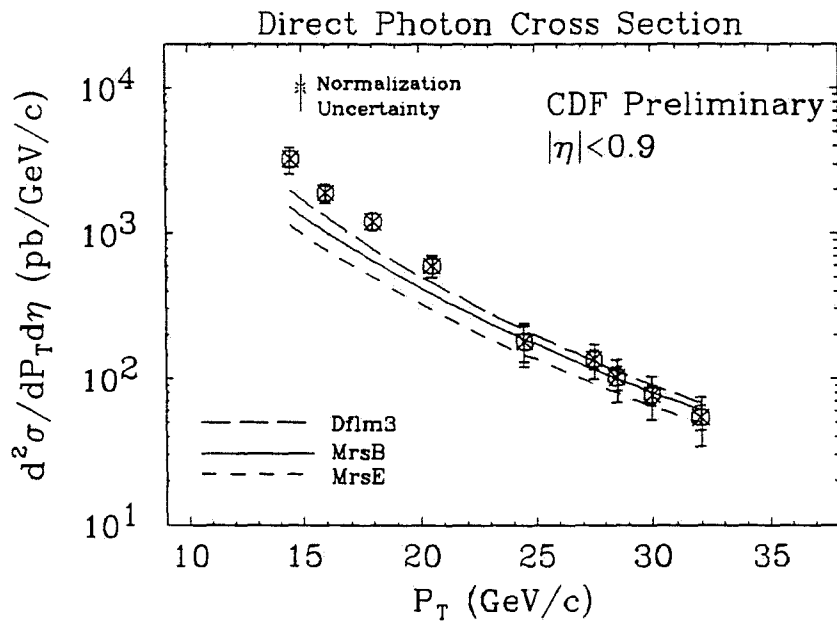


Figure 3-20: The direct photon spectrum from CDF, along with the predictions of leading order QCD.

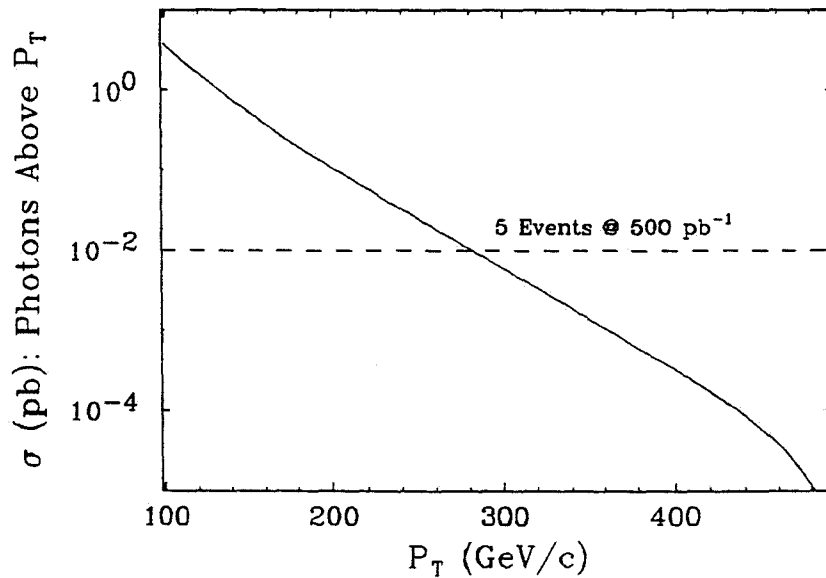


Figure 3-21: Integrated cross section for direct photons above a fixed E_t . Arrows indicate the reach for different amounts of integrated luminosity.

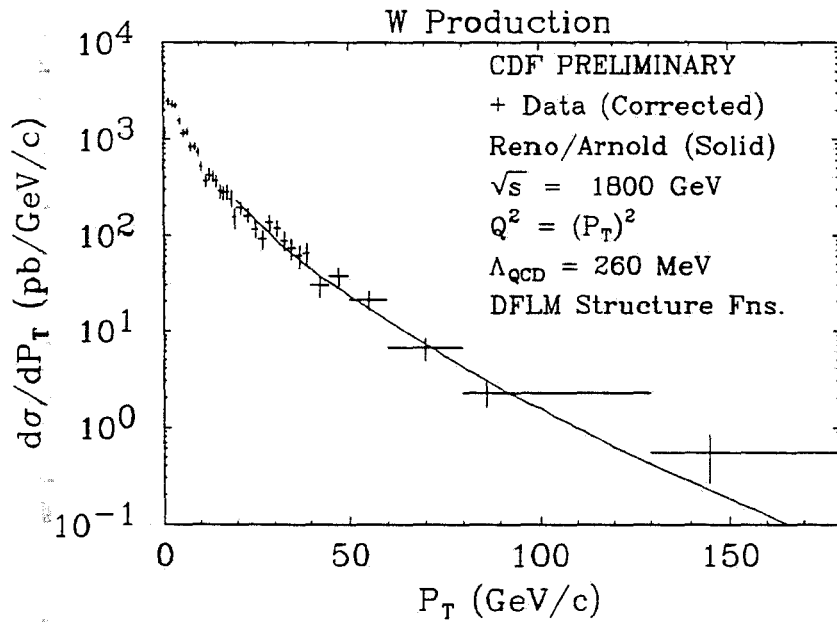


Figure 3-22: P_t distribution for W production from CDF compared to the order α_s^2 predictions of Arnold and Reno.

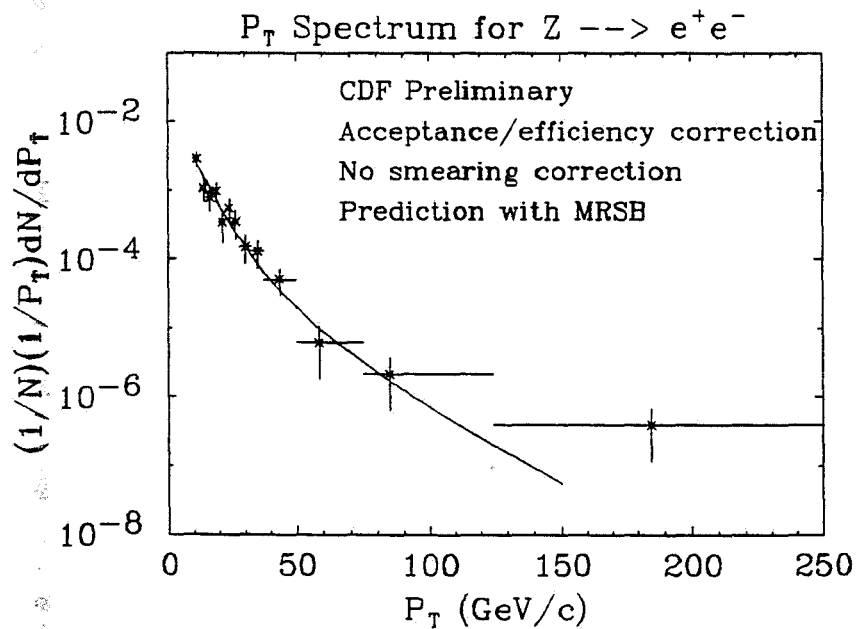


Figure 3-23: P_t distribution for Z production from CDF (points) compared to the order α_s^2 predictions (solid curve) of MRSB.⁶⁵

3.4 B Physics

In this section we consider some of the possibilities for b quark related physics with CDF at very high luminosity (500 pb^{-1}). CDF's capabilities in this area rely considerably on the use of its silicon vertex detector and on aspects of the trigger system which allow the proper event sample to be isolated.

At CDF, B particles are produced both as specific products of the decays of massive states, such as in the process $t \rightarrow Wb$ and as component of the QCD continuum. At high luminosity, CDF's sensitivity to higher mass states will increase. However effective suppression of the background from gauge bosons plus jet production will require the use of additional analysis handles such as the detection of associated B particles to enhance the signal. The use of this tag is presented in detail in the heavy quark physics discussion elsewhere in this section. At high luminosity, the large QCD production cross section will result in a very large sample of B 's for exclusive studies, lifetime, and mixing measurements. This topic represents a promising area of research for CDF relating to b quark production and decay. It will rely however upon the successful completion of a corresponding program at lower luminosity to be carried out during the 1991 run and the necessary enhancements to CDF's vertexing and trigger systems for high luminosity use. In particular, investigating exclusive B decays will require enhancements to the trigger system which allow for the efficient processing and collection of a properly enriched data sample. Furthermore, the early experience gained in the use of secondary vertex identification during the 1991 run will be important for developing instrumentation techniques for use at higher luminosity. Below we will consider these topics in more detail.

The detailed study of the B system will require copious production of B mesons. Two complementary paths are being pursued in the US - one is to build a difficult and expensive accelerator, a B factory, and to then have a relatively easy experimental task to measure the B's. (Even so, it still requires the construction of a large and expensive detector!) The other is to develop the instrumentation and techniques to exploit the existing Tevatron collider, which will produce 3×10^9 B's with $P_T > 10 \text{ GeV}$ in the region $|\eta| < 1.5$ in a 500 pb^{-1} run. We see this as an evolutionary program which will develop with experience and ingenuity, much as the studies of the K system or of dilepton production have evolved. We already observe, from our present data, an inclusive electron Pt spectrum consistent with that expected from B decay. The dilepton 'background' to the top search is consistent with expectations from B pairs. We see D^* 's and D 's quite clearly (Fig. 2-5), and studies of exclusive decays, such as $B \rightarrow \psi K_s^0$, are in progress. Another analysis in progress studies the production rate for B mesons at high P_T using the semileptonic decay modes: $B^{0,-} \rightarrow e^- \nu D^0 X$. The electron and the $D^0 \rightarrow K^- \pi^+$ decay are detected in b-jets. Figure 3-24 shows the $K^- \pi^+$ invariant mass spectrum for oppositely charged track combinations near high- P_T electron candidates. Figure 3-25 shows the invariant mass distribution for eD^0 obtained by subtracting the sidebands about the D^0 signal in Fig. 3-24 from the data centered on the peak. The subtracted distribution is confined to the region below the B-meson mass, as expected for the semi-leptonic final state.

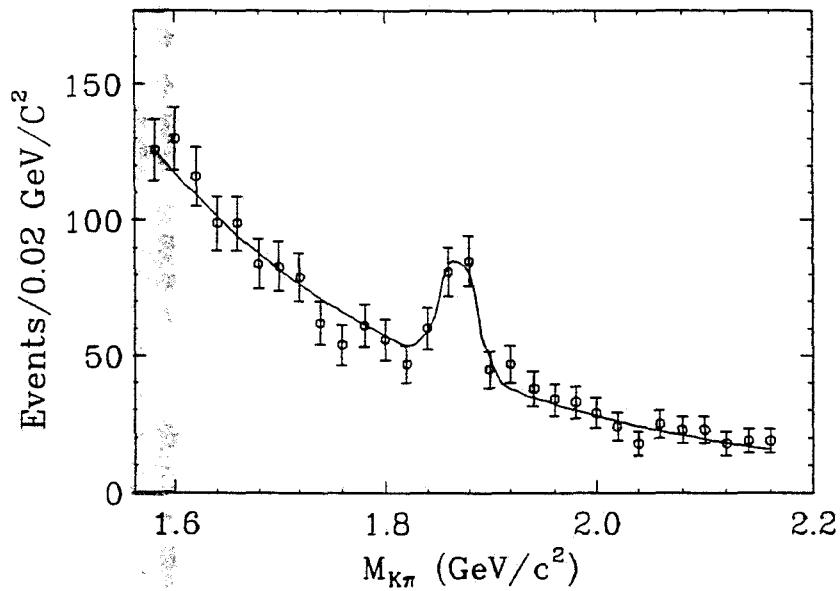


Figure 3-24: Invariant Mass Spectrum $K^- \pi^+$ ($K^+ \pi^-$) combinations for hadron tracks near a high- P_T e^- (e^+).

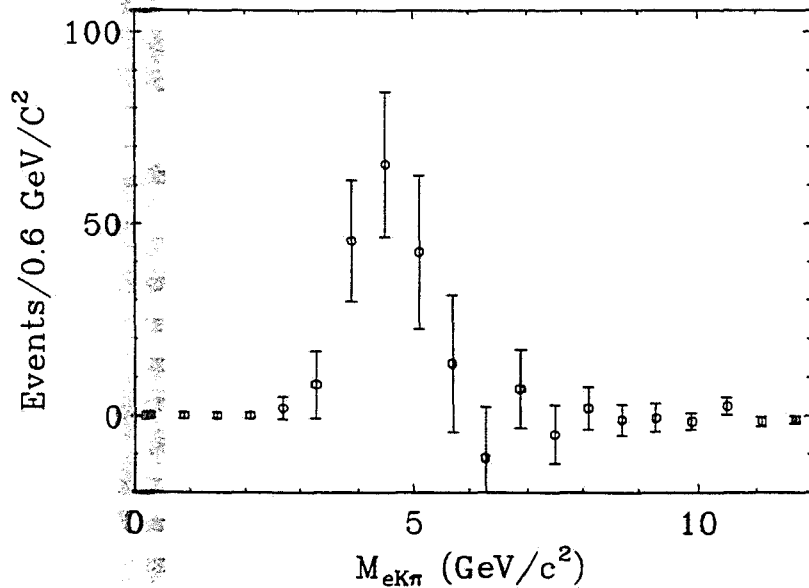


Figure 3-25: Invariant mass spectrum for $e^- K^- \pi^+$ ($e^+ K^+ \pi^-$) for combinations in the D^0 peak ($\pm 30 \text{ MeV}/c^2$) shown in Fig. 3-24. Sidebands ($\pm 90 \text{ MeV}/c^2$) in the $K\pi$ spectrum have been subtracted to reveal the $e^- D^0$ ($e^+ \bar{D}^0$) contribution. The spectrum peaks below the B-meson mass due to the missing ν and additional pions in the B semileptonic decays.

Exclusive Studies

The ultimate scale of the event sample available for exclusive studies is set by the total cross section above some reasonable trigger threshold for the lepton. A conservative estimate can be based upon the inclusive lepton sample collected in the 1988-89 run of CDF. Enhancements to the trigger system such as increased muon trigger coverage and online vertex or B topology triggers will allow us to lower these thresholds significantly, giving a much larger acceptance than in the past. An alternate sample selection could be based upon a high p_t $\psi \rightarrow l^+l^-$ trigger. This would be a smaller data set but contain less background.

In an inclusive single lepton sample, a typical analysis approach would be to look for the second B in an event tagged by a lepton with p_t below about $20 \text{ GeV}/c$. As a benchmark we use the inclusive lepton sample with the following cumulative assumptions:

1. $\sigma_{b\bar{b}}(p_{tB} > 10 \text{ GeV}/c) = 1.5 \mu\text{b}$ for $|\eta| < 1.5$
2. Branching ratio into one or more electron = 0.24
3. Branching ratio into one or more muon = 0.24
4. Probability for one lepton $p_t > 7 \text{ GeV}/c = 0.2$
5. Reconstruction and triggering efficiency for electrons = 0.3
6. Reconstruction and triggering efficiency for muons = 0.7

The electron and muon effective efficiencies are then 0.014 and 0.033 respectively. Assuming an integrated luminosity of 500 pb^{-1} the samples include 1.1×10^7 and 2.5×10^7 electron and muon decay candidates respectively. This sample exceeds a reasonable event writing rate and must be reduced and enhanced by specific triggering and filtering strategies, such as a vertex tag and some level of full reconstruction for the other B particle. Typical efficiencies for these could be in the range 0.05 to 0.3. CDF could, thus, be sensitive at the few event level to branching ratios as small as 10^{-6} . Enhancing the acceptance or further reducing single lepton p_t trigger thresholds will improve this significantly.

With a sensitivity of 10^{-6} CDF might detect classic rare B decays such as $B \rightarrow Kl^+l^-$ at the level of the Standard Model prediction. Such decays test the Standard Model at the one loop level. Limits might also be set for forbidden decays such as $B \rightarrow \mu e$. Correspondingly larger samples of B_s (not produced at the $\Upsilon(4S)$) exclusive modes could also be studied, such as $B_s \rightarrow \psi\phi$. While such modes will be observed in the 1991 run, the quantities available in a 500 pb^{-1} data set will be large enough to permit more accurate and systematic comparisons of B_s mass and lifetime with those of B_d and charged B 's. Significant samples of B baryons and B_c mesons will be produced as well.

Mixing

The determination of the parameters which describe mixing in the B^0 system are of fundamental importance in constraining the elements of the Cabibbo-Kobayashi-Maskawa (CKM)

matrix. The phenomenology of mixing in the B^0 system has been discussed by many authors⁶⁶. The parameter which determines the oscillation probability is the ratio $x = \frac{\Delta M}{\Gamma}$ where ΔM is the mass difference between the mass eigenstates and Γ is the average decay rate. The probability that a B^0 with mean lifetime, τ , created at $t = 0$, decays at t as a \overline{B}^0 is given by,

$$P(B^0 \rightarrow \overline{B}^0; t) = 0.5 \exp(-\Gamma t) (1 - \cos(\frac{x t}{\tau})).$$

Evidence for mixing has been reported in the B_d system by ARGUS⁶⁷ and CLEO⁶⁸ with $x_d = 0.7$. Significantly higher frequency oscillations are expected in the B_s system due to the estimated ratio of matrix elements $|V_{ts}|/|V_{td}|$. For the B_s system x_s is expected to be greater than ~ 3 . A measurement of x_s when combined with x_d from e^+e^- measurements will constrain the element $|V_{td}|$. A time integrated measurement of mixing will give no useful information on x_s or the CKM element $|V_{td}|$. For the B_s , where mixing is large, x_s can only be determined by measuring the time dependence of the oscillation. This is a very demanding measurement but would be an important result from a program of B physics at the Tevatron collider.

By using the vertex detector it may be possible to observe the time evolution of the $B^0 - \overline{B}^0$ system and thereby determine x_s experimentally. This measurement has been considered as the goal of a new experiment at the CERN collider⁶⁹ relying on the full reconstruction of 10^4 exclusive flavor tagged hadronic states. This approach is demanding and suffers because the fully reconstructed modes will be inefficient. As an alternative, an early study has been made to determine whether this measurement could be done with CDF by studying the decay vertex distributions of dilepton events. This "semi-inclusive" measurement relies on a considerably less sophisticated event reconstruction and trigger requirement than the CERN experiment.

In the dilepton decay vertex measurement, events of the type $p\overline{p} \rightarrow l^\pm l^\pm X$, where $ll = ee, e\mu, \mu\mu$, are used. The events are divided into two samples on an event by event basis depending upon whether the leptons are opposite sign or same sign. These leptons will be a combination of charged and neutral B decay products, mixed and non-mixed, as well as background. For each event, the ratio, $L_n = \frac{L_{decay}}{p_B}$, of the B decay length divided by the B momentum is entered for each B into the like- or unlike-sign distribution. The distributions are added and subtracted, bin by bin, to form a second set, SUM and $DIFF$. The former is just the decay distribution of all B 's in the measurement, an average over the lifetimes of B_s , B_d , and charged B mesons. The latter contains a non-exponential component determined by B_s oscillations above a background due to the non-mixed parts. To factor this background out, the ratio $DIFF/SUM$ is formed.

These distributions are shown in Fig. 3-26 for $x_s = 5$. For these figures, $b\overline{b}$ events were generated with ISAJET, demanding a lepton $p_t > 10 \text{ GeV}/c$. They are not smeared by finite resolution on the decay distance or the B meson momentum. In practice, the B meson momentum determination is the major limitation on such a measurement. In Fig. 3-27 the same set of plots for L_n are shown where instead the B meson momentum is estimated as equal to the lepton momentum. This is a reasonable approach since most lepton triggers in

CDF are biased towards B mesons which decay into relatively stiff leptons. Improvements will result if additional particles can be assigned to the B decay vertex, though at the expense of efficiency.

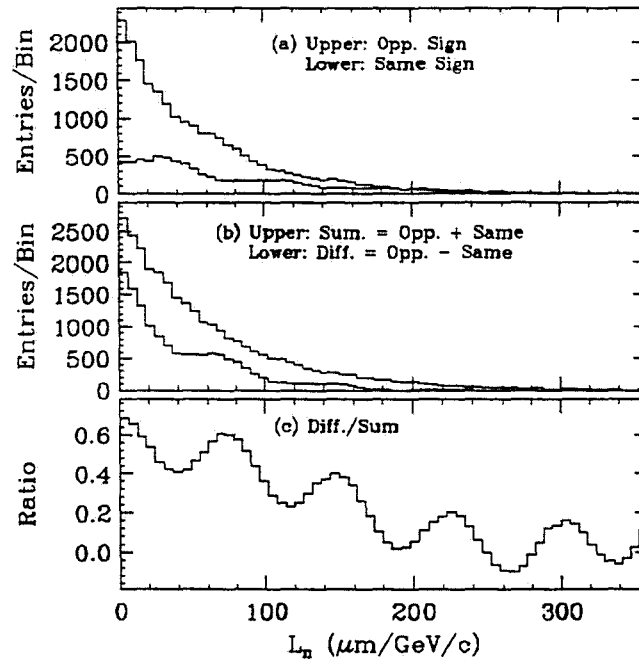


Figure 3-26: B^0 mixing with $x_s = 5$, distributions of L_n for (a) opposite (upper curve) and same (lower curve) sign events; (b) sum (upper curve) and difference (lower curve) of curves in (a); and (c) ratio of difference/sum.

An estimate can be made of the integrated luminosity needed to attempt such a measurement. This estimate will be based again upon acceptances and efficiencies which apply to the previous runs of CDF (as listed above in the discussion of exclusive studies), and so are conservative. For this analysis a sample of dileptons with both vertices measured is required. In addition to the factors listed earlier we take also, the probability of both leptons having $p_t > 5 \text{ GeV}/c$ to be 0.1 and the lepton vertex reconstruction efficiency to be 0.3. Then the efficiencies for each channel will be, $\epsilon_{ee} = 1.2 \times 10^{-5}$, $\epsilon_{e\mu} = 2.7 \times 10^{-5}$, and $\epsilon_{\mu\mu} = 6.4 \times 10^{-5}$. The total efficiency is 1.0×10^{-4} , resulting in $150 \text{ events}/\text{pb}^{-1}$ with both vertices measured. To resolve x_s to ± 2 units up to a value of ~ 10 we estimate that $\sim 10^4$ vertex measured pairs are needed. This implies that the integrated luminosity required approaches 70 pb^{-1} . With a data set based upon 500 pb^{-1} the mixing measurement can be done in significantly greater detail. It may be possible to reconstruct more of the tracks in the decay and thereby reduce the major smearing effect coming from the use of the lepton momentum as an estimate of the B momentum. Systematic effects and biases which will be

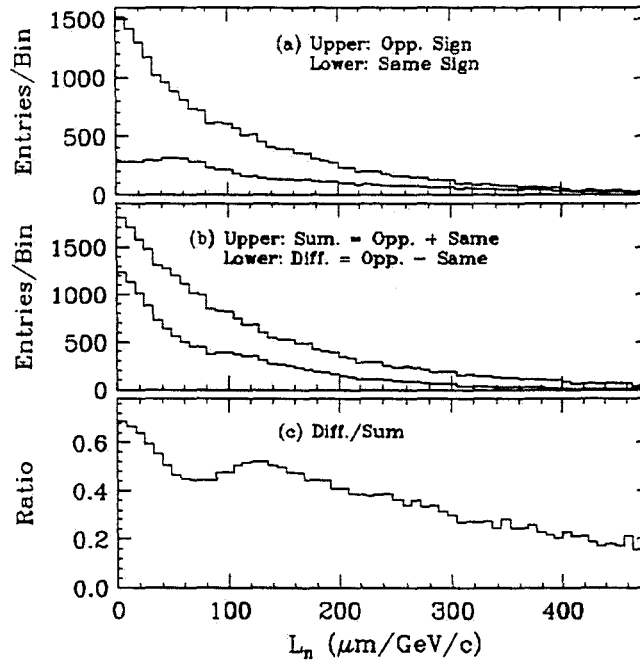


Figure 3-27: B^0 mixing with $x_s = 5$, distributions of L_n including effects of momentum smearing ($\sim 30\%$) resulting from the use of p_{lepton} as an estimate of p_B , for (a) opposite (upper curve) and same (lower curve) sign events; (b) sum (upper curve) and difference (lower curve) of curves in (a); and (c) ratio of difference/sum.

important to understand in such a measurement can also be studied with more precision. A luminosity of 500 pb^{-1} represents a comfortable statistical margin for the measurement of mixing in the B system at CDF.

3.5 Exotic Physics

SUSY

\tilde{A}_T is an important signature for SUSY physics. Searching for an excess of high \tilde{A}_T events allows us to set limits on SUSY production. With 4.4 pb^{-1} data, we are sensitive to masses of about $150 \text{ GeV}/c^2$. Our sensitivity is limited not by production cross sections, but by how well we can estimate the standard model \tilde{A}_T backgrounds. We use our CDF data set for this. For $\tilde{A}_T > 40 \text{ GeV}$, we have 98 events in our 4.4 pb^{-1} data set, which is consistent with the expected background of 92 ± 18 events. The uncertainty on the background is about 25%, and is dominated by the finite statistics of our W and Z data sets, which are used in the background estimation. With 100 pb^{-1} of data, we estimate that the background uncertainties will be less than 10%. This will allow us to probe supersymmetry to masses of larger than $220 \text{ GeV}/c^2$.

Leptoquarks

Leptoquarks are scalar, color triplet objects with lepton number. They are predicted in several theories like Technicolor or supersymmetry extensions. We are sensitive to two production mechanisms for Leptoquarks: Pair production, and Drell-Yan production of lepton+leptoquark. Leptoquarks are expected (if they exist) to conserve generation number. Then, pair production via gluon fusion will populate equally all three types of leptoquarks, while Drell-Yan production will generate almost exclusively first generation leptoquarks. Typical production cross sections for gluon fusion to form a leptoquark pair are: 1 nb ($M = 40 \text{ GeV}/c^2$), 0.01 nb ($M = 100 \text{ GeV}/c^2$), 1 pb ($M = 160 \text{ GeV}/c^2$). For Drell-Yan production, cross sections are up to eight times larger, depending on the model.

Leptoquarks decaying into quark+neutrino generate \tilde{A}_T signatures. An ongoing analysis of 4.4 pb^{-1} data indicates we will be sensitive to pair-produced leptoquarks with masses up to about $70 \text{ GeV}/c^2$. With 100 pb^{-1} , we will probe up to about $160 \text{ GeV}/c^2$.

For decays into quark+lepton, analysis of the Drell-Yan mode will be sensitive at higher levels, due to less background. (The main background is regular Drell-Yan lepton pairs.) A signal of 100 events should be visible above background. This means we will be sensitive to masses up to about $190 \text{ GeV}/c^2$ for this decay mode in 100 pb^{-1} data. Searches for second and third generation leptoquarks decaying into quark+lepton should be sensitive to about $160 \text{ GeV}/c^2$ with 100 pb^{-1} of data.

Charged Higgs

The top quark signal may be obscured if there is a charged Higgs particle at lower mass. Then the major decay mode of top could be $t \rightarrow bH^+ \rightarrow b\tau\nu$. This decay mode would not generate the electrons and muons used for conventional searches. However, depending on the mass of the top and charged higgs, \tilde{A}_T searches can be sensitive to these decays. CDF's $\tilde{A}_T > 40 \text{ GeV}$ observed cross section is about 25 pb , consistent with Standard Model expectations. The uncertainty on this expectation is about $\pm 6 \text{ pb}$. Therefore we are

sensitive to 15 pb of excess cross section. From Barger and Phillips, MAD/PH/484, we can see that this sensitivity to excess rates of large \tilde{A}_τ events can rule out the existence of top/higgs combinations of $50 \text{ GeV}/c^2 < M_t < 80 \text{ GeV}/c^2$, $30 \text{ GeV}/c^2 < M_H < 70 \text{ GeV}/c^2$, for branching fraction of H into τ larger than 10%-20%. An analysis of the 4.4 pb^{-1} data set is ongoing. We expect a search for this mechanism will be sensitive to $M_t = 140 \text{ GeV}/c^2$ in 100 pb^{-1} of data.

3.6 Rare Processes

There are some indications of "ZOO" events, which are defined as those where the expected rate in a given data run from known physics processes is very low - of order 1% probability or less. Interpretation of such events is a delicate matter. There are dangers in over- or under-interpreting their significance. Since there are many channels where such events could show up, it is not surprising that we have seen some. On the other hand, any one of these ZOO events might be the "tip of the iceberg", the first hint of new physics which might be confirmed with more statistics in future CDF runs. In this section, we describe briefly several of the classes of ZOO events found so far in the 1988-9 CDF data run, and speculate on the physics which might explain them *if they are not due to statistical fluctuations or detector inefficiencies*.

The first two items were uncovered in the study of high P_T distributions. The rest are individual ZOO events. Note that the "standard model probabilities" given below are estimates subject to a variety of uncertainties. One must be clever enough to base the estimate on the dominant process(es) leading to the observed topology. Such expectations could easily be wrong by factors of order 3-5.

Boson-Multijet Events

We observe two high $P_T Z$'s: a $Z \rightarrow e^+e^-$ with $P_T = 213$ GeV/c recoiling against two jets with observed E_T of 136 GeV and 54 GeV; a candidate for $Z \rightarrow \nu^+\nu^-$ inferred from a corrected \cancel{E}_T of ~ 230 GeV recoiling against four jets with observed E_T of 93 GeV, 90 GeV, 31 GeV and 10 GeV. These events seem well separated from the falling P_T spectrum of Z 's.

In an attempt to understand if this is a significant signal, all high $P_T W/Z \rightarrow$ leptons candidates were examined to see if they are consistent with the expected P_T dependence. For those recoiling against a single jet, the P_T dependence appears to be consistent with expectation, as are those events with high transverse momentum for the W or Z boson (P_T^{boson}) recoiling against multijets with $P_T^{boson} < 100$ GeV/c.

There appear to be five anomalous high P_T^{boson} events recoiling against multijets with P_T^{boson} above 125 GeV/c. They are well separated from the steeply falling low P_T^{boson} (< 125 GeV/c) events. In addition to the two Z events mentioned above, there are two W+multijet candidates (one $W^\pm \rightarrow e^\pm \nu_e$ and one $W^\pm \rightarrow \mu^\pm \nu_\mu$). All four events have P_T^{boson} roughly 50 GeV/c higher than the highest $P_T W/Z$ + single-jet event. Furthermore, all four events have a second jet with very high E_T (corrected E_T above 50 GeV). Three of the four have a third jet with corrected E_T above 20 GeV. This is extremely unlikely (of order 0.1 or less of W/Z + single-jet rate) if one assumes these events to be normal QCD production of high $P_T W/Z$'s. Thus, we only expect of order 0.05 such events in our data sample, while we see four events. The fifth candidate has three stiff jets ($E_T = 70$ GeV, $E_T = 50$ GeV and $E_T = 30$ GeV) and an electron with $E_T = 29$ GeV and corrected \cancel{E}_T about 180 GeV.

The number of such events is unexpected, considering either the boson + single-jet behavior or the behavior of the low- E_T part of the boson + multi-jet E_T spectrum.

High Pt Upsilon Candidates

Several candidates for low mass ($\sim 10 \text{ GeV}/c^2$) dileptons with P_T near $100 \text{ GeV}/c$ were observed. The presence of only a single Υ at this high P_T would be unexpected, but unremarkable. However, the presence of several such events suggests that we should watch this in future runs for interesting physics.

Diphoton + multijet event

We have one unusual diphoton + jets event. The three leading 'partons' are in a "Mercedes" topology, consisting of a 225 GeV (corrected E_T) jet, a $197 \text{ GeV } E_T \gamma$, and a second $98 \text{ GeV } E_T \gamma$ (Note that we can not tell whether these photon candidates are γ 's or π^0 's; there are no tracks pointing to those "photons", thus implying a fragmentation-z of at least ~ 0.95 if this is a π^0). There are also three softer jets of order $15\text{-}30 \text{ GeV}$. There is no significant \cancel{E}_T .

The (uncorrected) cluster summed E_T of this event is about 525 GeV . Only a few dozen events in the 1988-9 run have such large summed cluster E_T . The estimated probability of having two photons in an event with cluster summed E_T above 500 GeV is about 10^{-4} . We find only one single- γ + jet event with high summed E_T ($\sim 530 \text{ GeV}$). This has a more likely topology (photon directly opposite the jet in azimuth).

Trilepton - Jet event

We have one unusual $e+\mu+\text{jet}+\text{soft-}\mu$ event - our only dilepton top candidate. The E_T 's of the four "partons" are: 40 GeV ($\mu \#1$), 32 GeV (e), 11 GeV (jet; corrected E_T about 20 GeV), and 7 GeV ($\mu \#2$, at rapidity near 2). Known physics processes (excluding top) would give a probability of order 0.01. Among them :

- We expect one Z into τ pairs with subsequent decay into $e + \mu$ for e and μ P_T threshold of $15 \text{ GeV}/c$; for threshold of $30 \text{ GeV}/c$, the probability is less than 0.01. The event is even less likely if we put in the probability of the jet and the second muon.
- We expect 0.15 W pairs decaying into $e + \mu$. The P_T of the leptons are consistent with this hypothesis. However, if we take into account the jet and the second muon, the probability drops to ~ 0.01 .
- We expect 0.05 $W+Z$ or $W+\text{Drell-Yan}(\text{mass}>30 \text{ GeV}/c^2)$. This could explain the second muon. The dimuon mass is near $50 \text{ GeV}/c^2$. Taking into account the 20 GeV jet would reduce the probability ~ 0.01 .
- In contrast, the electron and $\mu \#1$ P_T is consistent with coming from $t\bar{t}$ assuming a top mass above $90 \text{ GeV}/c^2$. If the top mass is above roughly $120 \text{ GeV}/c^2$, the b jets from $t \rightarrow b + W$ would have E_T of order $15\text{-}30 \text{ GeV}$; 22% of the events would have one b jet decaying via $b \rightarrow \mu + \nu + c$, which would have $E_T(\mu)$ about $5\text{-}10 \text{ GeV}$. Thus, this event is entirely consistent with $t\bar{t}$ and a top quark mass above $\sim 120 \text{ GeV}/c^2$. It is also consistent with the expected cross section. We would love to have higher integrated luminosity and a hundred of these.

Concluding Remarks

The exploration of the highest available energies is one of the foremost goals of the US High Energy Physics program. CDF has already detected jet events with a parton-parton center-of-mass energy close to a TeV in an sample of 4.4 pb^{-1} . We also observe small numbers of unusual events with very high center-of-mass energies. The limitations are statistical only. The detector resolves the events unambiguously, such that each event carries a lot of weight. One needs, however, more than the handful of events we have now for discovery.

The Tevatron is unique, and will remain so for quite a long time, in being able to explore the energy region up to a TeV. There are likely to be big discoveries in this energy region, and with an improvement to two orders of magnitude larger than our present sample our physics reach is far beyond that available anywhere else. It is the discovery of something entirely new that is the big prize for Fermilab, and the Collider running at high luminosity is its best shot! We want to go for it with a detector able to accomodate and exploit these opportunities.

4 Hardware Upgrades

This section discusses our plans to upgrade CDF for the 1993 run. Figure 1-1(a) shows the detector as it was configured in the 1988-89 run. At this writing, construction is in progress to prepare CDF for the 1991 run. See Fig. 1-1(b). We will add a central muon extension (CMX) and a silicon vertex detector (SVX) to the system shown. The vertex time projection chamber (VTPC) will be replaced with a design better able to withstand the higher luminosity (VTX), and the forward tracking chamber will be abandoned.

Figure 1-1(c) shows the detector as proposed for the 1993 run in comparison with the 1989 and planned 1991 configurations. A more detailed view of the 1993 version is given in Fig. 4-1. An overview of the strategy was presented in Sec. 1. This section discusses the upgrade in terms of each of the major subsystems. While all are discussed, the "big ticket" items in the proposal are: a new plug scintillation calorimeter to replace the gas calorimeters, a radiation-hardened replacement for SVX, improved muon coverage by moving the muon toroids closer to the central detector and major modifications to the data acquisition electronics. We also need substantially enhanced offline data analysis facilities and discuss them in this section. Cost estimates are given in Sec. 5 as a CDF budget request plus a separate request for offline computing resources.

Since much of the work and cost scales with the number of detector channels, we summarize in one place (Table 4-9) the number of readout channels associated with each system. For 1993, the front end electronics must be rebuilt for all Rabbit channels.

System		Rabbit Channels			LRS1879 Channels		
		1989	1991	1993	1989	1991	1993
CEM	Central EM ADC's	960	960	960			
CEG	Central EM ADC's (x16)	960	960	-			
CES	Central EM Strips	9216	9216	9216			
CET	Central EM TDC's			480			
CHA	Central Hadron ADC's	768	768	768			
CHG	Central Hadron ADC's (x16)	768	768	-			
CHT	Central Hadron TDC's	384	384	384			
WHA	End Wall Had. ADC's	768	768	768			
WHG	End Wall Had. ADC's (x16)	768	768	-			
WHT	End Wall Had. TDC's	288	288	288			
CCR	Central Crack Detectors	480	480	480			
CPR	Central Pre-Radiator	-	1536	1536			
CDT	Central Drift Tubes	3024	3024	3024			
CMU	Central Muon	3456	3456	3456			
CMUP	Central Muon Upgrade				-	864	950
CMEX	Central Muon Extension				-	1632	2208
PEM	Plug EM ADC's	6912	6912	-			
PES	Plug EM Strips	1488	1488	-			
PEA	Plug EM Anodes	272	272	-			
PHA	Plug Hadron ADC's	1728	1728	-			
PHW	Plug Hadron Wires	480	480	-			
FEM	Forward EM ADC's	5760	5760	-			
FEA	Forward EM Anodes	1200	1200	-			
FHA	Forward Hadron ADC's	2880	2880	-			
FHX	Forward Hadron Wires	1120	1120	-			
FMU	Forward Muon Wires				4608	4608	6000
FMS	Forward Muon Pads	2160	2160	-			
FMS	Forward Muon Scintillator	-	-	2160			
CTC	Central Tracking Drift Ch.				6180	6180	6180
VTPC	Vertex TPC Wires				3072	-	-
VTPC	Vertex TPC Pads (FADC's)				1500	-	-
VTX	Vertex Time Projection Ch.				-	8448	8448
FTC	Forward Tracking Radial Ch.				3024	-	-

(continued)

(continued)							
System		Rabbit Channels			Fastbus Channels		
		1989	1991	1993	1989	1991	1993
SVX	Silicon Vertex Detector				-	10000	-
SVX	Rad-Hard SVX				-	-	10000
	Plug Pre-Radiator ADC	-	-	736			
	Plug Pre-Radiator TDC	-	-	736			
	Plug Strip Chambers	-	-	9000			
PSEM	Plug Scintillator ADC's (EM)	-	-	2688			
	Plug Scintillator TDC's (EM)	-	-	1344			
PSHA	Plug Scintillator ADC's (Had)	-	-	912			
	Plug Scintillator TDC's (Had)	-	-	456			

Table 4-9: Number of readout channels for each of the CDF subsystem detectors for the 1988-89 run and as planned for 1991 and 1993. Note that the SVX does not use LRS 1879's. Instead it uses a Fastbus-based sequencer. The SVX chips do a sparse scan readout of 48,000 (150,000) channels for the 1991 (1993) run.

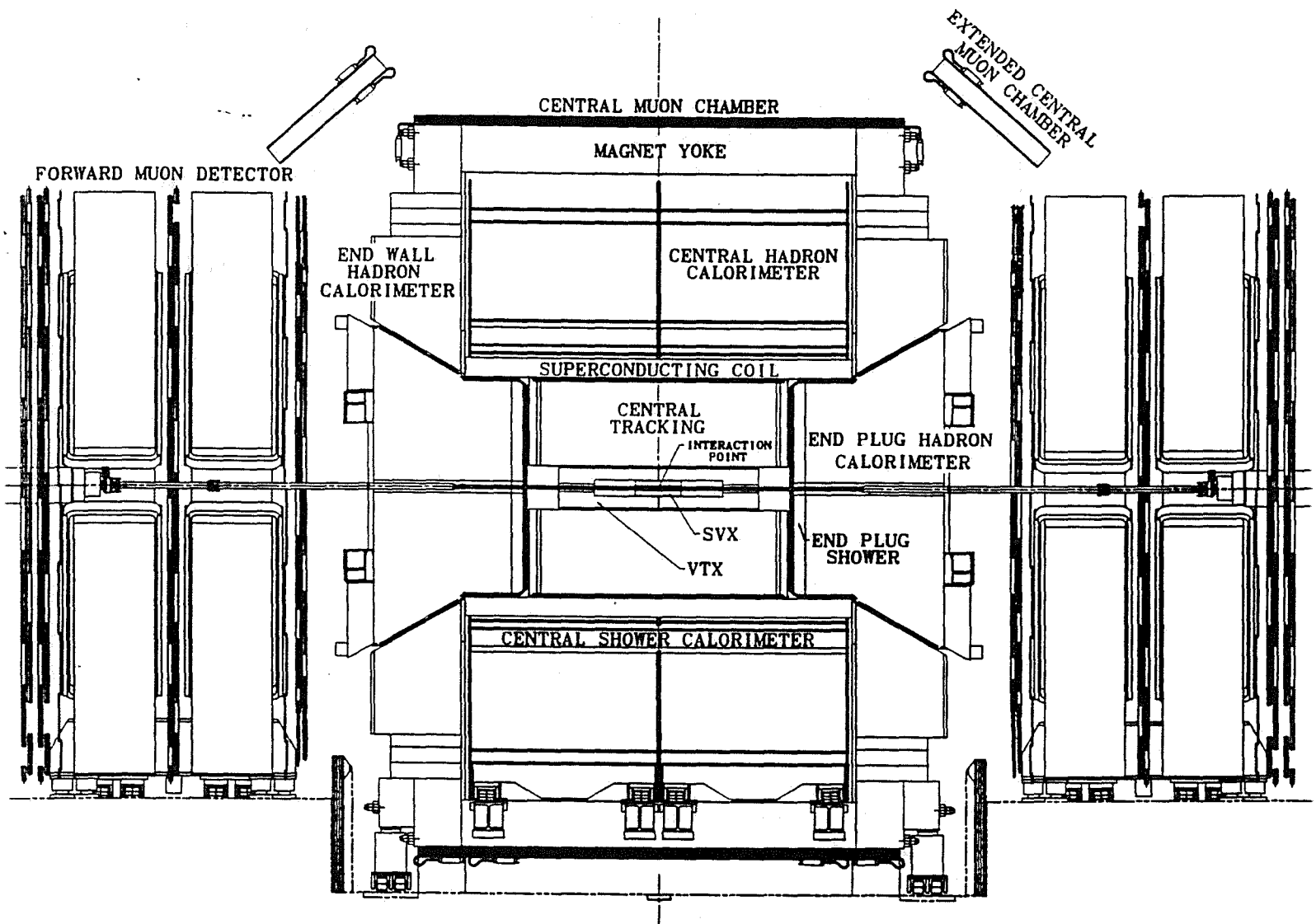


Figure 4-1: A view of the CDF detector for the 1993 run, showing relationships of the various subsystems with the new plug calorimeter and the relocated forward muon system.

4.1 Tevatron Upgrade

The Tevatron upgrade will occur in several phases.

- Separators are being installed in the ring to reduce the beam-beam interaction. Planned completion: 1991.
- The bunch structure will be changed from the present 6-bunch operation, with a 3.5 μsec interval between beam crossings, to 36-bunch operation with 395 nsec between crossings. Details of the bunch parameters are given in Table 4-10. Planned completion: 1993.
- A rapid-cycling Main Injector will replace the present Main Ring in all its functions. Planned completion: 1994.

These upgrades will benefit all parts of the Fermilab fixed target and collider programs and will provide a new 120 GeV slow spill at 2 μA for fixed target experiments.

Quantity	Value
Circumference	6.283185(3) km
Single-turn Period	20.9586 $\mu\text{ sec}$
Number of RF buckets	1113 = $3 \times 7 \times 53$ = 21×53 = 3×371
RF Period	18.831 nsec
RF frequency	53.105 MHz
36-Bunch Collider Operation	
Number of Groups of Populated Bunches	3
Populated Buckets per Group	12
Interval Between Populated Buckets	21 RF Periods = 395.4 nsec
Length of Populated Interval	11 \times 21 RF Periods = 4350 nsec
Length of Empty Interval	140 RF Periods = 2636 nsec

Table 4-10: Tevatron Parameters Governing Timing of Bunch Crossings

The implications for CDF are considerable. Most important, the physics reach of the detector will be extended by the higher luminosity. This, however, does not come for free. Much of the present data acquisition system will have to be replaced in order to avoid an unacceptable increase in dead time due to the shorter bunch spacing. A Level-0 trigger

mounted directly on the detector must be designed and built. Shorter signal-collection times are an important consideration. Individual detector systems will have to survive in a much more intense radiation field, both in terms of tolerable instantaneous noise levels and long term damage.

4.2 Plug and Forward Calorimeters

Extensive R&D is in progress by members of CDF to study the properties of various calorimeter technologies for use at angles below $\sim 35^\circ$. This region is presently served by gas calorimeters in the plug (PEM, PHA) and forward (FEM, FHA) regions.

The increased Tevatron luminosity and 400ns bunch spacing in the 1993 run pose a number of serious technical problems for the gas calorimeters. R&D is taking place (bench tests and test-beam work) to understand how they can be kept operational for future runs. Faster response times and lower noise levels can be achieved. However, the chamber high voltage will have to be reduced to prevent glow mode at very high luminosity and to reduce aging. This will result in some deterioration of the calorimeter energy resolution. Thus, the gas calorimeters may eventually have to be replaced if CDF is to operate successfully at the high luminosities planned for the upgraded Tevatron. We should be prepared for this possibility as early as the 1993 run.

Work is in progress to develop scintillation plastic as a potential replacement for the gas detectors. Our R&D efforts are following two scintillator technologies: tiles and fibers. Prototypes of each have been designed and are scheduled for test beam studies. Both share many of the advantageous characteristics described in detail in the following section, and preliminary designs indicate that they are not very different in cost.

In this document we present the plans and a cost estimate for the more conservative scintillator technology: tiles. This would allow CDF the most flexibility in carrying out its upgrade program, and would cause the least disturbance to the existing detector. The fiber design is an exciting technical challenge which, however, is less conservative in our present understanding. As an example of the possible use of fiber, a section below discusses an alternative scenario with a fiber-only EM calorimeter section together with a tile hadronic section.

Vigorous R&D will continue in all three technologies. As results from the test beam and other studies become available we will continue to evaluate the plans for the plug/forward calorimetry for 1993 and beyond, including whatever planning is necessary to keep the gas calorimetry as a fallback option for any part of the plug/forward system.

4.2.1 Plug Scintillation Calorimeter

A key element in CDF's upgrade program is the possible replacement of the gas calorimeters in the plug ($38^\circ < \theta < 10^\circ$) and forward ($10^\circ < \theta < 3^\circ$) regions with a single scintillator-based plug calorimeter. Like the central calorimeter, it would consist of a lead/scintillator electromagnetic shower calorimeter followed by an iron/scintillator hadron calorimeter. As will be discussed below, this new device offers several advantages: tripling the density of the EM calorimeter eliminates serious holes in the CDF electron and jet acceptance; the finely segmented preradiator and a position detector at EM shower max will allow a reduced trigger threshold for electrons and photons; calorimeter compensation ($E/H = 1$) improves jet resolution for better measurements of jet E_T 's and jet spectroscopy; removal of the forward calorimeters allows the muon toroids to be brought forward for increased muon

coverage; the scintillator/phototube system offers improved uniformity and gain stability; and a reduction in the manpower required for maintenance and calibration. Figures 4-2 and 4-3 show views of the detector in the present and proposed configurations.

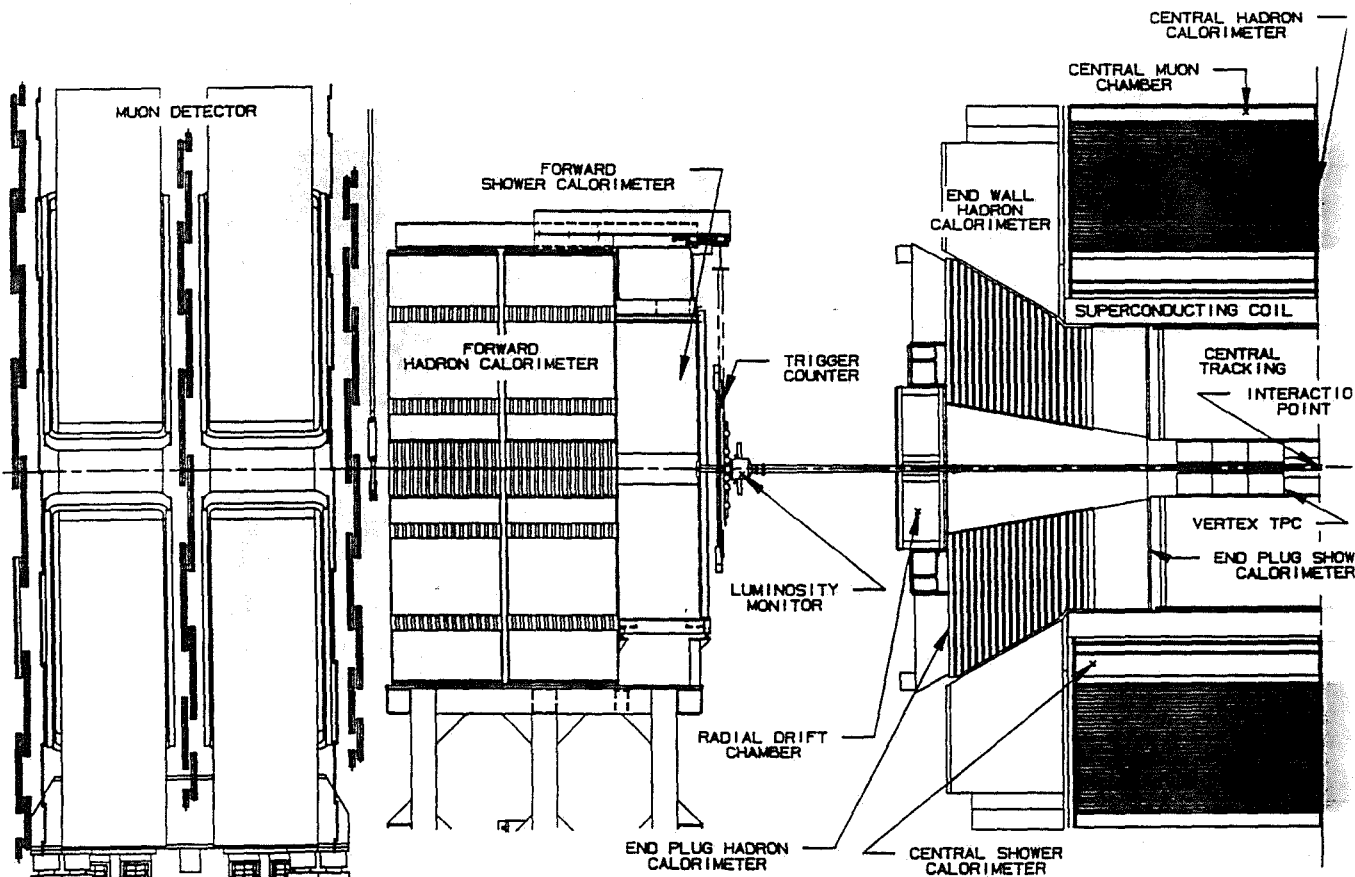


Figure 4-2: Side View of Existing CDF Detector

Tile Calorimeter Methods

An excellent technology for the hadron calorimeter and the EM preradiator and position detectors is a "tile" system constructed from scintillating plastic plates ("tiles") with wavelength-shifter optical fibers imbedded for readout. These tiles are assembled into planes of scintillator which replace the gas proportional chambers in the gaps between the existing absorbers. The projective towers are formed by the optical segmentation of the tiles within each scintillator plane. The clear optical readout fibers from each tile are led to phototubes outside of the calorimeter along the path currently taken by the electrical cables of the gas calorimeters. The "tile" technique has already been successfully employed in a full scale endplug calorimeter [BNL 814] as well as several smaller-scale calorimeters [ref UA1, D0, etc.].

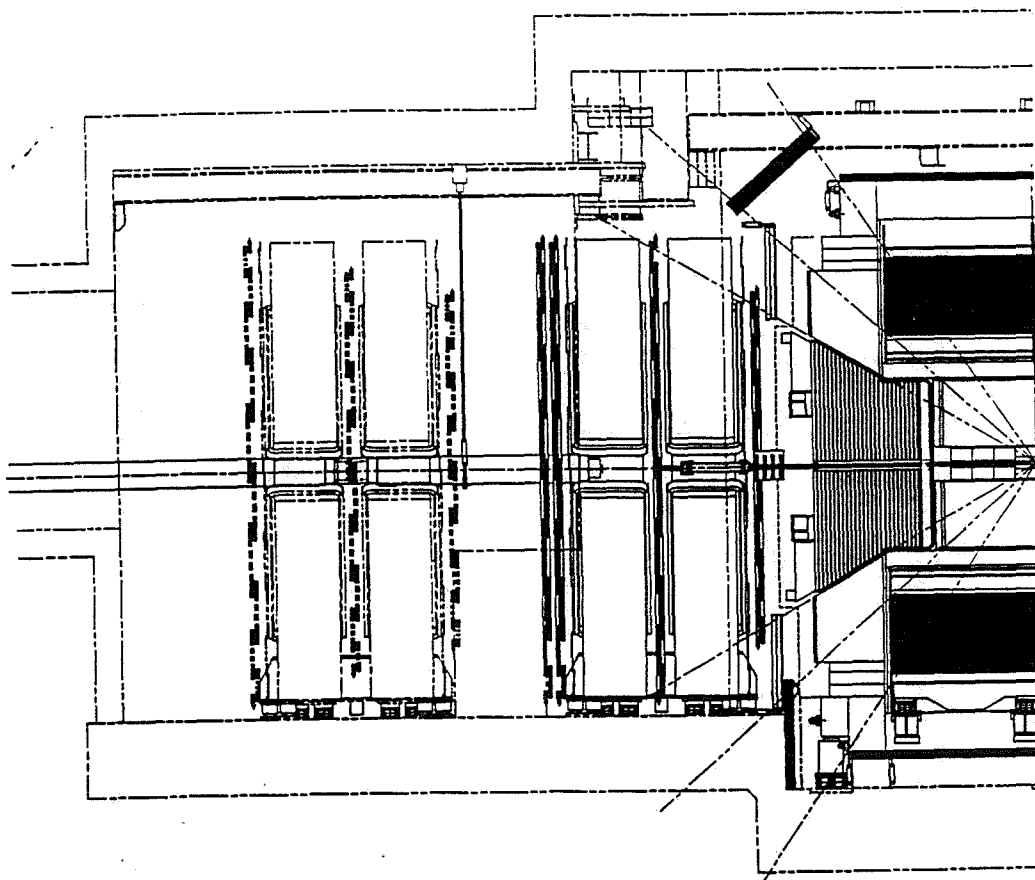


Figure 4-3: Side View of Upgraded CDF Detector. The plug calorimeter is now a single unit extending from 38° to 3° , and the muon toroids have been moved inwards. The density of the endplug EM calorimeter has been increased and the corner beveled to improve the hermeticity near the " 37° crack"

The "tile" configuration makes it possible to preserve the existing steel structure of the plug hadron calorimeter. By preserving this structure we gain several benefits: The cost of the new calorimeter is reduced by about \$400K, the cost of replacing the steel. Stainless steel and other non-ferromagnetic materials will be used for modifications to the absorber structure, so that the central magnetic field is unperturbed and no new field mapping is needed. Similarly, no new magnetic forces are induced on the solenoid. The mechanical and magnetic structure is essentially unchanged, so we can be assured of the mechanical integrity of the detector.

In the case of the EM calorimeter the "tile" technique uses lead plates instead of iron as the EM absorber. A second possibility is a lead/scintillator "fiber" EM calorimeter. For simplicity, this document assumes that the "tile" technique is utilized for both the EM and hadron calorimeter; the "fiber" option for the EM calorimeter is described in a later section. Prototypes of both calorimeters are being evaluated in the current (spring '90) test

beam at FNAL, so that results will be available in time for production decision later this year.

The technique of tile calorimetry has several pertinent features: The light yield of this configuration is quite high, about 10x larger than the conventional scintillator plate/wave-shifter bar strategy (for example CDF, UA1, UA2, or ZEUS). This high light yield ensures good EM energy resolution, and allows us to design a compensating calorimeter with either lead radiator or steel absorber. The small size and flexibility of the readout fibers allows us to retain the absorber structures which were originally designed for use with the gas proportional chambers. In addition, each tile can be made quite uniform, with an rms variation of light yield with position of about 1% (in contrast of up to 20% variation in a conventional plate/WLS bar device). The spatial uniformity of this technique provides benefits to both electron and jet physics.

New Calorimeter Geometry

The density of the new EM calorimeter is approximately 3 times that of the existing gas EM calorimeter, whether one uses the "tile" or the "fiber" configuration. This eliminates one of the major hermeticity problems currently faced by CDF, the "37° Crack". This arises from electromagnetic showers in the range $35^\circ < \theta < 40^\circ$, which clip the corner of the endplug calorimeter and reach EM shower maximum inside the dead material of the solenoid. The situation is aggravated by the sizable structural elements located near the ends of the solenoid. The solution to this problem is twofold: Firstly, by increasing the density of the EM calorimeter we reduce the width of the "central-endplug transition region" in which EM showers can deposit significant energy in the solenoid. Secondly, by beveling the corner of the EM calorimeter, one can arrange for a sharp transition between the situation in which all of the EM energy is deposited in the endplug, or in the central EM calorimeters.

The higher density EM calorimeter will require less space in z (along the beam axis). In the free volume, we will add four 2" stainless steel absorber plates to the front of the hadron calorimeter. This provides additional active shielding in front of the 30° readout crack in the hadron calorimeter, in addition to the obvious benefits of better hadronic energy containment and reduced hadron punchthrough into the muon detectors. Additionally, if the forward gas calorimeters are to be replaced, it will be necessary to insert a set of stainless steel absorber disks into the 10° hole in the plug hadron steel structure – the "miniplug".

The $\eta - \phi$ segmentation of the new plug calorimeter is shown in Fig. 4-4. In contrast to the old CDF plug and forward calorimeters, we choose not to maintain the constant segmentation in η which results in a very large fraction of channels at small angles. Instead, we maintain an approximately constant physical tower size. This has the effect of concentrating the channel count at smaller η , where high- P_T physics occurs and where the momentum analysis of the solenoid is available. Coverage of the very forward region $3 < \eta < 4$ is necessary primarily for missing E_T resolution. Montecarlo studies indicate that the missing E_T resolution is not significantly degraded by this coarse tower granularity in the very forward region. The number of towers is determined primarily by the requirement of maintaining the 24-fold ϕ -segmentation of the trigger.

The hadron calorimeter tower size is somewhat coarser than the EM calorimeter tower size. This is reasonable due to the larger spatial extent of hadron showers. Integral numbers of EM towers, typically four, project into a single hadron tower. This alignment of boundaries simplifies the hadron/EM energy cut used in electron identification.

	EM	HAD
Segmentation	$\sim 8 \times 8$ cm	$\sim 24 \times 24$ cm
Total Channels	2688	912
Energy Resolution	$16\%/\sqrt{E}$	$80\%/\sqrt{E}$
Light Yield (photons/GeV)	≥ 200	≥ 30
Thickness	$22 X_0, 1 \lambda_0$	$7 \lambda_0$
Density	$0.6\rho_{Pb}$	$0.75\rho_{Fe}$
Unit Sampling Cell	2.5mm Scint + 5 mm Pb	2.5mm Scint + 2" Fe
Number of Samples	24	25
Expected E/H	1.06	1

Table 4-11: Overview of Proposed Calorimeter Upgrade. The EM (HAD) resolution is for a single electron (pion).

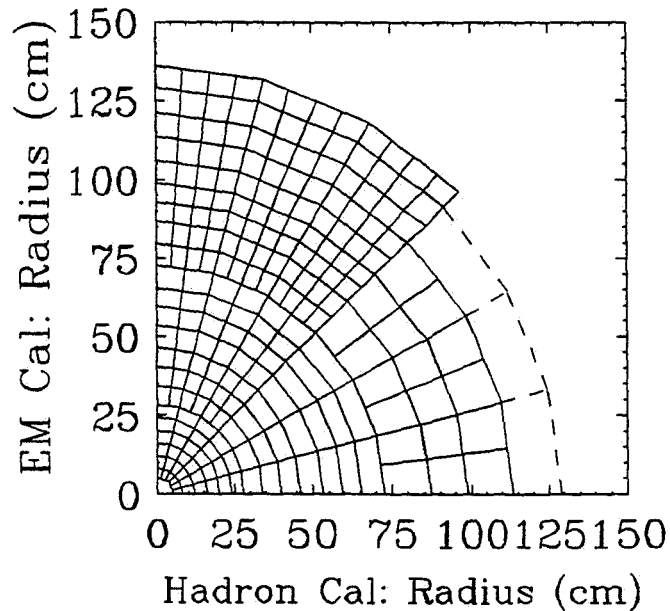


Figure 4-4: $\eta - \phi$ segmentation of the EM (top) and Hadron (bottom) Calorimeters. The electromagnetic section has $56 \times 24 = 1344$ towers, and the hadronic section has $19 \times 24 = 456$ towers, for a total of 1800 Photomultiplier tubes on each endplug. The outermost hadron segment (with 24-fold ϕ -symmetry) is actually part of the endwall hadron calorimeter.

Mechanical Considerations

The mechanical design of the tile-based calorimeter is largely determined by the decision to retain the iron of the plug hadron calorimeter. Several significant modifications are required:

1. A stainless steel insert ("miniplug") closes the hole from 10° to 3° in the existing hadron plug. This consists of a series of 2" stainless steel disks which are welded into the center holes of the existing 2" iron plates. The axial forces on individual iron plates (which are currently taken up by a set of support bars on the interior of the 10° hole) are transferred to either a stainless pipe or a set of Inconel rods at the interior of the stainless disk inserts.
2. Four additional 2" stainless plates are added to the front of the hadron calorimeter. This requires unbolting and replacement of the external support bars at the outer edges of the front of the hadron calorimeter, but no other changes to the structure of the device. These disks extend down to 3° and do not require "miniplug" inserts.
3. The increase in the weight of the plug from approximately 120 to 140 tons may require reinforcing the support arms. The support arms themselves are believed to be strong enough but their anchoring into the iron return yoke may need strengthening. This is under study.
4. The suspension of the lead plates in the plug EM calorimeter will be accomplished in a manner similar to the current PEM. The significant differences are the i) the new higher-density EM calorimeter is 25 cm deep instead of 60cm, which reduces the lever arms and the stresses on the structural members, ii) the lead sheets extend down to 3° instead of the current 10° , and iii) the outer 15cm of the corner is beveled at 38° for improved EM resolution near the " 37° crack".

Phototubes and Electronics

The phototube ADC/TDC cards required for the system are essentially identical to those used in the central calorimeter. Slight modifications may be necessary on the trigger output signals on the PM ADC cards. These cards contain all necessary circuitry for calibrations involving charge injection, flasher systems, and source current monitoring. The software and calibration procedures associated with these cards will be taken from those used in the central calorimeters.

The specification and testing of photomultiplier tubes is straightforward. Numerous CDF collaborators have experience with PM tube test procedures. The small cross section of the readout fiber bundle (0.5 cm^2) makes 1" diameter phototubes a practical and economical choice. The small tube size simplifies the mechanics and magnetic shielding of the PM housings.

The phototube mounting and cabling system is as follows. Optical fibers from both the EM and Hadron calorimeters are led out the 30° crack along the path currently taken by the readout cables for the gas calorimeter. These are led to an array of 1800 phototubes

and bases which are mounted along the 13m circumference of the back edge of the plug. We anticipate grouping the 1" PM tubes in mechanical modules containing 8-12 PMTs, so that the modules would be spaced at an average separation of 2-3" along this circumference. The axis of the PM tubes may be either parallel to the beam pipe, or radially away from it. In any case, the HV and signal cables are then routed to the readout crates and HV distribution racks currently used for the gas calorimeters. The minimum number of "Rabbit" readout crates required for the Phototube ADC's is: $(1800 \text{ channels}) / (12 \text{ channels/card}) / (20 \text{ cards/crate}) = 8 \text{ crates}$. Sixteen readout crates with power supplies already exist on each endplug. This leaves 8 crates at each end for preradiator, shower position detector, and PM TDC electronics (if required).

Calibration System

The calibration system will be similar to that which has successfully maintained calibrations to 1% accuracy in the central calorimeter. It will make use of charge injection, light flashers, and movable radioactive sources to measure the response of the scintillator, phototubes, and electronics. The chief design issues here are the number and locations of the imbedded sources, and their allowed motions. In the case of the hadron steel there is more than ample room for source motion over an entire plane of scintillator, since the scintillator tile assemblies are much thinner (3-4 mm) than the gas proportional chambers (15mm) which they replace. In the case of the EM calorimeter the constraints on space and dead areas are more severe, and a suitable compromise must be worked out. This task is made easier by the fact that the region which one has to monitor carefully for the first signs of radiation damage is a relatively small volume near EM shower max and close to the beam pipe.

The required calibration fixtures will be prototyped in the ongoing test beam cycle, using the existing test beam fixturing and infrastructure.

Preradiator and Shower-Max Position Detector Systems

The EM calorimeter design contains a preradiator and readout. It is a lead plate of $1.5 X_0$ thickness, followed by tiles of the same size and construction as the EM tiles. The expected light yield at the phototube is 4 pe/mip. For e/π separation, a cut of 5 mips (20 photoelectrons) is anticipated. The fibers are read out by multi-channel phototubes, Hamamatsu 64 channels/tube, with current quantity cost of \$2000. Although these devices suffer from about 5% cross talk between adjacent channels, this is not a problem for either preradiator or the position detectors at shower maximum. The phototubes are read out by special high-density ADC cards (32 channels/card), with relaxed specifications on dynamic range and linearity. Each channel has a digital fast out bit available for triggering. The estimated cost of each card is \$700.

A position detector is also placed at EM shower max. It too is composed of scintillating tiles with fiber readout. The size of the tile is approximately 2cm in ϕ x 8 cm in η , mapping 4 tiles to each EM tower. The total channel count is 10720 tiles. These are read out by multi-channel phototubes, and use the same tube and electronics as the preradiator.

Expected position sensitivity is of the order 3mm. One bit/channel is available for a fast trigger.

Trigger Upgrades

The trigger will benefit in several ways from the scintillator plug upgrade.

1. On the basis of our experience with the central calorimeter, we expect that neutron-induced noise spikes ("Texas Towers"), as well as low-level coherent noise pickup, will be absent in the new plug. This will allow us to lower the Missing E_T thresholds, as well as to remove several potentially problematic cuts (put in specifically to reject gas noise) in the Level 2 trigger.
2. A low E_T plug electron trigger will be possible, using the additional information from the EM shower position detectors and (if necessary) the preradiator. The current 23 GeV E_T threshold for plug electrons is uncomfortably inefficient even for W physics. The electron signature information available to the trigger will include: an isolated shower profile in the strip detectors at EM shower max, matching with an appropriate energy deposition in the preradiator for the hit tower, in association with an isolated EM cluster in the EM calorimeter, and with little hadronic energy in the hadron compartment(s) behind it. In addition, fine ϕ matching between the position detector and a (future) track processor in the plug region is possible.
3. The intrinsically fast response of the phototube signals will significantly relax the timing constraints on the Level 0 trigger. We note that this could be a make or break issue for the survival of the existing CTC track processors, which require a level 0 signal within ~ 800 ns of the beam crossing.

Scintillating Tile Fabrication

The basic tile unit (fig. 4-5) is a keystone-shaped scintillator plate of typical dimensions 6x6 cm, the pad size of the tower. Each tile has a "U" shaped channel formed in it. A wavelength shifter fiber of diameter 0.5 mm is glued into this channel. This fiber collects the scintillator light produced in the tile. At the point that the fiber leaves the tile, it is spliced onto a clear optical readout fiber (of typical length 3m) which carries the light to the phototube.

The construction of a tile unit then consists of 3 principal operations: the manufacture of the tile; building the spliced fiber; and gluing the two pieces together. Quality control must be provided as needed at each stage of manufacture.

The tile pieces will be laser cut from plates of the bulk scintillator. This is a standard process previously used by CDF, ZEUS, and others. Laser cutting provides the flexibility to produce the large number of individual tile designs needed for projective towers in a plug calorimeter, at reasonable cost. The "U" channel of size 1 x 1 mm will also be created, using the laser beam at a lower power. First-round prototypes obtained from Laser Services, Westford, MS (the firm which cut the ZEUS scintillator) were very successful,

generating cuts and channels which are superior to those obtained by diamond fly-cutters. A second round of 20-100 tile sets is undergoing assembly into an EM test calorimeter module for the test beam.

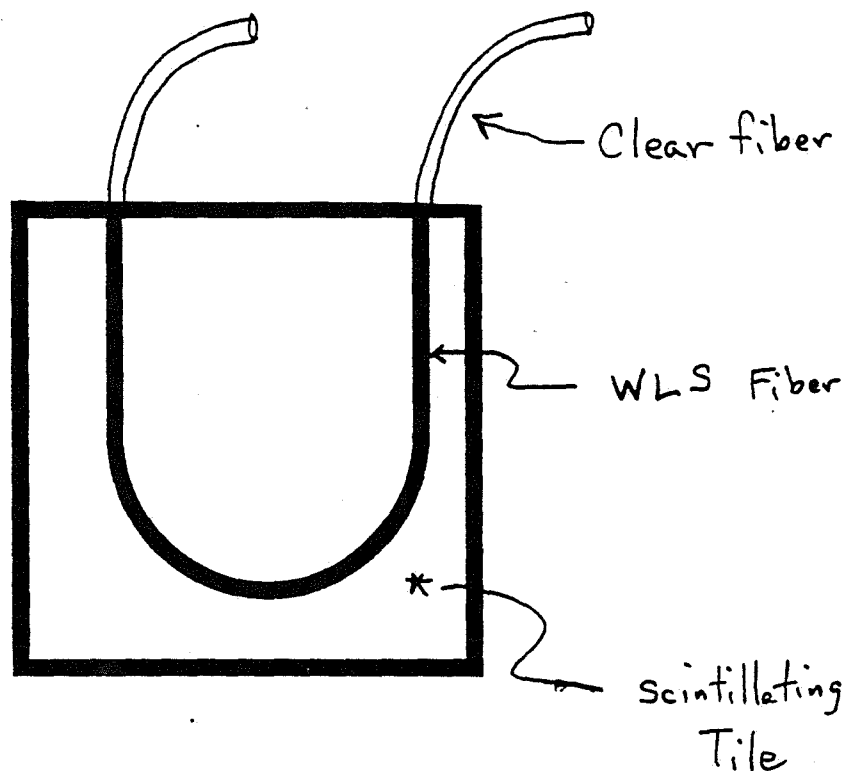


Figure 4-5: Scintillating tile with waveshifting optical fiber imbedded into it. The wavelength shifting fiber in the tile is spliced onto a clear optical fiber for readout.

After the tile pieces are formed, the edges of the tiles are painted with optical white paint. This enhances the light yield and uniformity of response, and prevents optical crosstalk from neighboring tiles.

The spliced fiber assemblies are constructed by heat-welding wavelength shifter fibers to clear fibers. The technique is as follows: First, squarely cut the ends of the fibers to be spliced. This can be done by hand with a razor blade, or in production with the fiber cutting machine such as the one built by M. Mishina and C. Lindenmeyer. (Since the ends of the fibers will be melted at the joint, the only important criterion is that the fiber cut be relatively square). Next, insert the ends of the fibers to be joined into a capillary tube which fits tightly about the fibers. Finally, briefly heat the tube to about 200 degrees F. At this point, the fibers have melted together and fused. As the joint cools, the welded fiber pulls away from the capillary tube due to its higher thermal coefficient of expansion, and can easily be removed from the tube. Initial studies indicate that splices made with this technique have optical transmissions of $\sim 95\%$, with splice-to-splice variation of $\sim 2\%$.

The fiber is then manually loaded into the U-channel. The tile is then clamped onto a smooth surface (mylar film) and degassed optical epoxy glue is injected into the region around the fiber through a laser drilled hole of 0.5 mm diameter through the back surface of

tile at the apex of the "U".

Tile Assembly into "Sectors"

The tile units are then assembled into 15° "sectors" before insertion between the absorber plates of the calorimeter. These "sectors" provide mechanical support and positioning of the tiles. The faces of each sector are covered with a wrapper/mask that optically isolates the tiles and corrects tile-to-tile nonuniformity in the manner used by ZEUS.

The entire sector assembly is then inserted into a computerized test fixture. Using a 25 millicurie Ru107 source with appropriate scintillator telescopes and/or MWPC's, one can obtain an accurate response map of a single tile in approximately 10 seconds. This response map is used to calculate the correction mask pattern, which is computer plotted onto a reflecting foil mask. Tiles that fall outside of selection criteria are discarded. The correction mask is applied to the entire assembly, and the final uniformity of the resulting sector is verified with the radioactive source. A production line for this procedure is being set up in the FNAL Scintillator Fabrication Facility (Lab 6).

An Alternative Fiber-Only EM Configuration

An alternative to the tile design is a scintillation fiber calorimeter, for which a realistic design is rapidly evolving. The idea is to embed scintillation fibers longitudinally in an absorber matrix so that the scintillation light generated in the fibers is brought to the rear end of the calorimeter module where phototubes are mounted. Extensive study by the SPACAL group at CERN has demonstrated that such a technique is an excellent way to build a crackless high resolution calorimeter.

With a fiber configuration for the plug EM section, the fibers would be embedded in lead, and the entire assembly would be mounted on the front of the plug hadron steel. Taking canonical values, the lead to fiber volume ratio is 4 to 1 and the radiation length is 7 mm. Such a composition will give us an energy resolution of $15\%/\sqrt{E}$ for electrons.

The scintillation fibers in the EM segment are 1.2 mm in diameter and spliced to clear readout fibers which guide the light to the rear end of the end plug. In order to reduce the cross section of the readout fiber bundle we plan to use a new type of fiber with a small diameter core doped with wave shifter. The clear fiber only reads out the wave-shifted core thus reducing the cross section significantly. It has been measured on a commercially produced sample that the light coupling efficiency is 1/2 with cross sectional area reduction of 1/4.

A very basic requirement for good uniformity is the fiber quality control. The diameter tolerance of commercially available fibers is already quite satisfactory ($\sigma \sim 0.5\%$). The attenuation length which depends on the material purity and drawing process is also under a good control. We do need a slightly better control of the fiber to fiber uniformity of the light output. Presently the variation is $\sigma \sim 13\%$ without any selection, and is being improved. We are designing a setup which tests large numbers of fibers semi-automatically so that we can sort the fibers. Thus the fibers within the same tower should have the same

response within several % which is necessary to insure a response uniformity of better than few % for electrons.

We are making several prototype modules of fiber configurations for the plug EM section and are planning to test them in MT beam in the near future.

Radiation Damage Issues

Radiation damage is an obvious worry for scintillator based calorimeters at high luminosity, especially at low polar angles. Substantial progress has been made in this area for the purposes of SSC calorimeters. The situation at CDF is better by a factor of more than 100, due to differences in beam energy, luminosity, total cross section and particle multiplicities.

Clearly, the new plug has to be able to survive several years of operation in $\mathcal{L} = 10^{32}/cm^2/sec$ environment. At these luminosities the radiation dose is primarily due to beam-beam interactions and can be estimated fairly accurately. The maximum radiation dose is confined to a rather short region around the electromagnetic shower max, and will be of the order of 1 Mrad/year at $\theta = 5^\circ$, and 10 Mrad/year at $\theta = 1.7^\circ$. The radiation dose at a fixed distance from the interaction point has very strong angular dependence, $\sim \theta^{-3}$.

Our Japanese CDF collaborators, in conjunction with Kuraray Ltd. (formerly Kyowa Gas) have produced numerous samples of scintillating fiber, plate, and pellets containing new shifter dyes and compositions which are expected to exhibit significantly enhanced radiation hardness. These are undergoing testing here and in Japan, and are being incorporated in the calorimeter modules now being prepared for the test beam.

The primary effect of radiation damage to scintillator is the result of a substantial shortening of the attenuation length, due to damage of the bulk polymer. This effect is strongly dependent on the wavelength: the longer the wavelength, the smaller the effect. Thus we plan on using "green" scintillator tiles (Kyowa SCSN81 doped with Y7) for the tiles, which are more radiation resistant by virtue of the longer wavelength of the transmitted light. The waveshifting fiber will be doped with an orange dye (Kyowa O-2 or equivalent) which shifts the transmitted light further away from the spectral region in which radiation damage occurs. Multi-alkali photocathodes have reasonable quantum efficiency for these wavelengths. Our prototypes tile assemblies using these materials yielded light levels corresponding to more than 200pe/GeV.

An elementary feature of the tile design which provides great radiation resistance is simply to keep the optical paths short, particularly for unshifted light in the regions of high radiation damage. Thus an attenuation length for unshifted light of 50cm (which would be problematic in the central EM calorimeter) would have very little effect for the 1-2cm optical paths inside the small tiles in the EM calorimeter near the beam pipe.

Prototypes, Milestones.

1. Construction of small EM test beam prototypes to verify uniformity and light yield.
2. Construction of a 30° sector of tiles for insertion into the plug hadron iron test beam

fixture.

3. Establish Lab 6 production facility for scintillating tile assembly.
4. Design and testing of calibration system components.
5. Final design of mechanical modifications to the plug steel structure.
6. Modification of the test beam fixture to allow insertion of tile assemblies which extend below 10° .
7. Sector-sized EM and Hadron calorimeter prototype assemblies.
8. Technology decision for EM calorimeter, final mechanical design.
9. Decision to proceed with upgrade for '93 run; begin modifications to the steel structure at end of '91 run.
10. Procurement and testing of photomultipliers; construction of phototube bases and mechanical fixturing.
11. Production of additional electronics cards for phototube readout.
12. Test beam calibration of EM and Hadron tile sectors during "92" collider shutdown.

Feature	Benefit
Scintillator based Calorimeter	Calibration stability. Fast time response. Energy resolution. Noise-free operation. Reduction in number of different types of electronics channels in detector.
Phototube Readout	Reliable, stable and fast trigger. Lower electron trigger threshold.
Single unit extending from 38° to 3°	Eliminates "10° crack". Eliminates the separate forward calorimeter. Muon toroids can move forward for improved muon coverage.
High-density EM section	Eliminates the 37° crack. Increases depth of hadron calorimeter.
Retain Existing Steel Structure	Cost. Minimize mechanical disturbances. No need to re-map field.
Tile Readout	Proven technology [BNL 814]. High light yield. Tower Geometry with Depth Segmentation.
Finely segmented preradiator	Electron identification. $e/\pi/\gamma$ separation.
Position detector at EM shower max.	Electron identification. $e/\pi/\gamma$ separation.

Table 4-12: Features and Benefits of Proposed Calorimeter Upgrade.

4.2.2 Gas Calorimeters

The assumptions of this section are that the CDF 1991 run will have a peak luminosity of 5×10^{30} and that the 1993 run will have a peak luminosity of 2×10^{31} . The 1993 run will have 36 bunches and a beam crossing time of 400 ns.

The problem introduced by the 400-ns bunch spacing is one of integrating the charge from the gas calorimeter pads in less than 400 ns. The source capacitance for a tower can be as high as 150nf in the plug leading to signal risetimes into 10ohms of 1.5 microseconds. This problem is being addressed in two ways. The first is to break the tower up into many peices therefore reducing the magnitude of the source capacitance for each piece, putting a pre-amp on every piece and then adding the signals together and into the normal rabbit front end. The second is to pursue signal shaping at the front end with the towers as they are. We have demonstrated that a single pad can be integrated in 200ns and

have designed a system with a pre-amp on every pad. There are 250,000 pads total for the gas calorimetry. The cost for producing these pre-amps for the entire system is estimated to be \$250K. A prototype of this system is being built and will be tested in MTEST. The problems of real estate for the pre-amps and power dissipation of the pre-amps appear surmountable. It appears from our initial tests that the gas calorimeters can be read out in a timely fashion during 36 bunch running.

The next problem to face is one of "glow mode" in the chambers. That is, sustained current drawn followed by a HV trip. We do not yet know at what luminosity for the present gas gain, "glow mode" would set in. It has not set in yet, as has been evidenced by the fact that the frequency of HV trips was the same during the 1987 run at a luminosity of 5×10^{29} as the 1988/89 run at a luminosity of 2×10^{30} . We have made studies of the chambers using radioactive sources to determine at what current per unit area the chambers start glowing. We have calculated the current drawn per unit area in the chambers in B0 due to minimum bias events, at a luminosity of 2×10^{31} and at our present gas gain. The estimated current is always at least a factor of two less than the current necessary to make the chambers glow. Since this estimation makes some assumptions, test beam studies of glow mode at different gas gains and different high voltages must also be made this year to determine the feasibility of running the chambers at high luminosities. It is foreseen that we will lower the gas gain by reducing the high voltage on the anode to reduce the risk of glow mode. The effect on the energy resolution of lowering the high voltage, has not been studied carefully and must be studied in the testbeam this year. We know that reducing the gain a factor of 4, lowering the voltage approximately 150 volts, changes the resolution by less than 30%. It will be noted that the energy resolution in the plug and forward are not critical to most physics measurements. We believe that the HV on the chambers could be lowered sufficiently to stay clear of glow mode and still keep a reasonable working energy resolution. Lowering the gas gain will also improve the saturation effects in the electromagnetic calorimeters. At the moment we are limited in the Z mass resolution in the forward by a lack of knowledge of the response of the calorimeter to electrons with greater than 200 GeV. Again we will have to measure the saturation in the electromagnetic calorimeters as a function of the gas gain in the testbeam.

We have studied the effect of worsening the energy resolution on various physics processes. If we take as the worst case for energy resolution that the resolution, $\sigma(E)$ becomes twice the current $\sigma(E)$, what happens?

- The jet trigger thresholds would have to be raised approximately from 60 to 68 GeV in the plug and from 60 to 62 GeV in the forward.
- The Δ_T resolution for real two-jet events calculated with an energy resolution twice that of the present calorimeters would change from $0.94/\sqrt{E_T}$ to $1.0/\sqrt{E_T}$ in the Plug Calorimeter and from $0.94/\sqrt{E_T}$ to $0.96/\sqrt{E_T}$ in the Forward Calorimeters.

These are not considered significant effects.

We have studied the effect of increased resolution on the ability to measure the P_T spectrum for W's in W + one-jet events. We see no appreciable change in the Monte

Carlo P_T distribution for these W 's.

In short, although we are continuing studies of the effects of the energy resolution on physics processes, our preliminary conclusion is that the energy resolution of the plug and forward calorimeters are not important.

Another important consideration is eliminating texas towers from the data and the trigger. This is done by interleaving the readout of each tower, (effectively making even- and odd-layer readout), and requiring that both samples have some fraction of the total energy of the shower. That is, that the energy can not all be in one layer.

Gas gain was monitored in the 1988/89 run using detector-located monitor tubes. The gain was monitored to 3% continuously throughout the run and the gains were downloaded to the MX's whenever the gas gain changed by greater than $\pm 3\%$. The downloading was quite time consuming, requiring a full download of the MX's. We have demonstrated a working system which changes the voltage as a function of the gain continuously in such a way that the gas gain remains constant and no downloading is necessary. This is being used in the testbeam calibrations. In conjunction with this, new gas-gain-monitoring systems are being considered which are simpler and rely on standalone non-RABBIT DAQ systems.

In conclusion, the gas calorimeters should work well for the 1991 run. Testbeam studies of both the glow mode and integration time are underway to determine the viability of the gas calorimeters for the 1993 run.

4.3 Central Drift Chamber

This section covers planned Central Tracking Chamber (CTC) modifications for data taking at higher luminosity in 1991 and 1993. Tests are in progress for these future runs. A detailed description of upgrade options and test results is given in Ref. 70. A summary is given here.

If the CTC is operated at the same gain as in the 1988-89 run, three problems occur at high luminosity: glow mode, field voltage sag, and aging. Space charge effects are not expected to be large in 1991 and 1993, and can be corrected for in software. To counter possible future glow-mode problems and to reduce aging, we plan to operate the CTC and reduced gas gain.

A new preamp for the CTC has been designed, built, and tested with a 10' long "prototype" with a single axial cell. The noise levels already measured will permit future operation of the CTC with a gas gain of 1/10 to 1/3 that used in 1989.

R&D is continuing on the preamp gain and filtering. With the resulting improvements in pulse rise and fall times and other planned improvements to the amplifier-shaper-discriminator circuits (ASD) the two-track resolution should be improved by a factor of two.

For the 1991 run we will install the new preamps and ASD's where they are most needed: in the inner three super layers. For the outer six super layers, we will keep the existing preamps but add pulse transformers to reduce noise. Additional high voltage lines will be connected to the center points of each axial field chain to reduce sag. For the 1993 run, this work will be extended to all superlayers.

It is difficult to predict the rate of aging beyond 1993. The integrated luminosity through the chamber is so small compared to that expected in the future that we have only a "point", but no "slope" from which to extrapolate. So far, no significant deterioration of performance has been observed. The reduction in gas gain is specifically intended to prevent or minimize deterioration in the future runs with much higher integrated luminosity. A bench test will be performed with the "prototype" chamber. However, given the ambiguity in interpreting such tests, we will have to be alert to these issues as the 1991 and 1993 runs proceed. If evidence for aging or other problems are encountered in the 1991 run, we will need to proceed with design and construction of a replacement chamber as quickly as possible.

4.4 Vertex Time Projection Chambers

VTPC Performance during the 88/89 Run

The VTPC operated reasonably well during the 88/89 collider run. Many modules experienced DC current leakage problems outside the active region, but this did not affect the tracking performance or cause the experiment to suffer significant dead time. The current leakage was kept under control by the addition of approximately 0.5% water to the argon ethane 50/50 gas mixture. Spatial distortions due to positive ions in the drift region at high luminosity were studied offline and for the most part corrected for in the analysis. These measurements and associated calculations indicate that the space charge distortions will make the VTPC inoperable at $\mathcal{L} > 3 \times 10^{30}$.

The spatial accuracy of the VTPC is approximately $\sigma = 400 \mu\text{m}$ per hit at $\theta = 90^\circ$ and degrades at smaller angles to about $950 \mu\text{m}$ at 25° . Using tracks which point within 1 cm of the z vertex position, it was found that a primary VTPC track points to the vertex with an accuracy of $\sigma = 2 \text{ mm}$ along the beam direction and that the interaction vertex is determined to an average accuracy of 0.5 mm. The fast VTPC vertex finding routine was updated to find multiple interactions in the same event. Due to secondaries, very low momentum particles, spirals, and possibly some residual distortions due to space charge, the routine can only reliably separate vertices spaced by about 5 cm.

VTX Upgrade in Progress

Due to positive ion distortions in the drift region, the VTPC will be essentially inoperable at $\mathcal{L} \sim 3 \times 10^{30}$, so it must be replaced for the next collider run. In addition, the structure must be rebuilt to allow space for the SVX. The new vertex chamber (VTX) will also drift electrons in the z direction, but the drift gap is smaller (4 cm versus 15 cm). Further, pads have been eliminated to reduce mass and power dissipation from the accompanying electronics. The smaller drift gap and higher drift field of the VTX reduces the positive ion distortions by almost two orders of magnitude, thereby allowing operation for at least the next two collider runs.

The 4-cm drift gap means that the VTX (using conventional gases) will be sensitive to two crossings in 36 bunch operation of the Tevatron. As in the case of the CTC, one can discriminate against tracks from an out-of-time crossing by demanding a link between cell (or module) boundaries. We will investigate faster gases (e.g., CF_4) which may allow the separation of crossings in 36 bunch operation.

The central VTX modules, including those to which the SVX is mounted, have 16 sense wires per octant (compared to 24 sense wires per octant in the entire VTPC). In all there are 18 modules with 16 sense wires per octant, and 10 modules on the ends with 24 sense wires per octant. The spatial accuracy of the VTX is $\sigma \sim 200 \mu\text{m}$ at 90° , about a factor of two better than the VTPC. However, the vertex resolution in the beam direction is likely to be comparable due to multiple scattering in the SVX. Fast vertex finding routines have been written for the VTX which take into account the shorter module spacing.

Alternate VTX modules are rotated by 11.3° in ϕ , so that VTX tracks can be matched to CTC r - ϕ segments in the plug region to better than the CTC's two-hit resolution (~ 2.5 mm). Because of the increased number of proportional chambers, VTX tracking in the forward region should be considerably better than the present VTPC forward tracking. The path integral in radiation lengths of the combined SVX and VTX is about 50% larger than that for the VTPC in the central region and is approximately the same as the VTPC in the plug region. Production of the chamber and associated electronics began in the fall of 1989 and will be completed in approximately one year.

4.5 Silicon Vertex Detectors

CDF is currently building a Silicon Vertex Detector (SVX) to be installed for the 1991 run. The device, shown in Fig. 4-6, employs 4 layers of silicon microstrip detectors at radii between

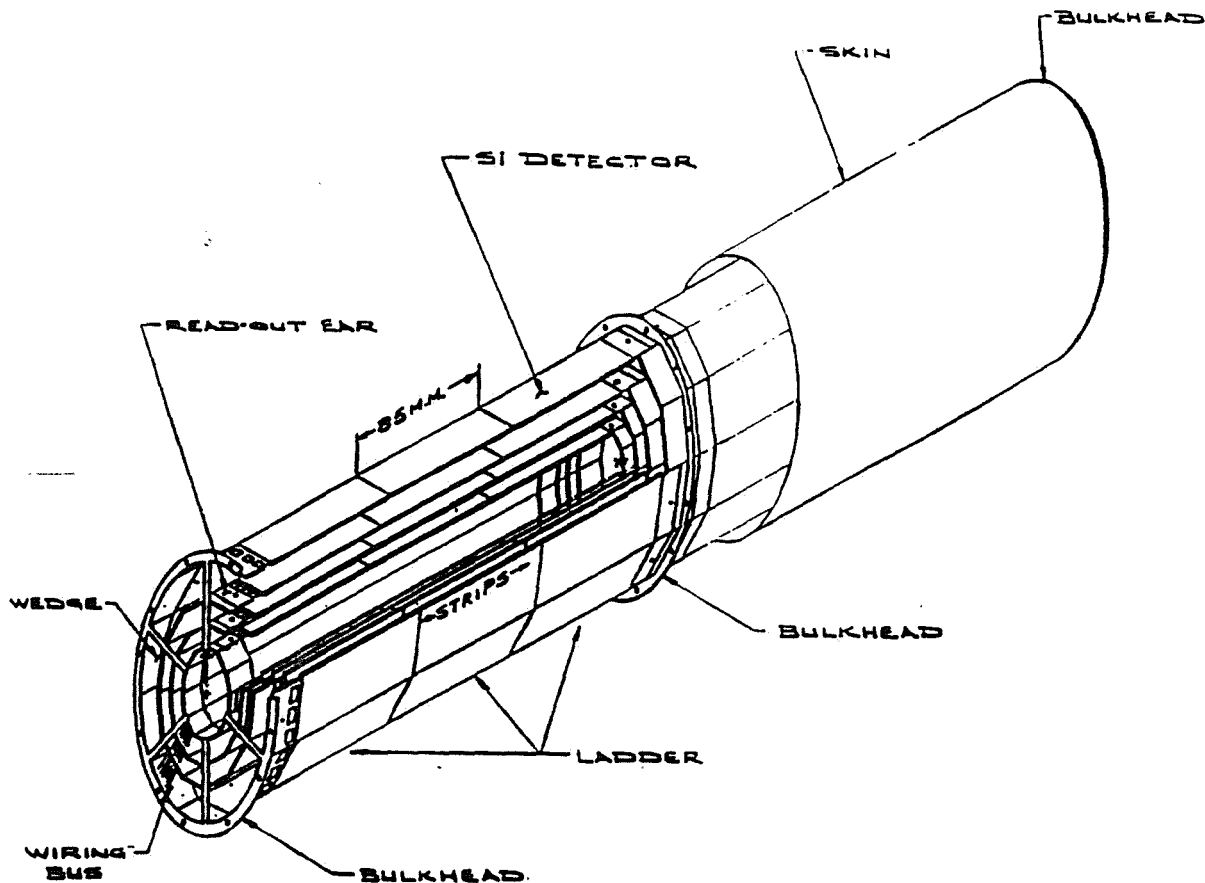


Figure 4-6: Drawing of the SVX detector.

3 and 8 cm from the beamline. Good geometric acceptance is achieved with respect to the long Tevatron bunch by implementing separate barrel arrays, 25 cm in length, on either side of the interaction point. The 25 cm barrel is achieved by a series connection of 3 microstrip detectors in length. The expected impact parameter resolution is shown in Fig. 4-7. For high momentum tracks, the expected resolution is $15 \mu\text{m}$.

The indispensibility of vertex reconstruction for top tagging has been emphasized in Sec. 3-3.2, and the profound potential for B physics with high luminosity at the Tevatron has been discussed in Sec. 3-3.4. We therefore consider, here, a possible scenario for an SVX upgrade in the 1993 run. The upgrade is motivated partly by the necessity of faster readout

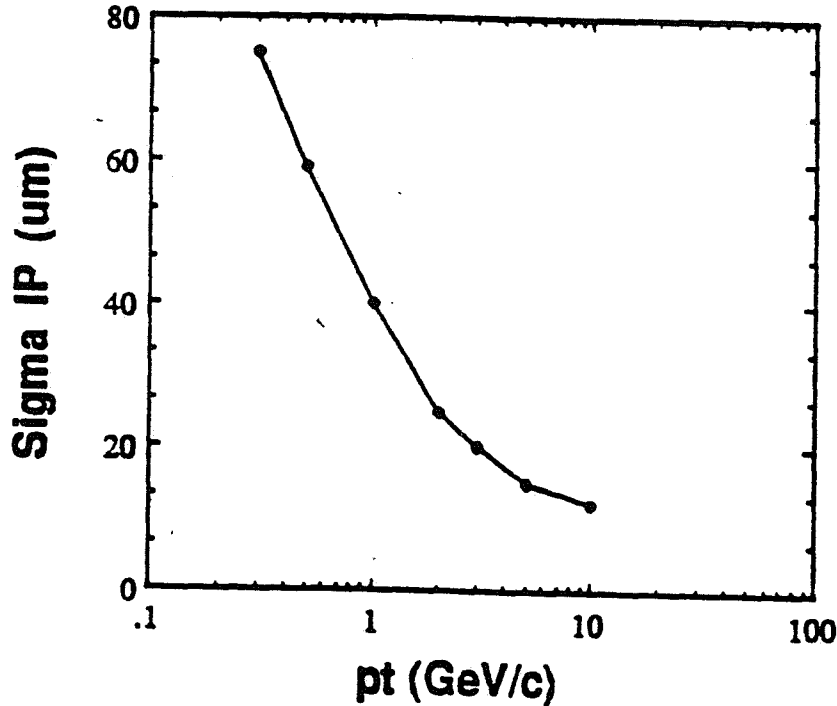


Figure 4-7: SVX extrapolated Impact Parameter Resolution vs track P_T .

times required for multibunch running. In addition, we expect that the experience gained with the SVX in the 1991 run will make reasonable a number of enhancements. Necessity and enhancement are combined into the following brief proposal.

It is important, however, to note that the 1991 run will be the FIRST experience with a silicon vertex detector at a hadron collider, and that much of what we might want to do in 1993 depends on what we will learn. We may discover that the present geometry is perfectly optimal, and that the most appropriate upgrade is simply to replace the readout, maintaining the present detectors and superstructure, at great savings. Or we may discover some novel physics that motivates a much more ambitious upgrade. The spirit of this section is to present a likely option, with the proviso that only time will tell.

Essential Upgrades

The settling time for the present SVXD readout chip is about $1 \mu\text{sec}$, clearly unsuitable for multibunch running. The fundamental bandwidth limit is the signal to noise ratio, and, in particular, the difficulty of achieving low noise with our rather large source capacitance of 30 pF. The most straight-forward way to decrease the noise and the readout time is to decrease the source capacitance. To do this, we would eliminate our series readout scheme and put separate readout chips on each of the silicon detectors. This has the additional advantage of adding a factor of 3 in z segmentation. It will, however, require a significant

rebuild of the mechanical support, cable connections, and cooling. There are other good reasons for rebuilding the ladders. Increased leakage currents from radiation damage will pose a problem for our DC coupled electronics. This could be solved by an AC coupling hybrid to go between detectors and the new chips. Alternatively, we may wish to consider AC coupled detectors, or other new detector technologies (see below). Finally, note that radical changes in the design of the CDF Data Acquisition System or the SVX readout chip could necessitate rebuilding parts of the electronics in the downstream region of the readout.

Enhancements

The straight path to a program of high sensitivity B physics requires addition of a secondary vertex trigger. Such a device would have the bonus capability of tagging unexpected short-lived objects. Promising schemes with associative memories or neural networks are under development at Pisa, CERN, Michigan and FNAL, and we anticipate employing one for the 1993 run.

Simulation studies show a 30% increase in B tagging efficiency for an inner layer at a radius of 0.5 inches. This new Layer 0 would require a new set of silicon detectors, their associated readout hybrids and new cables, some mechanical contrivance to support the new layer within the existing SVX superstructure, and a new 1 inch beryllium beam pipe. The new silicon detectors could employ the usual microstrip geometry with a smaller, 25 μm , pitch. However, we may wish to add more segmentation in z, or consider a new technology, such as double sided or pixel detectors. More generally, we may wish to redesign some of the other ladders in order to best exploit the nascent technologies. For example, the use of pixels or double sided detectors for the new inner layer AND the outermost layer would have obvious advantages for pattern recognition.

4.6 Muon Systems

The replacement of the CDF forward calorimeters by a compact plug design allows the toroid muon system to be moved closer to the interaction point, thereby closing a significant gap in the muon coverage. A new muon chamber/scintillator system will provide the necessary increase in area and redundancy. The physics motivation and performance are discussed here .

Introduction

If the forward calorimeter is replaced by a compact detector inside the plug, the present 2-meter-thick toroid system may be moved 5 meters closer to the interaction point. The toroid system at the new location will provide a momentum measurement from 6° to 25° . The front and middle chambers extended to the full radius of the toroids will tag muons up to 41.5° . The proposed muon coverage is summarized in Table 4-13. Roughly speaking,

Muon Detector Subsystem	Angular Range (deg)	Rapidity Range	Trigger
Current FMU	3 - 7	2.8 - 3.6	not in 1989 trigger
	7 - 16	2.0 - 2.8	
CMU + CMX	41.5 - 90	0 - 1	
Moved up Toroid	6 - 25	1.5 - 2.8	track sees two toroids
	25- 30	1.3 - 1.5	track sees one toroid
	30- 41.5	1.0 - 1.3	track sees endwall only

Table 4-13: CDF Muon System Coverage

this proposal doubles the forward acceptance for many of the interesting muon production processes at CDF.

The momentum resolution of the toroid system in the new position ties on smoothly with the resolution obtainable in the central tracking chamber as shown in Fig. 4-8. Below 25° , the external toroid momentum resolution is multiple Coulomb scattering limited at 16 %. In the range 25° to 30° , the single front toroid instrumented as described below is capable of a 30 % momentum measurement at $P_T = 40$ GeV when the vertex constraint is applied. The region of overlap between the toroid and CTC measurements starts at about 14° where a muon from B_0 crosses one superlayer. At 25° , a muon is observed in three superlayers of the CTC with a P_T resolution of 15 % at $P_T = 40$ GeV. Thus the proposed detector configuration provides a muon momentum measurement over the entire angular range . Other advantages to the compact detector configuration include a reduction of decay in flight background below 10° by a factor of three and reduction in noise resulting from albedo from the quadrupoles.

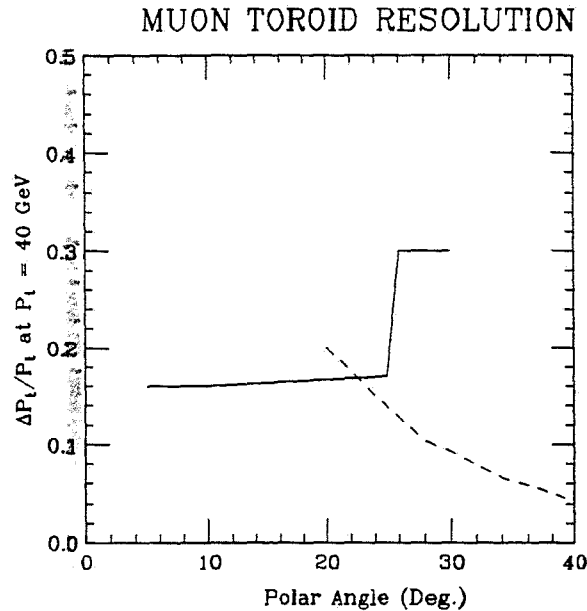


Figure 4-8: The momentum resolution $\Delta P/P$ as a function of polar angle. The solid line represents the resolution achieved from the toroid chambers alone. It has a step function at the point where tracks miss the last chamber. The dashed line gives the resolution which is obtained from the central drift chamber.

Muon Physics

Muons have played a key role in the most prominent analyses of the past run. The cleanest limits on the top quark come from the $e-\mu$ mode, and the $\mu-\mu$ and e or $\mu + \text{jets} + \text{soft } \mu$ (from a B or C quark) contribute substantially to the overall limit. The one candidate we have for a top quark has two muons in it (one in the forward toroids). The high precision Z mass measurement used both $e-e$ and $\mu-\mu$ modes, and the cross-check of having both modes was crucial. The important scale uncertainty of the calibration of the electromagnetic calorimeters was set by the mass scale of the ψ and Υ measured in the muon modes. The W mass measurement uses both the muon and electron modes, and similarly relies on the consistency of the two for understanding of the systematics of the two different lepton measurements. Searches for exclusive decays of the B meson rely on the muon modes, as well as measurements of the structure functions at very low x from Drell-Yan spectrum measurements in progress. Finally, inability to detect muons is a problem to all measurements that rely on missing \vec{A}_T , as the P_T of unidentified muons is (largely) lost. In an experiment searching for rare new phenomena, detector hermiticity is very important. One does not want events which appear to be anomalous because ≥ 50 GeV/c of transverse momentum is carried off by a muon which is completely undetected.

The clearest goal of the collider is to discover or further limit the mass of the top quark. A $t\bar{t}$ system (produced by gluon fusion) is expected to decay to a pair of b quarks and a pair of W's. The principal decay channels by which this process may be observed against

the background from multijet systems produced by QCD processes include one or more leptons plus jets. The angular distribution of dimuons triggers from $t\bar{t}$ events for various masses of the top is given in Table 4-14. Inclusion of the angular region covered by the

	<i>Central - Central</i>	<i>Central - Forward</i>	<i>Forward - Forward</i>
$M_t = 70$	750	350	56
$M_t = 90$	233	94	14
$M_t = 110$	82	36	5

Regions:

41.5° - 131.5°	“Central”	Central+extension
25°-30° & 150°-155°	“Gap”	Tagged only
6°-25° & 155°-174°	“Forward”	Pushed up FMU with trigger

Table 4-14: Angular distribution of dimuon triggers for $t\bar{t} \rightarrow \mu^+\mu^- + X$ for various values of the top mass for a 500 pb⁻¹ run. Both μ 's are required to trigger with $P_T > 6$ GeV .

toroids in the new position increases the dimuon acceptance by about 50% over the central region alone, even for heavy top mass. If a signal is found in single lepton events, coming from the leptonic decay of one of the real W's from heavy top, one may seek confirmation by tagging of the b's through their semileptonic cascade. Flavor tagging of b jets through muons may be expected to be important for other processes including the study of direct b-bbar production. The increased muon coverage will also benefit searches for exotic particles.

Toroids

The present system consists of a pair of one meter thick toroid magnets in both the forward and backward directions. Each toroid has an outer radius of 150" and inner radius of 18". The coils were operated with 1000 Amperes and the magnetic field varied between 1.6 and 2.0 Tesla. During the 1991 run, we intend to operate with 500 Amperes to save power with 0.1 Tesla less field. The magnet pair splits along the vertical centerline and each half may be rolled independantly. At the new location, the toroids would be positioned in front of the low beta quads. Opening the end-plugs of the detector requires that the toroid system be split apart a few feet and moved along the beam direction. It is necessary to split the toroids in order to clear the vertical support rods for the quadrupole focusing magnets. The fringe field of the magnets at the location of any proposed plug phototubes is readily shielded. It is expected that the chambers could be located as close as 4.6 meters from B0, limited by the plug support arms. The present position of the front chambers is 9.7 meters from B0.

Instrumentation Upgrade

We propose to replace the toroid muon detectors with a chamber/ scintillator system optimized for the new location . This replacement will provide finer segmentation in the

scintillator trigger system, increased redundancy throughout the muon chamber tracking system for triggering and unambiguous momentum measurement, and extend the chamber area to provide a muon stub tagging capability in the endwall region. (The present system is described in Ref. 18).

We have taken the following requirements for the new design:

1. Operation with 36 bunches and $\times 50$ increase in luminosity,
2. Increased redundancy in tracking,
3. A multilevel trigger capable of a variable P_T threshold between 5 and 20 GeV.

The proposed design consists of three detector stations per end as in the present system. (See Fig. 4-9.) Each station contains a scintillation counter mosaic plane for trigger-

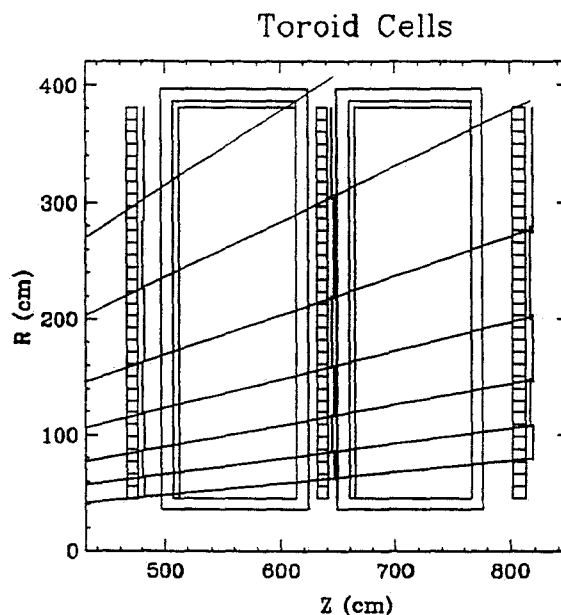


Figure 4-9: A diagram of the cell structure of the proposed modifications to the forward muon system. R is the radial distance from the beam axis. Z is the distance along the axis measured from the nominal beam crossing point - the detector center of symmetry. There are three detector stations per end as in the present system. Each contains a scintillation counter mosaic plane for triggering and for timing and azimuth measurement. Each also has a drift chamber containing four wire planes in an open cell geometry measuring drift time along the radial bend direction.

ing and timing and azimuth measurement, and a drift chamber containing four wire planes in an open cell geometry measuring drift time along the radial bend direction. The scintillator provides a fast Level 0 trigger. The scintillator hit times will be recorded to determine the crossing number of a track allowing chamber drift times integrating over more than one crossing. The scintillator determines the track azimuth to 5° , supplanting the role of the

pads in the present system. The chambers provide a muon stub at each measurement station, in contrast to the single hit pair of the present system, for improved noise rejection.

The scintillator segmentation is 5° in azimuth by about 0.3 in pseudorapidity requiring a total of 2592 channels. Three planes of scintillator rather than two are used to increase the redundancy. The segmentation corresponds exactly to the current pad segmentation and is 15 times finer than the current counter segmentation. During the 1989 run, the occupancy in two planes of 15° counters corresponded to about two counter pairs per minimum bias event. The large hit rate was ascribed to uncorrelated albedo particles from the quadrupoles. The increased segmentation is sufficient to reduce the accidental Level-0 trigger rate to several tens of kiloHertz at a luminosity of 5×10^{31} .

Two thirds of the plastic is in hand in the form of the present 15° paddles. A single $3/4$ " Hamamatsu phototube glued directly to each paddle without a light guide has high efficiency. In order to conserve space between the toroids, we are also exploring readout of the scintillator tiles with wavelength shifter fibers coupled to clear fibers which would run to multianode photomultiplier tubes on the outer radius. A coincidence of three projective counters defines a Level 0 trigger which imposes a very loose transverse momentum cut. As in the present system, a discriminator-base combination would be used and differential ECL logic signals shipped upstairs. These signals would be recorded in TDC's with 10 ns timing resolution thus determining the crossing and track azimuth.

The new drift chamber system doubles the number of hits per track compared to the present system by providing four radial position measurements per station with an assumed spatial resolution of 250 micron. Unlike the present system which has projective cells which increase in size with polar angle and distance from B0, the drift cells are identical in size reducing (by a factor of 36) complications in construction, high voltage distribution and monitoring, and reducing the overall channel count. All chambers extend to the full radius of the toroid. In particular, the front chambers provide a muon stub in the endwall region which may be matched to a CTC track.

As currently envisioned, the drift chambers are similar to the forward muon chambers of the ZEUS detector. Each chamber consists of an Aluminum U-channel wedge shaped frame containing 32 cells in the radial direction of 5.2 cm drift corresponding to a maximum drift time of approximately 1 microsecond in Ar-Ethane. Cells are separated by grounded foil cathode planes of low mass to minimize delta-ray production in the chamber while providing electrical and mechanical isolation. Each cell contains four slightly staggered sense wires in depth alternating with potential wires at positive high voltage and a set of field shaping electrodes. Conventional field shaping with wires or conducting strips may be used. We are also exploring the use of high resistance carbon loaded Kapton bonded to the front and back covers of the chambers for continuous field shaping.

The chambers may be constructed in overlapping octants or, as in the present system, in 15° azimuth sections with wire signals OR'ed over an octant. The number of wire channels is 6144 compared to 4608 in the current system. In the octant construction, alignment should be easier.

The number of wire planes and the open cell geometry are motivated by observa-

tions of muon track contamination in the present data. The observed probability of a delta ray or shower accompanying a muon in the present system is approximately 50%. This noise rate is reproduced by detailed GEANT simulation of the present toroids and chambers. The noise hits not only lead to possible ambiguity in the momentum reconstruction but complicate the trigger - a large trigger rate results from soft muons with accompanying delta ray hits which satisfy a stiff track criteria. In order to impose a high P_T threshold which rejects such events without a multiplicity cut with its consequent 50% efficiency, the soft noise particles must be recognized and rejected on an event by event basis.

The sources and spectra of excess hits accompanying a muon signal have been studied by GEANT simulation. A 100 GeV muon exiting one meter of iron and measured with a chamber consisting of a 1 mm Al wall and 1 cm of Ar-Ethane is accompanied by one or more extra charged particles 20% of the time. This noise rate is a slowly varying function of the muon energy. Three quarters of such events contain only one or two electrons or positrons. The extra particles are produced in the last few mm of the steel or in the chamber wall with a broad angular distribution and typically several MeV of kinetic energy. Such particles are rather penetrating and can be scattered randomly by further chamber walls impeding track reconstruction. The r.m.s. projected angle of noise particles is about 25° . Even particles generated in the front chamber wall are expected to be typically separated from the muon track by several centimeters in the last plane and readily identified. While further simulation work is required, we expect to reduce the effective contamination rate to a few percent per station thereby increasing the effective track efficiency by a factor of two.

Trigger

Implementation of a high threshold trigger is complicated by the combination of the finite vertex distribution and the presence of multiple interactions - no single projective road accepts all stiff tracks and the possible vertices will not be available until L3 processing. Thus a high P_T trigger must make a measurement of sagitta not relying on projective geometry.

Representative bend angles and sagittas are given in Table 4-15. Segmentation at the level of 5 mm in radius is required at the trigger level.

The improved redundancy will be sufficient to allow the rejection of track segments at a station at wide angles to the muon direction. A complete trigger design has not been made but is expected to have the following elements:

- L0 provided by a scintillator coincidence,
- L1 consisting of separate pieces of information: a segment angle measurement for the fast tracking hardware with 10 ns (5 mm) resolution to provide a loose P_T cut below 25° and a muon tag in the front station between 25° and 30° ,
- L2 high P_T trigger formed from the correlation of segments found at Level 1 between chamber stations.

θ (deg)	P_T (GeV/c)	$\Delta(\theta)$ (mrad)	Sagitta (cm)
7	5	26	1.2
	10	13	0.61
	15	9	0.41
25	5	91	4.5
	10	46	2.2
	15	30	1.5

Table 4-15: Representative bend angles and sagittas in the toroid system.

The drift chamber signals are received upstairs in PSL FASTBUS TDC's and made available to the trigger via the auxillary connector. One possibility for trigger implementation is that each signal is sent to an eight bit shift register clocked at 10 megahertz. Each shift register bit corresponds to a 0.5 cm radial bin. For each station, the L0 result is used to address the corresponding range of wire data to three segment finding units each requiring three of 4 hits on a segment. By comparing to a prepared list of masks, each segment finder produces a list of segments containing segment position, angle, and quality information. A Level-1 trigger similar to the central muon stub trigger is also under consideration. Track segment information is fed to a track processing unit which performs a linear least squares fit determining track momentum and track quality information.

The inclusive muon trigger cross section estimated from present data leads to a rate of ≥ 1 Hz for a 15-GeV/c threshold at a luminosity of 5×10^{31} as shown in Table 4-16. Multiparton triggers would take advantage of lower threshold muon signals.

P_T threshold (GeV/c)	Cross section (cm^2)
5	6×10^{-32}
15	6×10^{-33}
20	2×10^{-33}

Table 4-16: Estimated trigger cross sections in the toroid system.

Mounts

Reproducible chamber alignment is extremely important to the momentum resolution above 100 GeV and nontrivial for a system of this size where straightthrus do not exist. To ease this problem we anticipate mounting the chambers directly on the toroids to reduce the number of degrees of freedom. The counter alignment is much less critical and we would suspend

the counters from the existing movable chamber support system. It may be also possible to incorporate the scintillator onto the rear face of the chamber module.

Resolution

The expected momentum resolution as a function of momentum has been estimated, taking into account multiple Coulomb scattering correlations in an optimal fit as described in Ref. 71. In Fig. 4-10, the solid curves (a-d) show the resolution for muons below 25°. The two

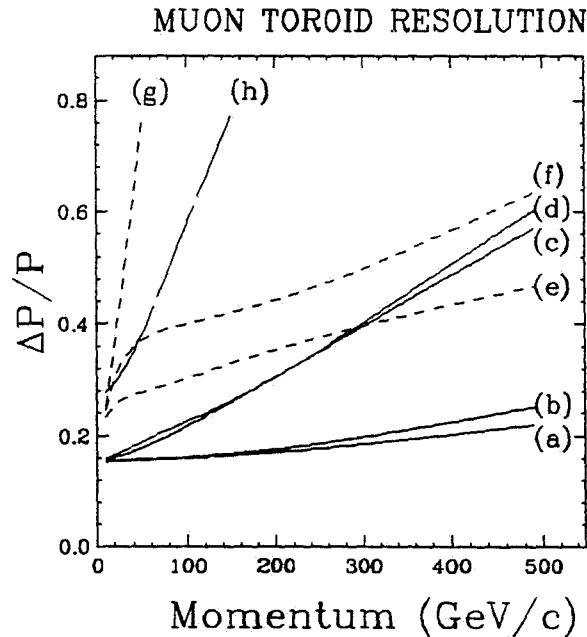


Figure 4-10: The expected momentum resolution as a function of momentum. The various curves are explained in the text.

lowest curves (a-b) show the resolution with and without the constraint of a vertex provided by the VTX chambers. With the assumed spatial resolution of 250 micron per wire, the resolution is multiple scattering limited for all momenta accessible to this experiment and the vertex constraint does not provide a significant improvement. The upper curves (c-d) show the resolution for 2-mm spatial resolution corresponding to a 1-mm alignment error. The actual resolution should lie between these sets of curves.

The dashed curves (d-h) show the resolution for muons between 25° and 30° which pass through only one toroid. In this angular region there is good CTC coverage for momentum measurement but a sign determination would be a useful check in matching tracks. The short dash curves (e-g) assume 250 micron space point resolution. The uppermost curve (g) is the resolution of the entrance and exit angle measurements of the toroid chambers alone. The middle curve (f) shows the effect of including the vertex constraint. Above about 40 GeV, the multiple scattering in the plug calorimeter is sufficiently small that the vertex and entrance point have sufficient lever arm to give a good entrance angle measurement with the

middle toroid chamber providing an exit point measurement. The bottom curve (e) results if the polar angle measurement of the VTX chamber is included. The long dash curve (h) shows the case in which the vertex and VTX stub angle are included and the toroid chamber spatial resolution is degraded to 2 mm. In order to resolve the sign of 100 GeV muons in the toroid in this angular region, submillimeter alignment errors must be achieved .

4.7 Data Acquisition Electronics

Plans for a new data acquisition system for CDF began early in 1989 and settled into something like their present form at the Breckenridge workshop in August, 1989. A lengthier discussion of those plans can be found in Ref. 72. This section summarizes the broad features.

Design Guidelines

The principal constraints driving the design for an upgraded CDF data acquisition system (DAQ) are the increased luminosity and the modified bunch structure in the upgraded Tevatron. Further, we wish to enhance the strengths of the present system, and to eliminate its weaknesses. Below are listed the assumptions and global criteria and goals used in the design concept presented in this section.

1. Tevatron Luminosity $\mathcal{L} = 10^{32}/\text{cm}^2/\text{sec}$.
2. The bunch crossings will be spaced at 395 nsec intervals, with some larger gaps between groups of crossings.
3. The capacity to handle events to be digitized and sent to Level-3 will be > 100 Hz.
4. The dead time during system operation at 100 Hz will be $< 16\%$, with individual goals of 5% for Level-0 and Level-1, 5% for Level-2 trigger, and 6% for scanning.
 - This requires an on-detector Level-0 trigger and
 - a zero-dead-time pipeline at the front end.
 - Digitizing and transfer of data to buffers must be accomplished in 0.6 msec or less.
 - All subsequent parts of the DAQ system should have sufficient bandwidth and buffering to avoid any further dead time.
5. The system up time, i.e. time available for actual data collection as opposed to calibrations, startup and other non-data operations, will be $> 95\%$ of delivered usable beam.
6. Each calorimeter front-end amplifier card will have its own 16-bit ADC. There will be no digital traffic on these cards during conversion.
7. Transport through the DAQ will be data-driven, i.e. there will be no holdup in transmission when both data and an available transmission channel exist. This implies the following design guidelines:
 - parallel paths from each Rabbit crate or SSP to a FIFO data concentrator,
 - parallel paths (4 to 8) from the FIFO data concentrator to Level-3.
 - data flow should be driven by state registers, pre-loaded scan lists and pre-loaded destination address stacks wherever possible;

- control communication governing data flow should be limited to nearest neighbors wherever possible, and should be accomplished by direct connections rather than by system-wide broadcast messages;
 - All channels will be digitized and sent to Level-3 for each event. Channel addresses will not be part of the data. The additional bandwidth required is more than offset by elimination of the delays involved in formation and downloading of scan lists for each event.
 - Level-3 processors will be responsible for any *in situ* manipulation of data which is required. Such functions include sparsification, application of pedestal and gain corrections, calibration, re-formatting and YBOS bank formation.
8. Control functions and data flow will occur on separate paths in the DAQ during data acquisition. This restriction will not necessarily hold during run initialization.
 9. The present capability to partition the system for calibration and debugging will be maintained.
 10. The design must provide for calibration, monitoring, error reporting and diagnostic functions.
 - It must be possible to connect diagnostic tools, such as a PC, from the control room to the front-end cards.
 - The states of the front-end, FIFO data concentrator and Level-3 must be available continuously in one place for operators and for error-detecting programs.
 11. The output event rate to tape must be increased to at least 10 Hz total capacity by providing parallel output streams.
 12. The system should be expandable, i.e. there should be provision to add new detector subsystems and associated readout, more bandwidth to the data paths by additional parallel channels, and more computing power in the form of more and faster processors.

Overall System Description

Figure 4-11 gives an overall block diagram of the system. The two major subsystems of the detector, tracking and calorimeters, present somewhat different problems and are shown separately. The calorimeter front-end analog-to-digital converters (ADC) and associated electronics reside in the Rabbit crate system located on the detector. Time-to-digital converters (TDC) exist at present only for the central hadron calorimeter phototubes (CHA), but will be added for all phototube towers in the upgraded detector. TDC's for tracking are commercial Fastbus modules located outside the collision hall. In our design, data from these devices is moved in parallel over roughly 160 to 200 parallel cables (> 1 GB/sec total bandwidth) to FIFO buffers at the input of data concentrators. Thus, extremely high bandwidth exists from the front end to the first multi-event buffer.

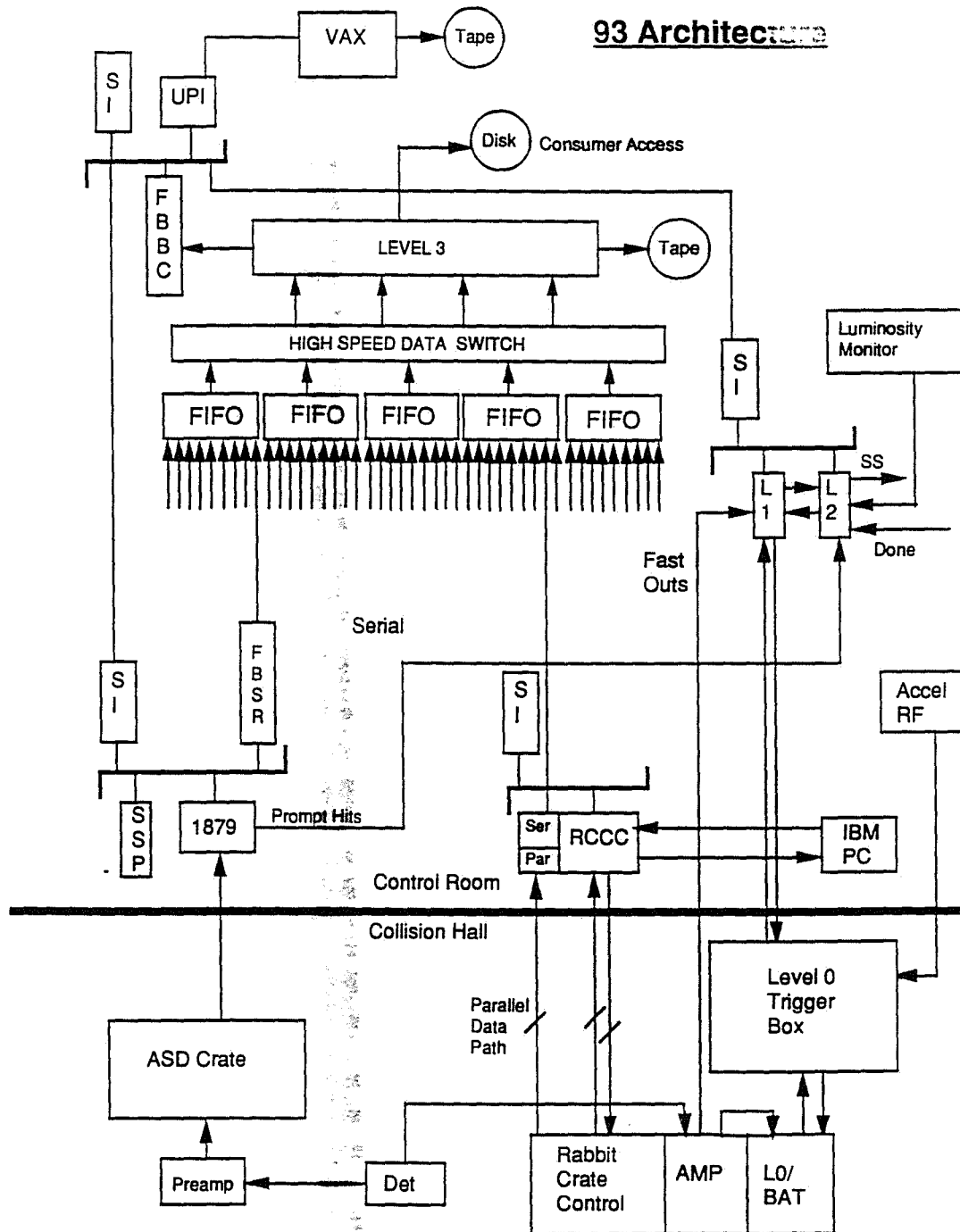


Figure 4-11: Block Diagram of the major components of the proposed CDF data acquisition system. Over 130 Rabbit crates contain the front-end electronics and ADC's for calorimeters. Data from the TDC modules (1879's) are collected in roughly 30 SSP modules in Fastbus. Data cables from each of the Rabbit crates and SSP's carry the data in parallel to the scanner/data-concentrator where all data from a single event are buffered and routed to a Level-3 processor, and, if the event is accepted by Level-3, to tape. The dedicated data paths are shown as groups of parallel lines. Separate dedicated paths exist for triggering and control.

The data concentrators gather data from a subset of the crates (Rabbit or Fastbus) serving the front end systems and concentrate them into a large fragment of the total data for a single event. We estimate six to eight such devices will be needed, depending on details of the technical design. Each communicates over a separate high bandwidth connection to a high-speed data switch which routes the event fragments to the proper buffer in the Level 3 farm.

The switch is not defined at present. At least three candidate designs have been proposed by technical groups at Fermilab. We are also investigating the applicability of commercial switching systems rated at the appropriate overall bandwidth.

All technologies under consideration have the feature that all cables to the Level-3 farm can be operating simultaneously. The Level-3 farm consists of an event-oriented multi-processor architecture with high-speed I/O and large CPU power. It is discussed at greater length in a later section.

The following sections deal with individual components of the system. Parts of it already exist in the present system and meet the criteria we have established. These will be retained.

Front End Calorimeter Electronics

The design guidelines above implied several changes in the characteristics of the present front end electronics. We expand that discussion here.

1. A local Level-0 Trigger is required.

There is no longer enough time between crossings to send analog signals upstairs to make a trigger decision. A local Level-0 trigger must be provided on the front end that is capable of making a trigger decision every 395 nsec and that incurs no dead time until a Level-0 trigger is accepted.

2. Zero-dead-time front-end pipelines are required.

Presently, with the exception of the LeCroy TDC's which can buffer one event, there is no buffering of events in the front end. Even with a local Level-0 trigger, it will take some time to process the event, and get a signal back to the front end gate control to stop the acquisition of signals. This implies that the front end will need pipelining or buffering to store events while Level-0 makes a decision.

3. Increased readout speed is required.

As the interaction rate increases, the readout speed must be increased to keep the dead time below the 6% limit. At 100 Hz, the system must be capable of reading out an event from the front end in 0.6 msec. This limit is defined by the capabilities of the LeCroy TDC's which will be read out in parallel with other elements of the front end electronics.

4. Optimize data flow path to Level-3.

The present data flow path is over the Fastbus network, where data transmission

requires bus arbitration in a network carrying other traffic. To reduce the data burden on the network, two time-consuming operations are performed on the critical path. The data are sparsified by the front-end scanners to reduce event size before transmission to the Event Builder. Subsequently, the Event Builder must unscramble the data before the event can be built. For better efficiency and speed, separate, highly-parallel data paths are to be provided for the front end to push data directly, with no processing to a "FIFO data concentrator" for routing into Level-3, bypassing the Fastbus network. Sparsification, pedestal and gain corrections, re-formatting and YBOS bank formation can be done in Level-3 which is highly buffered, highly parallel and easily expanded.

Interface to the Trigger System

One of the design criteria is to keep as much of the existing system intact as possible. Given the limitations of the present front end circuitry, it is clear that most of these boards must be replaced. The trigger electronics, on the other hand, is fully developed and well integrated into the rest of the system. If we add a Level-0 trigger to provide a rejection factor of about 200, then Level-1 and Level-2 could continue to function as they do presently, 15 KHz into L1, 5 KHz into L2.

Retaining the trigger system implies keeping the analog-based fast out cables connected to it. This means that those detector systems that have fast outs in the present system will continue to have this circuitry on them in the upgraded system, including the cable connections to the Level-1 processors. The same characteristics which presently govern their operation will continue to apply.

RABBIT Electronics

The front end must provide some method of storing events locally, long enough for a Level-0 trigger decision to be made. That capability does not presently exist. Thus, all front end cards in the RABBIT system must be replaced. This includes approximately 2500 amplifier cards, 150 crate controllers, and 150 BAT gate generator modules. We plan to retain the RABBIT crates and 400 Hz power supplies.

The front end channels will need to have analog memory elements in order to provide time to make a Level-0 decision. The best estimate for the length of storage needed is 1.2 μ sec, or three events deep at the 395-nsec cycle. This is based on the estimated decision time required in the Level-0 electronics and associated cable and propagation delays. It is proposed to use analog delay lines for the implementation. These devices have been around a long time, are well understood, and are relatively straight-forward to implement. Further, there are several existence proofs that a large system using analog delay lines can be built and operated to 14 bits of precision. A recent example of this technique is the liquid argon calorimeter electronics for E706 here at Fermilab, which has 10,000 channels. Delay elements of 1 or 1.5 μ sec are feasible, with delay/risetime ratios in the range 6 to 10.

The analog delay line configuration is shown in Fig. 4-12. The device has a 395 nsec tap that is used to form the signal that is sent to the Level-0 trigger. The event continues

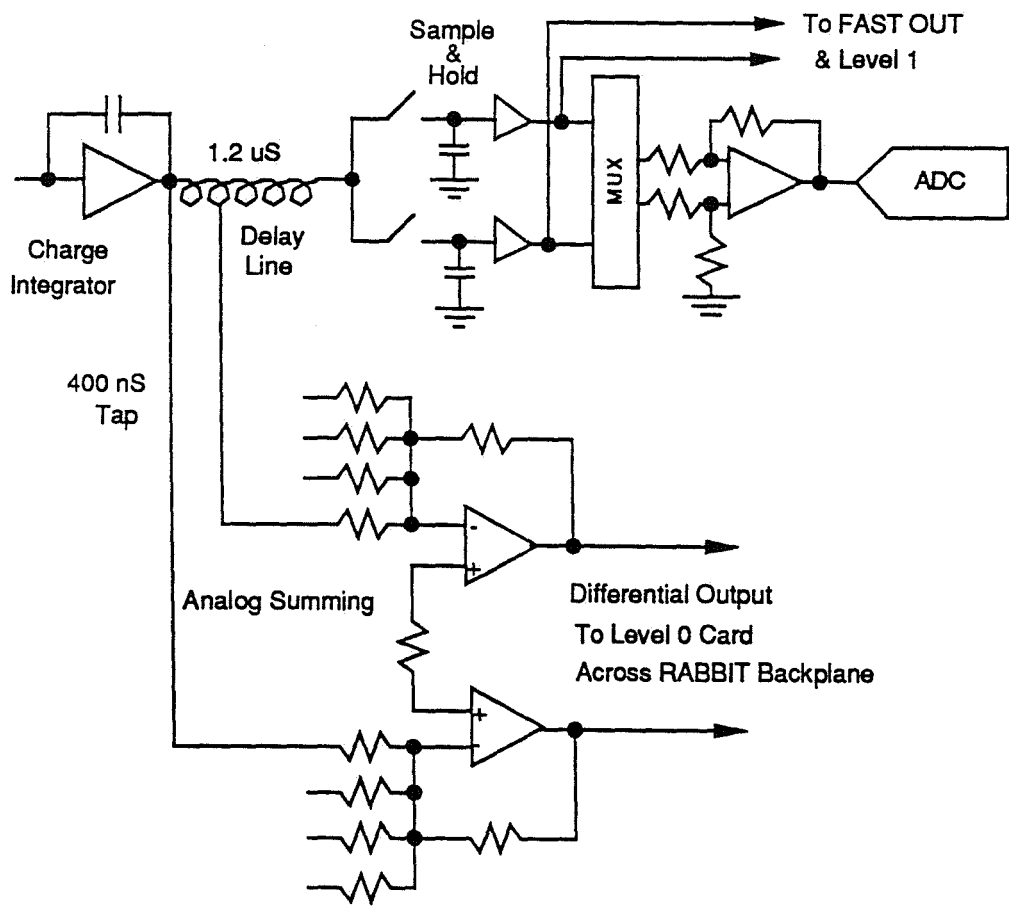


Figure 4-12: A circuit diagram of the basic elements of the proposed front-end electronics. Included are: pre-amp, 1.2 μ sec delay line with a tap at 400 nsec for fast output to the Level-0 trigger, the before-after sample-and-hold circuitry gated by Level-0.

down the delay line, to emerge at the time that a Level-0 decision has been made for that event. Either the sample-and-hold switches are opened, thereby capturing the event, or they are left closed to wait for the next event.

Cost estimates are in the range \$5.00 for a delay to risetime ratio of 6, to \$15.00 for a ratio of 10, in quantity. Since it is not possible to purchase these devices off the shelf, an R&D effort needs to start early in the project to work with any interested, qualified vendors to ensure that the part will meet the specifications.

Other possibilities for the analog memory are the use of switched capacitors as an analog ring buffer or a linear pipelined array. Switched capacitor techniques are emerging as viable analog storage methods. However, they are typically realized in ASIC designs, which represent a substantial development project. Also, there are questions about the precision, calibration, and complexity of these schemes, given the need for continuous clocking and the fact that the capacitors are on the chip. For these reasons the switched capacitor schemes are not proposed as the primary implementation of analog storage elements on the front end.

Having provided a way to store events in analog form locally on the front end, circuitry must be provided to form a Level-0 trigger. The approach is to treat each RABBIT crate as a unit in which Level-0 trigger towers can be formed. This is accomplished by analog summing of the appropriate calorimeter channels to form a trigger channel. Thus, Level-0 looks for single trigger towers over one or more thresholds as a means for making a decision.

To form a Level-0 trigger we plan to send analog signals from all of the trigger channels in a crate to a special Level-0 receiver card located in the crate. These cards receive analog signals from the front end cards, each pair of which is dedicated to a single trigger tower formed on the front end cards. The analog signals are then input to comparators, where several thresholds may be applied. This scheme essentially incorporates much of the functionality of the present Level-1 trigger into Level-0. The ability to mask off individual trigger channels is provided for on this card. Also, it would be necessary to have an independent read out path that is separate from the normal data acquisition system, for checking the performance of the Level-0 circuitry.

Concerning the front end scanning, one of the specifications is to read out the detector in 0.5 msec to the precision that we presently have (16-bit ADC with 14 bits precision.) Given the present technology of ADC converters, it is difficult to achieve this goal without adding more ADCs to the crate, working in parallel. The proposal is to put an ADC on every front end card in the crate. The compact disk industry has created a huge market for 16-bit ADCs, driving the cost down far enough so that it is feasible to consider such a scheme. (Burr Brown presently has a 16-bit monolithic ADC which has 14 bits of precision and sells for under \$50.00.)

With this scheme, every channel is digitized without doing any pedestal subtraction or data sparsification. These functions would be performed in Level-3. This has the advantage that pedestals are taken in the same way as data, thereby reducing errors associated with performing these functions differently. Also, this scheme has the potential of reducing the event building operation, since data are always sent to Level-3 with the same channel structure.

As an estimate for the time required to perform a readout operation, consider a typical crate with 20 cards with 32 channels on each card. The ADC mentioned above digitizes in 4 μ sec, with 2 μ sec additional time needed per conversion for settling. The time to digitize a 32 channel board is then 192 μ sec. If all boards are digitizing in parallel, the digitization time is still 192 μ sec. The parallel digitization will be done synchronously by a clock line across the RABBIT backplane, driven by the new gate generator module.

The digitized data from each channel are stored locally on each board. The memory of each card is read out sequentially after all of the digitizers are finished. The read operation is a 16-bit parallel data transfer across the RABBIT backplane, controlled by the new RABBIT crate controller which contains the scan list. This is attractive in that it minimizes the digital activity during the conversion process. If 16-bit words can be read out across the RABBIT backplane in 100 nsec, then for the above example it would take an additional 64 μ sec to read out the 640 channels, for a total of 0.25 msec. Additional overhead is estimated to be approximately 0.25 msec, for a total of 0.5 msec.

The front end crate controllers push the data upstairs over a unidirectional, dedicated bus. It is desirable to make this a parallel bus, since the data push operation is simplified. Serial transfers tend to be more complicated than a parallel transfer, and require synchronization and clocking that are otherwise unnecessary.

The link to Level-3 would bypass the MXs and Fastbus. The data are pushed up the cable to a module that contains a FIFO from which it is routed to one of the parallel Level-3 nodes for pedestal subtraction, threshold testing, event building, and other processing. Note that this implies getting rid of the MXs, and shifting the distributed functionality of the combined EWE/MX/Fastbus system that we presently have to a central location in Level-3, where the processing power is expected to be capable of handling these operations with very little additional overhead.

The MXs are to be replaced by a module that interfaces between Fastbus and the RABBIT crate controller. The new function of this interface is primarily passive during data-taking, being active only to issue start scan messages and to receive the DONE signal back. It is used for downloading the scan lists at the beginning of the run, running diagnostics, and providing the readout path for the special trigger functions. It also acts as an interface between the RABBIT crate and a personal computer to perform other diagnostics.

In principle, the module that contains the FIFO that receives the digitized data from downstairs could be part of the system that interfaces between Fastbus and the RABBIT crate controller. This would make the packaging problem easier, and also enhances the ease of debugging crate problems. However, there must be no interference in the flow of data from the RABBIT crate controller into Level-3 by the Fastbus interface during data taking. Any monitoring of the data flow must be entirely passive at this point in the system, except to disable the data flow entirely.

Tracking Electronics

The LeCroy 1879 TDC's are used in the tracking systems in CDF, as well as the muon systems. The present plan calls for these detectors to be retained in the upgrade, albeit in a modified form. The electronic requirements will be similiar to the present configuration. The electronics consists of preamps on the chambers, Amplifier-Shaper-Discriminator (ASD) boards which receive the preamp signals, LeCroy 1879 TDC's, and the SSP scanners which read out the TDC's.

Some of the preamps and ASD cards for the CTC system will be changed for the run in 1991 as described elsewhere in this proposal. Concerns about running at the increased rate in 1993, i.e. saturation, rise and fall time response, and baseline shifts are being addressed in these modified designs. The VTPC will be replaced by the VTX for the 1991 run, so it will have new preamps to begin with. The new muon systems will also have new preamps, which are being designed to operate in the upgraded environment. The ASD cards which receive the preamp signals are satisfactory for operation in 1993.

The LeCroy 1879 TDC's presently take 0.6 msec to encode the hits from all 96 channels on a board. It then takes 250 nsec per data word read into the SSP. Each hit produces two data words, one for the leading edge and another for the trailing edge of the chamber pulse. The pulse width information is used offline to reject chamber afterpulses and other spurious hits. These pulses tend to be narrower than genuine hits. Presently, a typical event produces 2200 hits per SSP in the CTC. The total dead time is 1.7 msec, (0.6 msec for TDC encoding and overheads, and 1.1 msec to read the data from the TDC's.) Given that the upgraded accelerator runs in the 36-bunch mode, implying that the number of interactions per crossing is comparable to what it is now, it is anticipated that the number of hits per event will not dramatically increase. Thus, the system as presently operated misses the dead time goal of 0.5 msec by a factor of almost four.

There are several options to available to make the Lecroy TDC's work in the up-graded system. One is to do away with the double reads of each hit channel. An unanswered question concerns what effect this will have in the off line analysis. Another option is to use the double buffer feature in the TDC's. The encoded data is stored in a separate buffer in the TDC so that it is possible to make the TDC live again immediately following completion of encoding. This presumes that the buffer can be read before another digitization occurs. There is also a question about noise sensitivity of the live TDC's to the digital traffic generated by the encoding process. Another possibility is to increase the number of SSP's to achieve the faster readout rate.

New Devices involved in Front End Electronics

- RC2 - Rabbit Crate Controller is the device which resides in the Rabbit Crate and provides control access to the front end cards. It controls the digitization of each channel and provides the parallel data path to the data concentrator.
- RC3 - Rabbit Crate Controller Controller resides upstairs and provides a read/write control path to the RC2 and the front end cards. Everything that is hardwired at the

crate level can also be controlled remotely from the RC3. In one option under consideration, the functions of this controller may be combined with that of the FIFO/Data Concentrator.

- FIFO/Data Concentrator. This is a key device in assembling data from Rabbit and Fastbus crates into large event fragments for transmission to Level 3. The number of lines coming into it will be of order 16 to 32 depending on details of available board real estate. Each incoming line is served by a FIFO buffer to store the data along with headers and trailers containing event ID and partition information. The data concentrator sequentially transfers the data for a single event from each FIFO to the output line along with routing information to direct it to the proper buffer in Level 3.
- Data Switch. As mentioned earlier, several options for this device exist. Our primary efforts at present are to define it so that details of the rest of the system can be designed.
- SSG - Start Scan Generator. This device has been specified, but is not yet designed. It controls the front-end readout.

Level-0 Trigger

The final Level-0 trigger logic collects the signals from the Level-0 cards in each front end crate and then makes the Level-0 decision. It will accept electrons, muons, jets and low threshold dileptons. Preliminary designs for the Level-0 trigger are described in CDF Note 1167.⁷³

Level-1 and Level-2 Triggers

There is a strong desire to retain as much of the Level-1/Level-2 trigger system as possible. The requirements to do this are:

1. The signals from the detector must be made available in analog form and correspond to the $\eta - \phi$ mapping of 0.2 by 15° .
2. The tracking system must be able to provide a list of stiff tracks in a few μsec .
3. The muon systems must be able to provide a list of muons (η , ϕ , and momentum) within a few μsec .
4. The method of making decisions based on a list of items generated by the cluster finder must still be valid.

The trigger is designed around a detector geometry of 0.2 units in η by 15° . This mapping is repeated for electromagnetic and hadronic calorimeters. Also the muon and track hits are mapped into the same geometry. New detectors in CDF will generate trigger signals in the same organization.

The tracking system currently reconstructs stiff tracks in a few μsec . The tracks are used in the trigger system to identify muons by matching with the muon chamber hits and electrons by matching with electromagnetic calorimeter clusters. This ability will be exploited even more heavily in order to achieve improved rejection rates in the Level-2 trigger.

The drift times in the muon chambers will be large compared to the Level-0 decision time. Scintillators will be added to the muon system in order to generate the Level-0 trigger. These signals will not have enough geometric resolution to be useful in Level-2, consequently there will be separate trigger signals generated for Level-2 which have position and momentum information. This will be used along with the tracking and calorimeter information in the Level-2 trigger to identify muons in various $\eta - \phi$ regions. Figures 1-2, 1-2 and 1-4 illustrate the strategies used in various ranges.

A factor of four speed improvement in the Level 2 processors from the 1988-1989 run is expected for the 1991 run. This will reduce the time associated with the Level-2 decision but does not increase the rejection factor. Additional rejection is required for the operation at luminosities of $\geq 5 \times 10^{31} \text{cm}^{-2} \text{sec}^{-1}$. Studies of additional algorithms which can be implemented are in progress. For example, beyond 1993 the electron algorithm could be improved if the strip chamber information from the EM calorimeters were available in the Level-2 trigger.

Luminosity Monitor

There are two components used in measuring the integrated luminosity: the live time and the instantaneous luminosity. The measure of live time will be kept in the Level-0 decision crate. In previous CDF runs the primary measure of luminosity has been the beam-beam counters. These will become less useful as the average number of events per crossing approaches 1, roughly 6×10^{30} for 6 bunches and 36×10^{30} for 36 bunches. These will be augmented by four counter telescopes, each with an effective cross section of 0.4 mb, one-hundred times smaller than that for the present system. The new monitors will be cross-calibrated with the BBC's at luminosities below $10^{30} / \text{cm}^2 / \text{sec}$. The BBC's will still retain the ability to tag halo particles associated with the incoming beam.

Accelerator transducers can be used to calculate what the luminosity should be, using the individual bunch intensities, the β^* , and the beam profile from flying wires. The present accuracy is about 7%, and we believe that this can be improved.

4.8 Level 3 Trigger: Online Analysis and Event Filtering

Table 4-17 gives a list of operating parameters for the Level-3 micro-processor farm as it was configured for the 1988-89 run (see Fig. 4-13), along with those planned for subsequent runs. The 1988-89 version of Level-3, based on Fermilab's VME-resident ACP-I system, was rather well matched to the capacity of the DAQ system, trigger algorithms and output tape capacity during Spring, 1989. At that point, a rich set of programs used most of the available memory and CPU time in Level-3. For the 1991 run, both the event rate into Level-3 and the computing time per event are expected to increase to the point where 300 to 500 mips of CPU power will be required.

Quantity	1988-89	"1991"	"1993"
Event Rate (Hz)	~4	30	100
CPU-time/event (mips-sec/event)	9.2	15	≥30
Total mips needed	37	500	≥3000
Processor Type	68020	R-3000	R-?000 or ?
Processor Speed (mips)	0.8	15	50
# Processors	58	32	≥ 64
Total Capacity (mips)	46	480	≥ 3200
Real time/event (sec)	11.5	1	≥0.64
No. Branch Bus Cables	1	2	4
Event Size (MBytes)	0.15	0.25	≥0.3
Data Rate (MB/sec)	0.75	7.5	30

Table 4-17: Level-3 Parameters For Recent and Future Runs

To provide this, we have decided to replace ACP-I with RISC-based microprocessors, interfaced to VME, with at least 15 times the CPU power of ACP-I. This offers a natural growth path for subsequent runs in 1993 and beyond. Two options have been studied, both based on the MIPS Corp. R-3000 processor: ACP-II or Silicon Graphics. We have connected both to the DAQ network with interfaces to Fastbus and the Farm Steward μ VAX. Data have been written to and read from memory with verification for periods of order 24 hours with no detected data errors. The data rates are consistent with rated bandwidths of the data channels, 10 MBytes/sec or above in both cases and more than sufficient for our needs. Details of directing and control of data flow all appear to be straightforward. Results to date indicate that, while either will work, the Silicon Graphics system is the better choice, and we assume that in subsequent discussion.

The Level-3 architecture planned for the 1991 run is shown in Figs. 4-14 and 4-15. There will be two event builders, each pushing data over a branch bus to half the Level-3 Farm. Control and communication with the DAQ supervisory process will continue to be

done by the Farm Steward. Data output will be to several streams:

- An express-line stream at about ~ 1 Hz through the VAX system and onto Exabyte 8500 8mm tape drives.
- A "solid-gold" subset of the above, top candidates and other highly interesting events, will be logged to disk and retained for several days for closer examination.
- A non-express-line stream at up to ~ 8 Hz onto four Exabyte 8500 8mm tape drives in parallel directly from Level 3, without event-by-event intervention from the VAX.

This is discussed at greater length in the following section dealing with RUN_CONTROL.

We plan to confront all the technical problems of Level-3 in time for solutions by the 1991 run so that the 1993 architecture (Fig. 4-16) will be an expansion of the 1991 architecture:

- Expand to four the number of branch bus cables into Level-3.
- Expand the number of processors in Level-3 to 64.
- Take advantage of any faster processors available at the time, e.g. the MIPS R4000 will soon be on the market and is rated at 50 MIPS.

A number of design issues are being worked on and seem to have viable solutions with the tools at hand:

1. Efficient polling can be accomplished by putting the present VME crate controllers (in slave mode) on the Silicon Graphics VME bus.
2. Expanded buffering can be handled in the Silicon Graphics memory with local buffer management.
3. Diagnostic programs have been re-written for the Silicon Graphics I/O and memory architecture and are being used in present tests.
4. The primitive operations needed for run startup, program loading, database access, etc., have been tested successfully. Plans are being made to integrate them into the Farm Steward and similar processes.
5. Test Stand simulation of the DAQ system message traffic with Level 3 should be re-written for Silicon Graphics by Summer, 1990.

At this writing, development of this new architecture for Level 3 is progressing amazingly well. We see no insurmountable problems for its timely implementation in a rather conservative design. A number of potential commercial developments have been discussed which would provide far more flexible and reliable operation at extremely high bandwidths in the future.

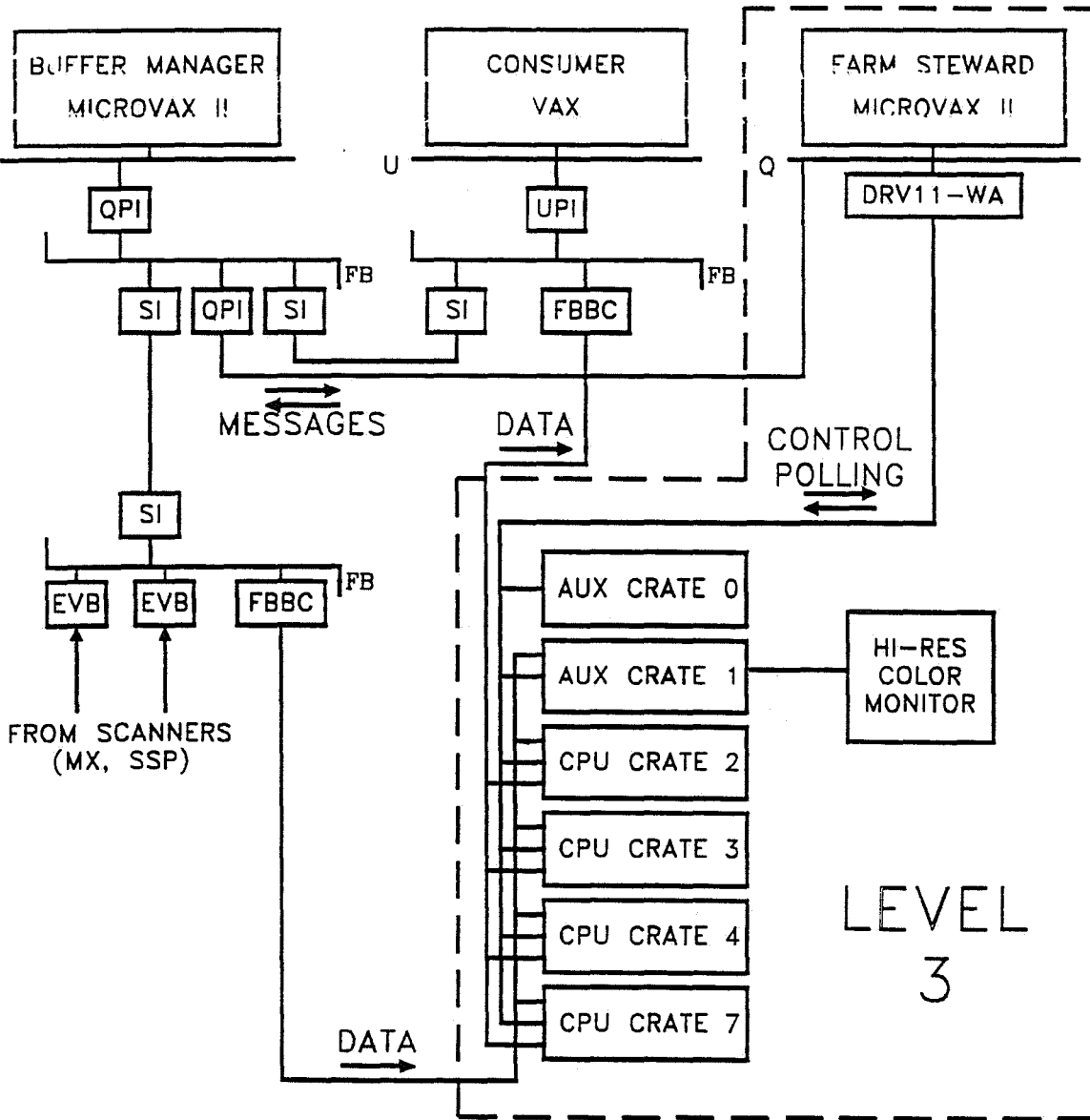


Figure 4-13: Relationship of the Level 3 VME crates to the DAQ system in the 1989 Run. Three branch bus lines provided high speed connections into VME crates for data input from the Event Builder (EVB), control, downloading and polling by the Farm Steward, and data output to the Buffer Multiplexer. The Farm Steward exchanged Fastbus messages with the Buffer Manager to direct the flow of event data to/from the individual nodes in the VME farm. It also sent messages to a specially equipped farm node which controlled a video monitor to display the farm status.

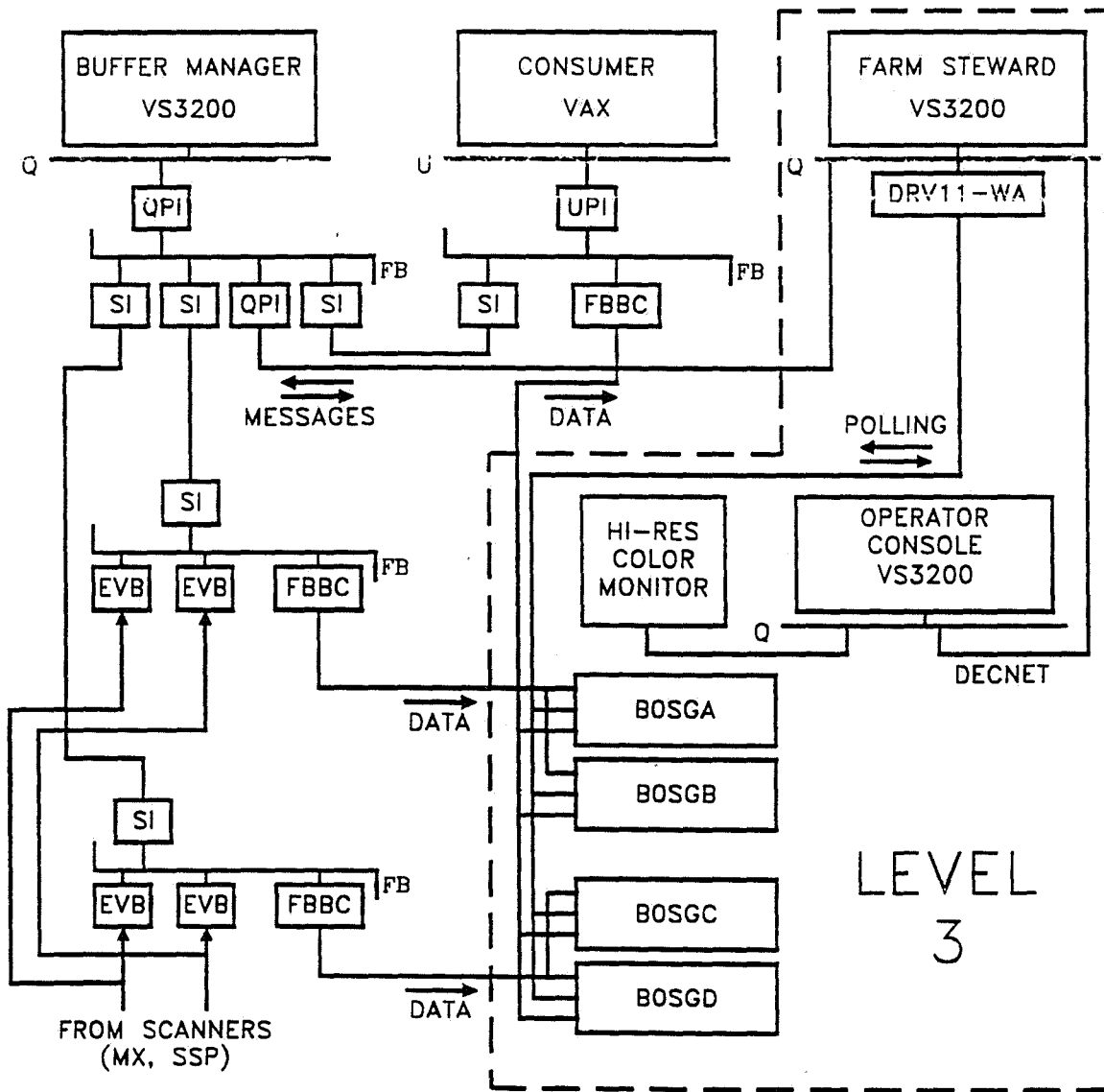


Figure 4-14: Relationship of the Level 3 VME crates to the DAQ system in the 1991 Run. The DAQ connections are similar to those in 1989 (Fig. 4-13) except that there are two Event Builders, each serving half the Level 3 farm over an independent branch bus. The main computing engines for Level 3 will be four Silicon Graphics boxes, each containing eight R3000 RISC processors benchmarked at about 15 MIPS. Ten VME slots for external I/O are provided in each box. Figure 4-15 shows details of the Silicon Graphics boxes and external connections.

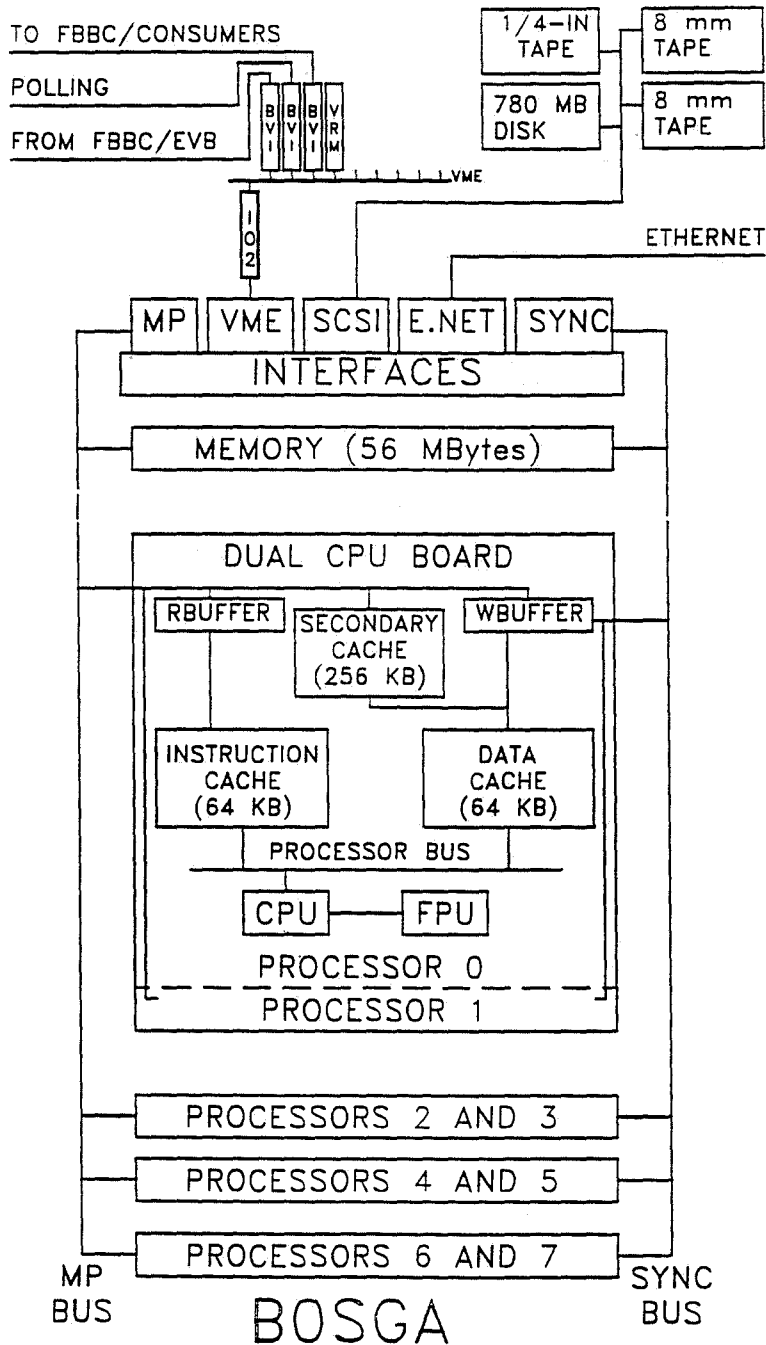


Figure 4-15: A diagram of one of four Level 3 Silicon Graphics boxes for the 1991 run. The VME connections for data I/O and control are similar to the 1989 run. The IO2 board is an interface between VME and the internal bus which maps VME addresses onto virtual memory. The box contains eight processors and 64 MBytes of shared memory, and has a UNIX operating system. The internal structure of one of the eight processors is shown. It has 64 KBytes of primary instruction cache and the same amount of primary data cache, plus 256 KBytes of secondary cache.

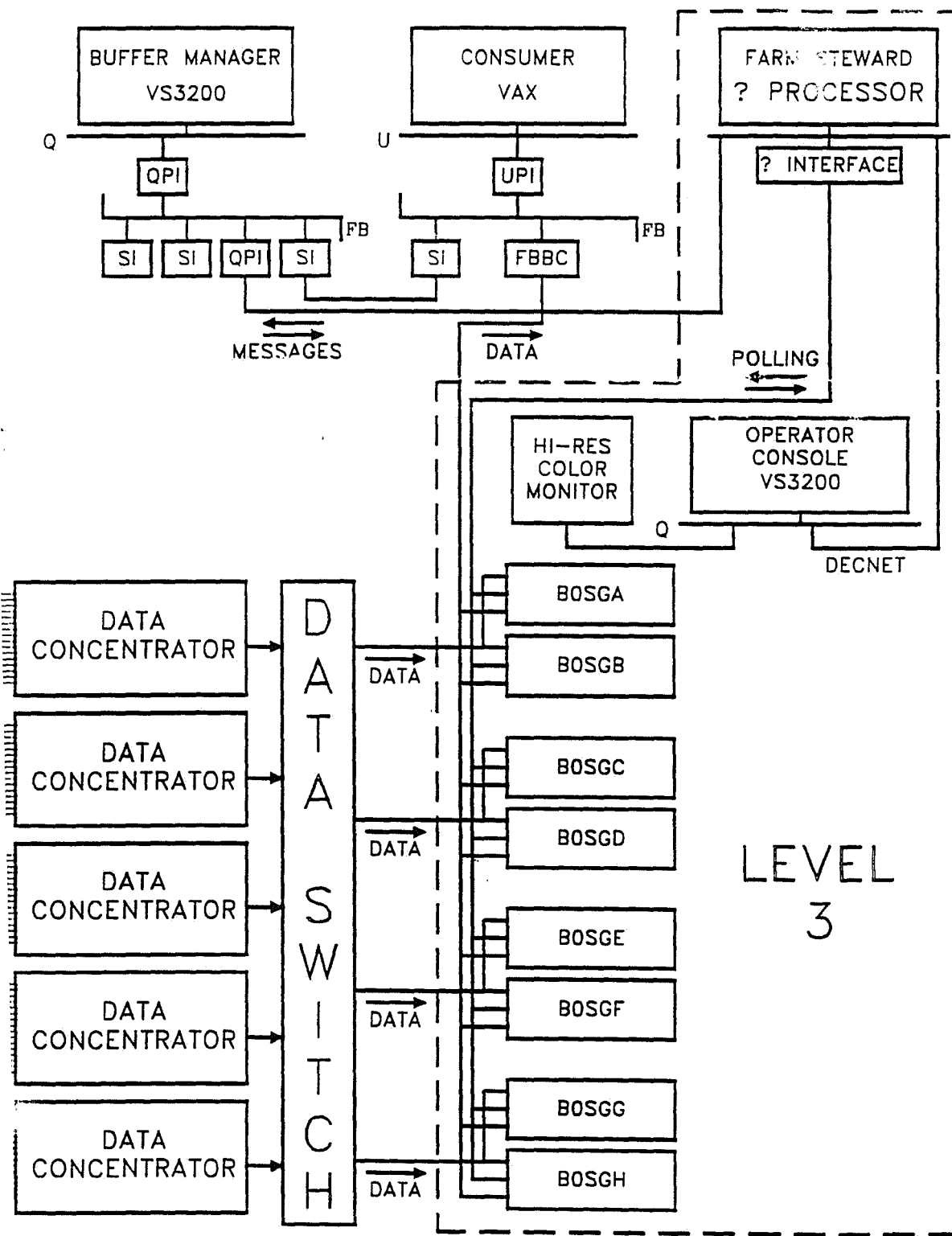


Figure 4-16: Relationship of the Level 3 to the DAQ system in the 1993 Run. The Silicon Graphics system for 1991 (Fig. 4-14) is expected to follow an appropriate growth path into 1993, with the number of boxes doubled and the R3000 CPU's (15 MIPS) replaced by R4000 (estimated at 50 MIPS). The number of branch bus connections from a high-speed switch in the DAQ should be four or eight depending on bandwidth of the technology selected.

4.9 Online Computing: RUN_CONTROL

In the CDF online system, VAX computers are used for high level control and monitoring functions. Such functions include hardware initialization and diagnostics for the trigger, Level 3 system, FASTBUS system and front end electronics; data logging, calibration, and processes that monitor the quality of the incoming data and from these data determine some global calibration parameters. The calibration data base is maintained on the CDF VAX cluster. The hardware voltage monitoring and high voltage control was also run from a VAX. Plans for this system are discussed elsewhere.

During the detector checkout phase, and during down times during the run, the detector is divided up into partitions operated in parallel for checkout and maintenance, each under the control of a separate VAX.

During normal data taking with the entire detector active, the control and monitoring functions are distributed among several of the nodes in this cluster. The existing computers used for these purposes include two VAX 750s, one VAX 785, three VAX 8350s, and several μ VAX's. These provide multiple-user access to the DAQ and detector subsystems during tune-up at the beginning of the run, consumer processes during data collection, and redundancy in case one of the VAX's fails. In addition the cluster contains redundant HSC controllers, 8mm tape drives. Critical disks are shadowed.

For the next (1991) CDF run, we plan to retire the VAX 750's and begin migrating these higher level functions to μ VAX workstations. Such workstations offer the advantage of greatly improved CPU performance at nominal cost, and an integrated graphics display station with a window based user interface. Some of the control and diagnostic programs will be modified to better take advantage of this capability.

For the 1993 run, at least some of the above functions such as data logging and some monitoring and calibration will be performed by the Level 3 system. However it is likely that some of these monitoring functions and most initialization and diagnostic functions will still be performed by the VAX's. It will still be important to support a number of checkout activities in parallel (and thus multiple detector "partitions") particularly given the large amount of new electronics to be debugged. For the 1993 run, we plan to complete migration of these functions to workstations, and retire the VAX 8350's.

The increased reliance on workstations will place greater demands on the performance and reliability of the boot nodes for those workstations. Thus, by the 1993 run we plan to upgrade the present μ VAX 3500 server and also to provide redundancy for this function. In addition, large upgrades in disk storage capacity will be required.

For data logging in the 1988-89 run, CDF had a single output stream from Level 3 to processes running in the VAX system and onto 9-track magnetic tape. During the run as a test, Exabyte 8mm tape drives were added and recorded the same data redundantly with the 9-track drives. This exercise proved successful. In 1991 and subsequent runs, as discussed in the section on Level 3, the plan is to write to multiple data streams:

- An express-line stream at about ~ 1 Hz through the VAX system and onto Exabyte 8500 8mm tape drives.

- A "solid-gold" subset of the above, top candidates and other highly interesting events, will be logged to disk and retained for several days for closer examination.
- A non-express-line stream at up to ~ 8 Hz onto four Exabyte 8500 8mm tape drives in parallel directly from Level 3, without event-by-event intervention from the VAX.

These drives are expected to be able to write data at 500 KB/sec, corresponding to approximately $\sim 5 \pm \sim 2$ events per second per drive based on the expected event size.

At present, 8mm tape seems to be most cost effective recording medium with adequate bandwidth in terms of both drive and media cost. Other possibilities, such as 4mm DAT tape, 3480 tape cartridges, and optical disks are more expensive and/or cannot write data at a sufficiently high rate.

4.10 Offline Computing

Experience from the 1988/9 run

In the 1988/9 run CDF recorded 6-million events, representing 0.7 Terabytes of raw data. Event reconstruction took on average 250 million instructions per event and produced event records of about 200 KB. Subsequent compression, filtering, and analysis has required additional resources at Fermilab amounting to 150 MIPS of CPU and 50 GB of disc, including 40 distributed workstations, the latest of which consist of a Vaxstation 3100 (4.5 MIPS) plus one WREN-V disc (0.6 GB), and an 8mm tape drive.

During the past run, CDF made substantial progress in dealing with large data sets, and making them accessible to a large international collaboration. Preliminary results based on highly selected subsamples of the data were presented in conferences during the running period. This experience gives a firm basis to understand and extrapolate our needs in the coming runs where we expect substantial increases in the luminosity and number of exciting events. One major issue is having the offline system ready at the start of the collider run. Among other things, this requires having a robust development environment available to CDF in the periods between runs. Another major issue is fast and convenient access to large datasets for the large CDF collaboration. The available resources for the 1988/9 run were marginal at best. We will require substantial improvements particularly in fast access media and networking in order to deal with data from future runs.

Needs for the 1991/2 run

In the 1991/2 run the initial upgrade of the Level 3 trigger system will enable CDF to write out an "express-line" of chosen events at 1 Hz. There will be an additional 8 Hz of non-express-line events taken with lower thresholds and/or looser cuts for determination of backgrounds and efficiencies, and for more inclusive analyses. An estimate of our offline needs for the 1991/2 run is summarized in Table 5-30.

(A) Express-line event reconstruction and analysis :

Writing events at 1 Hz CDF will record up to 10-million raw express-line events (approx. 1.3 Terabytes) onto 8-mm tape during the 1991/2 run. The express-line sample alone could be twice the size of the entire 1988/89 data sample. Furthermore, we must plan to reconstruct and filter express-line events in essentially real time to enable the resources to be available after the run for processing sub-samples of the non-express-line data for background and efficiency calculations, for detailed Monte Carlo calculations, and for reprocessing of subsamples of express-line data when needed.

We will require the following resources to be able to analyse the 1991/2 data:

1. CPU for reconstructing events and producing DSTs from raw data: 500 MIPS.
We estimate 500 million instructions per event in 1991/2, the increase with respect

to the reconstruction of events from the 1988/9 run coming partly from the increase in number of detector channels (and in particular the increased tracking capability of CDF) and partly from the increased complexity of the events (in particular the increased rate of multiple interactions).

2. 8 mm tapes for DST production: 500 double density double speed cassettes.
If these are not available we will use single density cassettes, changing to double density when possible.
3. 8 mm robotic storage devices for DST's: 5 Robots.
Each robot is assumed to store 100 double density tapes, and serve four 8mm tape drives. This will enable all DSTs to be spun within a 1 to 2 week period.
4. CPU for filtering DSTs and producing compressed data sets (microDSTs): 100 MIPS.
5. Mass storage for filtered DST events:
This is a critical item and is addressed separately below.
6. Mass storage for compressed data sets : 100 GB of high speed disc and four 8 mm drives.
Assumes an event compression factor of 10 in producing microDSTs. This will enable 50% of the express-line to be placed on disc and made available to the distributed CDF workstations at Fermilab. The compressed data sets will also be written to tape for distribution to the outside institutions.
7. 8 mm tape copying: 20 dedicated 8 mm drives.
For duplication of microDST tapes and highly selected DST samples before distribution to the outside institutions.
8. Distributed workstations:
The 40 CDF workstations currently at Fermilab will need to be maintained, upgraded, and replaced as they age, or as cheaper and better devices become available. We will need to supplement the present workstations with enhanced disc space (2 GB will be sufficient to store most highly selected working data samples) and dual 8 mm drives to reduce traffic to the central mass storage devices.
9. Analysis engine: 400 MIPS + 40 GB Disc
Based on our present experience additional analysis needs after production require approximately 0.6 times the CPU needed for production.
10. High bandwidth networking:
CDF will require high bandwidth links between the production and analysis CPU engines, the mass storage devices, and the 8 mm robotic tape drives. We will require FDDI networking as soon as it becomes available at Fermilab.

(B) Non-Express-Line data :

The upgraded level 3 trigger system will enable about 80-million non-express-line events to be written to tape during the 1991/2 run. These data will contain event sub-samples that will need to be analysed after the run to extract information about backgrounds and efficiencies. We plan to use the Level 3 and production CPU to reconstruct these data as needed. Processing the non-express-line data will require storage of at least 16-million additional DST event records, requiring 800 double density 8 mm cassettes and 8 robots each with four 8 mm drives.

Mass storage for filtered DST events

The accessibility of the very large DST data sample limits both the scope and rate of the present CDF analysis. In the future we will need to be able to store the bulk of the express-line DST events on a mass storage medium that can be accessed by the distributed CDF workstations at Fermilab, and by the main CDF analysis engine, via high bandwidth links. By the end of the 1991/2 run we would like to be able to store 50% of all the express-line DST events (1 Terabyte) on a medium that can be accessed by 40 CDF workstations with reasonable seek and read times. Since mass storage technology is improving rapidly with time we feel that it is too early to identify the best medium for the 1991/2 run. However as an example we consider in the following a solution based on 8 mm tapes stored in robotic devices.

We envisage filtering the DST data onto 8 mm tapes stored in 5 robotic devices, and sorted according to trigger type. Each robot would serve 50 double density cassettes, and four 8 mm drives.

Other technologies (for example optical discs) should also be considered before a final choice is made. We stress here that we consider making the bulk of the CDF express-line DST events accessible to the widest possible community within CDF to be a crucial goal.

Needs for the 1993/4 run

To store and access the 1993/4 data we will need additional 8 mm tapes and robots (if 8 mm tapes are the storage medium of choice) in quantities similar to those needed for the 1991/2 run. We will also require additional CPU power to cope with further increases in the number of detector channels and event complexity and more extensive Monte Carlo calculations of rarer processes.

Our estimates for the additional resources required in 1993/4 over and above those needed for 1991/2 data analyses are given in Table 5-31.

4.11 Miscellaneous Systems

Limits and Alarms

Limits and alarms will be substantially improved for the 1991 run. The exact plan for this is under discussion at this writing. One of the options is that the CDF experiment be fully integrated into the ACcelerator control system NETwork (ACNET). This is described at length in CDF Note 1112.⁷⁴

Calibrations

Two important facets of the CDF DAQ system are the implementation of online calibrations and monitoring of the data flow. These tools are invaluable for maintaining the integrity of the output stream. Obviously, we will retain and improve the capabilities we already have, as well as add new tools to monitor the changes envisioned for the 1993 CDF DAQ upgrade.

The plans and budgets for individual detector upgrades and the DAQ upgrade provide for hardware features needed for calibration.

We have studied what revisions will be needed for calibration procedures and this is described at length in CDF Note 1150.⁷⁵

5 Cost Projections

5.1 Budget: Plug Calorimeter

A budget for the scintillator plug upgrade is presented below. In addition, budgets are presented for a plug pre-radiator and for strip chambers.

Plug Scintillation Calorimeter Costs

The costing scenario for the scintillator plug assumes the following:

- use of the existing plug iron assemblies,
- new lead for the Plug EM section,
- extending coverage down to 2° ,
- add stainless steel re-entrant plates, and insert disks,
- 24 EM plates, 0.5 cm lead, 0.25 cm plastic,
- 25 hadron plates, 5 cm iron, 0.25 cm plastic.
- Scintillator cost: $\$200/\text{m}^2$, (KYOWA SCSN 81)
- Shifter Fiber cost: $\$0.25/\text{m}$, (KYOWA Y-7, 0.5 mm diam.)
- Clear Optical Fiber cost: $\$0.10/\text{m}$.

The cost of an average tile ($10 \times 10\text{cm}^2$, EM and $20 \times 20\text{cm}^2$, Hadron) is estimated as follows:

- Scintillator: $\$2$ EM, $\$8$ Hadron
- Laser cutting (25 cm/min, $\$100/\text{hr}$): $\$2$ EM, $\$4$ Hadron
- Grooving (Laser machining) $\$1.00$
- Shifter fiber 20 cm/tile $\$0.05$
- Clear EM fibers, 2 legs, 4 m each: $\$0.80$
- OR, Clear Hadron Fibers, 2 legs, 2 m each: $\$0.40$
- Assembly, testing, insertion, 1 man-hr/tile: $\$10$

This yields a cost of $\$15.85/\text{tile}$ for EM and $\$23.45/\text{tile}$ for hadron. The costs per tower are $\$380.40$ for EM and $\$586.25$ for hadron.

The high voltage power is assumed to be $\$70$ per channel. This estimate is based on a CAEN system using a Model A 119A Manual Controller, a Model CY 117A CAMAC Controller, 31 Model PS 35-100 Supplies and 69 Model SY 170 Dividers. Readout electronics are assumed to cost $\$52/\text{channel}$. There are 3600 channels, and the budget provides for test stand, spares and empty channels on multi-channel electronic boards at system boundaries.

Item	Number	Unit Price	Total Price (\$1000)
EM towers	2688	380.40	1,022
Hadron towers	912	586.25	534
Lead and Stainless Steel			300
Phototubes	3800	120	456
High Voltage Power (Channels)	3800	70	266
Misc. (PM Socket, Cables...) per chan.	3800	50	190
Monitoring System (Flasher, Source)			300
Test Equipment			100
Readout Electronics: ADC channels	4000	52	208
Readout Electronics: TDC channels	4000	52	208
Total Cost			3,584

Table 5-18: Tile Scintillator Plug Calorimeter Costs

Plug Pre-Radiator

Item	Number	Unit Price	Total Price (\$1000)
1.5 X ₀ lead preradiator (per pound)	2300	2	5
Tiles and fiber	2688	15.85	41
Phototubes	50	2000	100
Readout ADC	90	700	63
High Voltage (per channel)	50	70	4
Bases, connectors, etc. (per channel)	50	1000	50
Assembly (1 technican-year)			35
Subtotal			298

Table 5-19: Plug Pre-Radiator Costs: Scintillating tiles with waveshifter fibers.

Plug Strip Chamber

Item	Number	Unit Price	Total (\$)
Tiles	10752	15.45	166
Phototubes	180	2000	360
Readout cards	360	700	252
High Voltage (per channel)	180	70	13
Bases, connectors, etc. (per channel)	180	1000	180
Assembly (3 technician-year)			105
Subtotal			1076

Table 5-20: Tiles with fiber readout to multi-channel phototubes.

5.2 Budget: Silicon Vertex Detector

Item	Number	Unit Price	Total Price (\$1000)
New Chip R&D, rad. hard production			300
New Hybrids, connectors, cables			150
New Silicon Detectors			500
Microbonds			150
Tooling			250
1-inch Be Pipe			100
New Fixtures and Supports			250
New DAQ Electronics			350
Secondary Vertex Trigger			350
Subtotal			2,400

Table 5-21: Silicon Vertex Detector Costs.

5.3 Budget: Muon Detectors

Item	Number	Unit Price	Total (1000)
Wire Chambers			
Chamber Planes	6		400
Additional TDC's	16	6,000	96
Chamber Mounts			50
Gain Monitor/HV Control			5
Cables			10
Projective Scintillators			
PMT/lightpipe/base	2448	220	539
Cut existing Scint.			15
Additional Scint. Sheet	48	850	41
Revise exiting mounts			10
96-channel TDC's	34	5,000	170
Labor			50
Toroids			
Revise Toroid Support			25
Electronics: Calibration/Triggering			
Level 0 Projective Mosaic			35
Level 1 Angle Cuts			250
Wire pulsing			20
Scintillator Pulsing			20
Level 2 High P_T			75
Crates/Power			30
Additional Power Supplies			10
Additions to Gas System			5
Packing/Shipping			5
Subtotal			1,861

Table 5-22: Forward Muon Costs

5.4 Budget: Data Acquisition System

Electronics Hardware

The largest budget items in the DAQ system are those which scale as the number of channels. These include Rabbit cards and parts for the front-end pre-amp/delay-line/ADC, RC³ cards, cables, etc. The channel count for existing systems which will be retained, and for CMEX is 23,568. We allow an additional 20% for test stands, spares and round-up, i.e. logical division of channels into readout groups which leaves some boards only partially populated. The table below is based on this number. Additional electronics for new detectors are included in the individual budget estimates for those subsystems.

We assume that there will be 32 channels per card, i.e. a total of about 1000 Rabbit cards, including test beam and spares. The delay lines cost about \$20 each, and each card will have a \$200 ADC. The rest of the board will be similar to the existing system where we have experience with the costs for boards and components. The cost per board will be somewhat greater than that for the present boards because we must change from double-sided to multilayered. This also implies increased stuffing cost. Including delay lines and ADC's, we estimate \$1500 per board. This works out to a subtotal of about \$47/channel. Pro-rated costs for RC³ cards and other parts of the system which scale roughly as channel count bring this up to \$52/channel. This figure is used in the budget estimates for the various new detector subsystems.

For the data concentrator, it is assumed that the FIFO's will serve 16 serial-input channels. Since failure of the data concentrator would bring the entire experiment down, we plan a "hot spare" and a small offline test system.

The table below summarizes the estimated costs of all the new parts of the DAQ system up to the Fastbus to Branch Bus interface to Level 3.

During production we will need to hire about 7 temporaries for between one and two years. Additional operating costs for tooling, testing and prototyping are estimated at about \$200,000 for these tasks.

Item	Number	Unit Price	Total Price (\$1000)
* Front End Cards for 28,000 channels	875	1,500	875
Tooling, test equipment, overhead			300
Other Rabbit System Cards			
* Rabbit Backplanes	80	750	60
* BAT	80	600	48
* Crate Controller (RC ²)	80	500	40
* Level 0 Interface Card	80	1,000	80
* System Interface Card (RC ³)	40	7,000	280
Fastbus Crates	4	10,000	40
Segment Interconnects	4	5,000	20
Display Modules	4	2,000	8
Level 0 Trigger Crates (with cards)	2	50,000	100
Tevatron Interface/Clock/Control			50
Luminosity Monitor			50
Interface to LeCroy 1879 Crates (FBSR)	33	7,000	231
Fastbus Crates	7	10,000	70
Segment Interconnects	7	5,000	35
Display Modules	7	2,000	14
Data Concentrator			
* FIFO Cards	10	5,000	50
FIFO Cards for test stand	5	5,000	25
SSP's	3	10,000	30
Buffered FBBC Cards	20	5,000	100
Special FB Backplane	3	4,000	12
Fastbus Crates	2	10,000	20
Segment Interconnects	2	5,000	10
Display Modules	2	2,000	4
Temporary workers for 2 years			280
Subtotal			2,832

Note: Items marked * are used in per-channel cost estimate of \$52 for the Rabbit system. This is used to scale additional Rabbit electronics costs in other tables.

Table 5-23: Data Acquisition Electronics Costs

Level 1 and Level 2 Trigger

Item	Number	Unit Price	Total Price (\$1000)
Processor speedup, trigger options for new detectors			500
Subtotal			500

Table 5-24: Level 1,2 Costs

Level 3

The Level 3 budget is based on the assumption that the architecture planned for the 1991 CDF run can be expanded from four to eight Silicon Graphics 4D/220 servers, and that 50-MIPS CPU's will be available to replace the currently available 15-MIPS units. Further, it is assumed that each server will have expanded disk storage and tape drives

A full time Systems Manager/Programmer should be added to the CDF staff to maintain the system. Roughly 500 sq. ft. of space will be needed on the 3rd floor of B0 for CPU cabinets, VME crates, I/O devices and support. Software licences at approximately \$50,000 and installation costs of about \$20,000 are assumed to come from operating costs.

Item	Number	Unit Price	Total Price (\$1000)
CPU Power (MIPS)	3000	450	1,350
Disk Controllers and Drives (4 GB/box)	32	2900	93
Tape Controller and Two Drives per box	8	7000	56
High Bandwidth Links, Interfaces/Cable			80
Subtotal			1,579

Table 5-25: Level 3 Costs

5.5 Budget: Online Computing

Item	Number	Unit Price	Total Price (\$1000)
Graphics Workstations			75
Program Development Workstations			75
MicroVax Server			150
Upgrade disk storage (GB)			100
Upgrade HSC controller			150
8-mm Tape drives			50
Subtotal			600

Table 5-26: Online Computing Costs

5.6 Budget: Miscellaneous

Item	Number	Unit Price	Total Price (\$1000)
Central Tracking (CTC) Pre-Amps			98
Subtotal			98

Table 5-27: Costs for Miscellaneous Items

5.7 Budget Summary

The table below summarizes the total budget. A 20% operation contingency is added, and then an additional contingency is added for an assumed 6% escalation per year. This calculation is shown in Table 5-29 which gives the funding profile from FY91 to FY94.

System	Price (\$1000)	Staff
Plug/Forward Calorimeter	3,584	Labor incl.
Plug Pre-Radiator	298	Labor incl.
Plug Strip Chambers	1,076	Labor incl.
SVX replacement	2,400	
Forward Muon	1,861	Labor incl.
DAQ Electronics	2,832	1 FTE Dig.Eng. 7 temps
Level 1-2 Trigger	500	
Level 3 and data logging	1,579	1 FTE programmer
Online Computing (Run_Control)	600	1 FTE programmer
Miscellaneous	98	
Subtotal	14,828	
Contingency (20%)	2,966	
Total Estimate "1990 dollars"	17,794	3 FTE + 7 temp.
Contingency (escalation)	2,542	
Total Estimate "then year"	20,336	3 FTE + 7 temp.

Table 5-28: CDF Upgrade Budget Summary

5.8 Funding Profile

Year	1990 \$1000		"Then Year" (\$1000)
	Cost	Cost + 20%	
FY91	2,400	2,880	3,053
FY92	6,700	8,040	9,034
FY93	5,000	6,000	7,146
FY94	728	874	1,103
Total	14,828	17,794	20,336

Table 5-29: CDF Upgrade Budget Profile: in 1990 and "Then Year" Dollars

5.9 Budget: Offline Computing and Data Storage

The budget for CDF's offline computing needs is presented separately, so that it can be used as part of the laboratory's overall assessment of computing needs. A substantial part of the upgraded offline analysis capability must be present for the 1991 collider run, and the remainder for 1993. For this reason, two tables are presented. A funding profile is also presented, spanning three fiscal years.

A number of assumptions must be made in order to project the cost of computing.

- For a high-end Silicon Graphics system the cost per 15-MIPS CPU is \$22,500 (or \$1500/MIPS). We assume that the cost will be the same for a 50-MIPS CPU (\$450/MIPS) for the upgrade.
- High Performance (HSC-access) disk storage will cost about \$9,500/GByte.
- Lower Performance (Ethernet-access) disk storage will cost about \$2,900/GByte.

In addition to equipment, the CDF staff will have to be augmented by three FTE to develop, implement and maintain the file server, data handling, data distribution, management of offline production and related activities.

Item	Number	Unit Price	Total Price (\$1000)
CPU Power (MIPS)	1000	450	450
8 mm Robots	19	30K	570
8 mm Tape Drives	96	3K	288
Disc Storage, high speed access (GByte) Controllers, links, etc.	140	9.5K	1,330 330
8-mm Tapes	2,000	15	30
Workstation Upgrades			
2 GB disks	40	6K	240
8 mm drives	40	2.5K	100
Subtotal			3,338
Contingency (20%)			668
Total Estimate "1990 dollars"			4,006
Contingency (escalation)			332
Total Estimate "then year"			4,338

Table 5-30: Offline Computing Costs for the 1991 Run

The funding profile for offline computing needs is based on a staged acquisition before, during and after the 1991 run, and additional acquisitions in preparation for the 1993

Item	Number	Unit Price	Total Price (\$1000)
CPU Power (MIPS)	1000	450	450
8 mm Robots	20	30K	600
8 mm Tape Drives	40	3K	120
Disc Storage, high speed access (GByte) Controllers, links, etc.	100	9.5K	950 250
8-mm Tapes	3,000	15	45
Workstation Upgrades	40	5K	200
Subtotal			2,615
Contingency (20%)			523
Total Estimate "1990 dollars"			3,138
Contingency (escalation)			599
Total Estimate "then year"			3,737

Table 5-31: Offline Computing Costs for the 1993 Run

run. Purchases will be delayed as long as prudent in order to take advantage of constantly improving price/performance ratios.

Year	1990 \$1000		"Then Year" (\$1000)
	Cost	Cost + 20%	
FY91	2,128	2,554	2,707
FY92	1,210	1,452	1,631
FY93	2,615	3,138	3,737
Total	5,953	7,144	8,075

Table 5-32: CDF Offline Computing Budget Profile: in 1990 and "Then Year" Dollars

6 Participating Institutions and Physicists

Argonne National Laboratory

Blair, R. Kuhlmann, S. Nodulman, L.
Proudfoot, J. Wagner, R. G. Wicklund, A.

Brandeis University

Blocker, C. Bensinger, L. Kirsch, L.
Behrends, S. Students

University of Chicago

Frisch, H. J. Shochet, M. Grosso-Pilcher, C.
Campagnari, C. Contreras, M. Eno, S.
Miller, M. Sullivan, G. Students

Fermi National Accelerator Laboratory

Amidei, D.	Atac, M.	Beretvas, A.
Berge, J. P.	Binkley, M.	Chadwick, K.
Cihangir, S.	Cooper, J.	Crane, D.
Elias, J.	Foster, G. W.	Flaugher, B.
Freeman, J.	Hahn, S. R.	Harris, R.
Hauser, J.	Huth, J.	Jensen, H.
Johnson, R. P.	Joshi, U.	Jovanovic, D.
Kephart, R.	Marriner, J. P.	Mukherjee, A.
Nelson, C.	Newman-Holmes, C.	Para, A.
Patrick, J.	Plunkett, R.	Schmidt, E. E.
Segler, S.	Theriot, D.	Tkaczyk, S.
Tollestrup, A.	Vidal, R.	Wagner, R. L.
Wainer, N.	Yagil, A.	Yeh, G. P.
Yoh, J.	Yun, J. C.	

INFN - Frascati

Bertolucci, S. Chiarelli, G. Cordelli, M.
Miscelli, S. Sansoni, A.

Harvard University

Brandenburg, G. Feldman, G. Franklin, M.
Geer, S. Phillips, T. Students

University of Illinois

Holloway, L. Errede, S. Liss, T.
Karliner, I. Gauthier, A. Students

Johns Hopkins University

Barnett, B. A. Matthews, J. A. J. Skarha, J.
Snider, F. Students

KEK - Japan

Mishina, M. Fukui, Y. Mikamo, S.

Lawrence Berkeley Laboratory

Carithers, W. Chinowsky, W. Ely, R.
Galtieri, L. Gold, M. Haber, C.
Kadel, R. Levi, M. Shapiro, M.
Siegrist, J. Tipton, P. Students

University of Michigan

Campbell, M. Chapman, J. Students

University of Pennsylvania

Hollebeek, R. Williams, H. Gladney, L.
Lockyer, N. Sinervo, P. Low, E.
Ragan, K. Students

INFN - Pisa

Bellettini, G. Scribano, A. Stefanini, A.
Rimondi, F. Ristori, L. Cervelli, F.
Menzione, A. Zetti, F. Bedeschi, F.
Belforte, S. Dell'Orso, M. Galeotti, S.
Giannetti, P. Grassman, H. Mangano, M.
Smith, D. Westhusing, T.

Purdue University

Barnes, V. Garfinkel, A. Laasanen, A.
Students

University of Rochester

Bodek, A. Olsen, S. Budd, H.
Sakumoto, W. de Barbaro, P. Auchincloss, P.
Students

Rockefeller University

Goulianos, K. White, S. N. Chapin, T. J.
Giokaris, N. Students

Rutgers University

Devlin, T. Watts, T. Buckley, E.
Mueller, J. Students

Texas A&M University

McIntyre, P. M. Webb, R. C. Bowcock, T.
Kamon, T. Students

University of Tsukuba

Kondo, K. Takikawa, K. Miyashita, S.
Kim, S. Nakano, I. Yasuoka, K.
Hara, K. Morita, Y. Funayama, Y.
Students

Tufts University

Sliwa, K. Students

University of Wisconsin

Pondrom, L. Carlsmith, D. Handler, R.
Bellinger, J. Wendt, C. Students

References

- [1] Design Report for the Fermilab Collider Detector Facility (CDF), D. Ayres et al., Fermilab, August, 1981 (unpublished).
- [2] The CDF Detector: An Overview, F. Abe et al., Nuclear Instruments and Methods, **A271**, 387 (1988).
- [3] The CDF Central Electromagnetic Calorimeter, L. Balka et al., Nuclear Instruments and Methods, **A267**, 272 (1988).
- [4] The CDF Vertex Time Projection Chamber System, F. Snider et al., Nuclear Instruments and Methods, **A268**, 75 (1988).
- [5] Design and Construction of the CDF Central Tracking Chamber, F. Bedeschi et al., Nuclear Instruments and Methods, **A268**, 50 (1988).
- [6] The Design and Construction of the CDF Central Drift Tube Array, S. Bhadra et al., Nuclear Instruments and Methods, **A268**, 92 (1988).
- [7] Radial Wire Drift Chambers for CDF Forward Tracking, M. Atac et al., Nuclear Instruments and Methods, **A269**, 40 (1988).
- [8] A Computer-Controlled Wire Tension Measurement System Used in the Fabrication of the CDF Central Drift Tube Array, S. Bhadra et al., Nuclear Instruments and Methods, **A269**, 33 (1988).
- [9] The CDF Central and Endwall Hadron Calorimeter, S. Bertolucci et al., Nuclear Instruments and Methods, **A267**, 301 (1988).
- [10] CDF End Plug Electromagnetic Calorimeter Using Conductive Plastic Proportional Tubes, Y. Fukui et al., Nuclear Instruments and Methods, **A267**, 280 (1988).
- [11] An Electromagnetic Calorimeter for the Small Angle Regions of the Collider Detector at Fermilab, G. Brandenburg et al., Nuclear Instruments and Methods, **A267**, 257 (1988).
- [12] The CDF Forward/Backward Hadron Calorimeter, S. Cihangir et al., Nuclear Instruments and Methods, **A267**, 249 (1988).
- [13] Calibration Systems for the CDF Central Electromagnetic Calorimeter, S. R. Hahn et al., Nuclear Instruments and Methods, **A267**, 351 (1988).
- [14] Response Maps of the CDF Central Electromagnetic Calorimeter with Electrons, K. Yasuoka et al., Nuclear Instruments and Methods, **A267**, 315 (1988).
- [15] Cosmic Ray Test of the CDF Central Calorimeter, R. G. Wagner et al., Nuclear Instruments and Methods, **A267**, 330 (1988).

- [16] Phototube Testing for CDF, T. Devlin et al., Nuclear Instruments and Methods, **A268**, 24 (1988).
- [17] CDF Central Muon Detector, G. Ascoli et al., Nuclear Instruments and Methods, **A268**, 33 (1988).
- [18] The CDF Forward Muon System, K. Byrum et al., Nuclear Instruments and Methods, **A268**, 46 (1988).
- [19] A Leveling System for the CDF Central Muon Chambers, G. Ascoli et al., Nuclear Instruments and Methods, **A268**, 41 (1988).
- [20] CDF Front End Electronics: The RABBIT System, G. Drake et al., Nuclear Instruments and Methods, **A269**, 68 (1988).
- [21] FASTBUS Data Acquisition for CDF, E. Barsotti et al., Nuclear Instruments and Methods, **A269**, 82 (1988).
- [22] A Two-Level Fastbus Based Trigger System for CDF, D. Amidei et al., Nuclear Instruments and Methods, **A269**, 51 (1988).
- [23] CDF Central Muon Level-1 Trigger Electronics, G. Ascoli et al., Nuclear Instruments and Methods, **A269**, 63 (1988).
- [24] A Fast Hardware Track-Finder for the CDF Central Tracking Chamber, G. W. Foster et al., Nuclear Instruments and Methods, **A269**, 93 (1988).
- [25] Integration of the ACP Multiprocessor Farm with the CDF Fastbus Data Acquisition System, B. Flaughner et al., IEEE Transactions on Nuclear Science, **NS-34**, 865 (1987).
- [26] Level 3 System at CDF, J. T. Carroll et al., Nuclear Instruments and Methods, **A263** 199 (1988).
- [27] CDF Physics Goals and Upgrade Plans for the 1991 Run. Fermilab, CDF Note CDF/DOC/CDF/CDFR/1039, October, 1989, (unpublished).
- [28] Transverse Momentum Distribution of Charged Particles Produced in $\bar{p}p$ Interactions at $\sqrt{s} = 630$ and 1800 GeV, F. Abe et al., Phys. Rev. Lett. **61**, 1819 (1988).
- [29] Pseudorapidity Distributions of Charged Particles Produced in $\bar{p}p$ Collisions at $\sqrt{s} = 630$ and 1800 GeV, F. Abe et al., Phys. Rev. **D41**, 2330 (1990).
- [30] Measurement of the Inclusive Jet Cross Section in $\bar{p}p$ Collisions at $\sqrt{s} = 1.8$ TeV, F. Abe et al., Phys. Rev. Lett. **62**, 613 (1989).
- [31] A Measurement of W Boson Production in 1.8 TeV $\bar{p}p$ Collisions, F. Abe et al., Phys. Rev. Lett. **62**, 1005 (1989).

- [32] Limits on the Masses of Supersymmetric Particles from 1.8 TeV $p\bar{p}$ Collisions. F. Abe et al., Phys. Rev. Lett. **62**, 1825 (1989).
- [33] Dijet Angular Distributions from $\bar{p}p$ Collisions at $\sqrt{s} = 1800$ GeV, F. Abe et al., Phys. Rev. Lett. **62**, 3020 (1989).
- [34] K_s^0 Production in $\bar{p}p$ Interactions at $\sqrt{s} = 630$ and 1800 GeV, F. Abe et al., Physical Review **D40**, 3791 (1989).
- [35] Search for Heavy Stable Charged Particles in 1.8-TeV $\bar{p}p$ Collisions at the Fermilab Collider, F. Abe et al., Phys. Rev. Lett. **63**, 1447 (1989).
- [36] A Measurement of D^* Production in Jets from $\bar{p}p$ Collisions at $\sqrt{s} = 1.8$ TeV, F. Abe et al., Physical Review Letters **64**, 348 (1990).
- [37] The Two-Jet Invariant Mass Distribution at $\sqrt{s} = 1.8$ TeV, F. Abe et al., Physical Review **D41**, 1722R (1990).
- [38] Measurement of the Jet-Broadening Parameter, Q_T , in $\bar{p}p$ Collisions at $\sqrt{s} = 1.8$ TeV, F. Abe et al., (In preparation, to be submitted to Phys. Rev. D).
- [39] Two Jet Differential Cross Sections in $\bar{p}p$ Collisions at $\sqrt{s} = 1.8$ TeV, F. Abe et al., Physical Review Letters **64**, 157 (1990).
- [40] Jet Fragmentation Properties in $\bar{p}p$ Collisions at $\sqrt{s} = 1.8$ TeV, F. Abe et al., (submitted to Phys. Rev. Lett.).
- [41] K. Alpgard et al., Phys. Lett. **115B**, 71 (1982).
- [42] G. J. Alner et al., Z. Phys. **C40**, 81 (1986).
- [43] G. J. Alner et al., Phys. Rep. **154**, 247 (1987).
- [44] D. Antreasyan et al., Phys. Rev. **D19**, 764 (1978).
- [45] G. J. Alner et al., Nucl. Phys. **B258**, 505 (1985).
- [46] Measurement of the Mass and Width of the Z^0 Boson at the Fermilab Collider, F. Abe et al., Phys. Rev. Lett. **63**, 720 (1989).
- [47] A Search for the Top Quark in the Reaction $\bar{p}p \rightarrow$ Electron + Jets at $\sqrt{s} = 1.8$ TeV, F. Abe et al., Physical Review Letters **64**, 142 (1990).
- [48] Search for New Heavy Quarks in Electro-Muon Events at the Fermilab Tevatron, F. Abe et al., Physical Review Letters **64**, 147 (1990).
- [49] Measurement of the Ratio $\sigma(W \rightarrow e\nu)/\sigma(Z \rightarrow ee)$ in $\bar{p}p$ Collisions at $\sqrt{s} = 1.8$ TeV, F. Abe et al., Physical Review Letters **64**, 152 (1990).

- [50] Search for a Light Higgs Boson at the Tevatron Proton-Antiproton Collider, by The CDF Collaboration, Physical Review **D41**, 1717R (1990).
- [51] New Top Results From CDF, by J. Walsh, Seminar presented at FNAL, March, 1990.
- [52] P. Langacker, Phys. Rev. Lett. **63**, 1920 (1989).
- [53] P. Nason, S. Dawson and R. K. Ellis, Nucl. Phys. **B303**, 607 (1988).
- [54] G. Altarelli et al., Nucl. Phys. **B308**, 724 (1988).
- [55] 'Detecting Very Massive Top Quarks at the TEVATRON', H. Baer et al., University of Wisconsin Preprint MAD/PH/540, Madison, Wisconsin, January, 1990.
- [56] Workshop on Top, Breckenridge, CO, August, 1989.
- [57] S. L. Glashow and E.E. Jenkins, Phys. Lett. B196, 233 (1987).
- [58] V. Barger and R. J. N. Phillips, Phys. Rev. D40, 2875 (1989).
- [59] S. Ellis, Z. Kunszt and D. Soper, Phys. Rev. **D40** 2188 (1989); U. of Oregon Preprint OITS 436 (1990).
- [60] E. Eichten, G. Kane and M. Peskin, Phys. Rev. Lett. **50**, 133 (1983).
- [61] J. Bagger, C. Schmidt, S. King, Phys. Rev. **D37** 1188 (1988).
- [62] E. Eichten, FERMILAB-Pub-85/178-T (1985).
- [63] E. Eichten and K. Lane, Phys. Lett. **222** 274 (1989).
- [64] P. Arnold and M.H. Reno, FERMILAB-Pub-88/168 (1988).
- [65] Martins, Roberts and Stirling, Z. Phys. **C42**, 277 (1989).
- [66] I.I. Bigi in Proceedings of the Workshop on Linear Collider *B* Factories, UCLA 1987, G. Stork editor, World Scientific, Singapore.
- [67] H. Albrecht et al., Phys. Lett. **192B**, 245 (1987).
- [68] A. Jawahery, in Proceedings of the XXIV International Conference on High Energy Physics, Munich, editors: R. Kotthaus and J. Kuhn, Springer-Verlag Berlin, Heidelberg 1989.
- [69] A. Brandt et al., Proposal to the CERN SPSC, CERN-SPSC/88-3 SPSC/ P238, January 1989.
- [70] CTC Upgrade Plans for 1991 and 1993 by A. Mukherjee et al., CDF Note CDF/DOC/TRACKING/CDFR/1151, 1990.

- [71] Forward Muon Resolution, by D. Carlsmith, CDF Note CDF/ANAL/MUON/CDFR/1111, 1989.
- [72] An Upgraded CDF Data Acquisition System, by G. Drake et al. CDF Note CDF/DOC/CDF/CDFR/1147, 1990.
- [73] Preliminary Design for the 1993 Level 0 Card and Level 0 Crate, by M. Miller et al., CDF Note CDF/DOC/TRIGGER/CDFR/1167, 1990.
- [74] A Proposal to Convert CDF to ACNET, by R. Johnson, CDF/MEMO/ONLINE/CDFR/1112, Fermilab, January, 1990.
- [75] Calibrations of the Upgraded CDF, by S. Hahn, CDF Note CDF/DOC/ONLINE/PUBLIC/1150, 1990.